UNIVERSITY OF SOUTHAMPTON

FACULTY OF ENGINEERING, SCIENCE AND MATHEMATICS

School of Civil Engineering and the Environment

Modelling Excavations in Discontinuous Rock Using the Distinct Element Method

by

Weiyu Bao

Thesis for the degree of Doctor of Philosophy

September 2005

UNIVERSITY OF SOUTHAMPTON

ABSTRACT

FACULTY OF ENGINEERING, SCIENCE AND MATHEMATICS
SCHOOL OF CIVIL ENGINEERING AND THE ENVIRONMENT

Doctor of Philosophy

Modelling Excavations in Discontinuous Rock Using the Distinct Element Method

by Weiyu Bao

The presence of discontinuities in rock mass distinguishes rock mechanics primarily as a study of discontinua. The behaviour of rock mass is significantly affected by the activity of excavation, which is usually a complex three-dimensional and dynamic process. The aim of the thesis is to investigate appropriate ways of modelling and analysis of excavations in discontinuous rock using the distinct element method. The distinct element method is suitable for problems involving assemblages of discrete blocks connected by interfaces. Discontinuous rock mass can be seen as such systems.

This investigation is carried out using a case study of the deep excavation of the permanent shiplock of the Three Gorges Project in China. A three-dimensional model (using the 3-Dimensional Distinct Element Code, 3DEC) is developed to simulate the construction of the shiplock by multi-staged excavation. The model is validated using available field data. The significance of modelling individual discontinuities and the excavation damaged/disturbed zone (EDZ) is demonstrated. A parametric study is carried out to investigate the sensitivity of the model to the properties and constitutive models of discontinuities, rock blocks and the EDZ. The sensitive parameters identified include discontinuity stiffness, rock modulus and simulation of EDZ. The model may be sensitive to joint friction angle depending on the overall discontinuity orientation relative to excavation, while it is generally insensitive to the other strength parameters of the discontinuities and rock blocks. The elastoplastic model (Mohr-Coulomb model) simulates the behaviors of both discontinuities and rock blocks better than the elastic model when material failure is present.

To assess the importance of using a three-dimensional model rather than the two-dimensional models usually employed in practice, a two-dimensional model (using the Universal Distinct Element Code, UDEC) is also developed. Its results are compared with field data and the results of the three-dimensional model. The three-dimensional model is found to reproduce the behaviour of rock mass better because of the more realistic assumptions made on stress conditions and discontinuity representation.

List of Contents

List of Contents

List of Figures

List of Tables

List of Figures

List of Tables

Acknowledgements

Finally, I can draw a period to the writing up of my Ph.D. thesis after years of struggling. It has been a long and enduring journey, but with joy and excitement.

I would like to thank my supervisors Dr Antonis Zervos and Prof. William Powrie for their patience and enthusiasm throughout the period, particularly for Antonis? invaluable input and editorial expertise in late stages. I would also like to extend my thanks to Mr Richard Harkness for his unreserved enlightening discussions and assistance.

It is gratefully acknowledged that Prof. Weishen Zhu and Prof. Shucai Li provided the field data and kindly offered me a chance to work and collect data in the CAS Wuhan Institute of Rock and Soil Mechanics, in Wuhan of China in 2002.

I would also like to thank all members of my family, the old ones and the young ones for their constant encouragement, supporting me and making me smile.

I am extremely grateful for the companion and extensive help from my fellow postgraduates and colleagues: Qinglai Ni, Joel Smethurst, Jo Clark, Martin Rust, Michelle Rust, Andy Cresswell, Toby Hayward, Steve Cox, Jeff Priest, Ming Xu, Xiangbo Qiu; and personal friends, old school mates and sports team mates in tennis, badminton and volleyball: Hee Thong How, Moss Sathoon, Yongqiang Zhuo, Lewis Park, Jia Liu and many others. You all have been cast in my memory of Southampton.

Thanks also go to Scott Wilson and my colleagues in the company who offered convenience in completing my thesis.

Chapter 1 Introduction

1.1 Introduction

Rocks are the principal subject of study in the science of rock mechanics. In contrast to other branches of geotechnical engineering such as soil mechanics wherein the materials are generally regarded as continua, the presence of discontinuities in rocks makes rock mechanics primarily a study of discontinua.

The term "discontinuity" describes all of the structural features that are pervasive in rocks, such as joints, faults, bedding, fissures, veins, foliations and more complex shear zones and altered contacts. The discontinuities dominate the behaviour of discontinuous rock mass. A substantial part of the deformation of rock mass, and sometimes even its failure in macroscope, can be attributed to slips of blocks along discontinuities rather than strain of the intact rock material. Therefore, in modelling excavations in discontinuous rock, it is important to take into account the discontinuities explicitly.

A numerical method commonly used to model the behaviour of discontinuous rock mass is the distinct element method. The advantage of this method is that it treats discontinuous rock mass as an assemblage of discrete blocks connected by interfaces that are able to simulate the motions (including large displacements of slip and opening) along discontinuities. However a systematic way and unified guidance are still lacking for simulating excavations in discontinuous rock using the distinct element method in various aspects.

Discontinuities are three-dimensional in nature and their deformation patterns are controlled by the spatial orientations and dips. Excavations are often complex three dimensional and dynamic processes; therefore they affect the behaviour of rock mass in all three dimensions depending on the spatial geometry of the excavation.

Despite the three-dimensional characteristics of the discontinuities and excavations, it is common in practice to use two-dimensional models to analyse excavations in discontinuous rock mass because they are easier to use and computationally cheaper. In particular two-dimensional models are suitable for cases where the spatial distribution of dominant discontinuities has a particular relationship to the problem geometry e.g. where discontinuity strikes are parallel to a tunnel or excavation axis, so that the rock mass behaves largely as in plain strain conditions. However this is rare in practice, and often the out-of-plane behaviour of

rock mass could be equally important to its in-plane behaviour. In such cases, two-dimensional models are inadequate to simulate the excavations of discontinuous rock mass because they compromise the effects of individual discontinuities and/or the three-dimensional characteristics of discontinuities and excavations, both of which are important for the characterization of the behaviour of discontinuous rock mass.

On the other hand, three-dimensional models are more difficult to validate because more information is needed and more computationally expensive, but they can simulate the reality more closely and reproduce richer deformation modes.

This research first highlights some of issues related to three-dimensional modelling using the distinct element method, where individual discontinuities and the three-dimensional characteristics of discontinuities and excavations can be taken into consideration. Secondly a comparative study between two-dimensional and three-dimensional distinct element modelling is carried out to explore the difference between their predictions and to discuss their suitable applications in practice.

1.2 Objectives

The aim of this project is to investigate appropriate ways of modelling and analysis of excavations in discontinuous rock using the distinct element method. Particular reference is made to data from the Three Gorges Dam Project. The specific objectives are:

1) To collate geotechnical analysis with field monitoring data from the shiplock of the Three Gorges Project;

2) To carry out a critical appraisal of methods of analysis of discontinuous rock using the distinct element method with reference to a parametric study based on the Three Gorges Project;

3) To study the influence of discontinuities on the behaviour of rock mass, particularly the effects of their mechanical properties and spatial distribution;

4) To investigate appropriate ways of taking into account the influence of excavation on the surrounding rock mass;

5) To compare the suitability of two-dimensional and three-dimensional distinct element modelling to model excavations in discontinuous rock.

1.3 Structure of the thesis

The thesis is divided into chapters as follows:

Chapter 2 Background

The significance of discontinuities and the effect of excavation on the behaviour of rock mass are discussed. The numerical methods available and the difficulties in modelling excavation in discontinuous rocks are reviewed.

Chapter 3 Three Gorges Project and the Shiplock

The geological conditions, material properties, structure of the shiplock, construction sequence, anchorage system and field instrumentation are presented.

Chapter 4 Case Study: Analysis of Field Data

The deformation monitoring data from survey measurements and inclinometers are presented and the factors influencing deformations are discussed. The deformations of Sec#17 and #20 of the shiplock are characterised and the extent to which relative movements occurred by slip along discontinuities is investigated.

Chapter 5 Construction and Validation of a Numerical Model for the Shiplock

This chapter presents how the numerical model is constructed and the in situ conditions simulated. The model is validated by comparisons with field data.

Chapter 6 Numerical Analysis

A program of parametric study of discontinuity properties, rock block properties and the assumed extent of the excavation damaged/disturbed zone (EDZ) of surrounding rock is presented. Results are compared with field data. The difference between 3D and 2D modelling predictions is investigated.

Chapter 7 Summary, Conclusions and Recommendations

This chapter summarizes the conclusions from research project. Recommendations for future work are made.

Chapter 2 Background

In this chapter, the significance of discontinuities and the effect of excavation on the behaviour of rock mass are discussed. The numerical methods available and the difficulties in modelling excavation in discontinuous rocks are reviewed.

2.1 Significance of discontinuities

Rock mass is distinguished from many other materials by the presence of discontinuities in it. The discontinuities play a dominant role in the overall behaviour and stability.
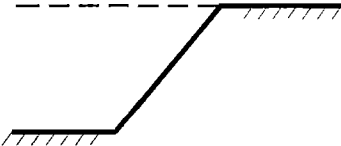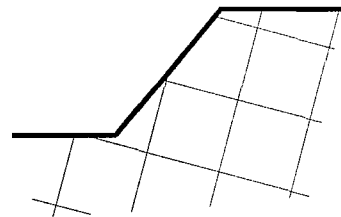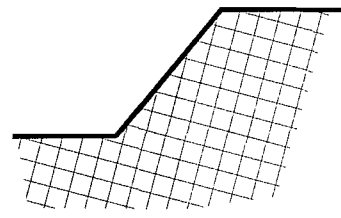
(i) Treat as uniform. (continuum)

Parameters from laboratory or in situ tests considered representative of mass properties.

(ii) Treat as discontinuous (discontinuum)

Discontinuities are considered individually.

(iii) Treat as uniform (equivalent continuum)

Influence of discontinuities is considered by reducing rock mass properties.

Fig2.1 Effect of scale of discontinuity (modified from Hayward, 2000)

It is well recognized that the scale of discontinuities relative to the dimensions of an excavation in rock has an important effect on the behaviour of rock mass (Bandis, 1981; Hoek, 1983; Cunha, 1990). As shown in Fig2.1, rock mass can be classified into three groups according to the scale of the discontinuities: (i) continuous, (ii) discontinuous, (iii) equivalent-continuous types. In general, continuum approaches can be used to analyze rock mass without discontinuities (Fig2.1, Type (i)), while discontinuum approaches can be used to simulate

4

moderately fractured rock mass of Type (ii) in which the response of individual discontinuities is of great importance. Type (iii) rock mass is for highly fractured or weathered rock mass where the orientation and inclination of discontinuities present no preferential sliding planes. Usually the equivalent-continuum approaches are more straightforward for rock mass of Type (iii) than discontinuum approaches, because it is almost impossible to identify the location, dimensions and mechanical properties of all the discontinuities involved. The equivalent-continuum approach treats rock mass as continua with reduced strength and stiffness to account for the effect of discontinuities.

However, it is rare that rock mass in a practical project fall clearly into one of these groups. A combination of discontinuum and continuum solutions is often used. The major discontinuities that dominate the behaviour of the rock mass are treated individually in modelling while other discontinuities are modeled by an equivalent-continuum approach. There is no definite guidance on which type of rock mass model should be used for different discontinuity orientations and spacings.

The relationship between the spatial distribution of discontinuities and excavation geometry may have an important influence on the stability of the excavation as shown in Fig2.2. The stability of an excavation also depends on the discontinuity spacing (e.g. Hoek & Bray, 1983, see Fig2.2). The excavation becomes less stable as more blocks are free to fall into it when the discontinuity spacing is decreased.

| (a) Stable | (b) Potentially unstable | (c) Potentially more unstable |
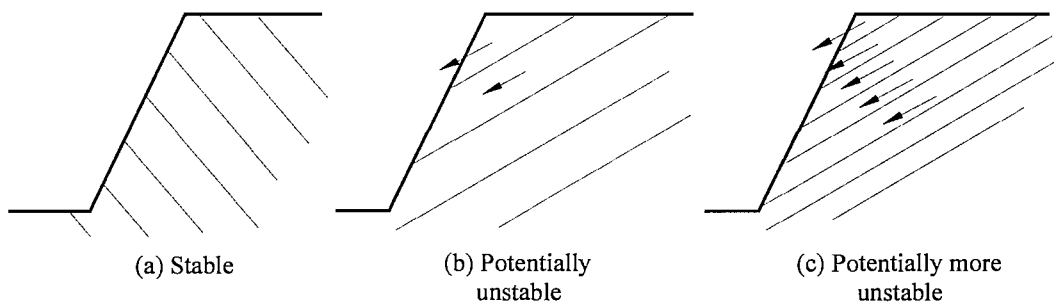
Fig2.2 Effect of discontinuity on stability of excavation

2.2 Properties of discontinuities

Discontinuities are characterized by physical parameters such as orientation, spacing, persistence, roughness, aperture and filling (ISRM, 1978; Weissbach, 1978; Barton & Bakhtar, 1983; Thomas, 1987; Heliot, 1988; Bandis, 1990). The mechanical properties of a discontinuity are closely related to its roughness, aperture, filling and/or the strength of the intact rock material.

Discontinuities show little or no tensile strength. The strength criteria proposed for discontinuities are usually based on their shear strength, e.g. the Mohr-Coulomb criterion, Goodman (1976), the Barton-Bandis criterion (Barton, 1973, Barton & Bandis, 1990), and the Saeb-Amadei model (1992). It is well recognized that the shear strength of joints depends on the effective normal stress and varies with shear displacement (e.g. Leichnitz, 1985; Barton et. al., 1985) (Fig2.3 (a)). For given normal stress and shear displacement, the shear strength of joints will depend on the relative contributions of shear dilation and basic friction components, which are in turn controlled by the surface roughness of the joint and asperity strength. The presence of water in a rock discontinuity may decrease the actual shear strength of the discontinuity by reducing the effective stress across it.

A discontinuity may close when subject to normal compressive load and shear when subject to shear load. The closure and shear deformations of discontinuities are related to the stress state by a normal stiffness and a shear stiffness. It is generally accepted that the normal stiffness of a discontinuity depends on the effective normal stress (Barton, 1973; Bandis, 1990). Increasing normal load causes a strongly non-linear reduction of the aperture, whereas on unloading the joint responds in a hysteretic and inelastic manner (Bandis, 1983). The shear stiffness depends on both the normal and shear stresses as shown in Fig2.3, where a typical plot of shear stress and normal displacement vs shear displacement of a discontinuity is shown.
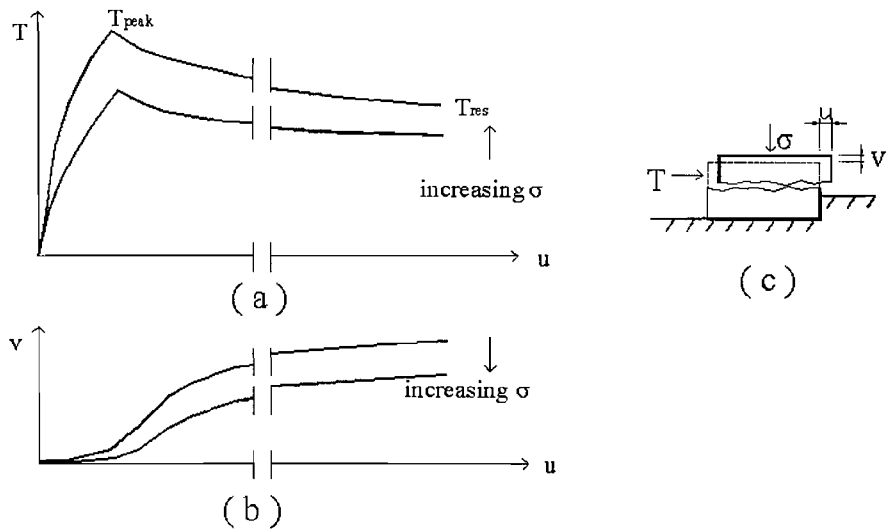
Fig2.3 Deformation of discontinuity (a) Shear stress vs shear displacement curves, (b) Normal displacement vs shear displacement (USACE, 1994)

During shearing of a joint, a component of normal deformation is produced known as dilation (Fig2.3 (a) and (c)). The joint dilation increases the shear strength of a joint and is characterized by a dilation angle. Joint dilation is strongly affected by boundary stiffness as indicated by Goodman (1980) and Skinas et. al. (1990). If the rock surrounding the joint is

deformable enough to absorb the normal displacements associated with dilatancy, shearing will take place under constant normal stress. Otherwise if the surrounding rock is stiff enough, dilation will be partially inhibited and normal stress will increase.

The presence of filling in a discontinuity has an adverse influence on its strength. The geometrical relation between the thickness of filling and the size of the asperities dictates the behaviour of a filled joint during shearing (Bandis, 1993; Toledo & Freitas, 1993). If the filling is thin, the effect will be a reduction in the basic friction angle of the joint. If the filling is very thick, the behaviour will be controlled by the filling material alone. Therefore, geological structures such as major filled faults or veins in rock mass may have a strong influence on the behaviour of rock mass. For discontinuities with fine-grained filling, the past stress history determines whether the filling behaves as a normally consolidated or overconsolidated soil. If significant displacement has occurred in the past, it makes little difference whether the material is normally consolidated or overconsolidated since it will be at or near its residual strength (USACE, 1994).

Although joint properties can be derived by analytical methods for some simplified cases (Singh, 1973; Gerrard, 1982; Fossum, 1985), the mechanical properties of discontinuities are conventionally measured in laboratory or field tests. However, it is important to recognize that joint properties measured in the laboratory are not always representative of those for real joints in the field (Pratt, 1974; Barton & Choubey, 1977; Bandis, 1981). Scale dependence of joint properties remains a major question in rock mechanics. Published results from field tests are limited.

2.3 Behaviour of discontinuous rock mass

Intact hard rock is usually considered to be a homogeneous continuous brittle material with a high strength (Griffith, 1924). Various failure criteria have been proposed for intact rock (Griffith, 1924; Jaeger & Cook, 1969; the Coulomb criterion; Bieniawski, 1974; Hoek & Brown, 1980 and 1988).

Rock mass are largely discontinuous, inhomogeneous, nonlinear and anisotropic because of the existence of discontinuities. When the discontinuities involved cannot be considered individually, their effects are taken into account by modelling them as an equivalent-continuum. Discontinuous rock treated as an equivalent-continuum usually has a reduced strength, stiffness and modulus and increased deformation compared with intact rock. The rock mass may exhibit plastic and creep behaviour. Since discontinuities in the rock mass offer little or no resistance to tensile stress, the tensile strength of a fractured rock mass is low compared with its shear and compressive strength.

One of the existing key problems is to determine the properties of rock mass when treated as an equivalent continuum. The mechanical properties of rock mass can be obtained by laboratory tests or field tests. However, there is potentially a scale effect involved and the cost of an extensive testing programme is high. In practice, therefore, it is common to derive the properties of the equivalent continuum analytically or empirically. Numerical methods are also used to investigate the effect of discontinuities on the equivalent continuum.

Analytical methods are limited to a few idealised cases for which mathematical formulation is possible, e.g. rock with two or three orthogonal joint systems (Amadei et. al., 1993). Empirical methods include rock mass classification systems that deduce the properties of discontinuous rocks from readily available discontinuity characterization and test data. The rock mass classification systems enjoy wide application because limited information is required to use them. Among the numerous classification systems, the most widely used include: Terzaghi's Rock Mass Classification (Terzaghi, 1946); Lauffer's Classification (Lauffer, 1958); Deere's Rock Quality Designation (RQD) (Deere, 1968); the Rock Structure Rating (RSR) Concept (Wickham et. al., 1972); the Geomechanics System (Bieniawski, 1979); and the Rock Tunnelling Quality Index Q-System (Barton et. al., 1974).

The effect of discontinuities on the properties of rock mass modelled as an equivalent continuum has been investigated numerically by Cundall (1988), Kulatilake et. al. (1992, 2001), Cai & Horii (1992), Zhang & Lu (1998), and by physical model tests (Yang et. al., 1998).
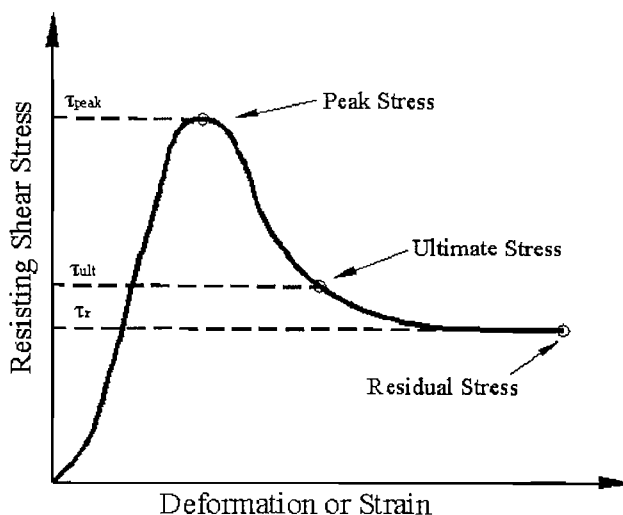
Fig2.4 Shear test failure as defined by peak, ultimate, and residual stress levels (after Nicholson, 1983)

The strength criteria proposed for discontinuous rock mass are generally expressed in terms of peak, residual, or ultimate shear strength, or as the shear strength at a limiting strain or displacement as illustrated in Fig2.4. The commonly used constitutive models for discontinuous

rock mass include the Mohr-Coulomb model (Fig2.5), bilinear model (Patton, 1966; Goodman, 1980) (Fig2.6), and the Hoek-Brown model (Hoek & Brown, 1980 and 1997; Hoek, 2000). The Mohr-Coulomb model is still widely used in spite of the drawbacks discussed by Brady & Brown (1993) because the required input parameters are more widely available than the parameters needed by the other models. Constitutive models considering discontinuity-induced anisotropy have been proposed by Duncan & Goodman (1968), Yoshida & Horii (1998) and Nawrocki et. al. (1999).
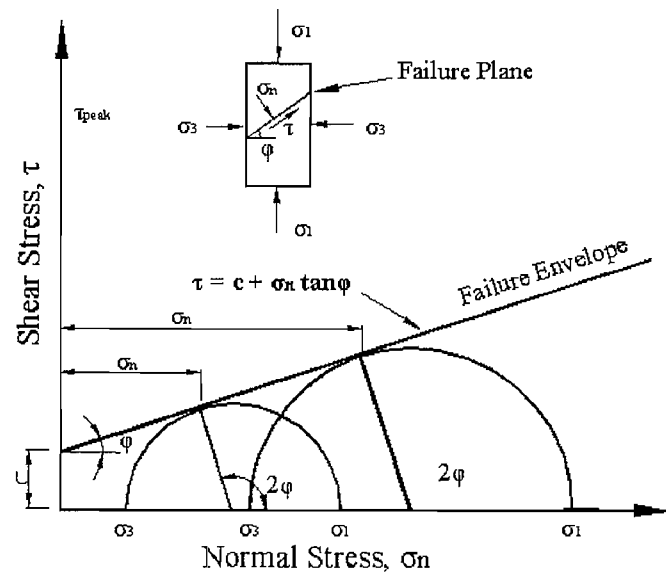
Fig2.5 Mohr-Coulomb failure envelope (after USACE, 1994)
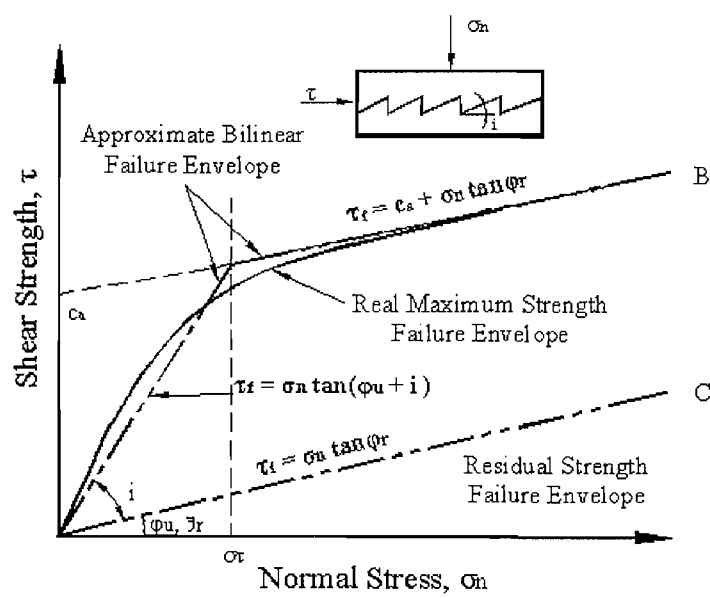
Fig2.6 Typical approximate bilinear and real curvilinear failure envelopes for discontinuous rock (USACE, 1994)

The effect of discontinuities on the deformation moduli of rock mass has been investigated widely, e.g. analytically by Goodman & Duncan (1971); and numerically by Gerrard (1982), Fossum (1985), Singh (1973), Chen (1989) and Wei & Hudson (1986). Heuze (1980) concluded that the deformation modulus of rock mass mostly ranges between 20% and 60% of the modulus measured on intact rock specimens in the laboratory. However due to the complex in situ conditions, there is no set guidance to evaluate the effects of discontinuities on the deformability of rock mass.

2.4 Excavation Disturbed/Damaged Zone (EDZ)

It is generally accepted that any excavation is surrounded by zones that have been damaged or disturbed due to the stress redistribution as a result of excavation. Such zones are often referred to as Excavation Disturbed Zone or Excavation Damaged Zone. Normally Excavation Damaged Zone is limited to the part of rock mass closest to the excavation which has undergone significant changes in geotechnical and hydraulic properties and where fracture propagation and/or the development of new fractures have occurred. Excavation Disturbed Zone is a zone further into the rock mass in which no major changes in geotechnical and hydraulic properties have occurred and changes in state are considered to be dominant (McEwen, 2003 and Emsley, et. al. 1997). However, in literature the term "EDZ" is used to refer to both Excavation Damaged Zone only and a combination of Excavation Damaged Zone and Excavation Disturbed Zone. In this study, the term "EDZ" will refer to the combination of both zones.

The majority of studies on EDZ are related to deep underground repositories for nuclear waste, in which EDZ is a major concern as it could produce adverse permeable pathways resulting in rapid transport of radionuclides in the rock mass immediately adjacent to the repository. A number of Underground Rock Laboratories (URL) have been set up throughout the world in different rock types to study the effect of EDZ on repositories. Studies find out that the definition and properties of EDZ are influenced by the type of host rocks, which are normally classified into four groups: crystalline rock, rock salt, indurated clay and plastic clay (European Commission CLUSTER, 2003 and Tsang, et. al., 2004). EDZs have been studied most frequently in crystalline rocks including the Canadian URL at Pinawa, both the Stripa and the 胴p? in Sweden, the Grimsel Test Site in Switzerland and at the Kamaishi in Japan. Most of the granite of TGP site is typical crystalline rock. Therefore this literature review focuses mainly on the crystalline rock.

Through these URLs, progressions on the study of EDZ in hard rock have been published in literature and various EDZ Conference Workshops including the NEA Workshop (NEA ISAG, 1998), the CNS Workshop (CNS, 1996), SEDE Workshop on EDZ (NEA, 2002) and CLUSTER EDZ Conference (European Commission CLUSTER, 2003). The main findings related to hard rock conditions can be summarized as follows (McEwen, 2003).

2.4.1 The concept and understanding of EDZ

The existence of EDZ as both Damaged Zone and Disturbed Zone is well recognized around excavations in hard rock. The extent and properties of EDZ depend upon the system-specific circumstances (rock type, in-situ conditions, geometry / orientation of excavated rooms, excavation techniques, liner design & emplacement, etc.). EDZ cannot be avoided but measures can be taken to minimise its effects such as a suitable support system, an appropriate layout of the underground openings and use of adequate excavation techniques.

Tsang et. al. (2004) proposed that three basic sources of damage be involved during the excavation stage. First, there is the potential for damage caused by the excavation activity itself; second, there are mechanical changes caused by stress redistribution around the excavation; and, third, there are effects of support system on rock deformation by anchorage or shotcrete etc.

For hard and brittle crystalline rocks, the excavation activity could by itself induce significant damage, depending on the excavation method used.

The stress redistribution caused by the excavation is the key cause of the EDZ in hard rocks, giving rise to tension, compression, and shear or deviatoric stresses in different parts of the rock around the opening. The EDZ in the crystalline rock type is more visible than in other three less competent rock types (Tsang et. al., 2004). If the rock does not fail, tangential compression occurring near the opening could reduce its radial permeability significantly by a factor of five or so. Therefore the effects on the repository system due to the formation of the EDZ may not all be negative and may not, in any case, be very significant. However, the permeability parallel to the drift wall is increased significantly, as much as by one order of magnitude (Tsang et. al., 2004), because of radial tensile stresses and shear stresses working to open existing fractures or create new ones. The effect most probably depends on the rock structure. The effect is found largest at the tunnel wall and extends about one drift radius into the rock as reported by Tsang et. al. (2004). When fracturing of the host rock is intense, the EDZ does not appear to represent an important issue, e.g. at Yucca Mountain (McEwen, 2003). In general, stress-induced excavation disturbance has much less influence on the hydraulic conductivity than excavation activities themselves, but it affects the rock to a larger distance.

An example from the Stripa project is reported by Pusch (2003) in which the EDZ around a blast tunnel extends to about 1 m from the periphery and is at least 100 times more conductive than the virgin rock. The surrounding stress-induced EDZ extends to about 3 m from the periphery and has an axial conductivity that is about 10 times higher than that of the virgin rock, while the radial conductivity is about 5 times lower than this conductivity.

Unlike in plastic rocks like salt or clay, which have some self-healing capacity, the structural damage in crystalline rock is irreversible.

Original stress condition in crystalline rocks is another important factor influencing the EDZ. EDZ in high stress environments, e.g. at the Canadian URL, are more extensive and more significant than those in low stress environment, e.g. in Scandinavia repositories, particularly with respect to providing continuous extension fractures parallel to tunnels. However, contradictory results are observed in a blasted test tunnel conditions of AECL project in Canada. The field data show a low conductivity in the EDZ around the tunnel in the very high stress conditions, in contrast to results from the Stripa project in Sweden (Pusch, 1989 and 2003).

After all, the EDZ was considered to be a long-term safety issue and have a major effect on the design and effectiveness of seals for repositories in crystalline rocks.

There have been a number of two-dimensional studies on the properties and extent of EDZ associated with underground excavations by Fairhurst & Damjanac (1999), Souley et. al. (1997) and Sellers & Klerck (2000). Analyses considering the spatial characteristics of discontinuities are reported by Damjanac (1996), Konietzky & Marschall (1996), in which the dimensions of both excavations analysed are small (2.4m and 2m diameter tunnels respectively).

2.4.2 Effect of construction methods

As the excavation activities cause significant damages in hard rock, the construction method used is a decisive factor to the EDZ. Comparative studies have been carried out to investigate the different effects of commonly used drill and blast method and tunnel boring machine (TBM) in the Stripa and the Zedex (Emsley et. al., 1997). Thus, if drill and blast methods are used, the EDZ could extend 0.1 to 0.75 m into the rock, increasing permeability by two or three orders of magnitude. If a tunnel boring machine (TBM) is used, the EDZ could be about 1 cm thick, with permeability increased by one order of magnitude. Pusch (2003) also found that the conductivity of a cross section of TBM tunnels is estimated to be no more than about 1 % of that of blasted tunnels. In contrast, such direct excavation damage is not so significant in the other three rock types, especially where a TBM is used (Tsang et. al., 2004).

2.4.3 Method to characterize EDZ

A number of geophysical methods have been used to characterize and measure the extent of the EDZ surrounding excavations in hard rocks. In particular, the acoustic emission-microseismic monitoring technique (AE/MS) has shown to be useful in revealing the extent of damage that develops around excavations during construction. Electrical and electromagnetic methods were also used to obtain hydrogeological information of the EDZ.

2.4.4 Directions of future study on EDZ

The literature shows that good understanding of EDZ have been achieved in deep repositories in hard rocks and some rock mechanics models have been developed to predict the location and extent of the EDZ around deep tunnels in hard rocks. This knowledge and the models are used to design underground excavations with better construction methods (such as improved blast designs), geometries and orientations that could significantly reduce and almost completely eliminate the EDZ in various projects.

It was proposed from last workshops (Tsang et. al., 2004; McEwen, 2003) that future study on EDZ in deep repositories in hard rock ought to address the anisotropic behaviour in deformation and flow within the EDZ,: time-dependency characteristics of EDZ validation of relevant geomechanical, thermal-mechanical and fracture flow models.

2.4.5 Differences between EDZ in repositories and in surface/shallow excavation

Compared to deep repositories in hard rock, the EDZ in shallow or surface excavations are far less studied in hard rock and less well understood. They share the concept and a number of characteristics presented above since both excavations are created in hard rocks. However, there are significant differences between them as summarized in the following (Goodman & Kieffer, 2000; Sheng et. al., 2002).

The excavation geometry for repositories are usually simpler for regular tunnels and drifts while shallow/open excavations are with more irregularities for the sake of functionalities, e.g. the TGP shiplock, underground power plan.

The stress conditions in shallow rocks are very different from those in deep rock. First, the overall stress level is much lower in shallow rocks. Secondly, the stresses in shallow rocks involve significant variations because it is easily affected by topography variation and affected by more geological structures while stresses in deep hard rocks are relatively consistent in a large extent.

In shallow/open excavations, the studies of EDZ focus mostly on deformation control and stability issues. Because of special functions the nuclear repositories serve for, the literature shows more emphasis is put on (a) the hydraulic/hydrogeological, thermal properties of EDZ, and (b) the effects of physical and chemical process on EDZ properties in long term rather than the effects from excavation.

All the differences result in that only a very limited part of the development achieved in repositories can be applied to surface/shallow excavations in rocks.

Unlike a number of URLs set up for repositories EDZ study, little work is found in literature on systematic investigation and characterization of the range and properties of EDZ in shallow/open excavations. Two-dimensional studies on the EDZ in surface excavations have been reported by Deng et. al. (2001) and Sheng et. al. (2002), both of which are based on the Three Gorges Project. Limited work on the EDZ in surface excavations in which three-dimensional effects have been taken into consideration is found in reference.

2.5 Modelling of excavations in discontinuous rock

For excavation in discontinuous rock mass, concerns may arise in two aspects: the overall stability and the conditions of rock mass after excavation.

As far as surface/shallow excavation is concerned, two major categories of analyses are commonly used: slope stability analysis and more complicated stress analysis to serve different requirements of projects. The stress analysis is normally carried out by computer programs, which are based on continuum or discontinuum methods.

2.5.1 Slope Stability Analysis

There are three basic modes of failure of excavations in discontinuous rocks: sliding failure (Fig2.7 (a-b)), toppling failure (Fig2.7 (c-d)) and sloughing failure (Goodman, 1989). The failure mode is controlled by the spatial distribution of discontinuities, the geometry of the excavation and the shearing resistance along discontinuities. Other factors that may trigger slope failure include erosion, ground water, temperature and in-situ stress (USACE, 1994). Accordingly, the available stabilization methods include alteration of slope geometry, dewatering, anchorage, and toe berm protection to prevent slaking and erosion effects.

Most of the conventional methods for rock stability analysis are based on limit equilibrium concept, but differ in the assumptions adopted to arrive to a solution for the factor of safety, e.g. Janbu's method (1973), Sarma's method (1973) and the method of slices. For sophisticated rock slope stability problems involving complexities relating to geometry, material

anisotropy and non-linearity, *in situ* stresses, the presence of groundwater and anchorage, numerical methods have to be used for a better understanding of potential failure mechanisms.

(a) plane sliding   (b) wedge sliding

(c) toppling   (d) block toppling
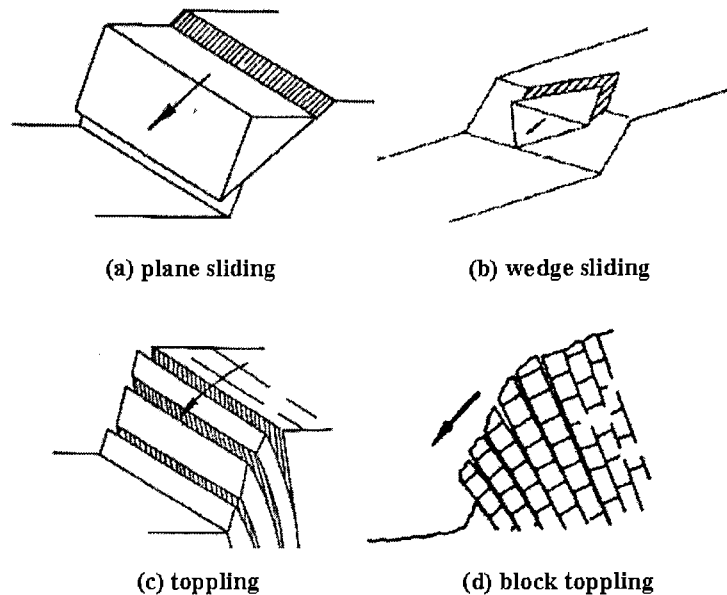
Fig2.7 Failure modes of rock slopes (a) planar sliding (b) wedge sliding (c) toppling (d) block toppling (USACE, 1994)

2.5.2 Stress analysis methods

The numerical methods available for stress analysis in rock mechanics can be grouped into three categories: (i) continuum methods including the finite difference method (FDM), the finite element method (FEM), and the boundary element method (BEM); (ii) discrete methods (or discontinuous methods) including the discrete element method (DEM) and the discrete fracture network (DFN) methods; (iii) hybrid continuum-discrete methods. Comprehensive reviews of numerical methods for rock mechanics have been presented by Jing & Hudson (2002) and Jing (2003).

In discrete methods, the rock in the domain of interest is modelled as an assembly of blocks connected by joints or interfaces. Discontinuities are represented explicitly. Discrete methods are thus suitable for engineering problems in which a finite number of well-defined components (e.g. blocks and discontinuities) dominate the behaviour of the rock mass. The global behaviour of the system depends on the individual behaviour of these components, and on the way they interact with each other. Both the individual behaviour of components and their interaction are usually defined using simple mathematical models.

In continuum methods, the problem domain is usually discretized into a finite number of sub-domains (elements) whose behaviour is approximated by simple mathematical descriptions

with a finite number of degrees of freedom. The discontinuities may be represented explicitly to some extent, using special elements. However, the continuum assumption implies that, at all points in the problem domain, the material cannot be torn open or broken into pieces. All material points originally in the neighborhood of a certain point in the problem domain remain in the same neighborhood throughout the deformation process. Large displacements caused by rigid body motion of individual blocks, including block rotation, fracture opening and complete detachments are impossible in continuum methods such as FDM, FEM or BEM, while they are straightforward to model in discrete methods such as DEM.

The choice between numerical continuum method or discrete method is in line with the characterization of the rock mass behaviour as indicated in Fig2.1. It depends mainly on the problem scale and discontinuity geometry. In general, continuum methods can be used for rock mass with no fractures or with many fractures where the orientation and inclination of discontinuities relative to the excavation geometry present no preferential sliding plane (Fig2.1). If few discontinuities are present, a continuum method can still be used in conjunction with special joint elements to model the discontinuities, provided that complete detachment is not possible. Discrete methods can be used to simulate moderately fractured rock mass of Type (ii) in Fig2.1 in which the response of individual discontinuities is of great importance. The discrete approach should be used in cases where the number of discontinuities that should be incorporated individually is too large for a continuum with joint-elements approach, or where complete detachment of individual blocks is possible.

However, in practice it is usually impossible to consider all discontinuities individually in a discrete model except for a number of important ones, e.g. major faults or veins, so the concept of an equivalent-continuum has to be adopted to incorporate the effect of other discontinuities.

2.5.3 Programs used in this research

In this research, a three dimensional distinct element program 3DEC and its two dimensional version UDEC (Itasca, 1998) are adopted to carried out the numerical analysis.

2.5.3.1 3DEC and UDEC program

The Three Dimensional Distinct Element Code (3DEC) is a commercial software for three dimensional numerical analysis based on the distinct element method for discontinuum modelling (Itasca, 1998). It is an extension of the two-dimensional program, UDEC (Universal Distinct Element Code, Cundall, 1980 and Lemos et. al., 1985). 3DEC can simulate the response of discontinuous media (such as jointed rock mass) subject to either static or dynamic loading. The discontinuous medium is represented as an assemblage of discrete blocks. The

discontinuities are treated as boundary conditions between blocks rather than special elements in the model. Large displacements along discontinuities and rotation of blocks are allowed.

Individual blocks can be either rigid or deformable. Deformable blocks are subdivided into a mesh of finite difference elements, and each element responds according to a prescribed stress-strain law, which can be linear or non-linear. The relative motion of blocks along discontinuities is governed by force-displacement relations for movement in both the normal and shear direction. Such relations for discontinuity deformation can also be either linear or non-linear. The contact forces and displacements at the discontinuities of a stressed assemblage of blocks are found through a series of calculations that trace the movements of each individual block. When a disturbance is applied at the boundary or in the model, movements propagate through the discontinuous medium in a dynamic process. The dynamic behaviour is described numerically using a time-stepping algorithm in which the size of the timestep is selected such that velocities and accelerations can be assumed constant within the timestep. This solution is identical to that used by the explicit finite difference method for continuum numerical analysis.

In this research, 3DEC and UDEC will be used to model one of the key sections in the Three Gorges shiplock. UDEC is a two-dimensional equivalence to 3DEC, but with more simulation capabilities. Efforts were made to ensure that the features and conditions in UDEC models are as close to those of 3DEC models as possible when 2D analysis results from UDEC will be compared with 3D analysis results by 3DEC..

2.5.3.2 Constitutive models for rock blocks

Among the available models for rock blocks in 3DEC and UDEC, three of them, i.e. null, elastic and Mohr-Coulomb model are most commonly used.

A null material is used to represent material that is removed or excavated from the model. The stresses within a null block are automatically set to zero.

The elastic model is available in isotropic and anisotropic form. The isotropic elastic model describes the simplest form of material behaviour, which is for isotropic, continuous materials that exhibit linear stress-strain behavior with no hysteresis on unloading. The anisotropic elastic model is used to represent materials that show a sharp difference in elastic properties for different directions. The model is applicable to the general case of elastic anisotropy; two particular cases of elastic symmetry are also considered explicitly, corresponding to orthotropic and transversely isotropic materials.

The failure envelope for the Mohr-Coulomb model corresponds to a Mohr-Coulomb criterion (shear yield function) with tension cutoff (tensile yield function) (Fig2.5). The shear flow rule is non-associated and the tensile flow rule is associated.

2.5.3.3 Constitutive models for joints

In 3DEC and UDEC, one of the joint models common to both is the commonly used Mohr-Coulomb model with tension cutoff. The shear flow rule is non-associated and the tensile flow rule is associated (Itasca, 1998). This model will be the default model for discontinuities unless stated otherwise.

In 3DEC and UDEC, a continuously yielding model is provided for discontinuities to account for non-linear behaviour such as joint shearing damage, normal stiffness dependence on normal stress, and decrease in dilation angle with plastic shear displacement (Itasca, 1998).

The essential features of the continuously yielding model are the following:

(a) The curve of shear stress/shear displacement tends toward a target or bounding shear strength τ_m for the joint—i.e., the instantaneous gradient of the curve depends directly on the difference between strength and stress.

(b) The target shear strength decreases continuously as a function of accumulated plastic displacement (a measure of damage).

(c) The dilation angle is taken as the difference between the apparent friction angle (determined by the current shear stress and normal stress) and the residual friction angle.

As a consequence of these assumptions, the model can reproduce the commonly observed peak/residual behavior of rock joints. Also, hysteresis is reproduced for unloading and reloading cycles of all strain levels, no matter how small.

Fig2.8 shows a typical stress-displacement curve for monotonic shear loading of a joint under constant normal stress. The shear stress increment is calculated as

$$\Delta \tau = F K_s \Delta u_s \qquad (2\text{-}1)$$

where F is a factor of tangent modulus dependent on the distance from the actual curve to target strength curve τ_m, and K_s is the shear modulus that can be expressed as a function (e.g. a hyperbolic one) of normal stress as far as it is consistent with experiment data.
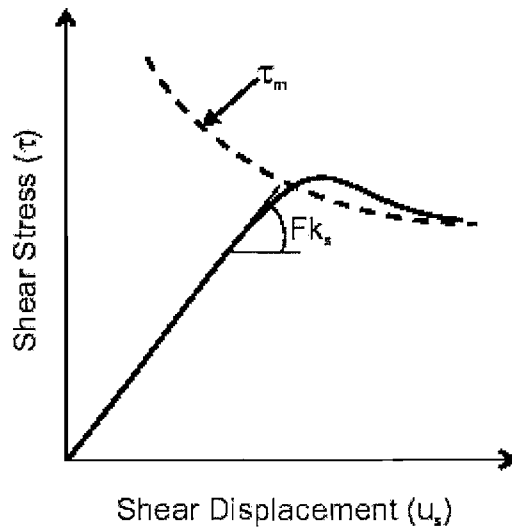
Fig2.8 Continuously yielding joint model: shear stress-displacement curve and bounding shear strength (3DEC Manual, 1998)

2.5.4 Difficulties in modelling excavations in discontinuous rock

The difficulties in modelling and analysing excavations in discontinuous rock can be summarised as follows:

(1) Geological conditions and material properties

Because of limited access underground, the available information on geological conditions including rock properties, discontinuities, in situ stress and groundwater conditions is always limited for rock mechanics problems. Therefore the input parameters for modelling by either the continuous or the discontinuous approach are difficult to obtain.

(2) Conceptual model for rock mass

The appropriate conceptual model for rock mass depends on the discontinuity system. Because both discontinuities and excavation have three-dimensional characteristics, in many cases two-dimensional models are not sufficient to model the behaviour of rock mass. Although general guidance is given on the applications of the continuous and discontinuous approaches, it is difficult to apply in practice as the real discontinuity system is far more complex than any of the simplified cases listed. In numerical modelling of discontinuous rock, it is usually necessary to adopt a combination of the discontinuous approach for important discontinuities and the equivalent-continuous approach for the blocks between. However, the difficulties arise in choosing which discontinuities should be simulated individually and how to determine the properties of the equivalent-continua.

19

Furthermore, the number of discontinuities simulated individually affects the computational efficiency considerably, and a compromise has to be made between an efficient model with fewer discontinuities and a more detailed model with less efficiency. This choice is particularly obvious for three-dimensional models.

(3) Effect of excavation

Excavation is a dynamic process in practice, and often in all three dimensions. The properties of rock mass are influenced continuously by construction activities, especially the rock surrounding the excavation that forms excavation disturbed zones (EDZ). The extent and properties of EDZ change with excavation level and are difficult to estimate as presented in literature research.

Chapter 3 The Three Gorges Project and the Shiplock

3.1 Three Gorges Project

The Three Gorges Hydropower Project is located along the Yangtze River in central China, about 360km upstream of the city of Wuhan (Fig3.1). The hydro scheme is designed to have a total installed capacity of 18,200 MW and will produce 84.7 billion kWh of electricity annually. It has a catchment area of one million km^2. Its benefits will include flood control, power generation and improvements to navigation and water supply for downstream regions.
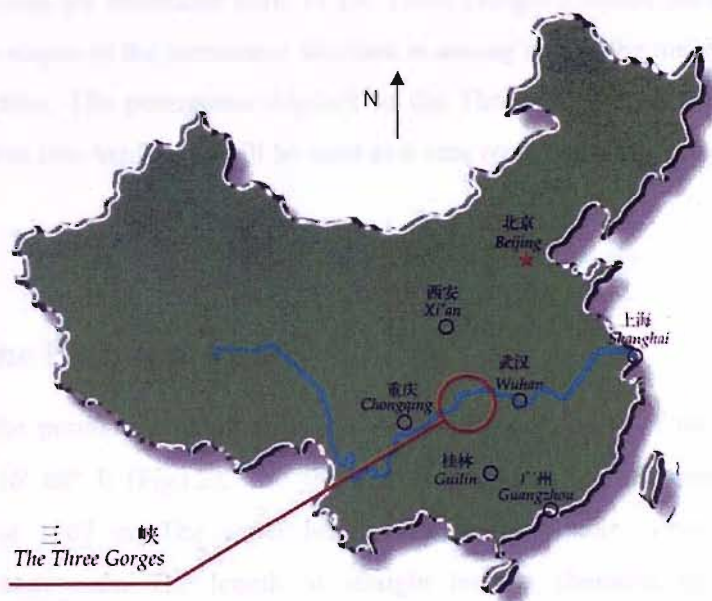
Fig3.1 Position of the Three Gorges Project, China

The main components of the Three Gorges Project include the dam, two power plants and the navigation facilities as shown in Fig3.2. The concrete gravity dam has a total length of 2,309 m along the axis, with the crest elevation at 185 m above sea level and a maximum height of 181 m from the ground. The spillway dam with deep outlets is placed in the middle, with dam sections and the power houses of the hydroelectric station on its two sides. The permanent

navigation structures consist of the permanent shiplock and a shiplift. The design capacity is 50 million tons of annual one-way navigation.

The construction of the Three Gorges Project is planned in three phases of a total period of 17 years:

Phase-1 from 1993 to 1997;

Phase-2 from 1998 to 2003; The major works of phase-2 include phase-2 cofferdams, construction of the spillway, left-bank dam section, the left-bank powerhouse, installation of part of power units, the continuing construction of the permanent shiplock and the shiplift. In 2003, the reservoir water level was raised to an elevation of 135 m above sea level and the first four generators started power operation. The permanent shiplock was put into use.

Phase-3 from 2004 to 2009. This phase will see completion of three major tasks: construction of dam section of 665m long on the south bank side, workshops for 12 generators on the south bank side and the vertical shiplift on the northern bank. Reservoir water level will be raised to 175m above sea level. A total of 26 power-generating units with a combined capacity of 18.2 million kilowatts will go into operation.

Given the enormous scale of the Three Gorges Project, the stability and deformation of the high slopes of the permanent shiplock is among one of the major technical difficulties in the construction. The permanent shiplock of the Three Gorges Project, which is formed by deep excavation into hard rock, will be used as a case record in connection with this study.

3.2 The Permanent Shiplock

The permanent shiplock is placed at the north bank of the Yangtze River, oriented at N110° 56' 08° E (Fig3.2). The shiplock is a double-line five-step flight system with a total length of 1607 m. The water head difference is about 113m between the upstream and downstream ends. The length of straight leading channels are 930m both upstream and downstream while the width of the leading channel is 180m for upstream and 180~220m for downstream. The dimensions of a single shiplock are 280m×37m×5m (length×width× minimum water depth). The shiplock is formed by deep excavation into granite to a maximum depth of 174.5 m below original topography. The average height of the slopes cut out is generally 70m ~120m. The height of the vertical sidewall of the lock is 50m-70m. The rock pillar uncut between the two locks forms the Middle Pier, which is 54m-57m in width and about 50m in height on average. The high slope walls are lined with thin concrete and reinforced by anchorage. The altitudes above datum level of the bottom of each step are 124.5m, 112.75m,

92.2m, 71.45m and 50.7m (Fig3.3). The total excavated volume of the permanent shiplock amounts about 40 million m^3, most of which is hard rock.
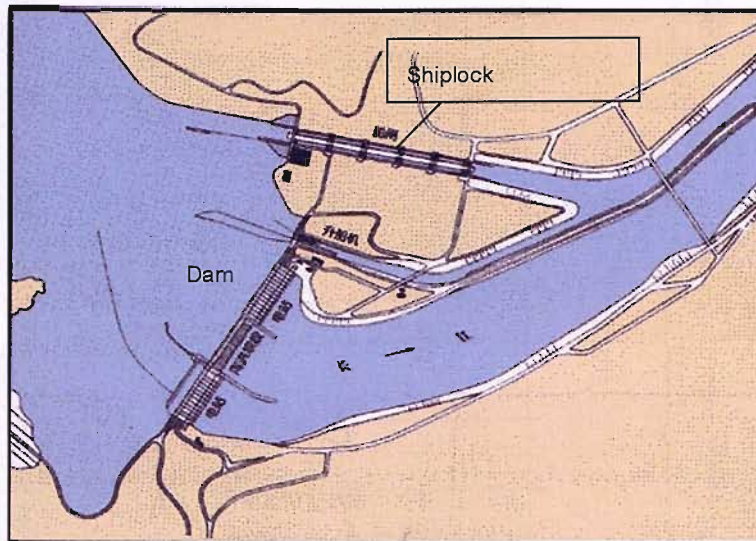
Fig3.2 Layout of the Three Gorges Project

The Sec#17 (abscissa 15675m) and Sec#20 (abscissa 15785m) are located at the head and in the middle of the third shiplock chamber respectively (Fig3.3). The third shiplock chamber sees the highest topography and deepest excavation in the permanent shiplock area. Furthermore, a number of major geological structures crossing the chamber have complicated it as a key issue of the construction of the shiplock. Therefore the Sec#17 and Sec#20 provide a representative case study of the research on modeling excavations in discontinuous rock. The slope profiles of Sec#17 and Sec#20 are shown in Fig3.4 and Fig3.5 respectively with excavation steps.

The structures of the shiplock head and chamber are mainly of reinforced concrete lining type (type I in Fig3.6) except for the walls of the first, fourth and fifth chamber, which are of a combined form of an upper gravity type on a lower lining type at (type II in Fig3.6). The sidewalls are detached from soleplate by structural joints. The thickness of sidewalls at the heads is 1.4~3.0m, 1.5~2.1m for chamber walls. The thickness of soleplate is 5~7 m.

The water conveyance system of the shiplock uses long galleries of inertial type. Two main conveyance galleries were designed, running symmetrically along the outside of the shiplock. The maximum total flow rate is 580 m^3/s.
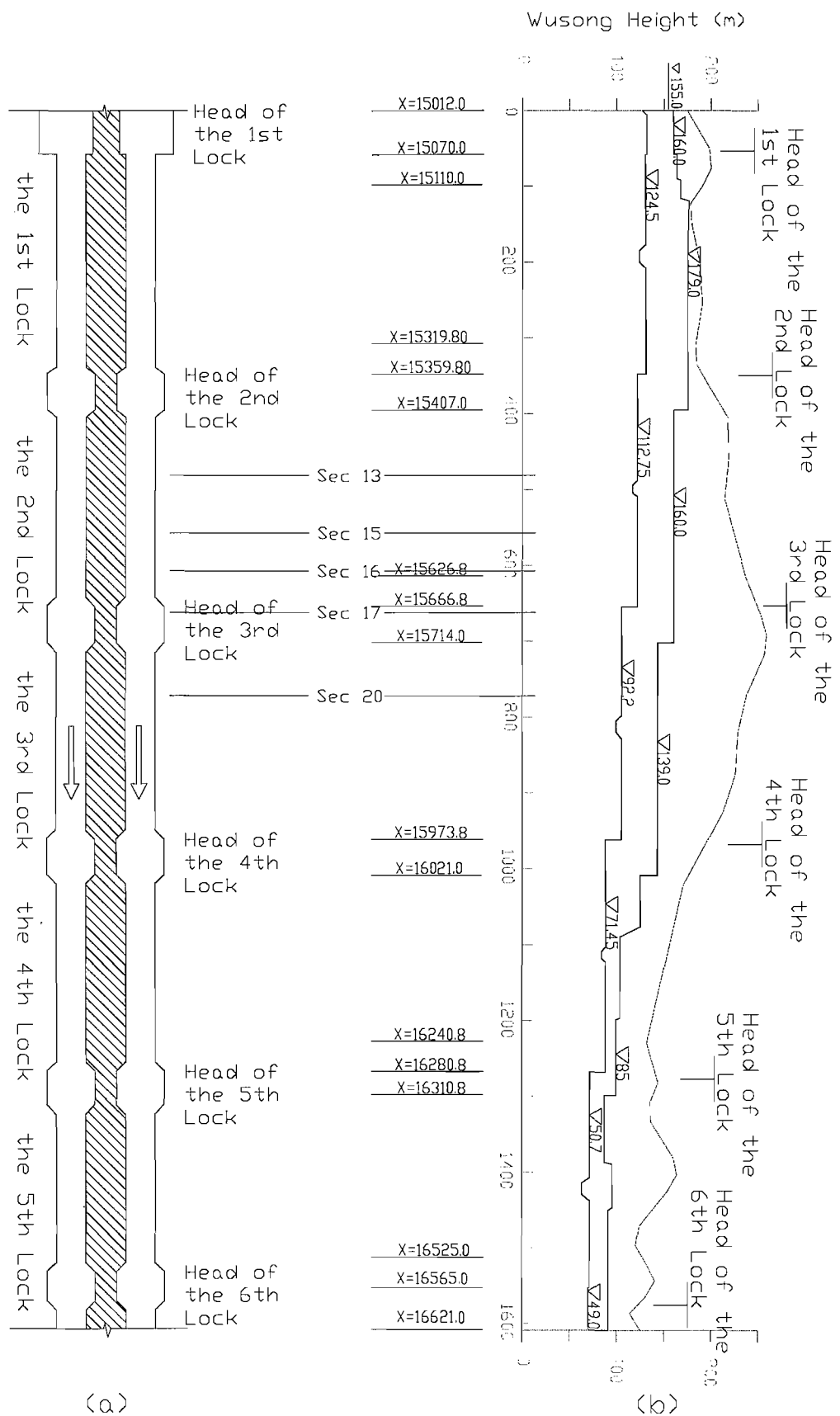
Fig3.3 Plan view (a) and long section (b) and of shiplock steps

24
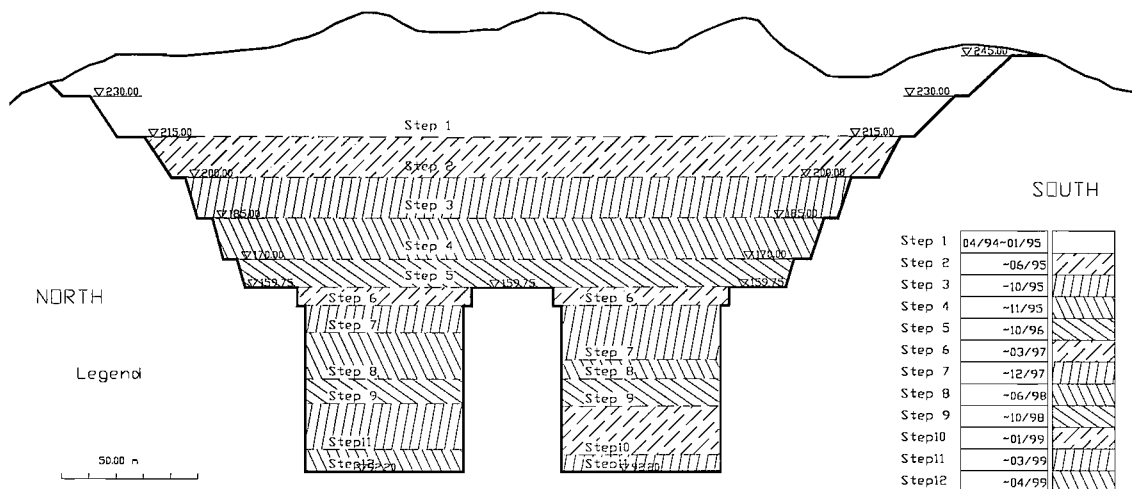
Fig3.4 Excavation stages of Sec#17
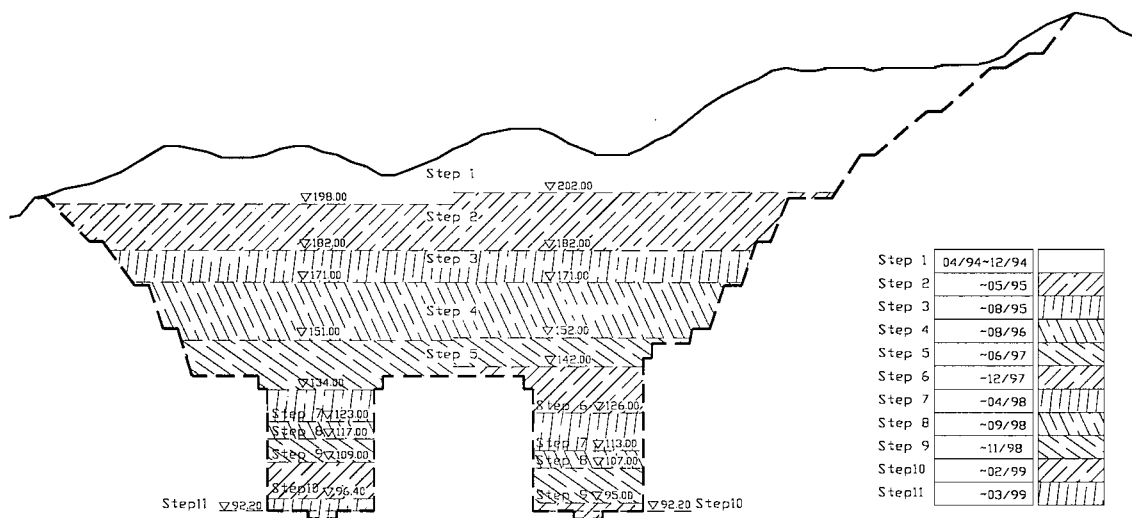
Fig3.5 Excavation stages of Sec#20

Fig3.6 Pure lining type (I) and combined type (II) of shiplock chamber wall (CWRC, 1997)

25

3.3 Engineering geology

The shiplock is overlooked by a ridge with a height of 250~266.7m above sea level, intersecting obliquely the axis of the shiplock at the head of the 3rd step. The ground level declines along both directions of the stream. The geomorphology at the second and the third chamber is shown in Fig3.3 and Fig3.7. The geological cross sections at Sec#17 and Sec#20 are shown in Fig3.8 and Fig3.9.
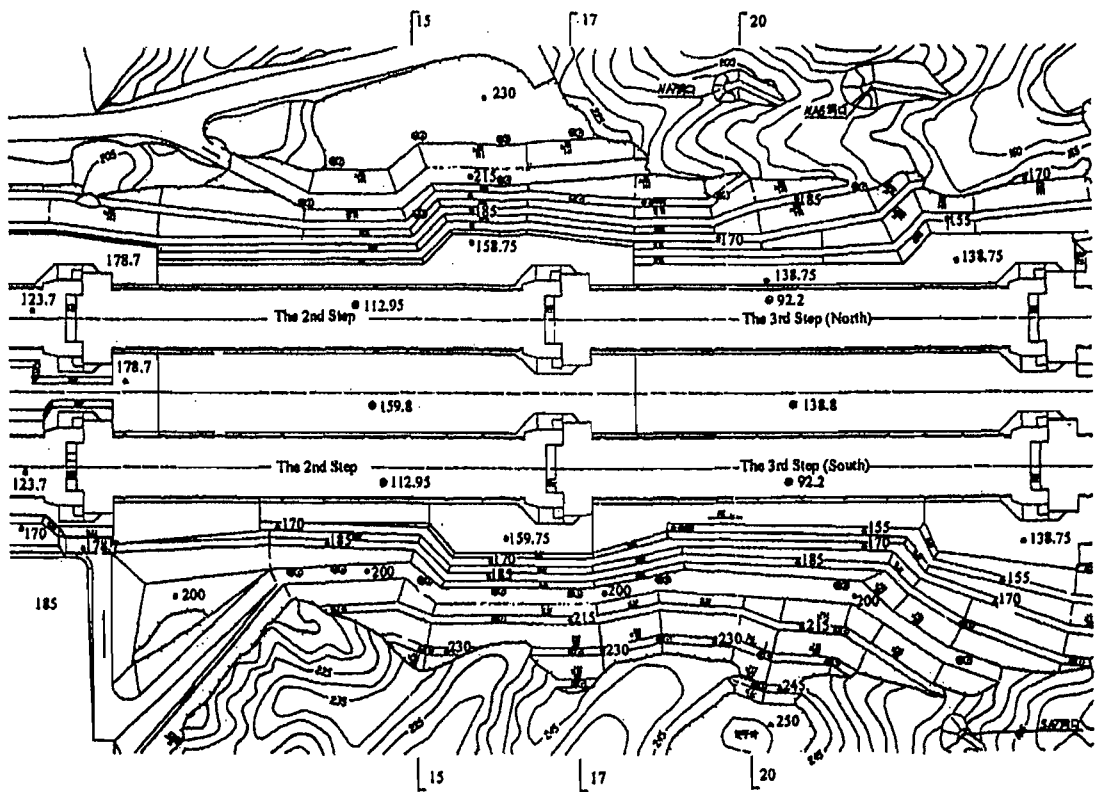
Fig3.7 Plan view of the permanent shiplock for the Three Gorges Project (Deng & Lee, 2001)

Geological Corss-section of 17-17' at Head of the 3rd Step of the Permanent Shiplock of the Three Gorges Project
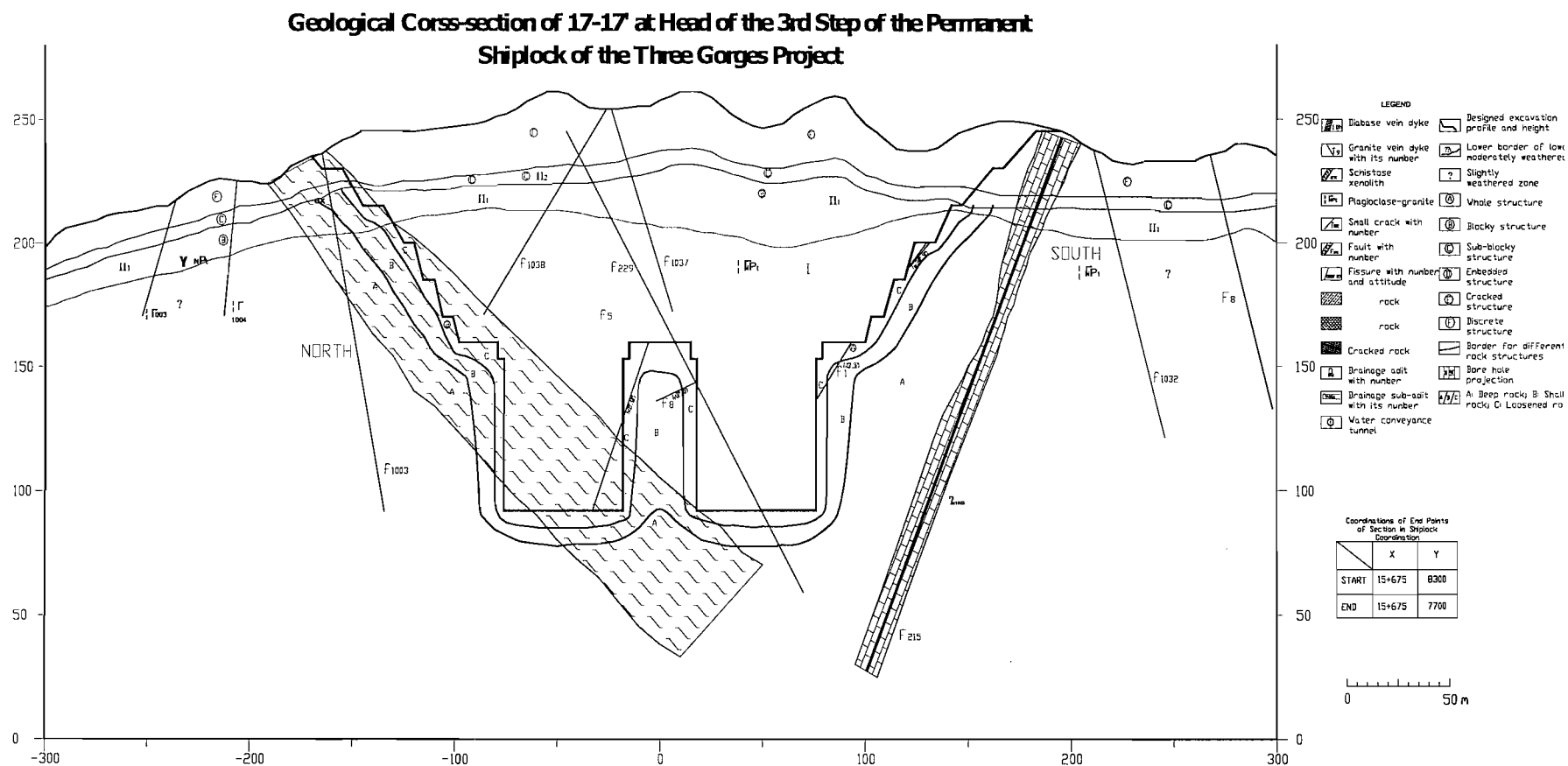
Fig3.8 Cross-section of Sec#17 at the head of the 3rd step

Geological Corss-section of 20-20' at Head of the 3rd Step of the Permanent Shiplock of the Three Gorges Project
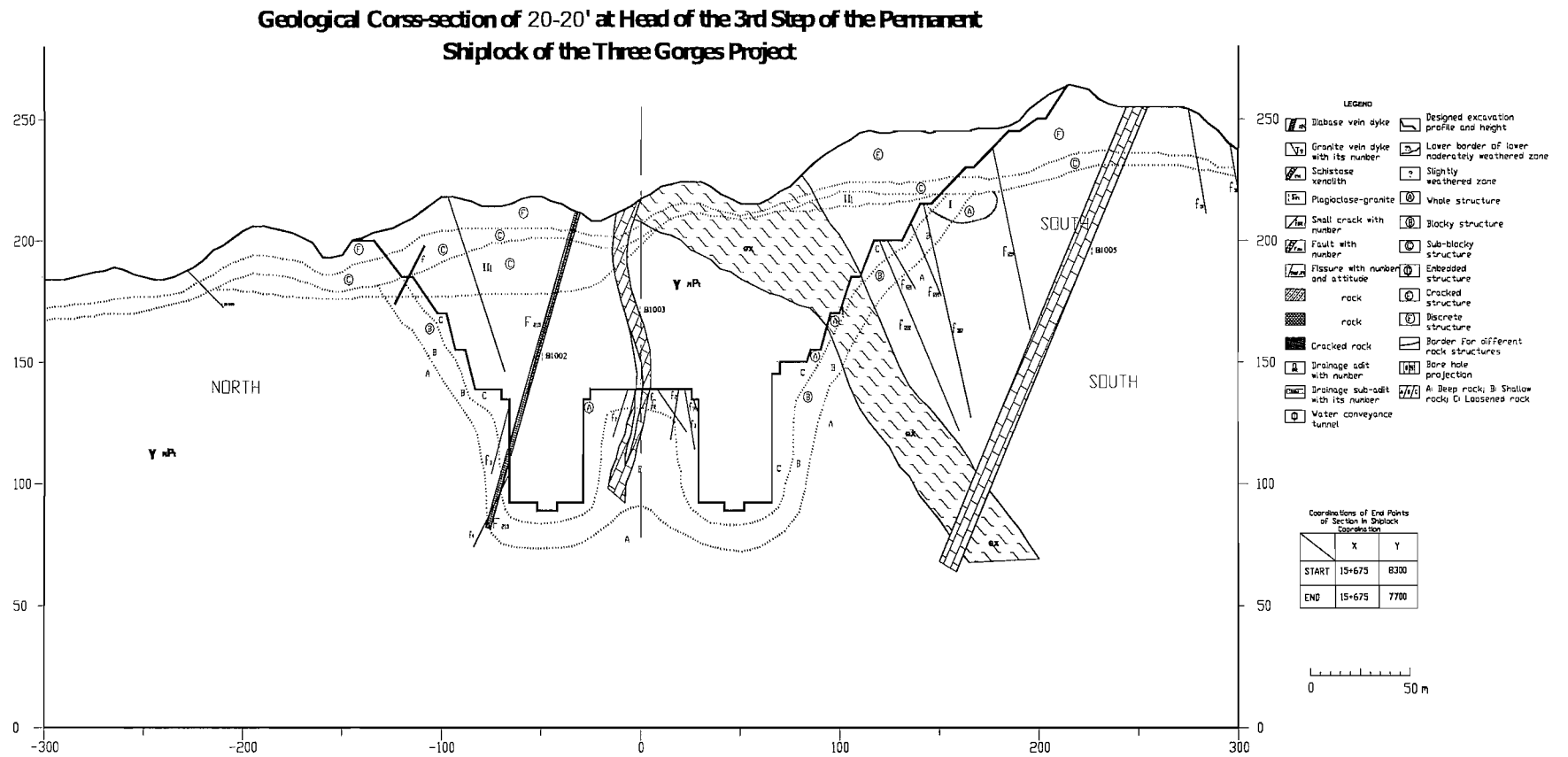
Fig3.9 Cross-section of Sec#20 in the 3rd step

3.3.1 Discontinuities

The dip direction of discontinuities is defined by the azimuth of the horizontal projection of the dip vector, measured clockwise from the north.

Surveying and exploratory adits indicated that the faults have an average spacing of 8~10m. 82% of them are of steep dips, and only 11 are longer than 100m with rough fault surface and well cemented tectonites. These faults are classified into four groups (Chen et. al., 1996):

(1) NNW group with a strike of 330~353°, dipping SW with a dip angle of 63~84°; 32.8%

(2) NE~NEE group with a strike of 40~85°, dipping NW mainly with a dip of 60~82°; 29.4%

(3) NNW group with a strike of 0? 5°, dipping NW mainly, with a dip angle of 65~85°; 26.1%

(4) NW~NWW group with strike of 270~330° dipping NE mainly. 11.7%

The faults in the NNW group are the most developed. Most of the faults are of less than 50 m long, 9 faults with a length of over 100 m. There are 4 faults intercrossing both south and north slopes, namely f_{1050}, F_{215}, F_{10}, f_{1096}. Faults mainly consist of cataclasite with fine cohesion except a small number of faults in NE~NEE group.

The fissures exposed by the exploratory adits and trenches can be characterized into 8 groups at four strikes as in Table3.1. The NEE group with steep dips is the most numerous and the most developed. Most fissures are no longer than 10m with mainly planar coarse fissure surfaces and are infilled. The strikes of the faults and fissures cross the axis of the shiplock at an angle of more than 30?

There is a majority of pre-Sinian period plagioclase-granite exposed in the shiplock area, in which a limited number of schistose xenolith and veins of pegmatite and diabase are embedded. A zone of schistose xenolith exists on the east slope of the ridge and across the third shiplock room with a 340~360° strike, SW dip and 40~80° dip angle (mostly 50~60° dip angles), and mostly a width of 12~35 m. The developed joints of amphibole-quartz-schist have the same strike as the strata and are closely contacted with surrounding rock. The veins have different orientations: (1) N50~70°E/NW60~85° for a length of about 200~1000m and width of about 0.3~2 m; (2) N0~ 30°W/NE55~85° for a length mainly less than 100m but sometimes larger than 500 m, and width about 1m. These veins have a similar mechanical strength to the plagioclase granite. The strength parameters for the discontinuities are shown in Table3.2.

Table3.1 Fissure grouping for the permanent shiplock area (Chen et. al., 1996)

Group	Strike direction	Dip	Dip angle	Persistence (%)	Development	Strike
1	60~85	NW	75	19.65	Most	NEE
2	60~85	SE	86	8.6	Secondary most	NEE
3	10~40	NW	71	10	Secondary most	NNE
4	24	SE	30	1.3	Undeveloped	NNE
5	330~355	NE	70	6.8	Undeveloped	NNW
6	330~355	SW	70	7.15	Secondary most	NNW
7	275~305	NE	75	7.25	Secondary most	NWW
8	275~305	SW	75	4.75	Undeveloped	NWW

Table3.2 Recommended shear strength parameters for discontinuities (Zhang & Zhou, 1999)

Discontinuity type		Shear strength		Characteristics of discontinuity
		f	C (MPa)	
Hard disc.	Straight smooth	0.55~ 0.65	0.05~ 0.15	Small faults, represented by f_{11} in 3001 adit, straight and smooth surface, sometimes slicken wall.
	Straight slightly rough	0.65~ 0.70	0.15~ 0.20	Main face of small faults, undulation of mm ~1cm.
		0.70~ 0.80	0.20~ 0.30	Normal fissure faces, undulation of mm to 1cm, $\leq$ 0.5mm for middle size specimen
	Undulate rough	0.80~ 0.90	0.30~ 0.50	Rough fissure faces and fault slickensides, undulation of 1~2cm, 0.5~1.0cm for middle size specimen
	Intensely rough	0.90~ 1.00	0.50~ 0.70	Unloaded fissure faces, undulation $\geq$ 2cm
Weak disc.	Cracked	0.60~ 0.70	0.07~ 0.10	Loosened or partly loosened interbeds in upper moderately weathered zone
	Embedded weak constitution	0.50~ 0.60	0.05~ 0.07	F_{23} mylonite and poor cohesive constitution of NE, NEE faults.

	Weak constitution	0.25~ 0.40	0.05~ 0.10	Weak constitution of F_{215}, strongly weathered, loosen and soft
	Mud-like	0.25~ 0.32	0.03~ 0.05	Mud-like sides of main face of major NNW, NNE faults, and other structures involving mud-like material.

3.3.2 Rock conditions and classification

The whole shiplock is based on hard plagioclase-granite.

The plagioclase granite may be divided into four zones according to its degree of weathering from top surface in sequence, these are completely weathered (IV), highly weathered (III), moderately weathered (II), slightly weathered and fresh zone (I). The thickness of the completely weathered zone is around 15-30m, but up to 38m in some places. The moderately weathered zone is further divided into upper and lower parts. The thickness of the upper moderately weathered zone is around 5-10m. The lower part has a similar strength to the rock in the slightly weathered and fresh zone.

The physical properties of the various rock types are listed in Table3.3.

On the sections along the shiplock axis, the slope profiles are designed according to the degree of weathering of rock that they are excavated in. The slope ratio of ramps along the slope is 1 in 1 (vertical to horizontal) in the completely weathered zone, 0.5 in 1 in the moderately weathered zone, and 0.3 in 1 in the slightly weathered / fresh zone. The sidewalls of the shiplock chambers are vertical with a height varying between 50-70 m.

Table3.3 Recommended physical properties of rocks (Zhang & Zhou, 1999)

Rock Type	Weathering zone	Comp. Strength(Mpa)	γ (kN/m³)	G (GPa)	Poisson's ratio	F	C(MPa)
Plagioclase-granite	Fresh	90~110	27	35~45	0.2	1.7	2.0~2.2
	Slightly	80~100		30~40			
				20~30	0.22	1.5	1.6~1.8
	Lower moderately	75~85	26.8	15~20	0.23	0.3	1.4~1.6
	Upper moderately	40~70		5.0~20	0.25	1.2	1
		15~20	26.5	1.0~5		1.0	0.5
	Highly	15~20		0.5~1	0.3		0.3~ 0.5
	Completely	1.0~2	26.5	0.02~ 0.05		0.8	0.1~ 0.3
Disc. filling — Influenced zone	Fresh	30~90	26.7	10~ 20	0.22	1.0~ 1.2	0.9~1.2
	Slightly	60~80			0.23		
	Moderately	30~60	26.5	5.0~10	0.25		
Disc. filling — F215 filling			25.6	0.2~ 0.5	0.3		

3.3.3 In situ stress

Site investigation shows that the geostress field in shiplock area changes gradually with depth (Fig3.10). Above a depth of approximately 150m, it is mainly tectonic geostress, while below a depth of 240m is generally gravity geostress. According to the site investigation bore holes and exploratory adits, the in situ horizontal stress in the shiplock area is approximately 7MPa at a small angle from shiplock axis, and a maximum of 11 MPa. The principal stresses change linearly with depth above/below 150m depth. The dominant direction of the compressive principle tectonic geostress is NEE above 165m depth where the principal horizontal stresses change direction, then changes to NNW below 165m (Fig3.11). Table3.4 shows geostress values at the ground floors of shiplock steps, which indicates a low geostress level.

Table3.4 Geostress at the ground floors of shiplock steps (Zhang & Zhou, 1999)

	1st step	2nd step	3rd step	Head of 3rd	4th step	5th step
Altitude (m)	123.70	112.95	92.20		71.45	50.70
Max horizontal principal stress (MPa)	9.50	9.70	9.97	10.65	9.70	7.72
Min horizontal principal stress(MPa)	7.20	6.86	7.50	7.69	7.35	7.23
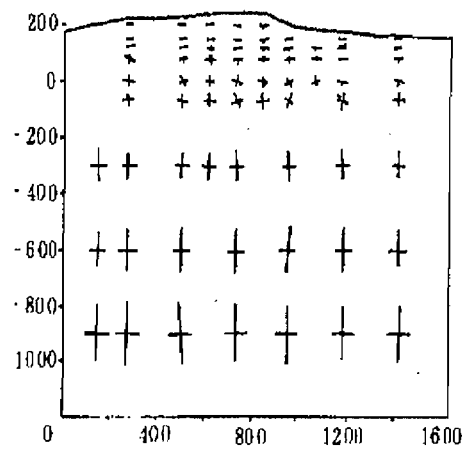
Fig3.10 Geostress field of the section at the head of the 3rd lock

α – Dip angle   β – Strike angle   σ$_h$ – Min Hor Prin Stress   σ$_H$ – Max
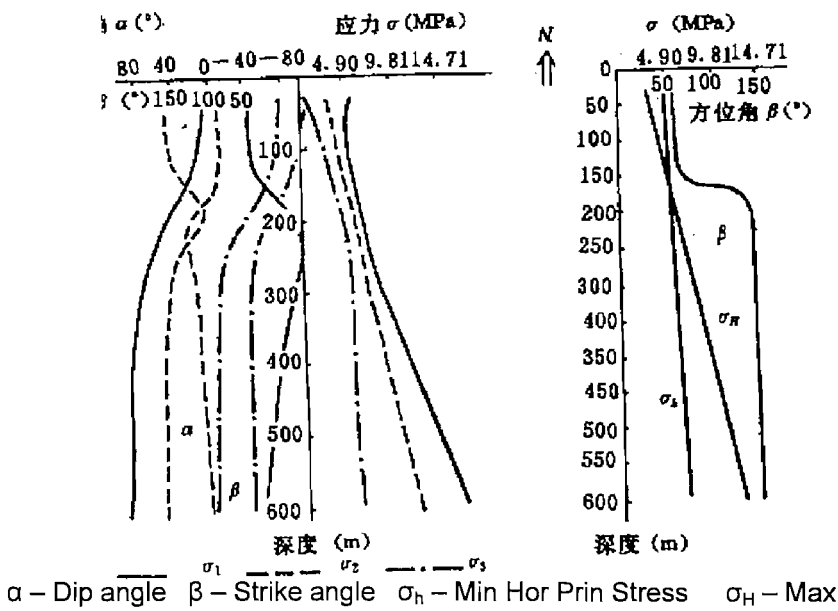
Fig3.11 Principal stresses change with depth (Liu et. al., 1992)

3.3.4 Groundwater conditions

The groundwater table is within the highly weathered zone or the upper moderately weathered zone. The annual variation in groundwater table is from 3m ~ 9m below ground level (Xu et. al., 2001). The completely and highly weathered zones are highly permeable with an average permeability coefficient of 1-5 m/d, 11 m/d at the most. The moderately weathered zone has most active groundwater flows along rock discontinuities showing considerable anisotropic permeability. The fresh/slightly weathered zones are poorly permeable at a permeability coefficient K of $(1.8-6.51)$? 10^{-7} cm/s or less and groundwater drains slowly. Some fractures containing vein water may reach a permeability of 1? 10^{-7} cm/s or higher (Shi & Huang, 1997). Rainfall is the main recharge source of ground water. The annual rainfall in the Three Gorges Project site area is 1272.1mm, with monthly distribution given in Table3.5 The rainfall in July and August pounds almost 1/3 of the annual rainfall mainly in rainstorms, most of which runs off to the river directly.

Table3.5 Monthly rainfall of the Three Gorges Project site area (mm) (Zhang & Zhou, 1999)

Month	1	2	3	4	5	6	7	8	9	10	11	12
Rainfall	17.9	31.1	62.4	102.6	168.2	154.7	230.0	217.2	102.2	97.4	66.7	21.4

3.4 Reinforcement

To ensure the stability of the high slopes during construction and long-term use, reinforcement comprising anchorage and shotcrete and a drainage system were provided.

3.4.1 Drainage system

The drainage system consists of a surface drainage system and an underground drainage system. The aim of drainage system is to block the infiltration of surface water and drain it away from slope area. The underground drainage system aims to lower the groundwater table and groundwater pressure by drainage adits and drainage holes. The underground system is the principle part of the overall drainage system.
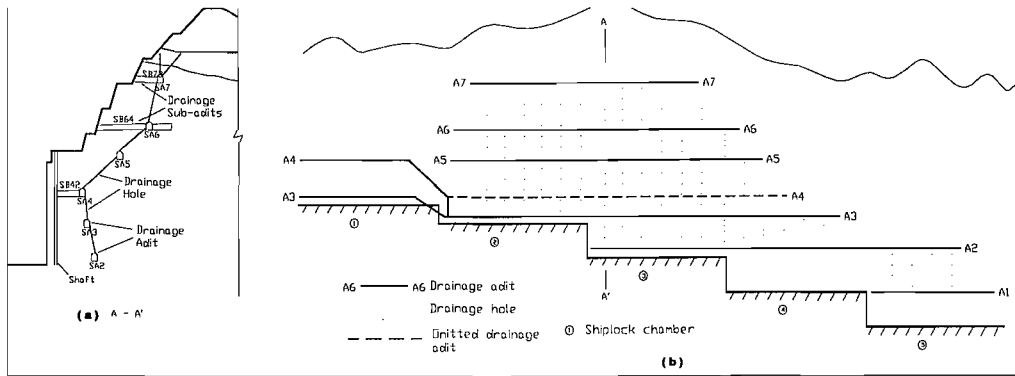
Fig3.12 Arrangement of the drainage system (a) on cross section and (b) long section (Zhao et. al., 1999)

The underground drainage system mainly consists of drainage adits and subadits on the horizontal plane and drainage holes penetrating into upper rock from adits on vertical planes, which form drainage curtains. In the drainage system, there are 7 levels of drainage adits on each side of the shiplock as indicated in Fig3.12. On each chamber, the height of the lowest drain adit is at approximately the level of soleplate while the top adit is approximately at the bottom of the weathered zone of rock. The horizontal adits also provide a construction tunnel for anchorage where applicable.

The drainage holes are designed from the drainage adits to spread upward into deep rock to collect groundwater from inside the slope. All drainage holes have a diameter of 91mm and a length of 30m with a spacing of 2.0~2.5m.

The surface drainage system includes inclined packways (benches), concrete catchwaters and drainage holes on slopes as shown in Fig3.13 for a typical slope step.

There is also a drainage network formed by horizontal and vertical prefabricated cement drainpipes of 300mm diameter at a spacing of 4m? 6m behind the thin lining walls of shiplock chamber.

35
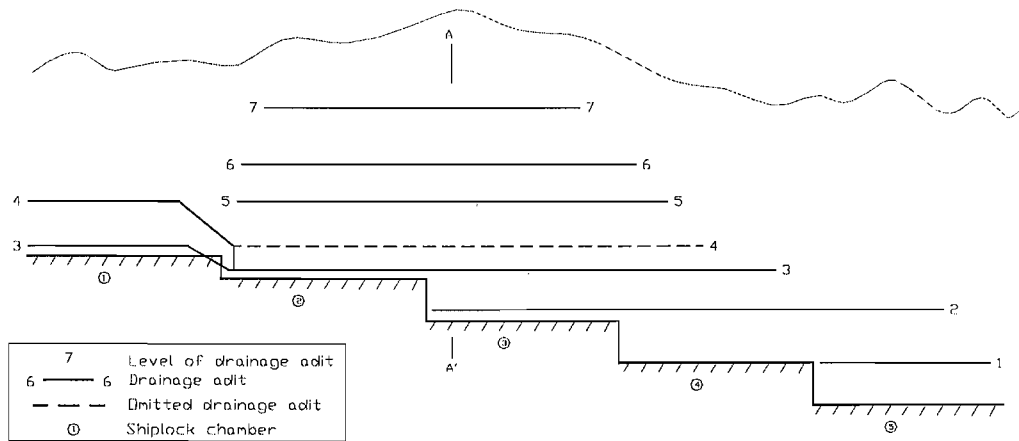
(a) Drainage system on long section
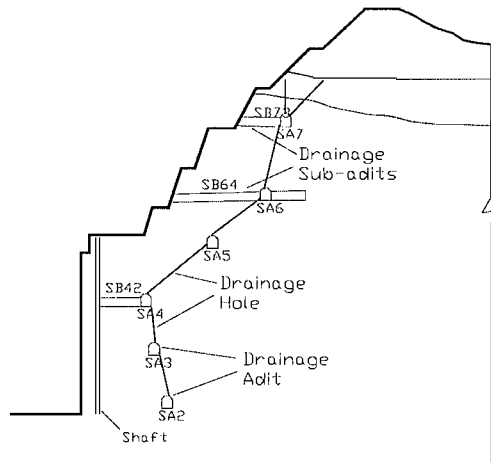
(b) Drainage on section A - A'

Fig3.13 Surface drainages for slopes

3.4.2 Anchorage system

Numerous anchors are designed as part of the slope reinforcement system (Fig3.14). The anchors adopted mainly include prestressed cable and rock bolts:

Pre-stressed cables were used for large unstable blocks, mainly in the Middle Pier and vertical chamber walls. Systematic bolts were used with wire mesh and/or grouting to lock slope surface generally and secure unstable blocks or wedges locally. The number of bolts to use was decided during construction using the observational method.

A typical anchorage design for a ramp is shown in Fig3.17. In total, the anchorage system comprises over 4000 prestressed cables, about 2000 cables prestressed to 3000kN by

observational method (Gao & Zeng, 2001), about 100 thousand systematic bolts and over 7000 systematic bolts (Chen, 2001).

(a) Reinforcement on slope

(b) Reinforcement on chamber walls

Fig3.14 Anchors designed for (a) slopes and (b) vertical chamber walls

3.4.2.1 Cables installed on the Middle Pier

Cables installed on the Middle Pier at the Sec#17 and Sec#20 are summarized in Table3.6 and Table3.7.

Table3.6 Prestressed cables installed at Sec#17

No.	Date/Period	Type	Elevation	Cables with labels	Len.(m)
1	30/12/97	Through	151.5	7MP (MC3-1-9 ~15)	53.2
2	12/03/98	Through	151.5	3MP (MC3-1-1 ~3)	45
3	29/03/98-31/03/98	North Blind	148.75, 146	20MNE (MD3-Z-44 ~63)	40
4	18/04/98	North Blind	152.5	5MNE (MD3-Z-11 ~15)	18
5	20/07/98-29/07/98	North Blind	146-138.75	24MNE (MD3-Z-16 ~26; 64~73; 84~86)	40
6	10/08/98	North Blind	141.25	10MNE (MD3-Z-74 ~83)	40
7	14/08/98	Through	138.75	3MP (MC3-2-5,7,8)	32.8
8	19/08/98-30/08/98	Through	143.5-141; 146;138.75	8MP (MC3-Z-27 ~34)+ 5MP (MC3-1-1 ~5)+ 9MP (MC3-2-4 ~15)	53.8
9	03/09/98	Through	138.75	3MP (MC3-2-1 ~3)	45.6
10	22/11/98	North Blind	121.5	8MNE (MD3-Z-24 ~131)	25
11	06/12/98	North Blind	127.5-124.5	16MNE (MD3-Z-108 ~123)	40
12	02/01/99	North Blind	121.5	3MNE (73-D-1 ~3)	20
13	13/01/99-28/01/99	North Blind	136.5-130.5; 130.5; 130.5	4MNE (MD3-Z-43, 105~107)	34.8
14		Through	136.5-130.5; 130.5; 130.5	26MP (MD3-Z-35 ~42; 87~104) +11MP (MC3-3-1 ~11)+ 5MP (73-C-1 ~5)	34.8
15	22/03/99	North Blind	118.5-112.5	14MNE (MD3-Z-132 ~155)	25

16		Through	118.5-112.5	10MP (MD3-Z-132 ~155)	25
17	17/08/99	South Blind	124.5-117.5	3MSE (69-D-1~3)	45
18	25/09/99	South Blind	103-100	2MSE (9921-D-1 ~2)	22

*All cables are horizontal and prestressed to 3000kN except where otherwise stated.

MP: Through cables; MNE: Blind cables installed at the north side of the Middle Pier; MSE: blind cables installed at the south side of the Middle Pier.

The number before MP, MNE or MSE indicates the number of cables installed and the characters in the parentheses show the label of each cable corresponding to Fig3.18.

Table3.7 Prestressed cables installed at the Middle Pier at Sec#20 (x =15,768 to 15,804m)

No	Date/period		Type	Ele (m)	Type & Num	Len.
1	08/03/99	10/03/99	South Blind	112-120	4MSE (72-D-1,~5)	40
2	14/07/99	17/07/99	Through	126.6-131	7MP (Z14-C-11,~35)	55.8
3	19/07/99	21/07/99	Through	109.-122.2	5MP (Z14-C-30 ~34)	56.4
4			South Blind	99-105	2MSE (109-D-6 ~7)	30
5	25/07/99		South Blind	123.5	2MSE (109-D-1 ~2)	30
6	29/07/99	31/07/99	Through	126-131	7MP (Z14-C-12,~39)	55.8
7	02/08/99		North Blind	125-127	2MNE (31-D-1 ~2)	25
8	04/08/99		South Blind	97-109	4MSE (96-D-1 ~4)	25
9	20/08/99		North Blind	100-104	2MNE (103-D-3 ~4)	25
10	29/08/99		Through	131	3MP (Z14-C-40 ~42)	55.8
11	01/09/99	02/09/99	Through	120-123	3MP (61-C-1 ~3)	55.8
12	06/09/99		Through	116	1MP (96-C-2)	55.8

*All cables were installed horizontally and prestressed to 3000kN except where otherwise stated.

MP: through cables; MNE: blind cables at north side of the Middle Pier; MSE: blind cables at south side of the Middle Pier.

The number before MP, MNE or MSE indicates the number of the cables installed and the string in the parentheses shows the label of each cables corresponding to Fig3.18.

(a) Anchorage on the north side of the Middle Pier

(b) Anchorage on the south side of the Middle Pier

Fig3.15 Layout of prestressed cables installed on the Middle Pier around Sec#17 and Sec#20

40

(a) Anchorage on the north slope (Prestressed cables)

(b) Anchorage on the south slope (Prestressed cables)

Fig3.16 Layout of prestressed cables installed on the north and south slope

3.4.2.2 Cables installed on the north slope

Cables installed on the north slope at the Sec#17 and Sec#20 are summarized in Table3.8 and Table3.9 and shown in Fig3.16.

Table3.8 Prestressed cables installed at the north slope of Sec#17

No	Period		Ele (m)	Type & Num	Angle	Len(m)
1	25/02/98	26/02/98	149.5-153.3	4NP (NC3-1-5~7)	0	30.5~35.1
2	12/03/98	16/0398	149.5-153.3	5NP (NC3-1-1,3~4,9~10)	0	30.6~45
3	21/09/98	27/09/98	131.5-133.8	7NP (NC3-2-3,5~10)	0	30.8~40.1
4	05/05/99		113.5	5NP (NC-3-3-2~6)	0	25.7~36.2
5	09/07/99		191.6	2NE (9926-D-1~2)	0	30
6	22/07/99		202.3	2NE (9912-D-1~2)	0	30

*All cables were prestressed to 3000kN and installed horizontally except where otherwise stated.

NP: through cables; NE: blind cables.

The number before NP and NE indicates the number of cables installed and the characters in the parentheses show the label of each cable.

Table3.9 Prestressed cables installed at the north slope of Sec#20

No	Period		Ele (m)	Type & Num	Angle	Len(m)
1	18/01/98	19/01/98	166	3 NE (ND3-1-28~30)	0	35
2	01/04/98		166	3 NE (ND3-1-25~27)	0	35
3	05/06/98	07/06/98	131.5	5 NP (NC3-2-33~34, 37~39)	0	41
4	17/06/98		131.5	3 NP (NC3-2-30~32)	0	41
5	05/07/98		131.5	2 NP (NC3-2-34~35)	0	41
6	31/01/99		113.5	2 NP (NC3-3-35~36)	0	36
7	20/03/99	24/03/99	113.5	7 NP (NC-3-3-26~32)	0	36
8	12/09/99	13/09/99	119-124	3 NE (84-D-1~3)	0	25
9	31/01/00		104-109	4 NE (116-D-8~11)	0	26-32

*For table notes see Table3.8.

3.4.2.3 Cables installed on the south slope

Cables installed on the south slope at the Sec#17 and Sec#20 are summarized in Table3.10 and Table3.11 and shown in Fig3.16.

Table3.10 Prestressed cables installed at the south slope of Sec#17

No	Period		Ele (m)	Type & Num	Angle	Len(m)
1	06/01/98		149-155.5	7 SP (SC3-1-3~9)	0	30-41
2	20/02/98	25/02/98	150.5-153	2 SP (SC3-1-10~11) + 12 SE (SD3-Z-19 ~30)	0	22-46
3	20/04/98	21/04/98	141.7-146	5 SE (SD3-Z-37~38, 47~48, 58)	0	26-30
4	12/05/98		141.7	1 SE (SD3-Z-57)	0	26
5	22/05/98	27/05/98	136.7-146	12 SE (SD3-Z-32~36, 54~56, 61~62, 65~66)	0	16-24
6	28/05/98	04/06/98	141.7-146	10 SE (SD3-Z-31, 41~46, 51~53)	0	16-20
7	07/10/98		131	2 SP (SC3-2-9~10)	0	33
8	23/12/98	26/12/98	131-133.5	6 SP (SC3-2-3~8)	0	22.5-27.8
9	05/05/99	06/05/99	114.5-117.7	4 SP (SC3-2-1~4) + 1 SE (998-D-1)	0	25.7
10	30/06/99		115-138.7	5 SE (120-D-1~5)	0	19.2-31.2
11	19/07/99		114.5	1 SP (SC3-3-5)	0	36.2
12	08/08/99	11/08/99	100.7-117.7	1 SP (SC3-3-6) + 6 SE (997-D-1, 3~6, 8) + 3 SE (129-D-7~9)	0	25-36.2
13	12/08/99		117.7	1 SE (997-D-2)	0	30

*All cables were prestressed to 3000kN and installed horizontally except where otherwise stated.

SP: through cables; SE: blind cables.

The number before SP and SE indicates the number of cables installed and the characters in the parentheses show the label of each cable.

Table3.11 Prestressed cables installed at the south slope of Sec#20

No	Period		Ele (m)	Type & Num	Angle	Len (m)
1	19/06/98		131.5	1 SP (SC3-2-35)	0	33.02
2	14/07/98	16/07/98	150.5-153	9 SP (SC3-2-26~34)	0	33.02
3	22/11/98	24/11/98	131	6 SP (SC3-3-28~33)	0	36.2
4	04/01/99	05/01/99	131-133.5	4 SP (SC3-3-24~27)	0	36.2
5	05/09/99		110.5-114.7	2 SE (107-D-1~2)	0	22
*For table notes see Table3.10.						

3.5 Instrumentation and monitoring data

3.5.1 Instrumentation

To monitor the conditions of shiplock during construction and future operation, a large number of instruments have been installed. These include: survey points for surface deformation, inclinometers and multi-point measurements for subsurface deformation, anchorage force, fissure opening, groundwater, temperature and rainfall measurement. The instrumentation around the chamber area of the 2nd and 3rd shiplock is shown in Fig3.17 and the availability of measurement data is summarized in Table3.12.

Table3.12 Summary of monitoring data

	Inclinometer	Survey points	Multi-point	Fissure	Ground water	Anchorage force	Temperature	Rainfall
Number	20	22	3	6	35	6		
Start Date	06/95	04/95	05/95	09/98	02/96	12/97	10/99	10/99
End Date	11/00	12/00	01/01	11/00	11/00	11/00	10/00	10/00

Deformation data from survey points and inclinometers form the majority of monitoring data. In total, 9 inclinometers were installed around Sec#17 and S11 inclinometers were installed Sec#20.

The sensitivity of the testing header of inclinometers is ? .02mm/500mm according to manufacturer. The global precision of the system is ? mm/15m. The measurement range is 0 - 53? An automatic recorder, which helps to minimise errors from artificial reading, was used to take readings (Fu, 1999).
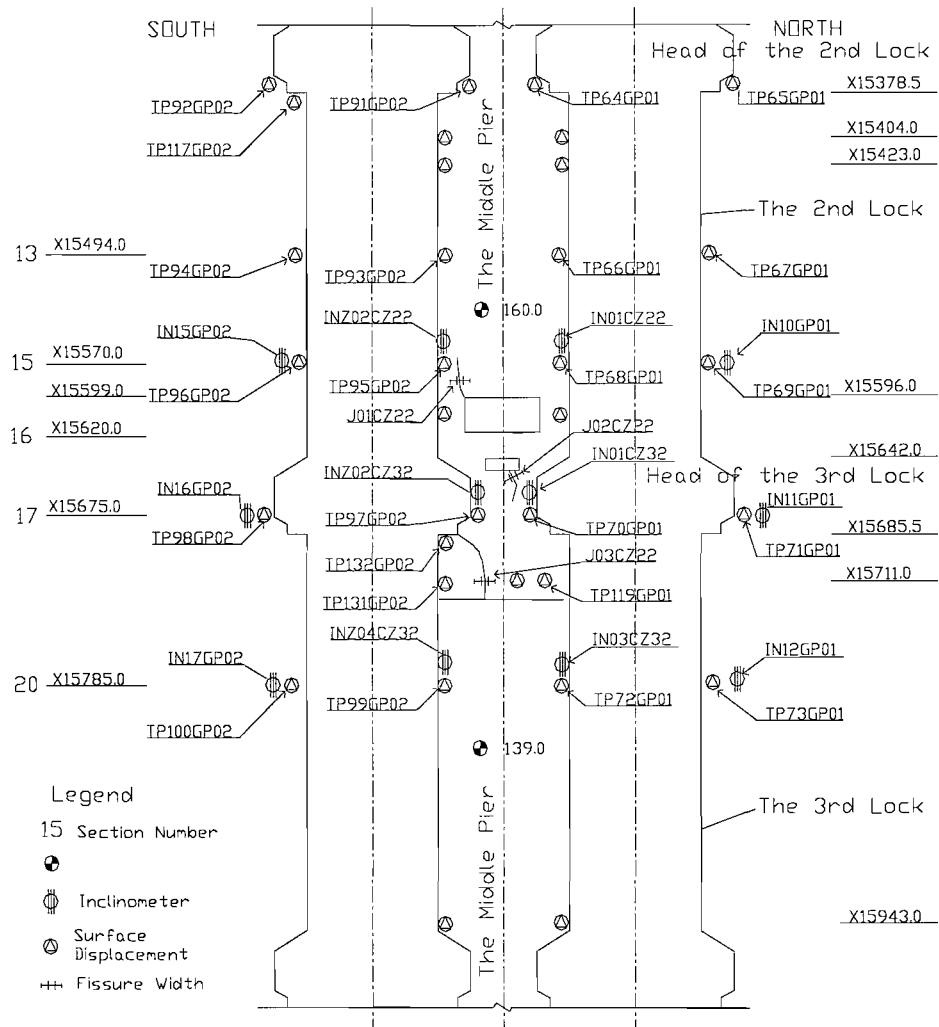
Fig3.17 Instrumentation around the area of the 2nd and 3rd lock chamber

3.5.2 Coordination system and sign conventions

In the coordinate system of the study, the Z axis is set in the vertical direction with positive direction pointing upward; the X axis is set in the horizontal plane parallel to the shiplock axis with positive direction pointing downstream, and the Y axis is set perpendicular to the X axis in the horizontal plane with positive direction pointing as shown in Fig3.18.

In the interpretation of deformation data, the following rules are followed:

(1) Dilation or compression of the Middle Pier is taken the difference between the y displacement of north and south side (north minus south). If the difference is positive, the Middle Pier dilates; if negative it compresses.

(2) Offset of the Middle Pier measures how much the Middle Pier shifts in the y direction, which is the sum of the y displacement of both sides (either surface or subsurface displacement). If positive, the Middle Pier moves towards the north as a whole, otherwise to the south.

(a) Cross-section view   (b) Plan view
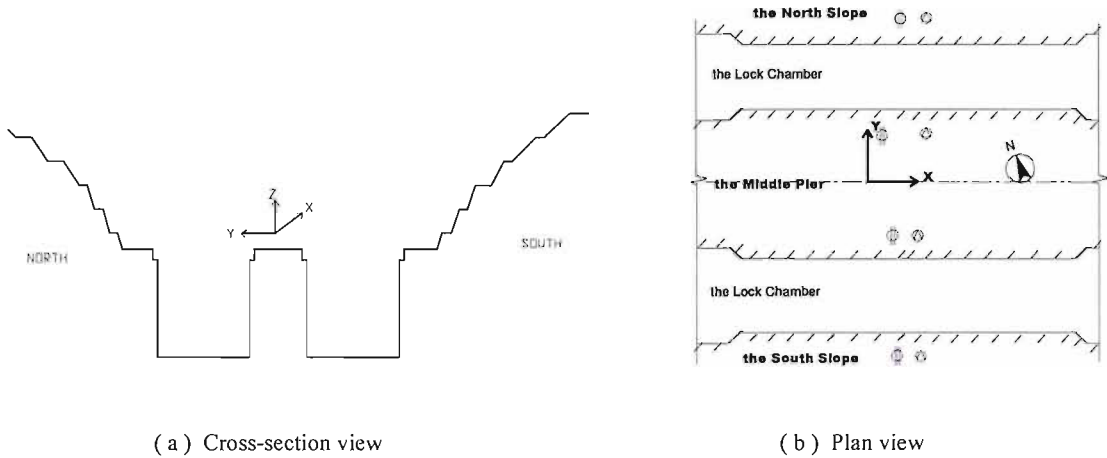
Fig3.18 Coordinate system of the study
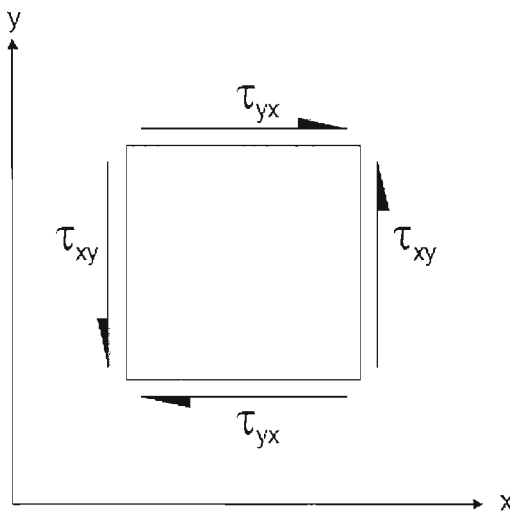
Fig3.19 Sign convention for positive shear stress components (Itasca, 1998)

The other sign conventions used for the study are listed as follows (Itasca, 1998):

Normal Stress — Positive stresses indicate tension; negative stresses indicate compression.

Shear Stress — With reference to Fig3.19, a positive shear stress points in the positive direction of the coordinate axis of the second subscript if it acts on a surface with an outward normal in the positive direction. Conversely, if the outward normal of the surface is in the negative direction, then the positive shear stress points in the negative direction of the coordinate axis of the second subscript. The shear stresses shown in Figure 2.20 are all positive.

Joint Normal Stress — Joint normal stress is positive in compression.

Joint Normal Opening — Joint opening is positive; joint closure is negative.

Joint Shear Stress — Joint shear stress is positive for the following direction of relative movement: ⇄.

Joint Shear Displacement — Joint shear displacement is positive for the following direction of relative movement: ⇄ .

Chapter 4 Case Study: Analysis of Field Data

In this chapter, a case study is carried out to analyze the field deformation data from the Three Gorges Project (TGP) site including surface deformations by survey points and subsurface deformations by inclinometers. The principles and methods used to process and interpret deformation data are firstly introduced. The deformation patterns of the Middle Pier and slopes in response to excavation are characterized. Various factors influencing the behaviour of rock mass are investigated. The case study of field data of the shiplock is presented in two separate parts, one for the Middle Pier and one for the slopes.

4.1 Deformation Data Processing

The sign convention and coordinate system used for the study are described in section 3.5.1. The survey data are presented as the "total deformation" since each instrument became operational. The subsurface deformation data from inclinometers are presented as displacements relative to the bottom of the inclinometer and relative to when each instrument became operational unless stated otherwise. The term "deformation increment" means the increment of deformation since the last measurement, unless explicitly stated as being "relative to" a certain date. For example, "deformation increment relative to 18/04/97" means the increment of deformation that occurred after 18/04/97.

Discontinuities are referred to by their identifying labels in the form "discontinuity no. (dip direction L dip angle)", for example "f5 (15°L68°)", where a discontinuity f5 is referred to with its dip direction and dip angle in brackets.

48

4.1.1 Inclinometer data

Inclinometers measure the relative displacements of rock along its length in two horizontal directions: the x direction (horizontal along the flow in the shiplock) and the y direction (horizontal, perpendicular to the flow in the shiplock). The original reading is taken as two digits after floating point in unit of mm. The relative displacement or relative displacement increment between any two points is calculated from the original readings. Commonly the displacement relative to the bottom is used in interpretation of inclinometer data. In this study, the term "inclinometer profile" means the shape of the curve of relative displacement along the inclinometer relative to the bottom unless stated otherwise.

The apparatus precision of the inclinometers used is 0.02mm per 0.5m (Fu, 1999). Although an inclinometer cannot detect rigid rotation or translation of itself, it is normally considered that the precision of the relative displacement among the inclinometer measurements is high. However, lower precision, e. g. between ? and ? 5mm in 30m (Dunnicliff, 1993), is commonly used in practice for this type of inclinometer, equivalent to ? .13 and ? .42mm per 0.5m, considering that measurements are taken in the field rather than under controlled lab conditions. Therefore the precision of inclinometer measurements is taken as one digit after the floating point in units of millimetres. Along the whole length of the inclinometer, it is still higher than the assumed precision of survey data (? mm).

When the absolute displacement is known for any point on the inclinometer, e.g. from survey data, the absolute displacement along the whole inclinometer can be calculated from the inclinometer measurements. If the bottom of an inclinometer can be assumed fixed, the displacement of the top of the inclinometer represents the absolute displacement and therefore agrees with surface deformation measurement. Equally, this comparison could serve as a rule to check whether the bottom of an inclinometer is fixed. When no corresponding absolute deformation is available for a certain inclinometer, the inclinometer measurements can still provide the history of the relative deformation along its length.

Poor installation quality and site accidental damage to the inclinometer may invalidate the reliability of inclinometer data. This will normally be reflected by abnormalities in interpretation of inclinometer data, e.g. the general trend of the data. Such abnormal data sets are excluded from the study.

From the above it is reasonable to assume that inclinometer data will have the same precision as survey data when used together or higher precision when used on their own.

4.1.2 Survey data and inclinometer data

As discussed above, survey data can be used in conjunction with corresponding inclinometer data to obtain absolute subsurface deformation by translating inclinometer profiles so that its reported displacements of its top match survey measurements.

The survey data generally provide a precision of ? mm. Therefore the precision of calculated absolute deformations is reduced to ? mm while the precision for inclinometer profiles remains what it is.

For an inclinometer, when the displacement of its tops is within ? mm of the survey data, its bottom can be assumed fixed and the inclinometer profiles represent the absolute displacement. Otherwise, inclinometer data should be adjusted by survey data when available to obtain absolute displacement.

For the inclinometers installed along the vertical walls of the shiplock chamber, it is reasonable to see that their bottoms remain stationary or move very little, since they are about 3m deeper than the bottom line of excavation geometry. For those inclinometers on the slope, their toes are expected to move along with the slopes and adjustment by survey data is needed to determine the actual displacement.

It is noted that the measurements of the top of inclinometers involve more errors because they were exposed on the excavation surface. Therefore the survey data are compared with inclinometer measurements at 0.5m below the top of the inclinometer in the analysis.

By comparing inclinometer data with survey data, the local deformation patterns of a slope in the range of inclinometer can be estimated. Three typical patterns are possible as summarized in Table4.1 and Fig4.1.

Table4.1 Local deformation pattern from inclinometer data and survey data

Pattern	Characteristics	Examples
Toppling	Relative deformation of the top of the inclinometer is in the same direction as the deformation suggested by the survey point	Fig4.1 (a)
Sliding	Relative deformation of the top of the inclinometer is in the opposite direction to survey data	Fig4.1 (b)
Translating	Relative deformation of the top of the inclinometer changes very little	Fig4.1 (c)

(a) Toppling pattern   (b) Sliding pattern   (c) Translating pattern

(S_s: Measurement of survey point; S_t: Measurement of top point of inclinometer; S_b: Actual displacement of the bottom of inclinometer. $S_s = S_t + S_b$)
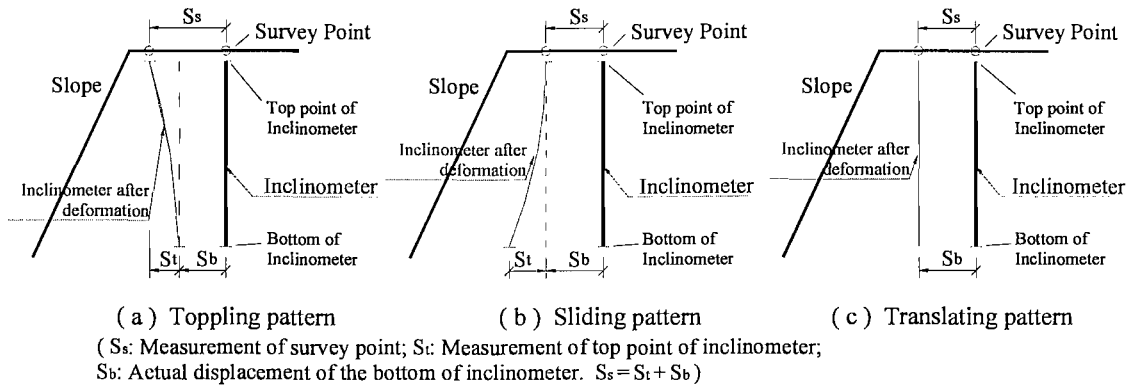
Fig4.1 Deformation pattern deduced by inclinometer and survey data

4.1.3 Factors influencing inclinometer data

Inclinometer data provide information on subsurface deformations, which are influenced by various factors as discussed before. To interpret data correctly, it is important to recognize the different effects of these factors on inclinometer profiles.

Excavation is the most influencing factor of inclinometer deformations depending on the excavation volume, excavation geometry or slope geometry, excavation sequence, excavation speed, distance of instrument from excavation etc. It is common to see inclinometer profiles change at the level of excavation stages.

Particularly the inclination angle of excavated slopes has an important effect on inclinometer profiles or may even change the deformation pattern of the slope. On a slope in toppling or translating pattern, the deformation at higher elevation is expected to be larger than lower part because (1) the whole slope generally deforms in a mode similar cantilever that is fixed at the bottom or translates; and (2) the higher part is allowed a longer period of time to deform because it is excavated earlier. On a slope in sliding pattern, an opposite case of the inclinometer profile is expected.

The slopes of the shiplock of TGP consist of a series of benches and ramps, which can be treated as single slopes in a small scale. Therefore the effects discussed above may be applicable as well (Fig4.2).

Discontinuities may influence deformations locally or globally depending on the scale, their orientation in relation with excavation, their strength and filling material. They result in jumps and changes of shape on inclinometer profiles. One of the common applications of inclinometer is to identify the slipping discontinuities. This is discussed in the following section.

51

Profile of IN09GP01(Sec#20N
Slope, 170m) on 16/05/98
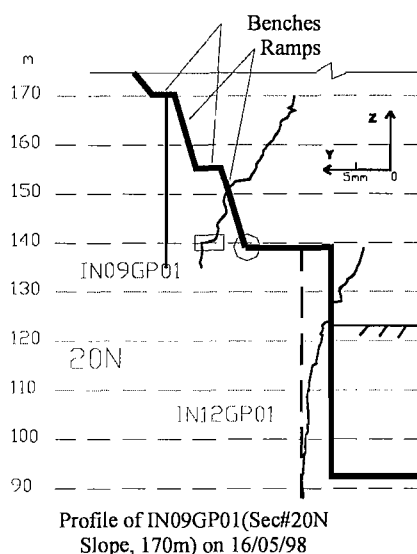
Fig4.2 Effect of slope geometry on inclinometer profile

Anchorages may have had an important effect on the deformation of the slopes. For example, prestressed cables that penetrate the entire width of the Middle Pier will restrict lateral expansion of the Middle Pier, which could be observed on inclinometer profiles. Systematic anchors installed along slope surface have an even effect on the slope surface, therefore it is difficult to observe their effect in inclinometer measurements.

Inclinometers close to the original ground surface may have been affected by the weathered zones because of weaker material properties in these zones. However it is important to note that there is no definitive boundary existing between weathered zones. Therefore this should not result in abrupt changes on inclinometer profiles.

The excavation damaged/disturbed zone (EDZ) formed around excavations is signified by reduced strength and increased deformability. The part of inclinometer embedded in the EDZ or different EDZ subzones may show different deformation profiles from other parts. Similar to weathered zones, there is no definitive boundary existing between EDZ subzones and unaffected rock and therefore no abrupt changes on inclinometer profiles may be observed inform the boundaries.

The original in situ stress field may influence deformations to a certain degree in form of the amount of stress release. Such effects are usually connected with original topography and excavation geometry.

Groundwater is not of concern in this study since sufficient dewatering measures were taken during construction of the shiplock.

4.1.4 Inclinometer and slips

Besides monitoring deformation profiles of slopes, inclinometers are also commonly used to identify slips along discontinuities. These are indicated by jumps or abnormalities along inclinometer profiles or inclinometer increment curves. In general, the slips observed in inclinometer measurements can be classified into the following categories:

(i) An obvious jump between neighboring or close points that indicates a relative displacement along discontinuities. These are mostly associated with original or newly developed discontinuities and around the range of cables.

(ii) Two adjacent slips within a certain distance corresponding to a slipping layer.

(iii) A turning point that results in a change in the trend of the profile or increment curve without any sudden jumps.

However not all abnormalities on inclinometer profiles are related to genuine slips. Many of them are actually due to noises or measurement errors, which are inevitable in field measurements. Therefore it is necessary to introduce a threshold magnitude for genuine slips to filter noise from inclinometer data.

The threshold will be based on "relative displacement" that means the horizontal distance between two points at different depths of the inclinometer. If the magnitude of a "jump" is below this threshold, the "jump" is attributed to noise in the data. If it is above the threshold, the "jump" is considered to indicate a slip. As discussed in 4.1.1, the inclinometer data are taken as one digit behind floating point in unit of mm. Therefore in the following, the threshold magnitude of a jump is taken as ? mm/0.5m (60mm in 30m) in the deformation profile.

For the cases of (i) and (ii), a single threshold of relative displacement between two depths is sufficient. However, the slips of the case of (iii) can be caused by more reasons than discontinuities and have to be identified by observations on the trend of inclinometer profiles.

In order to identify slips along discontinuities, it is important to know which discontinuities are intersected by each inclinometer, and at what depth. However a problem arises when the inclinometers do not lie exactly on the section of interest and the geological sections provide only "apparent" intersection depths. A correction is needed to account for the difference of intersection depth. The difference dz between the actual intersection depth and the "apparent" one can be calculated using geometrical considerations that relate it to the orientation of each discontinuity (azimuth and dip) and the distance dx of the inclinometer from

the section of interest. Examining the general case shown in Fig4.3 we can deduce the following formula for dz:

$$dz = dx \times \cos \beta \times \tan \theta \qquad (4\text{-}1)$$

In Equ(4-1), dx is the distance measured along x direction of the inclinometer from the section; dz is the difference in intersection depth caused by dx; $\beta = \alpha - 21° - 90°$; α is the azimuth of the dip direction measured clockwise from north; θ is the dip angle and 21° is the angle between the x axis (the axis of the shiplock) and the north.
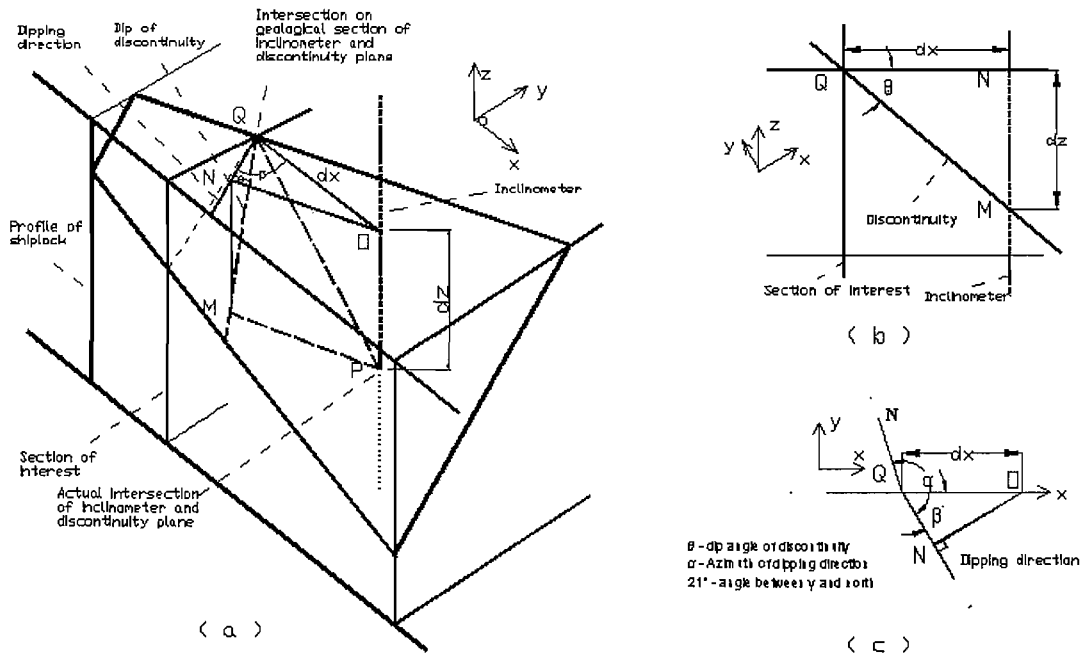
Fig4.3 Calculation of depth difference caused by the offsetting of inclinometer from section of interest

4.2 Deformation of the Middle Pier

The instrumentation on the Middle Pier includes survey points (marked with TP) and inclinometers (marked with IN) as shown on plan in Fig3.17 for Sec#17 and in Fig4.4 for Sec#20. The instrumentation details, operation period and number of available data sets are summarized in Table4.2.

(a) Section #17

(b) Section #20
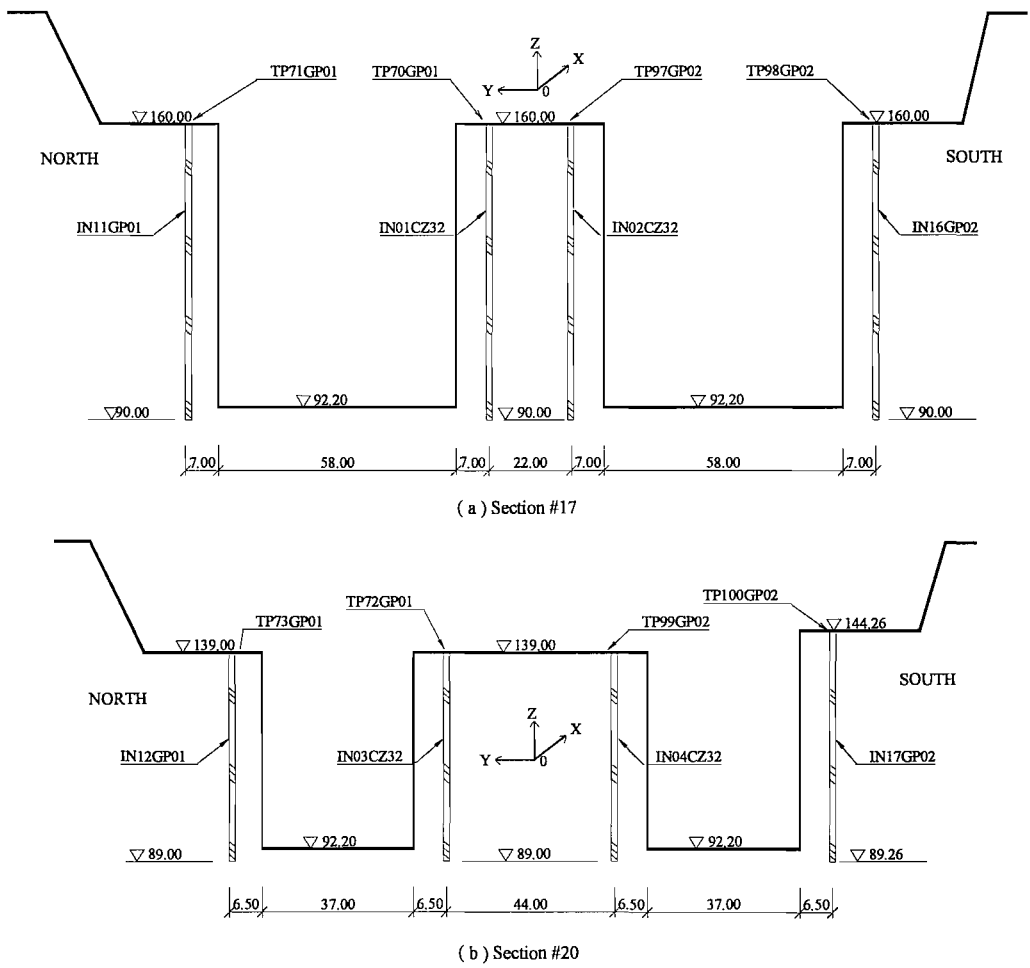
Fig4.4 Instrumentation of the Middle Pier area on Sec#17 (a) and #20 (b)

Table4.2 Instruments installed on the Middle Pier of Sec#17 and Sec#20

Position	Inclinometer	Ele (m)	Len (m)	Measurement duration		Num of available data sets
Sec#17 (X=15675.2m)	IN01CZ32	160	70	29/09/97	19/05/99	22
	IN02CZ32	160	70	29/09/97	14/09/98	16
	TP70GP01	160		16/08/97	11/12/00	41
	TP97GP02	160		16/08/97	11/12/00	41
Sec#20 (X=15782.3m)	IN03CZ32	139	50	12/01/98	01/10/99	21
	IN04CZ32	139	50	12/01/98	01/10/99	35
	TP72GP01	139		10/12/97	11/12/00	39
	TP99GP02	139		10/12/97	11/12/00	37

*X is the abscissa of the instrument in the global coordinate system of the shiplock. Sec#17 is at X=15675.0m and Sec#20 at X=15785.0m.

Elevation for inclinometer is taken as the elevation of its top.

4.2.1 Surface deformation of the Middle Pier

Deformation measurements from survey points are presented in this section on the x, y and z axis directions respectively.

4.2.1.1 x deformation (horizontal, along the flow)
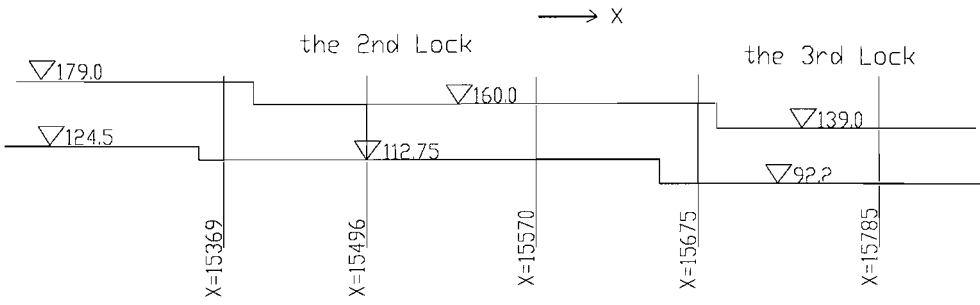
The x displacements from survey points are shown against time in Fig4.5 and Fig4.6 for Sec#17 and Sec#20 respectively together with excavation levels. With data of nearby sections provided in literature (Fu, 1999) in the region, a picture of surface deformation trend on the x direction is given in Table4.3.

It is shown in Fig4.5 and 4.6 that the x displacements at Sec#17 and Sec#20 are closely related to the excavation level. The magnitude of displacements increased steadily as excavation progressed and remained constant on average after excavation finished.

The survey points at Sec#17 show downstream displacement due to the step of excavation geometry there (Table4.3), while those at Sec#20 show upstream displacement but of a lower magnitude.

Obvious difference of displacement exists between the north and south side at both sections, which may be attributed to slips along discontinuities intersecting the shiplock axis not in right angle, e.g. TP97GP02 is located on the upper layer of the fault f_{229} that dips in the negative direction of the x axis (Fig3.8).

Table4.3 The x deformations on the top of the Middle Pier (Part of data from Fu (1999))

		15369-Sec#11	15496-Sec#13	15570-Sec#15	15675-Sec#17	15785-Sec#20	
Absciss a –Sec#		15369-Sec#11	15496-Sec#13	15570-Sec#15	15675-Sec#17	15785-Sec#20	
North side	Survey	TP64GP01	TP66GP01	TP68GP01	TP70GP01	TP72GP01	
	Disp(mm)	5.8	2.18	5.8	12.74	3.6	
	Direction	←	→	→	→	←	
South side	Direction	←	←	←	→	←	
	Disp(mm)	7.24	1.74	5.07	9.85	7.5	
	Survey	TP91GP02	TP93GP02	TP121GP02	TP97GP02	TP99GP02	
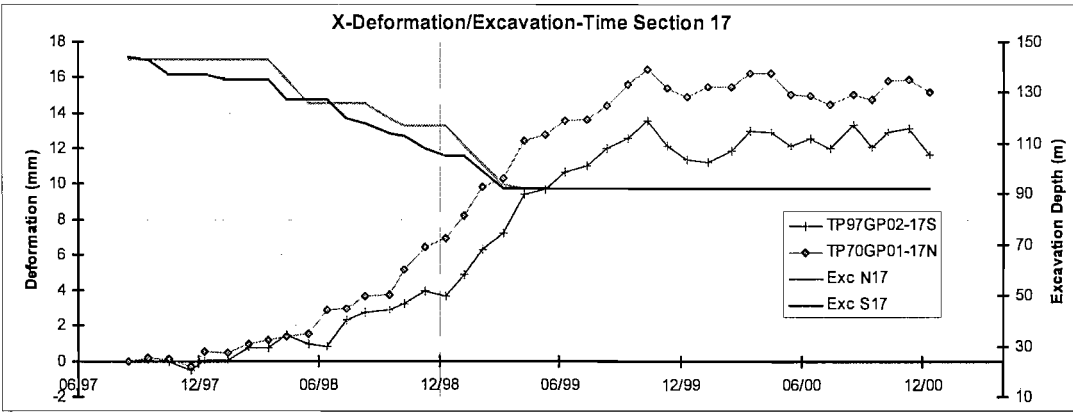
Fig4.5 The x deformation of the Middle Pier at Sec#17 from survey points
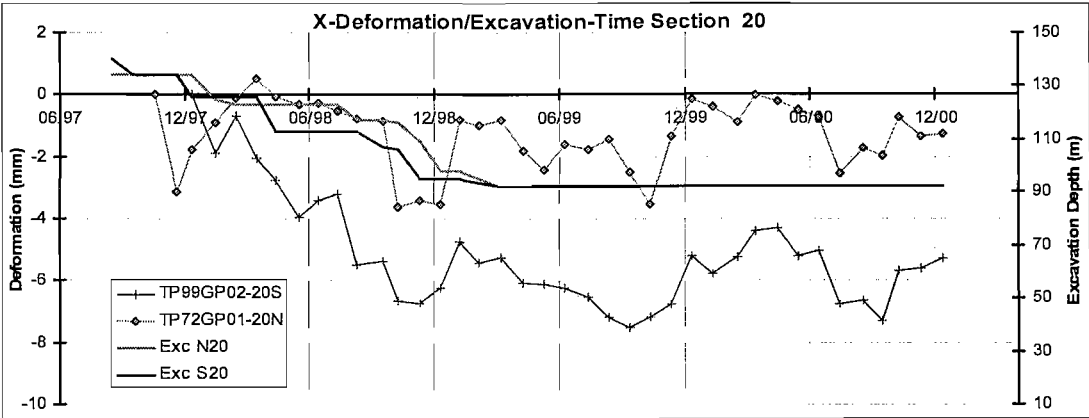
Fig4.6 The x deformation of the Middle Pier at Sec#20 from survey points

(a) Plan view
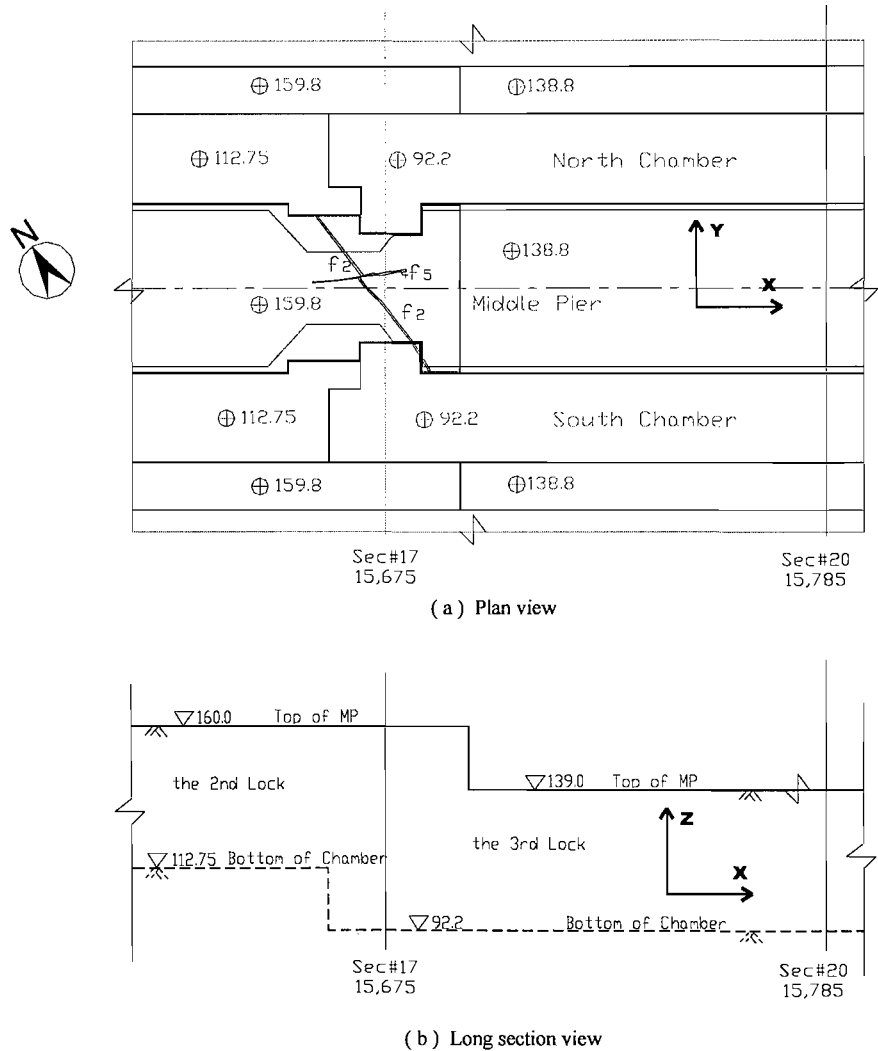
(b) Long section view

Fig4.7 Plan view and Long section of the Middle Pier around Sec#17

4.2.1.2 y direction (horizontal, perpendicular to the flow)

The y displacements of the survey points on Sec#17 and Sec#20 are shown in Fig4.8 and Fig4.9 respectively together with the calculated expansion in width and transverse displacement of the Middle Pier.

It is shown in Fig4.8 that Sec#17 expanded little throughout the excavation, while it deformed toward the north. This occurred despite that excavation in the south chamber preceded the north chamber. The displacement ratio at Sec#17 increased generally in line with the excavation depth. The displacement acceleration at 05/98 is related to the exposure of fault f5 (excavation level was from 135m in 04/98 to 126m in 05/98, Fig4.8 (b)) by excavation, which caused the upper part of the Middle Pier to move to the north as whole (Fig4.10).

In contrast to Sec#17, the Middle Pier at Sec#20 showed a large expansion in width (Fig4.9) with both survey points moving out into the chambers except for a southward initial displacement of the north survey point. The Middle Pier at Sec#20 moved slightly to the south as a whole, probably due to the existence of discontinuities on the south side (Fig4.11).
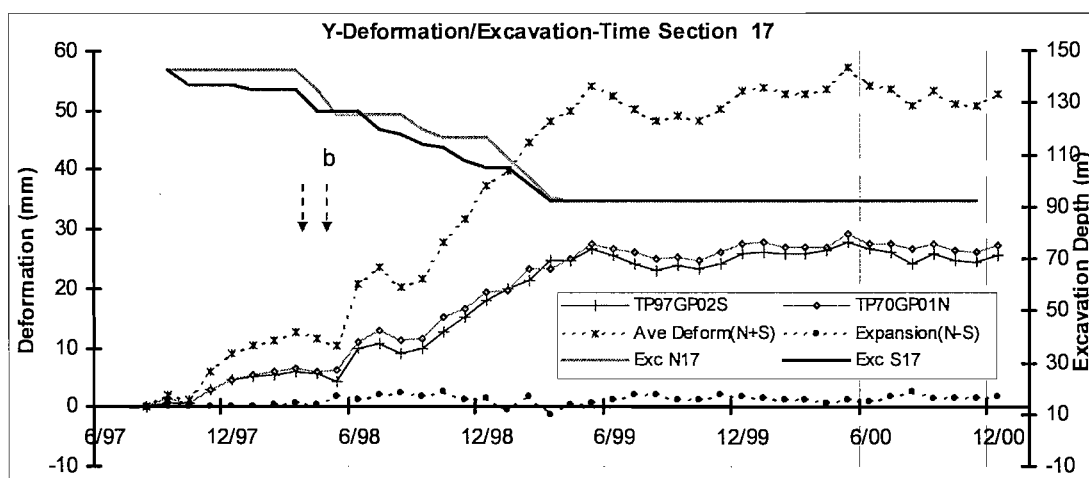
Fig4.8 The y deformation of the Middle Pier at Sec#17
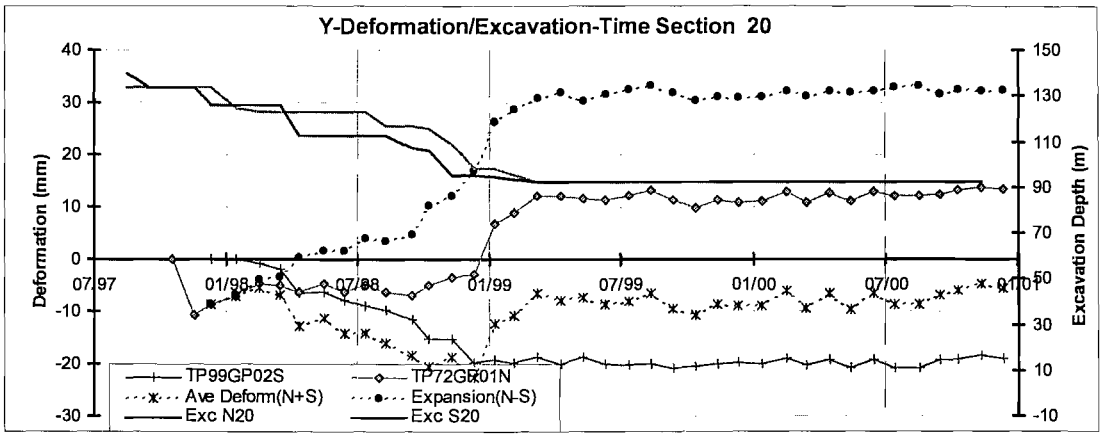
Fig4.9 The y deformation of the Middle Pier at Sec#20
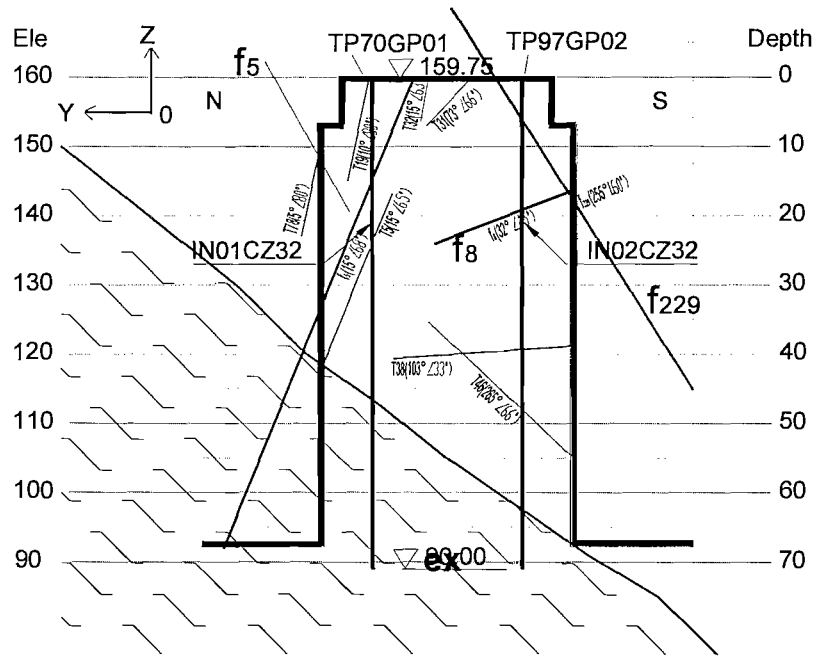
Fig4.10 Discontinuities on the Middle Pier at Sec#17
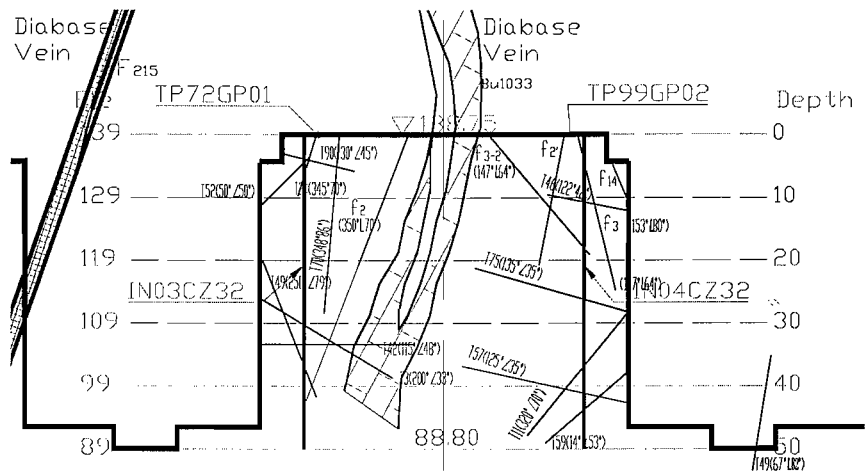
Fig4.11 Discontinuities on the Middle Pier at Sec#20

4.2.1.3 z direction (vertical)

The z displacements of the survey points on Sec#17 and Sec#20 are shown versus time in Fig4.12 and Fig4.13 respectively together with the excavation history. All survey points on Sec#17 and Sec#20 settled at different magnitude.

The abnormality of TP72GP01 (Sec#20, north) displacement curve coincides with the large changes of its x and y deformation (09/98~03/99, Fig4.6 and Fig4.9) at about the same time, which was probably due to an unknown error. Therefore these changes are ignored in the analysis.
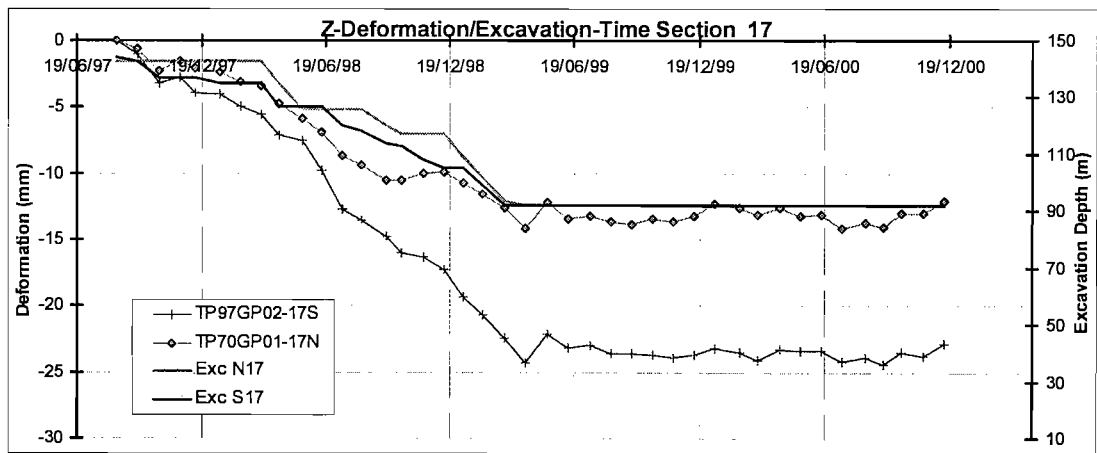
Fig4.12 The z deformation of the Middle Pier at Sec#17
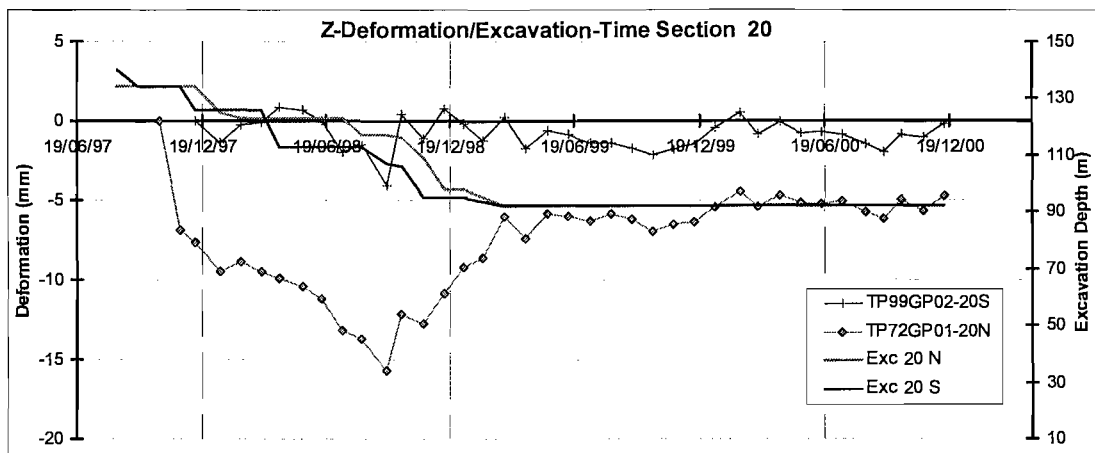
Fig4.13 The z deformation of the Middle Pier at Sec#20

4.2.2 Subsurface deformation of the Middle Pier at Sec#17

4.2.2.1 Inclinometer data

A total of 22 sets of readings were taken from inclinometer IN01CZ32 (north) from 09/97 to 05/99 as shown in Fig4.14. The data sets are consistent with the survey data in general (Fig4.15). Among them, the profiles of 09/98, 10/98 and 02/99 are not consistent with either survey point data (Fig4.15), or with the deformation profiles preceding or following them (Fig4.14). Therefore they are ignored in the analysis because of potential measurement errors that they contain.

A total of 14 sets of readings were taken from inclinometer IN02CZ32 (south) as shown in Fig4.14 from 09/97 till when the instrument was damaged by a site vehicle in 09/98. A general agreement in deformation trend can be seen in comparison with the survey data at TP97GP02 and the deformations measured by inclinometer were generally smaller than those measured by survey data (Fig4.16). Among them, the profiles of 02/98 and 08/98 are not consistent neither with survey point data (Fig4.16), nor with the deformation profiles preceding or following them (Fig4.14). Therefore they are ignored because of potential measurement errors that they contain.

Because the inclinometers are located close enough to Sec#17 (0.2m distance), there is no need to adjust the depth of intersections of discontinuities and inclinometers as described in section 4.1.4.

62
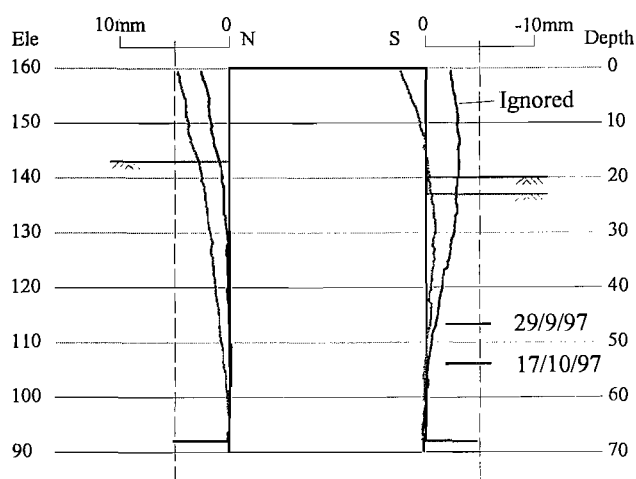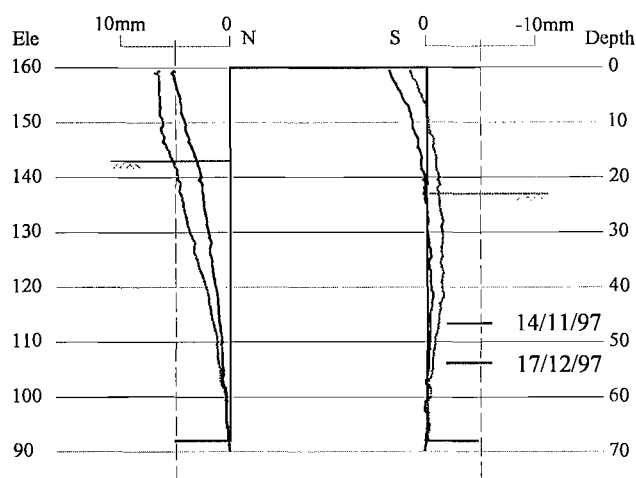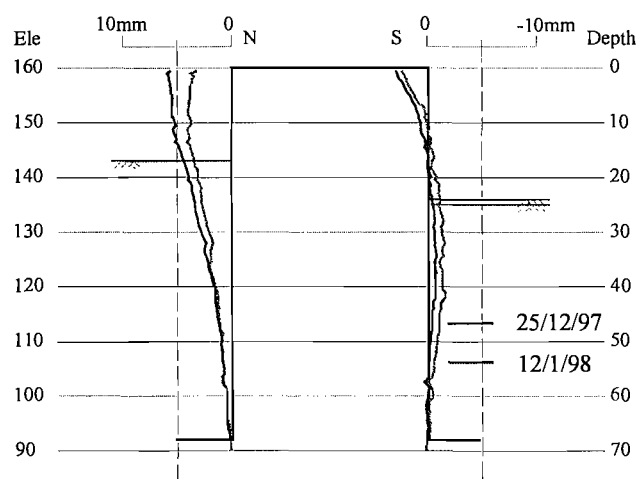
Fig4.14 (1)-(3) Inclinometer profiles of IN01CZ32 and IN02CZ32 (Sec#17)
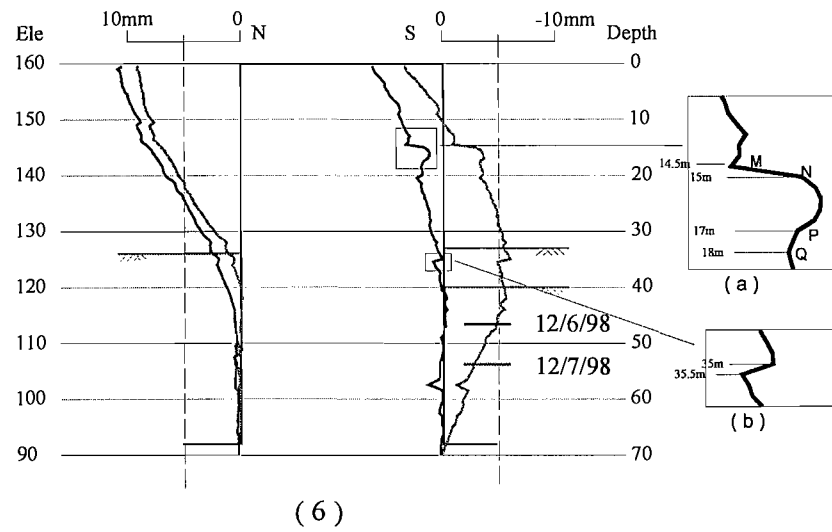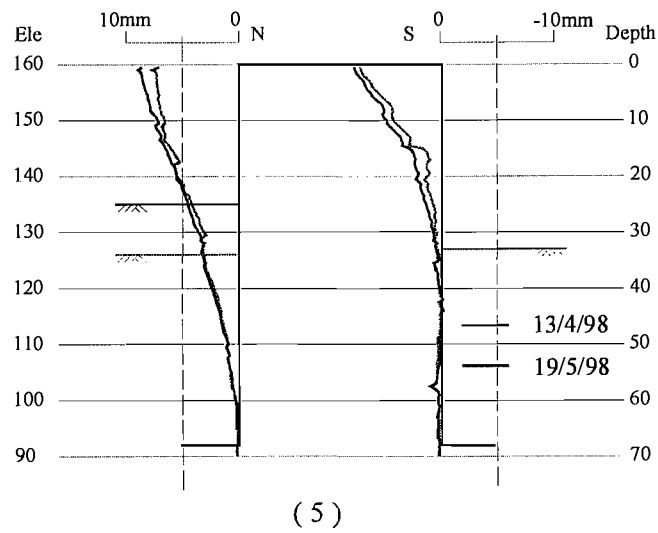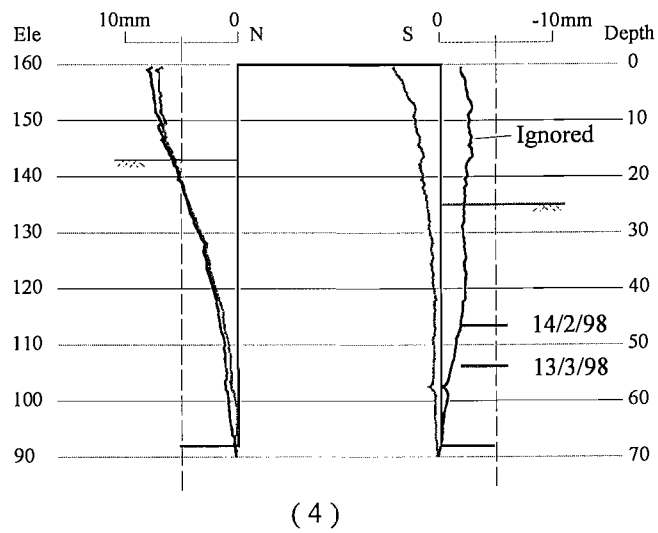
Fig4.14 (4)-(6) Inclinometer profiles of IN01CZ32 and IN02CZ32 (Sec#17)
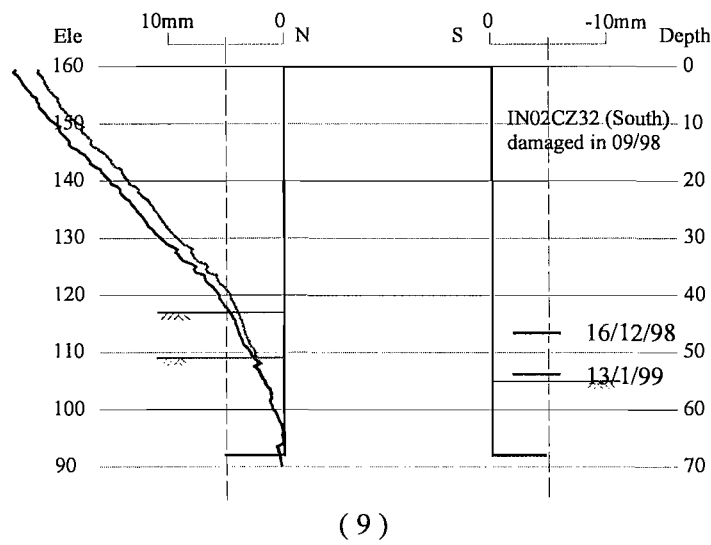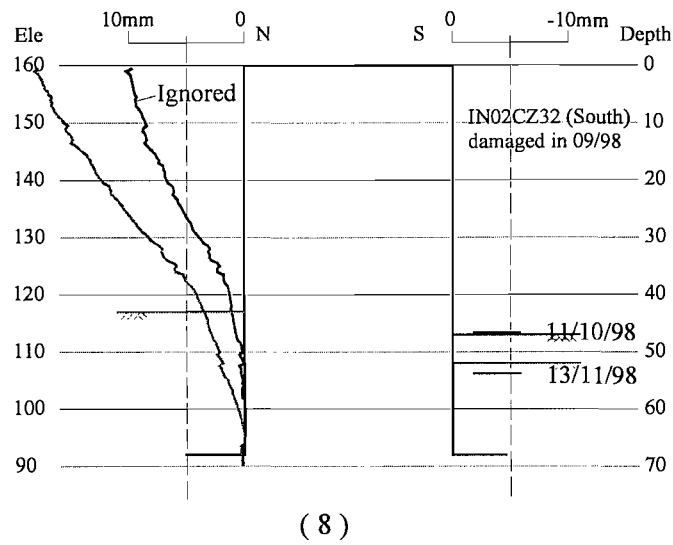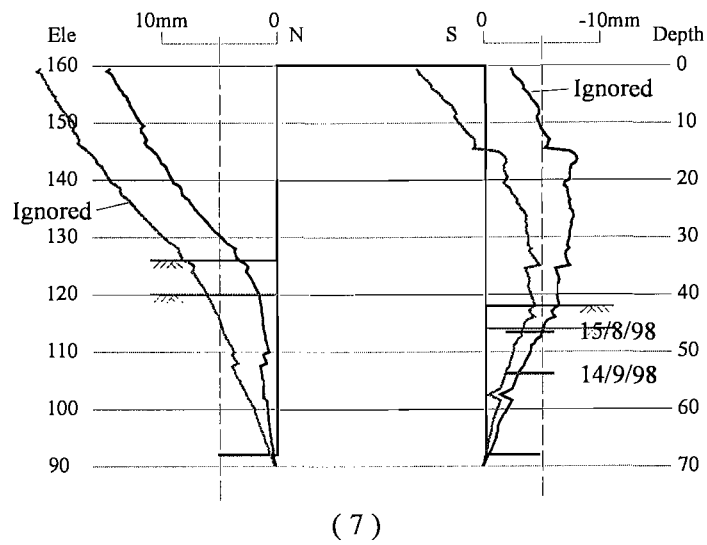
Fig4.14 (7)-(9) Inclinometer profiles of IN01CZ32 and IN02CZ32 (Sec#17)

(10)

(11)
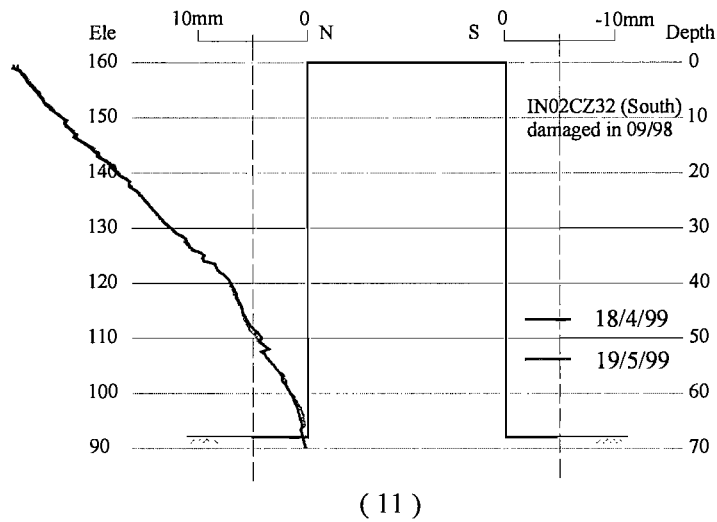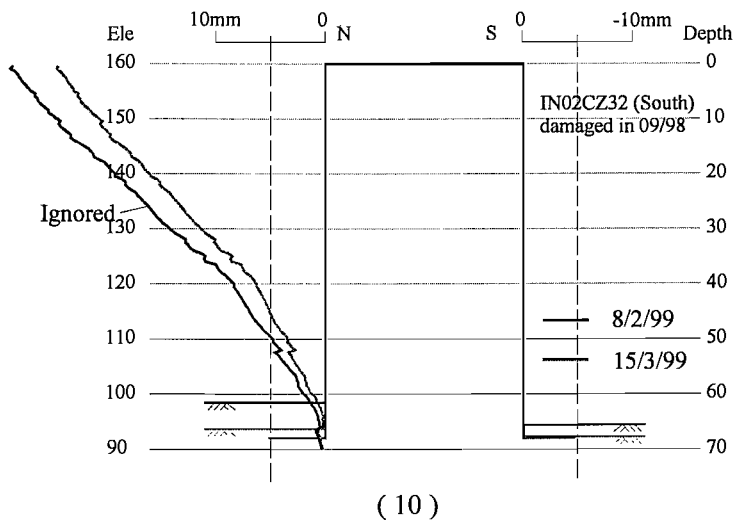
Fig4.14 (10)-(11) Inclinometer profiles of IN01CZ32 and IN02CZ32 (Sec#17)
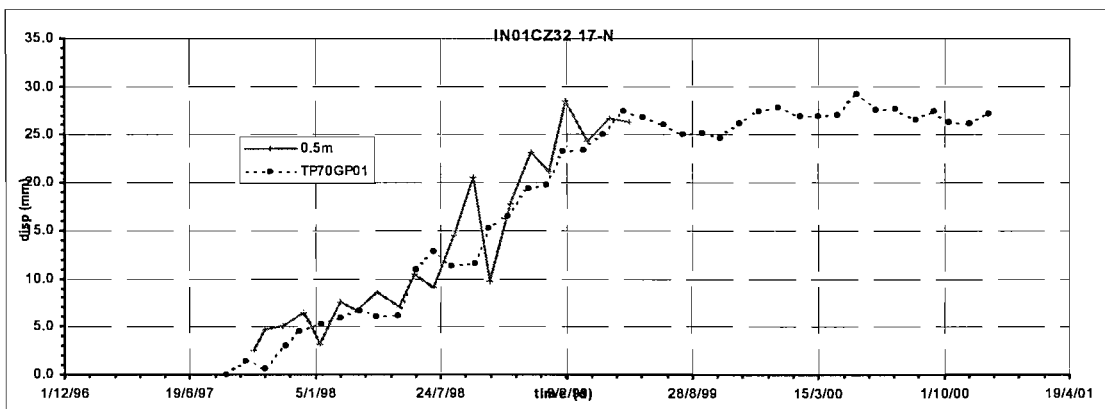
Fig4.15 Comparison between survey and inclinometer of northern side of Sec#17
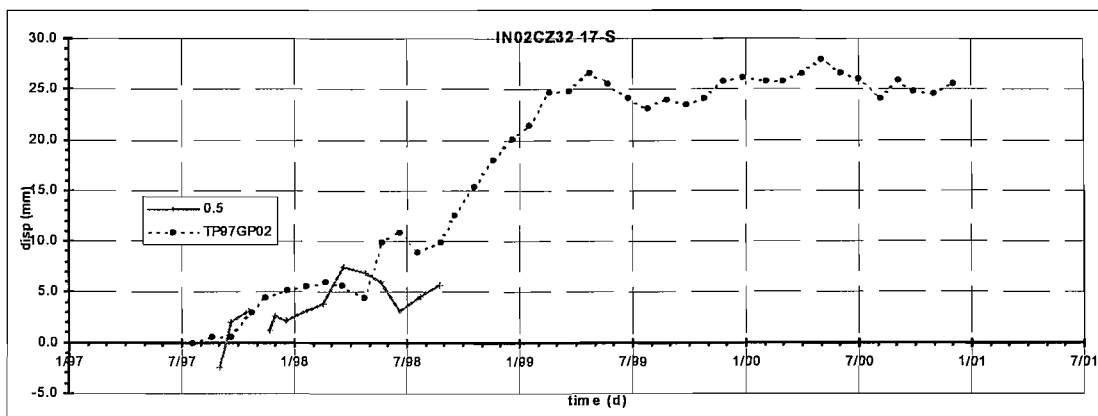
Fig4.16 Comparison between survey and inclinometer on southern side of Sec#17

4.2.2.2 Subsurface deformation of the Middle Pier

The deformation profiles during and after excavation are shown in Fig4.14 for inclinometers IN01CZ32 (north) and IN02CZ32 (south).

It is shown in Fig4.14 that the northern side of the Middle Pier moved to the north gradually in general as excavation proceeded with the exception of a few reversals to the south.

On the south side, the top part of the Middle Pier moved to the north while the middle part deformed to the south. The middle bulge was closely related to the excavation between 06/98 (32m deep) and 07/98 (40m deep) (Fig4.14 (6)), during which the fissure T_{38} was exposed at a depth of about 38m (Fig4.10).

The deformation of the upper part of Middle Pier is generally larger than that of the lower part because it was allowed to deform for a longer period and it is farther from the restraints of the uncut rock.

The Middle Pier at Sec#17 expanded laterally in early stage (before 10/97, Fig4.14) and moved to the north in general (Fig4.17). This is in line with the observations of EDZ made by Li (2002) claiming that the loosen area was larger on the north side.

4.2.2.3 Factors influencing the deformation

Possible reasons for the northern deformation of the Middle Pier towards the north at Sec#17 are:

(1) Excavation on the north side preceded the south side in early stages.

67

(2) There are two main sets of geological structures running NEE and NW-NWW crossing Sec#17 (Fig4.10). Most of faults and fissures on Sec#17 dip to the north on the cross section, e.g. the major fault f_5 (15 ∠68? intersecting the shiplock axis at a small angle of about 5° (Fig4.7) and the xenolith "ex" (Fig4.10). Other faults dipping to the south have low dip angles and intersect the shiplock axis at a larger angle on plan, e.g. f_{229} (255 ∠60? and f_8 (320 ∠45? intersecting the shiplock axis at approximately 55? and 60? respectively (Fig4.10). These faults have little influence on the y deformation of the Middle Pier. Therefore, in total the existing discontinuities tended to increase the deformation to the north due to their dipping direction and form potentially unstable blocks in some areas, which need reinforcement.

(3) Anchors, especially blind cables, may have had a local effect on the deformation of the Middle Pier. Through cables that penetrate the entire width of the Middle Pier also have restricted the lateral expansion. The pattern of anchorages applied on Sec#17 is described in Fig3.15 and Table3.6 and 3.7.

The effects of the anchorages on the deformation of IN01CZ32 and IN02CZ32 are summarized in Table4.4.

The EDZ subzones due to excavation may cause turning points or slips in the inclinometer profiles. For the permanent shiplock, the disturbed zone can be subdivided into a damaged zone 5-10m thick ("C" on the geological sections in Fig4.19) and an affected zone 10-20m thick ("B" on geological section in Fig4.19) (Sheng et. al., 2002).

In the shiplock area, the natural ground level on the north side is about 10~15m higher than on the south side, resulting in larger geostatic vertical and lateral stresses (Fu, 1999).
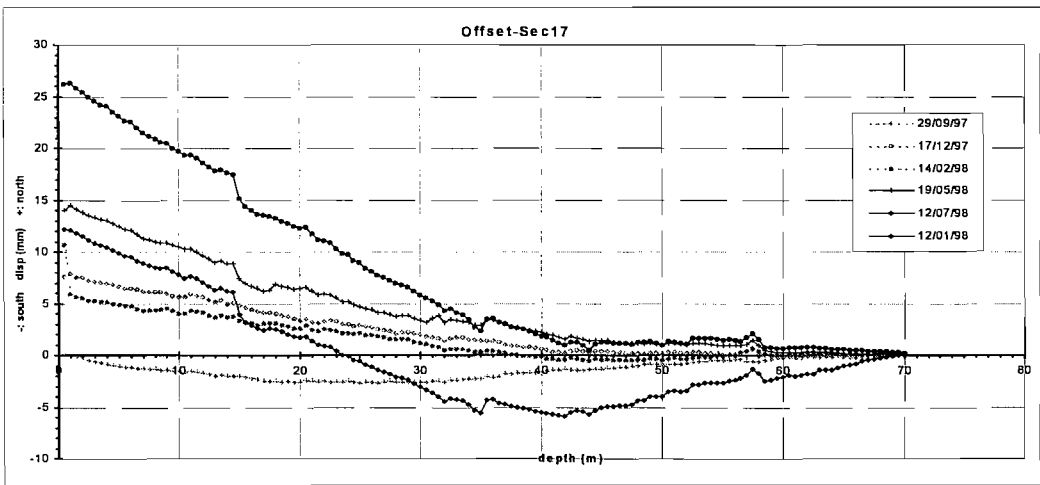
Fig4.17 Average displacement vs depth for the Middle Pier at Sec#17

Table4.4 Effects of anchorage on the deformation of the Middle Pier at Sec#17

	No	Effects
IN01CZ32 (north)	1	7 prestressed cables installed during 12/97 (No.1 in Table3.6) caused the upper part of IN01CZ32 to move back to the south (Fig4.14 (3))
	2	3 through cables and 25 north blind cables were installed at depths between 7m and 14m during 03/98 to 04/98 (No.3 and 4 in Table3.6). They may have been responsible for the reduced lateral expansion of the top 17m compared with the lower part during 05/98 (Fig4.14 (5)). The features on the displacement profiles on both sides of the Middle Pier are consistent with their expected effect of restraint provided by the anchorage installed.
IN02CZ32 (south)	3	The cables installed during 03/98 (at depth of 9m to 15m, No. 2 and 3 in Table3.6) restricted the lateral expansion of the Middle Pier (Fig4.14 (5)). It can be seen by comparing the expansion curves of 13/03/98 and 13/04/98 (Fig4.18) that the top 10m of the Middle Pier was actually compressed by prestressed cables.
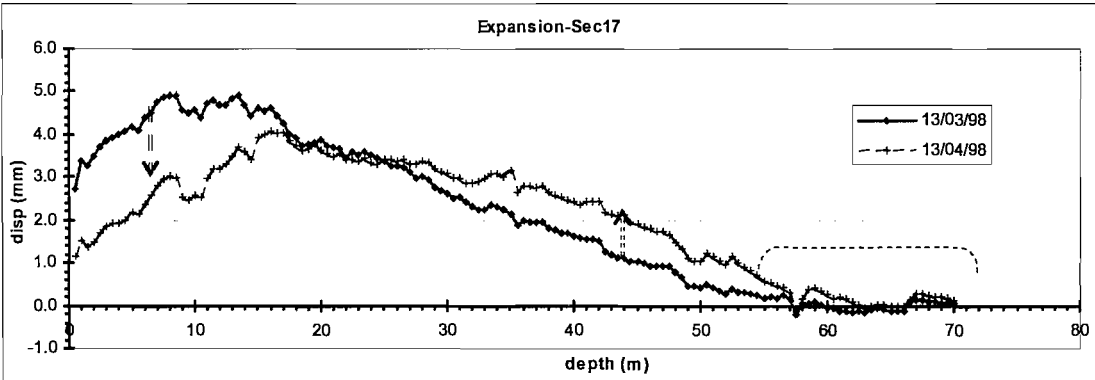
Fig4.18 Lateral expansion of width vs depth for the middle pier at Sec#17
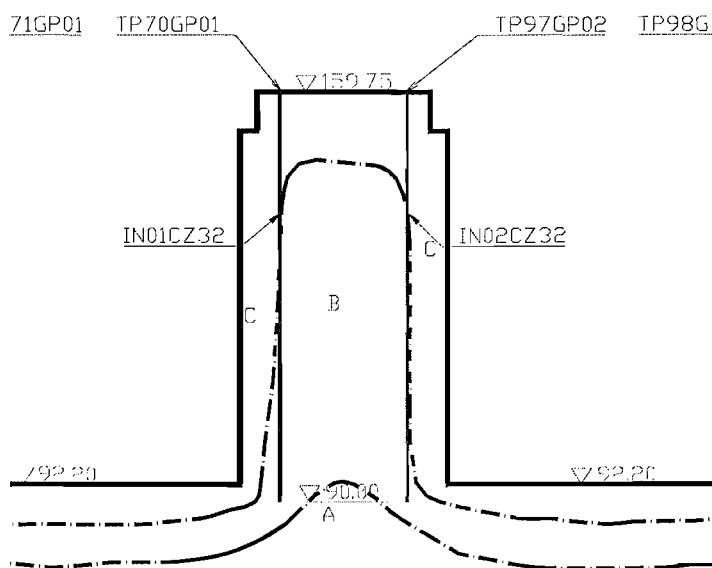
(a) Middle Pier at Sec#17
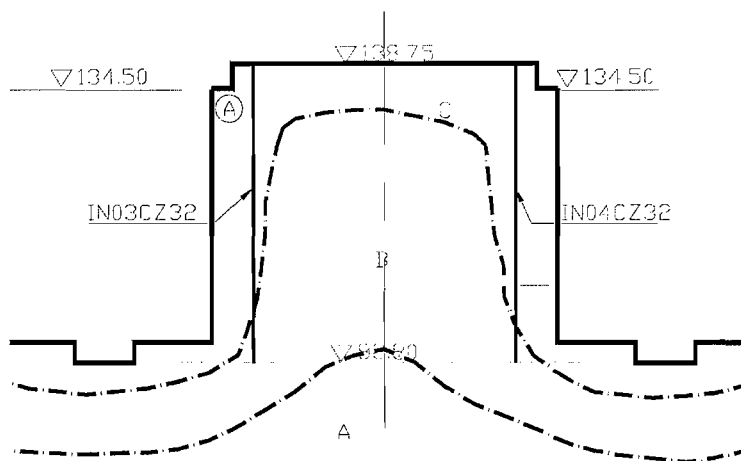
(b) Middle Pier at Sec#20

Fig4.19 EDZ subzones on the Middle Pier at (a) Sec#17 and (b) Sec#20 (Sheng et. al., 2002)

4.2.2.4 Slips on Sec#17

The definition of all three types of slips is presented in section 4.1.4. A few examples can be found in Fig4.11 (6), e.g. item (a) where two close slips (one between points M and N, the other one between points P and Q) form a sliding layer from N to P.

There were no valid jumps with relative displacement of more than 1.0mm/0.5m on the north side (IN01CZ32) before 06/98 (Fig4.14). On the deformation increment curve of 06/98

70

(relative to the previous reading), two slips can be seen at depths of 17.5m-18m and 31m-32m as shown in Fig4.20. The shallow slip could result from f_5 that crossed IN01CZ32 at a depth of about 15m. The lower slip is close to the intersection with fault f_8, which extends from the south side (Fig4.10).

On the south side, there was a slip at a depth of 14.5m-15m that coincided with fault f8 (Fig4.22 (a) and Fig4.20 (c)). The relative displacement across the slip increased quickly after 04/98 (Fig4.21), when excavation on the north reached f8 at depth of around 28m.

A second slip is apparent at a depth of 34.5m-35.5m on the south, around 3m above T38 (Fig4.22 (b) and Fig4.20 (c)). The relative displacement of the slip of 34.5m-35.5m increased quickly after 03/98 (Fig4.21) when the southern excavation level on the south side approached the depth of the slip. The upper part slipped toward the south relative to the lower part, even though T38 declines to the north at a low dip angle (Fig4.10), which could be caused by cables.
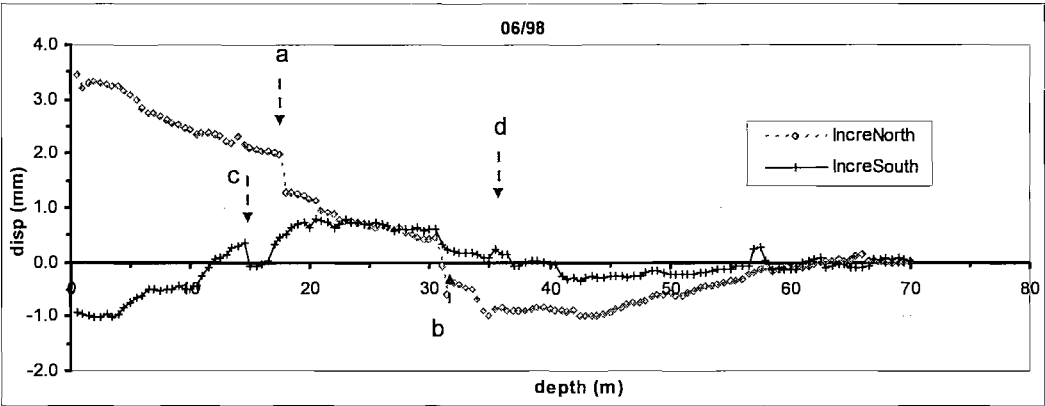
Fig4.20 Deformation increment of IN01CZ32 (north) and IN02CZ32 (south) in 06/98
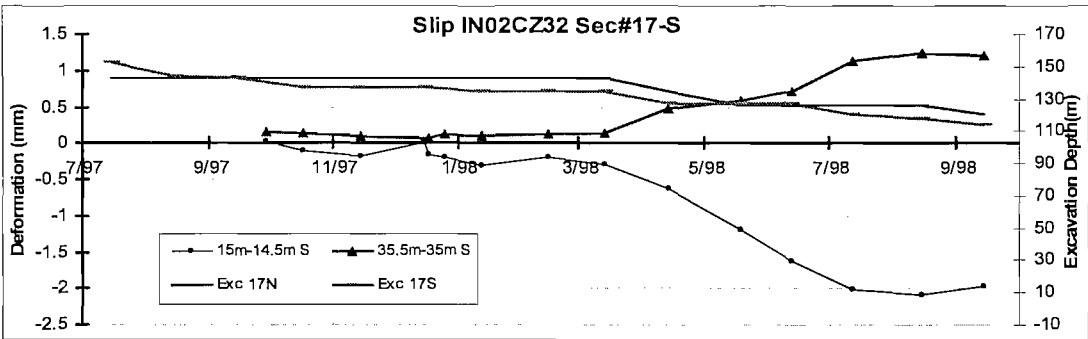
Fig4.21 Slip from depth of 14.5m-35.5m IN02CZ32-17 S

71
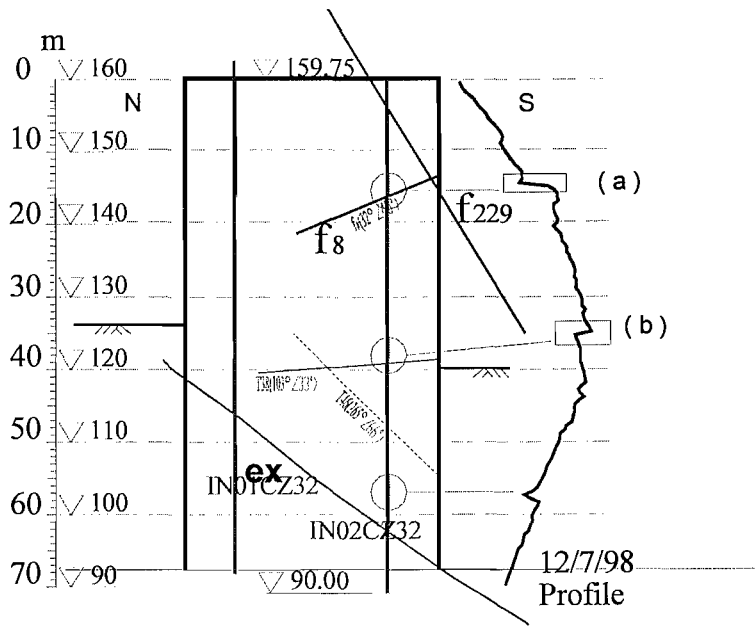
Fig4.22 Slips on deformation profile on IN02CZ32 (south) 12/7/98 (S)

4.2.3 Subsurface deformation the Middle Pier at Sec#20

The geological section of Sec#20 is shown in Fig4.11. There is a diabase vein ($\beta u1003$) of 8-10m thick crossing the top of the Middle Pier. The main faults are f_2 (350 $\angle 70?$, f_{3-2} (147 $\angle 64?$, f_2 (335 $\angle 352?$, f_{14} (170 $\angle 70?$ and f_3 (153 $\angle 80?$.

The Middle Pier at Sec#20 is about 56m wide and 46.5m high. The inclinometers IN03CZ32 (north) and IN04CZ32 (south) are 50m long.

4.2.3.1 Inclinometer data

Inclinometers IN03CZ32 and IN04CZ32 are located at abscissa of 15782.3m and 15782.5m respectively along the shiplock axis, which are effectively 2.7m and 2.5m upstream from Sec#20 (15785.0m) respectively. It is therefore necessary to correct the depths of intersection of the inclinometers with discontinuities on Sec#20 using the method presented in section 4.1.4. Table4.5 shows the corrected depths of intersection of IN03CZ32 and IN04CZ32 with the relevant discontinuities.

A total number of 21 sets of readings were taken at inclinometer IN03CZ32 (north) from 01/98 to 10/99 as shown in Fig4.23 with the excavation levels. Fig4.24 compares the survey data displacements with inclinometer data of IN03CZ32 at depth of 0.5m. The trends of both

curves are consistent (Fig4.24), although the inclinometer data show significant variations. The difference between the survey data and average top inclinometer data was generally constant. It also proves that the assumption that the bottom of the inclinometer remained fixed seems reasonable for IN03CZ32.

A total number of 35 sets of readings were taken at IN04CZ32 (south) from 01/98 to 11/2000 as shown in Fig4.23. The data at depths of 0.5m and 1.0m were ignored because the top of IN04CZ32 was hit during a site accident. Therefore inclinometer data of IN04CZ32 at depth of 1.5m is compared with the survey data in Fig4.25. The comparison shows that the trends of the curves are consistent, but with an even difference of 4-5mm or so (Fig4.25). As the comparison was made between two points at different levels, the proper inclinometer data at the top (0m depth) could be 1~2mm larger than displacement at 1.5m deep by prediction based in on the inclinometer profile. Furthermore the difference was mostly introduced in early stage before 07/98 (Fig4.25). A good agreement will be achieved if the comparison is made on displacement relative to 07/98. After all, the magnitude of the difference is within the precision of inclinometer, which is between ? and 25mm in 30m (Dunnicliff, 1993). Therefore the inclinometer data of IN04CZ32 are considered valid.

Table4.5 Actual depths of intersection of IN03CZ32 and IN04CZ32 with discontinuities (Depth is measured downwards from top of the inclinometer (or top surface of the Middle Pier). A positive sign shows that the actual intersection is below the top surface and a negative one shows that it is above)

IN03CZ32(15782.3m)			IN04CZ32(15782.5m)		
Discontinuity.	Depth (m)		Discontinuity.	Depth (m)	
T90 (30 ∠45?	3.6		f2' (335~352 ∠81?	-1.1~ -4.8	
T52 (50 ∠50?	2.9		f14 (170 ∠70?	-8.5	
T30 (345 ∠70?	9.4		f3 (153 ∠80?	-6.5	
T3 (200 ∠33?	30.0		T46 (122 ∠42?	8.8	
T42 (115 ∠48?	30.5		f3-2 (147 ∠64?	13.9	
T49 (258 ∠79?	47.6		T75 (135 ∠35?	24.4	
f2 (350 ∠70?	47.3		T11 (320 ∠70?	43.0	
T70 (348?∠ 6?	81.0		T57 (125?∠ 5?	39.3	
			T59 (14?∠ 3?	45.4	
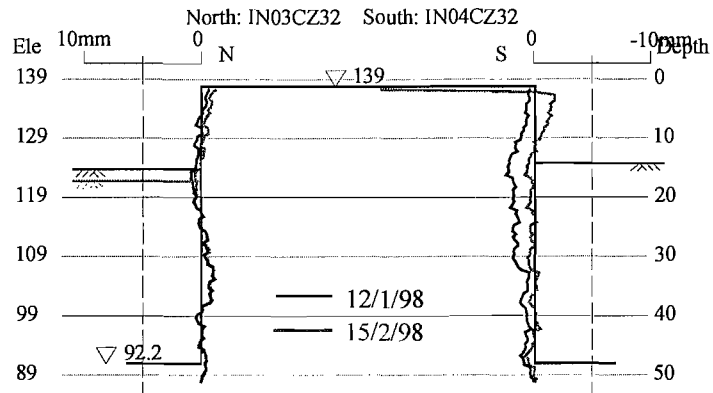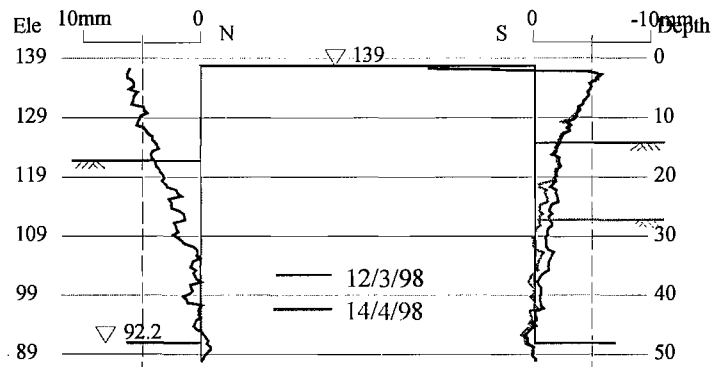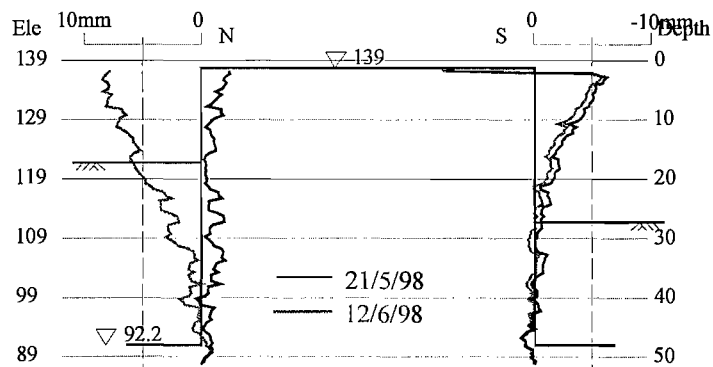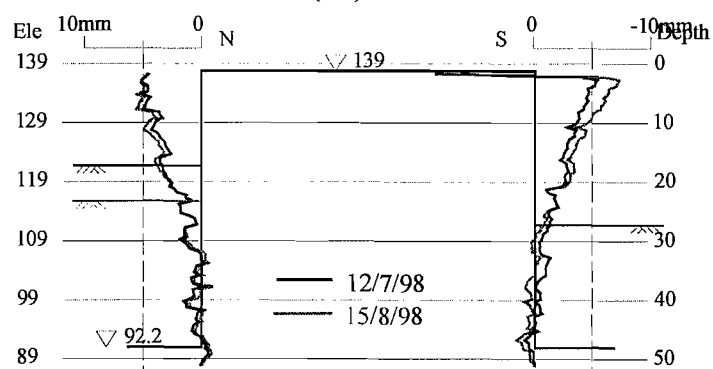
Fig4.23 (a-d) Inclinometer profiles of Sec#20 (IN03CZ32-N, IN04CZ32-S)

74
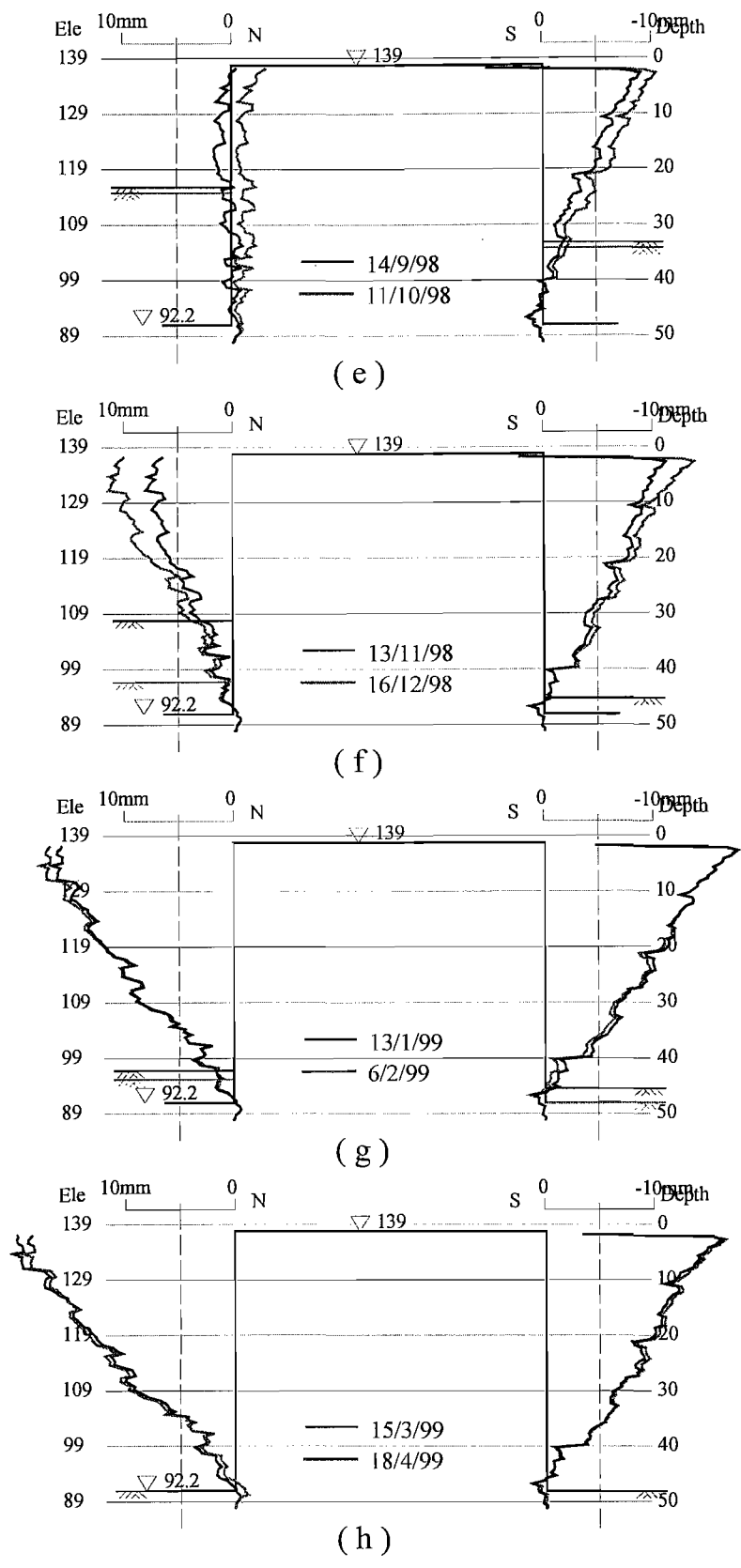
Fig4.23 (e-h) Inclinometer profiles of Sec#20 (IN03CZ32-N, IN04CZ32-S)

75
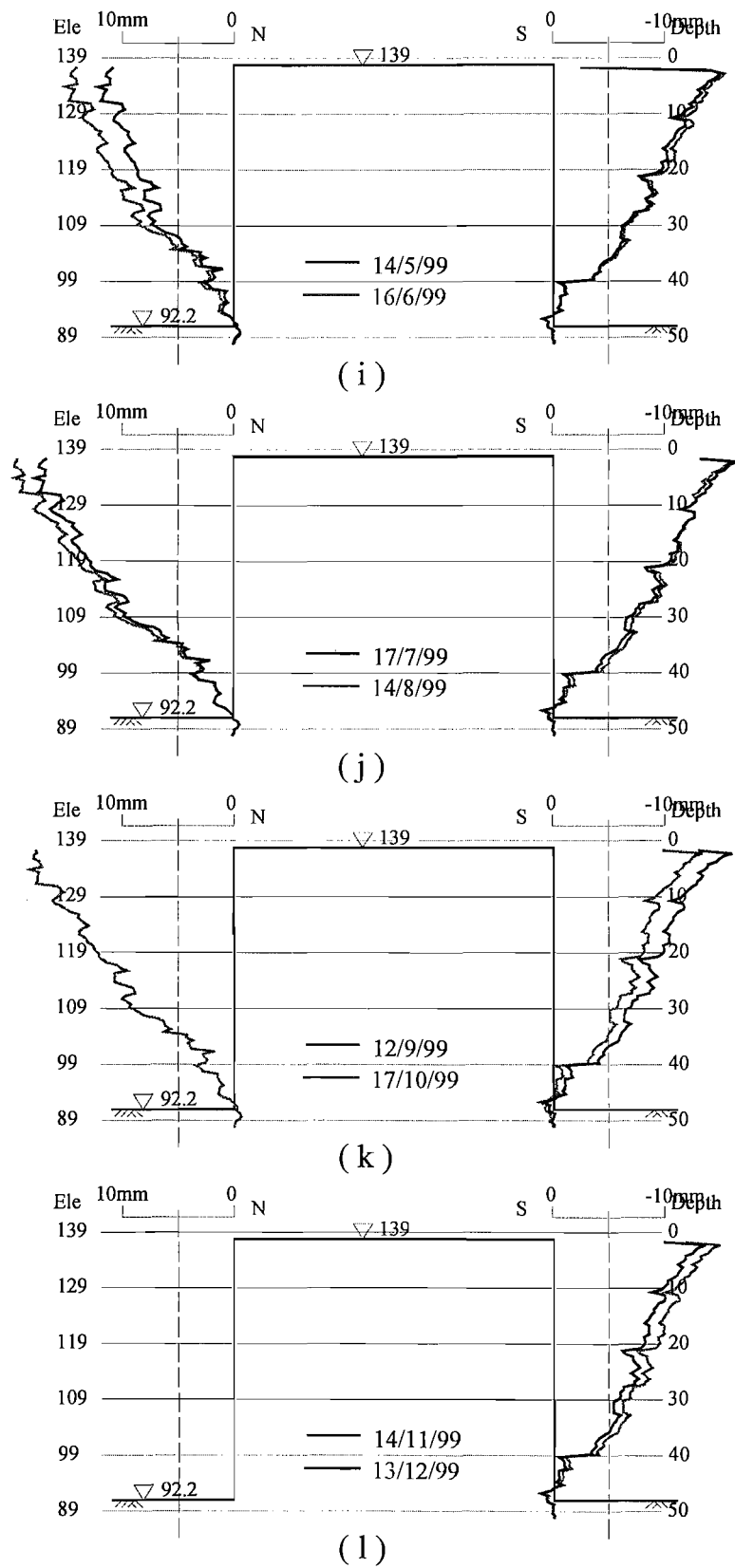
Fig4.23 (i-l) Inclinometer profiles of Sec#20 (IN03CZ32-N, IN04CZ32-

(m)

(n)

(o)

S)

(p)
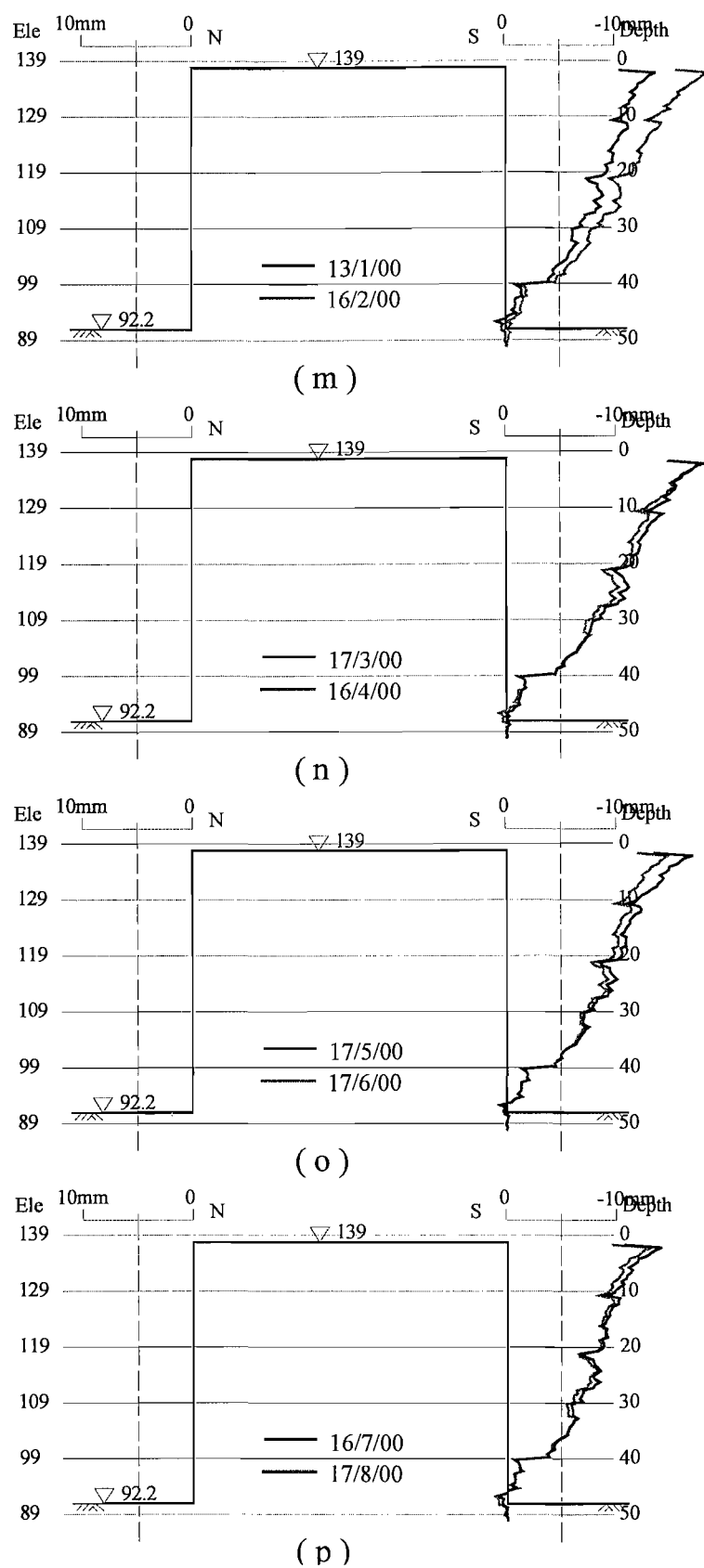
Fig4.23 (m-p) Inclinometer profiles of Sec#20 (IN03CZ32-N, IN04CZ32-S)

(q)

(r)
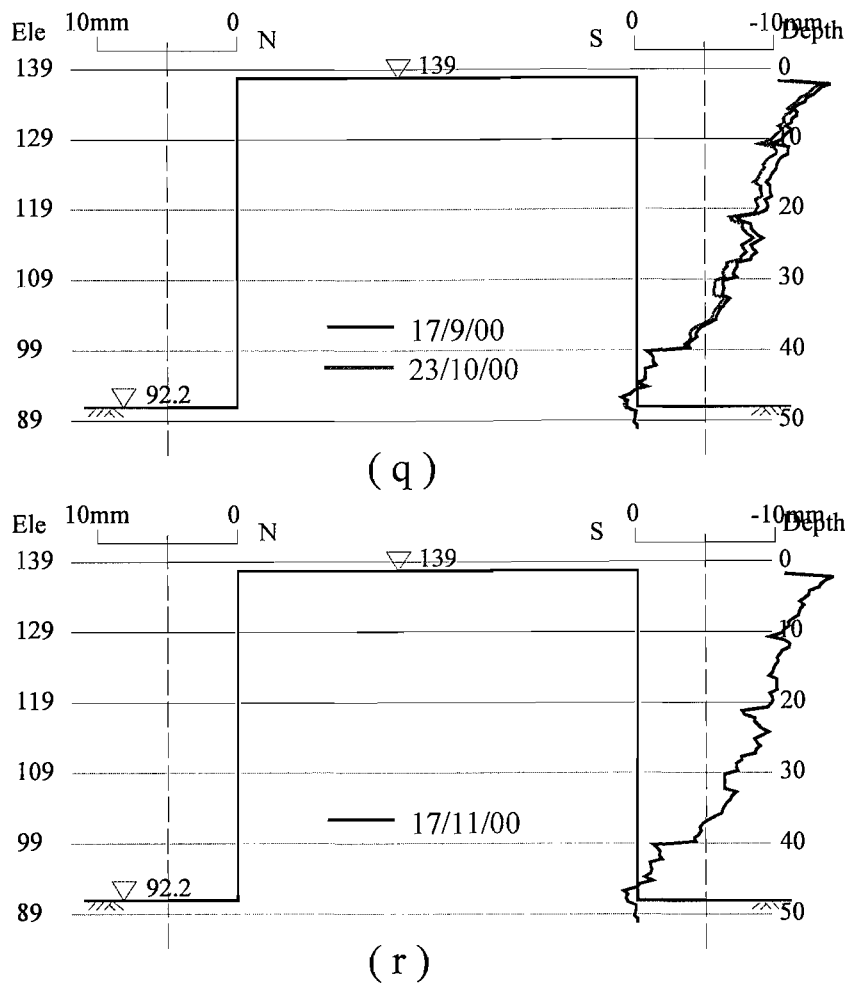
Fig4.23 (q-r) Inclinometer profiles of Sec#20 (IN03CZ32-N, IN04CZ32-S)
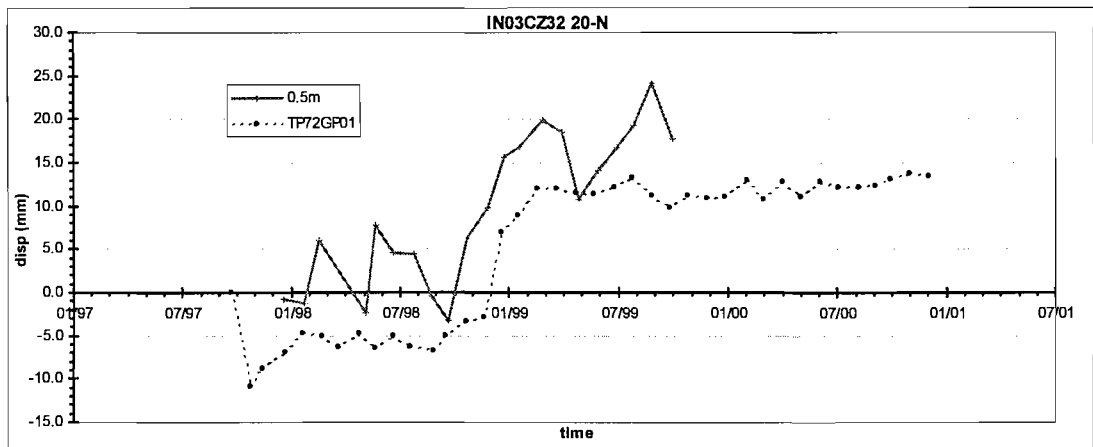
Fig4.24 Comparison between survey data and inclinometer data on the north side of the Middle Pier at Sec#20
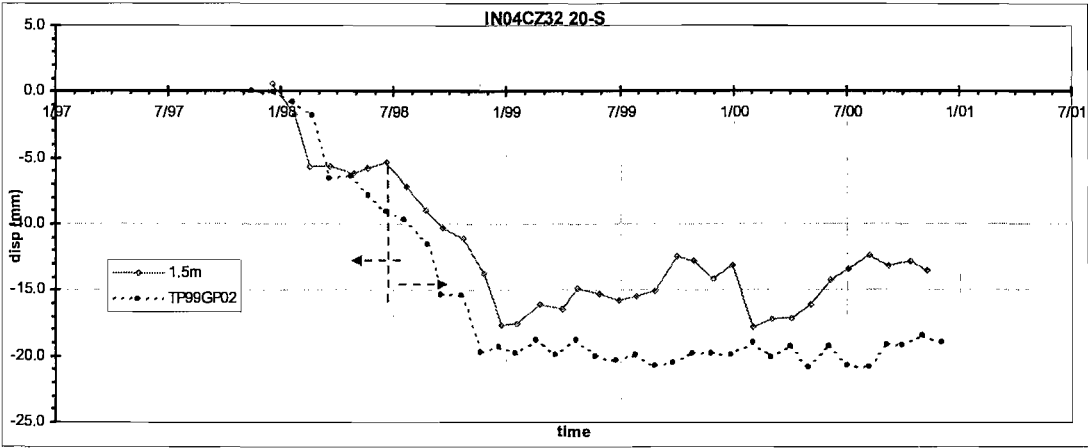
Fig4.25 Comparison between survey data and inclinometer data on the south side of the Middle Pier at Sec#20
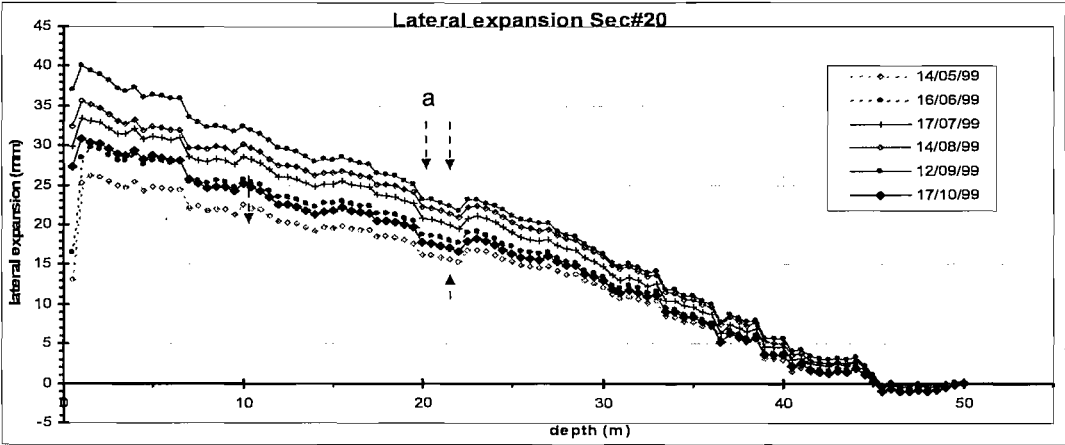
Fig4.26 Lateral expansion of the Middle Pier at Sec#20
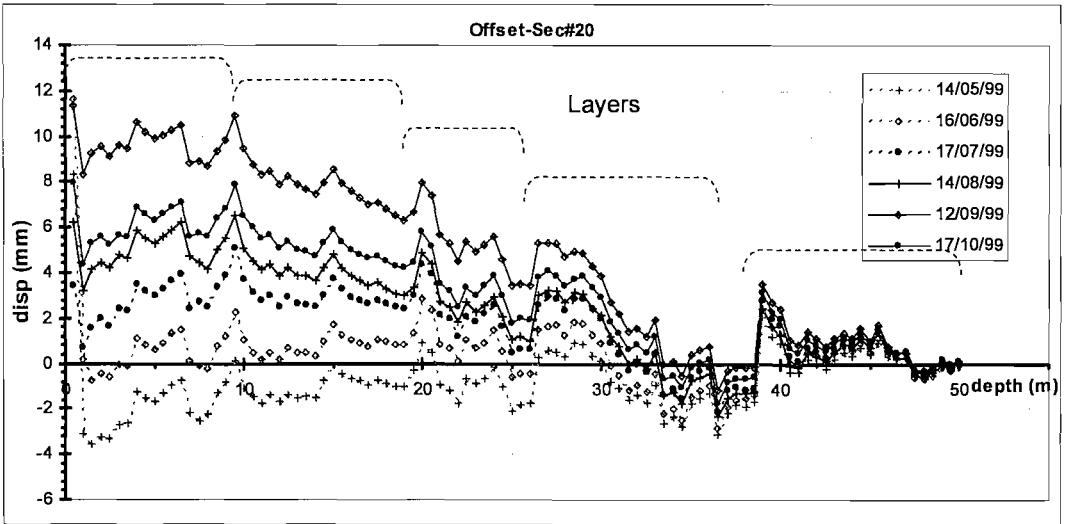
Fig4.27 Average displacement vs depth for the Middle Pier at Sec#20 (+:north; -:south)

4.2.3.2 Subsurface deformation of the Middle Pier

As shown in Fig4.23, the north side of the Middle Pier at Sec#20 moved generally to the north linearly with depth and was directly affected by excavation level. Large movements of IN03CZ32 to the north occurred after a deep excavation on the north (10/98 to 11/98 and 12/98 to 01/99, Fig4.23 (e-g)).

There was considerable noise in the measurements of IN03CZ32 of about ±1.0mm (Fig4.23). Comparing the profiles to the deformation increment curves relative to 03/98 as shown in Fig4.28 (a) and (b), we can conclude that most of the noise was introduced before 03/98, or even before 01/98, because the curves in Fig4.28 (b) are much smoother (less noisy) than those in Fig4.28 (a).
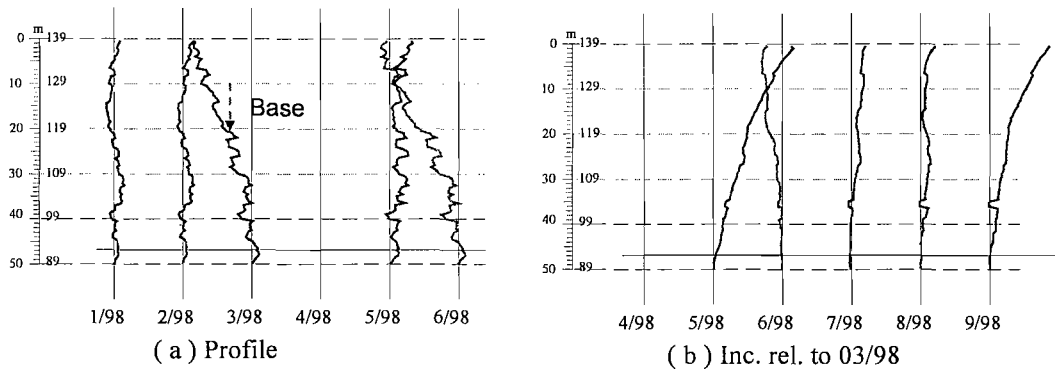
Fig4.28 Deformation and deformation increment curves of IN03CZ32 (Sec#20-N)

IN04CZ32 moved generally to the south (Fig4.23). During the period 01/98 to 01/99, the deformation to the south increased gradually as the excavation deepened. After 01/99, IN04CZ32 stopped moving to the south. The deformation profiles again show considerable noise, which is similar to that on IN03CZ32 and can be eliminated by changing the starting date.

IN03CZ32 and IN04CZ32 moved outwards by 24mm (at depth of 0.5m, Fig4.24) and 17.6mm (at depth of 1.5m, Fig4.25) respectively near the top. The lateral expansion of the Middle Pier at Sec#20 reached almost 40mm at the top in 09/99 (Fig4.26) as a combined result of both sides deforming into the chamber after excavation. Over all the Middle Pier moved slightly to the north slightly as shown in Fig4.27, which reveals a number of layers along the depth with different lateral deformation.

In total, the deformation pattern at Sec#20 is that the Middle Pier expanded similarly into the shoplock chambers with decreasing expansion from the top to bottom while the vertical center line moved little.

4.2.3.3 Factors influencing the deformation

The most important factor that influences the deformation at Sec#20 is excavation level as shown in Fig4.23. However a noticeable feature is that the deformation on one side is affected mostly by the excavation level on that side, but hardly by the excavation level on the other chamber. This is attributed to the large width of 57m of the Middle Pier at Sec#20, which weakens the effect of excavation on the far side of the Middle Pier. Unloading due to excavation caused the two sides to deform into chamber respectively.

The discontinuities influenced significantly the deformation pattern. Most of the discontinuities on the north side are dipping into the north. This tends to increase the deformation and form unstable blocks on the north side, while it is a mixed picture on the south side. Some of the discontinuities are directly or partly related to the slips on the profiles, which are discussed in more detail in following section.

MSE: blind cable on the south of the Middle Pier,prestressed to 3000kN;
MP: through cables penetrating the Middle Pier, prestressed to 3000kN.

(a) (b)
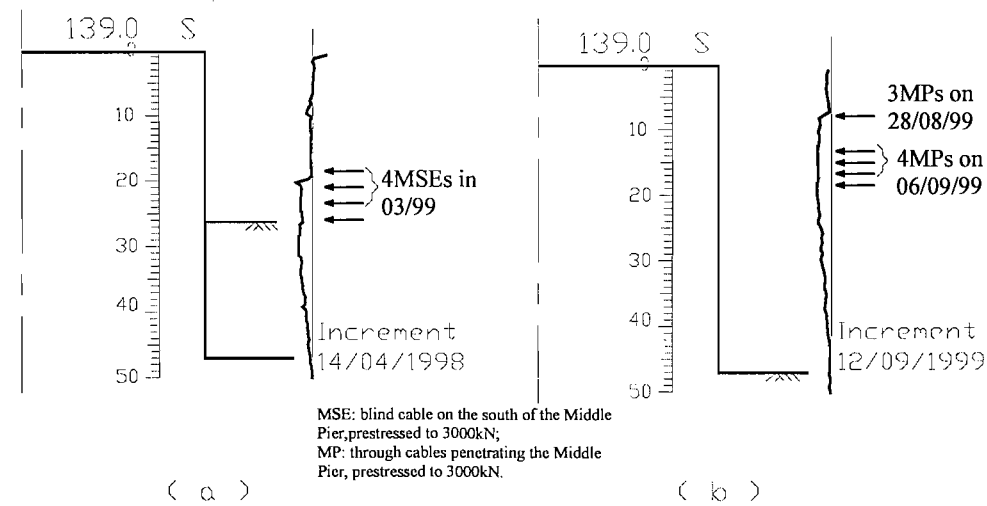
Fig4.29 Effect of anchorage on the deformation of inclinometers (Cables Nos.1 and 10~12 in Table3.7)

Anchorage is another factor influencing the deformation of the Middle Pier. The anchorage installed in the area of Sec#20 is summarized in Table3.7 and shown in Fig3.15. Two examples on the south side are shown in Fig4.29 (anchorage numbers 1 and 10 to 12 in

81

Table3.7). The effects of anchorage are more localized, e.g. between slips along discontinuities. The restraints that anchorages impose on the expansion are also shown in Fig4.26 (a).

4.2.3.4 Slips on Sec#20

The same classification and threshold value for slip (? mm/0.5m) described in section 4.1.4 are adopted for Sec#20. The major slips along IN03CZ32 (north) and IN04CZ32 (south) are summarized and analyzed in Table4.6 and Table4.7 respectively. To eliminate the noise discussed in previous section, the deformation increment relative to the last measurement and deformation relative to 02/98 are used to illustrate the slip pattern.

Table4.6 Slips on north side of Sec#20 (IN03CZ32)

Depth (m)	Fig	Rel. disp. (mm)	Description
4-3.5 7-6.5	Fig4.31 Fig4.30 (a)	1.05 -2.01	These two slips relate to fissures T_{90} (130 $\angle$45? and T_{30} (345 $\angle$70? respectively (Fig4.30 (a)), that form a layer of around 3m thick slipping to the north. The relative displacements of the slips increased as excavation activities progressed (Fig4.31).
30.5-30	Fig4.33 Fig4.30 (a)	-1.07	Fissures T_3 (200 $\angle$33? and T_{42} (115 $\angle$48? intersect the inclinometer at this depth (Fig4.32). This slip remained active and the relative displacement increased during excavation. There were quick increases of relative displacement in 03/98 and 06/98 (Fig4.33) when excavation level was about 15m above the depth of the slip.

06/02/99 Rel to 02/98
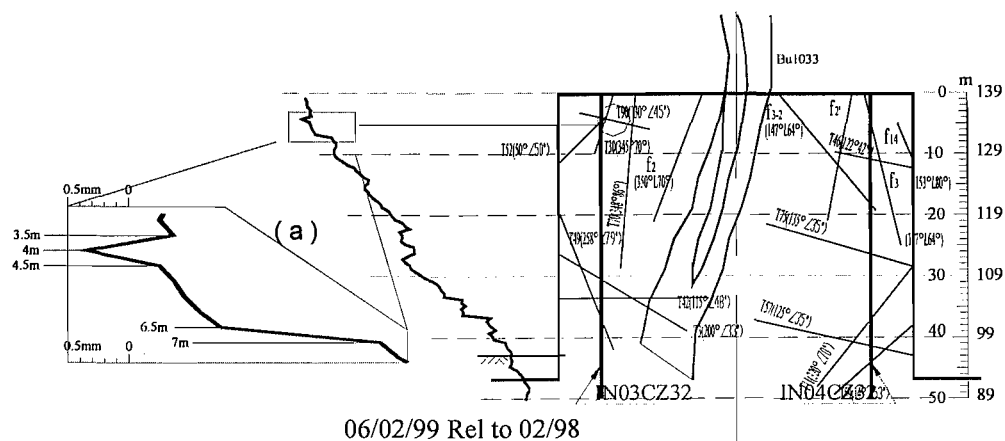
Fig4.30 Slips patterns at depths of 4m and 7m on IN03CZ32 (Sec#20-North)
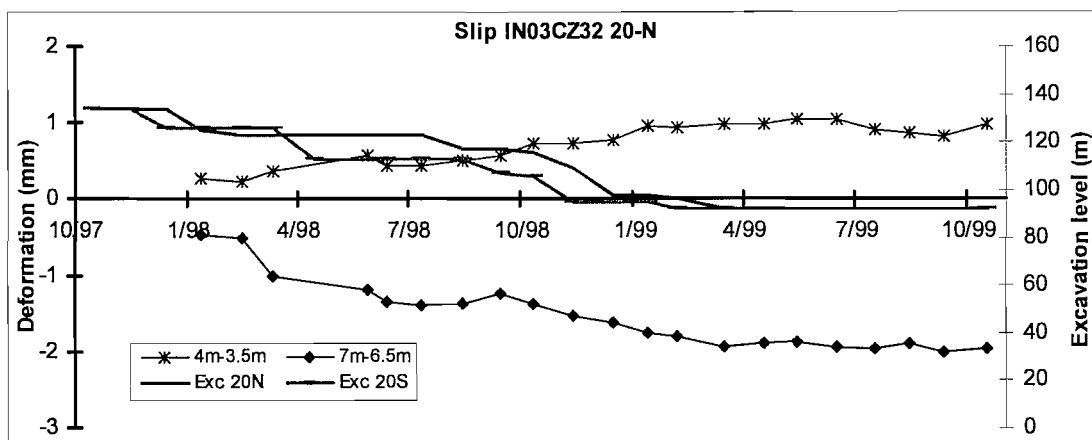
Fig4.31 Relative displacement at depth 4m and 7m of IN03CZ32 (Sec#20-North)

13/01/99 Rel to 02/98
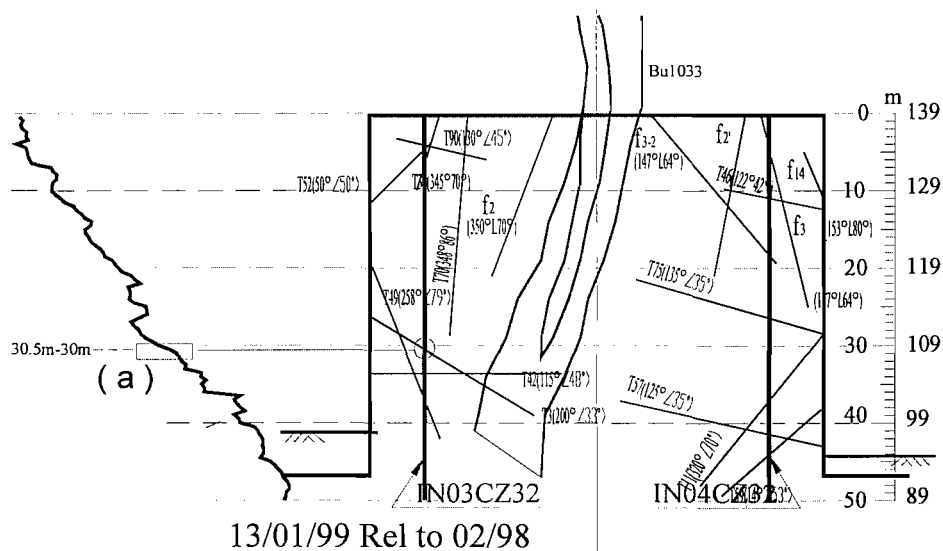
Fig4.32 Slips patterns at depths of 30.5m –30m on IN03CZ32 (Sec#20-North)
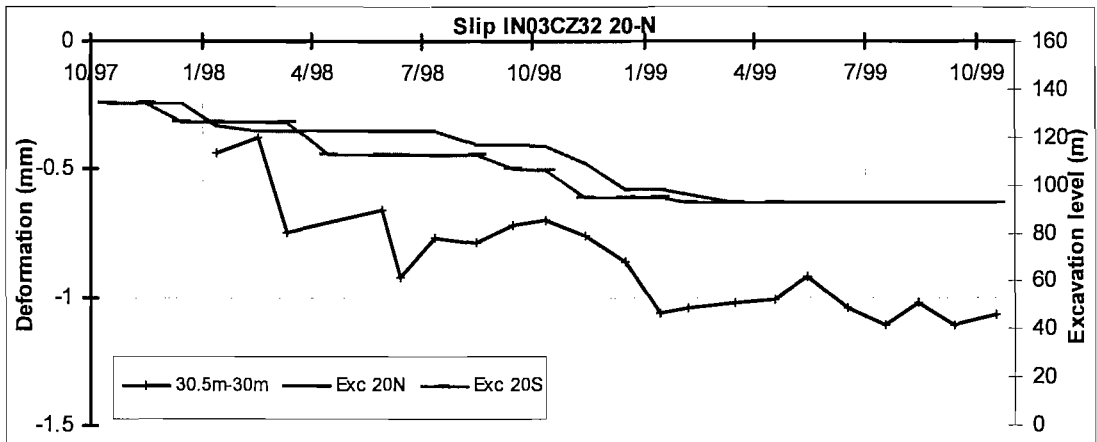
Fig4.33 Relative displacement at depth of 30.5m –30m of IN03CZ32 (Sec#20-North)

Table4.7 Slips on south side of Sec#20 (IN04CZ32)

Depth (m)	Fig	Rel. disp. (mm)	Description
10-9.5	Fig4.34 (a)	-1.39	The slip was possibly caused by fissure T_{46} (122 $\angle$ 42? (Fig4.34 (a)) that intersects IN04CZ32 at a depth of 8.8m and dipping to the south. The increase of relative displacement occurred mainly during excavation activities (Fig4.35).
26.5-26	Fig4.34 (b)	1.1	The slip possibly relates to T_{75} (135 $\angle$ 35? (Fig3.34 (b)). The slip was active during and after excavation (Fig4.35). The displacement started to increase quickly when the excavation exposed the fissure T_{75} during 04/98 (Fig4.23 (b)), and when excavation approached the bottom in 10/98. The prestressed cables (No 1 in Table4.5) may have been partly responsible for the development of the slip (Fig4.29 (a)).
39-38.5	Fig4.36 (a)	3.27	This large slip was possibly related to T_{57} (125 $\angle$ 35? (Fig4.36 (a)). The relative displacement was closely related to the excavation level. It increased quickly from 09/98 to 11/98, during which period the fissure was exposed (Fig4.23 (e-f)).
45.5-45	Fig4.37 (a)	1.13	This slip may be related to the fissure T_{59} (14 $\angle$ 53? (Fig4.37 (a)). Relative displacement started to develop from 10/98 when the excavation level approached the depth of the fissure (Fig4.23 (e) and Fig4.38).
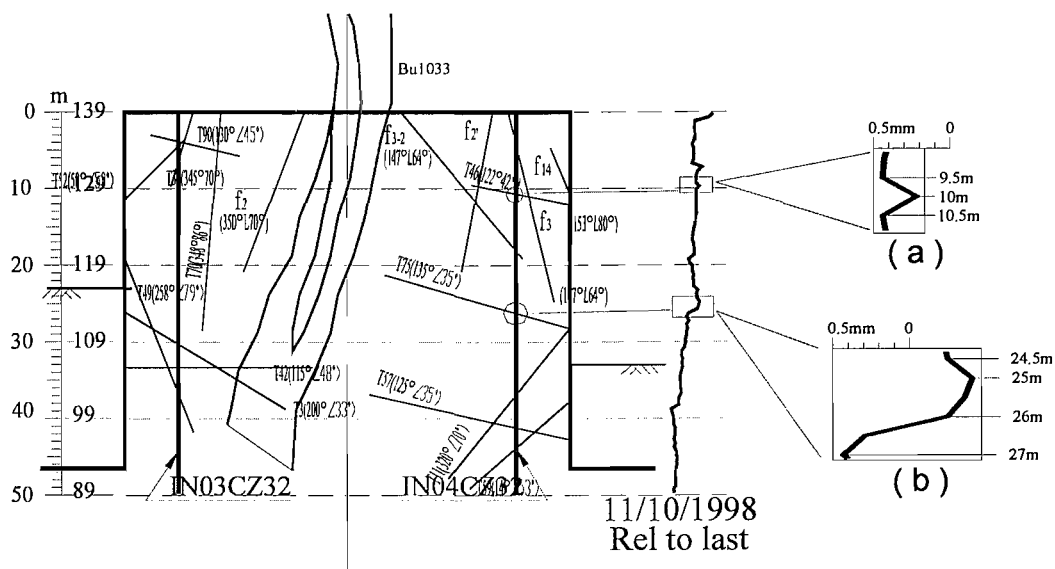
Fig4.34 Slips patterns at depths of 10m and 26.5m on IN04CZ32 (Sec#20-South)
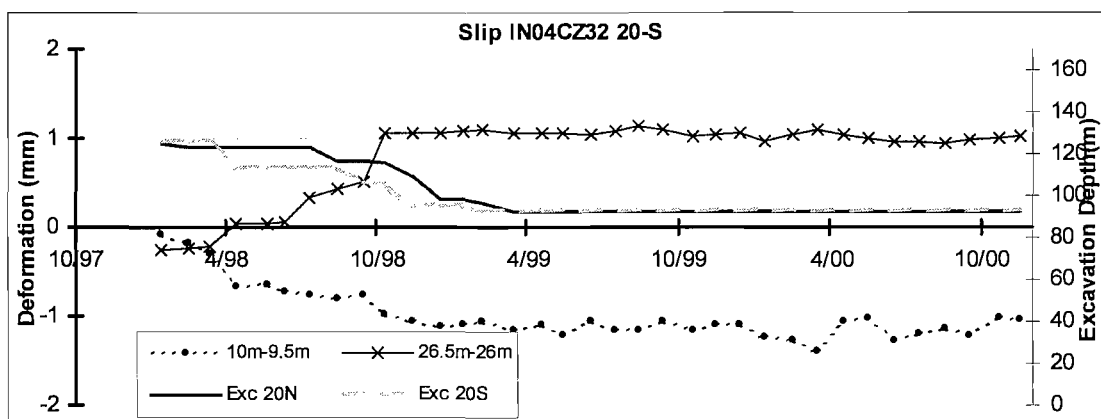
Fig4.35 Relative displacement at depth 10m and 26.5m of IN04CZ32 (Sec#20-South)
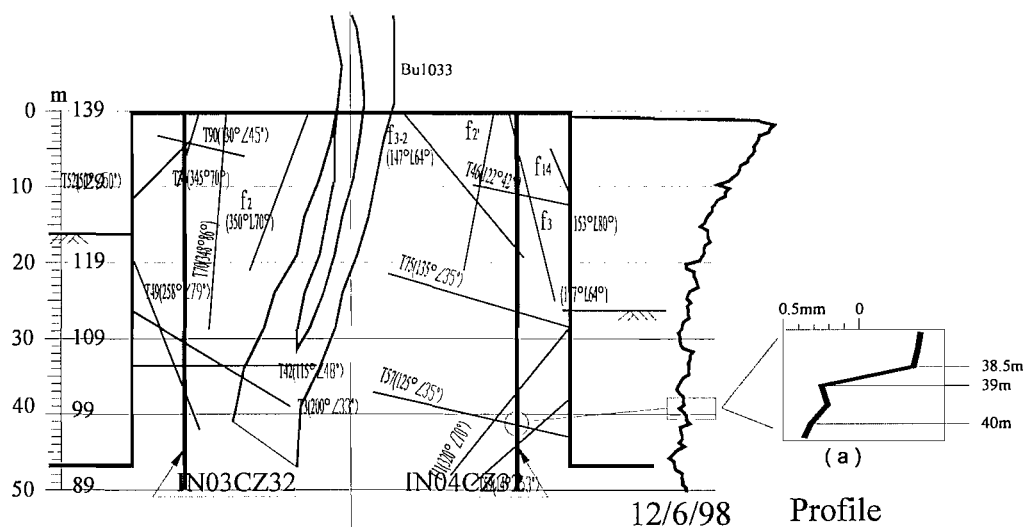
Fig4.36 Slips patterns at depths of 39m on IN04CZ32 (Sec#20-South)

85
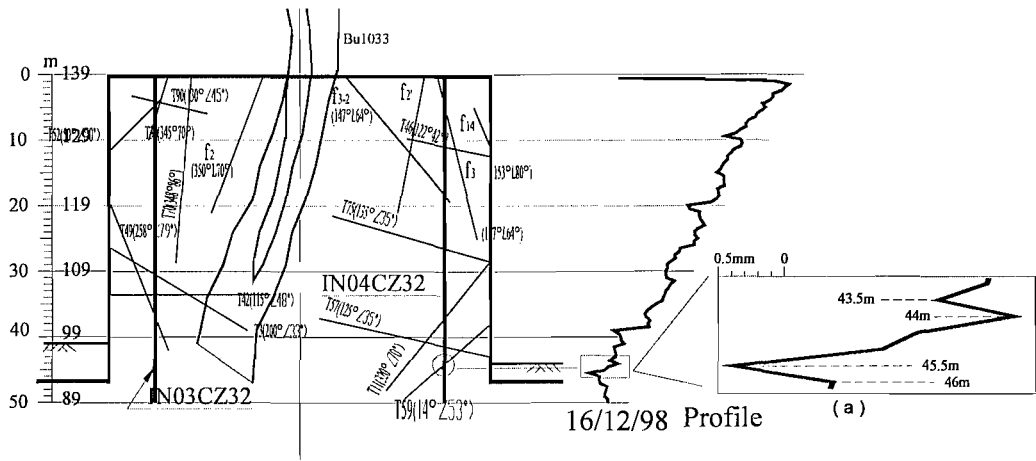
Fig4.37 Slips patterns at depths of 45.5m on IN04CZ32 (Sec#20-South)
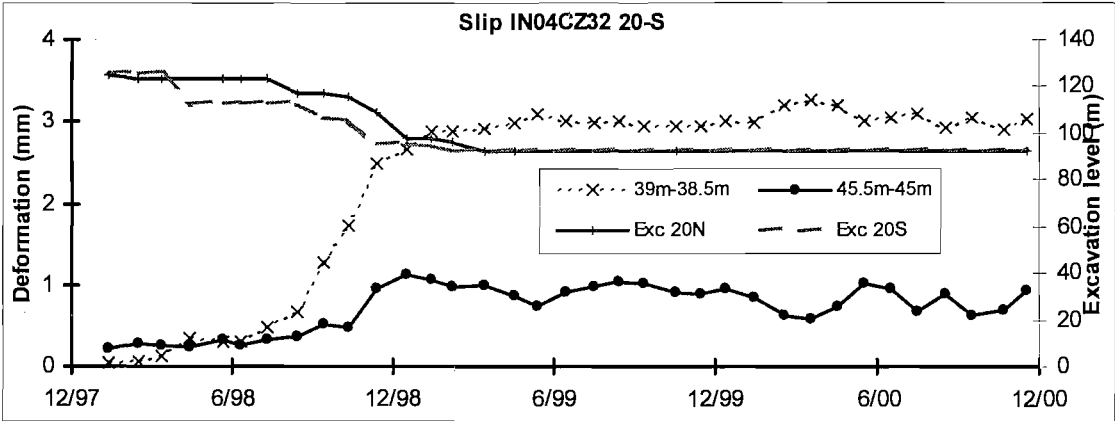
Fig4.38 Relative displacement at depths of 39m and 45.5m of IN04CZ32 (Sec#20-South)

4.3 Surface Deformation of Slopes

The instrumentation on the slopes of Sec#17 and Sec#20 is shown in Fig4.39 and Fig4.40 respectively and the relevant information is summarized in Table4.8.

There are no measurement data for point TP08GP01 because the instrument was broken. The points TP100GP02 and TP73GP01 are also ignored because of insufficient measurements available.

4.3.1 x deformation

The x deformations (along the axis of the shiplock) of the survey points are shown in Fig4.41 to Fig4.44 together with excavation history.

During excavation, most points on both sections moved little in the x direction before approximately 7/98 and their deformations accelerated between 07/98 and about 10/99.

The survey points on the slopes tended to move towards downstream in accordance with inclined bottom line of excavation along the shiplock axis. However, Sec#17 appears to be shearing with the south slope moving downstream while the north slope moving upstream slightly. On the other hand, Sec#20 appears to be translating with both of the slopes moving downstream similarly, as illustrated in Fig4.45, which shows the x deformations of survey points on the slopes at three different times.

At Sec#20, a collapse on the south slope caused an abnormality on the deformation of TP33GP02 during the month prior to 09/11/98 (Fig4.43). If the deformation during this period is discarded, the data follow the same trend as the other survey points on the south slope at Sec#20.

Table4.8 General information for survey points and inclinometers

Position		Inclinometer	Len (m)	Measurement duration		Data Sets	X* (m)	Ele (m)	Survey Point	Measurement duration		Data Sets
#17	North							230	TP10GP01	15/06/95	10/11/00	66
		IN04GP01	45.5	04/12/95	20/11/00	166	680.1	215	TP08GP01			
								200	TP11GP01	15/01/96	10/11/00	59
		IN08GP01	17.5	05/05/96	21/11/00	153	675.9	170	TP12GP01	15/11/96	10/11/00	49
		IN11GP01	70	12/03/98	18/11/00	30	668.3	160	TP71GP01	10/12/97	11/12/00	37
	MP	IN01CZ32	70	29/09/97	19/05/99	22	675.2	160	TP70GP01	16/08/97	11/12/00	41
		IN02CZ32	70	29/09/97	14/09/98	16	675.2	160	TP97GP02	16/08/97	11/12/00	41
	South	IN16GP02	69	12/03/98	11/05/99	13	672.6	160	TP98GP02	16/08/97	11/12/00	41
		IN13GP02	14	12/02/96	22/11/00	160	674.6	170	TP26GP02	15/11/96	10/11/00	49
		IN07GP02	30.5	06/12/95	03/08/98	91	680.3	200	TP27GP02	15/11/95	10/11/00	61
		IN06GP02	36.5	21/06/95	19/12/00	181		230	TP28GP02	15/04/95	10/11/00	69
								245	TP29GP02	15/04/95	10/11/00	72

#20	North	IN05GP01	35.5	21/01/96	15/11/01	166	776.0	200	TP13GP01	15/01/96	10/11/00	59
		IN09GP01	35	05/05/96	21/11/00	154	777.4	170	TP14GP01	15/04/96	10/11/00	56
		IN12GP01	51	12/03/98	18/11/00	23	782.4	139	TP73GP01	14/06/98	10/08/98	3
	MP	IN03CZ32	50	12/01/98	17/10/99	21	782.3	139	TP72GP01	10/12/97	11/12/00	39
		IN04CZ32	50	12/01/98	17/11/00	35	782.5	139	TP99GP02	10/12/97	11/12/00	37
	South	IN17GP02	61	12/03/98	17/11/00	32	782.6	150	TP100GP02	10/12/97	14/06/98	6
		IN14GP02	25	27/02/96	22/11/00	156	784.9	170	TP33GP02	15/11/96	10/11/00	49
		IN11GP02	30.5	21/12/95	18/11/00	163	775.8	200	TP34GP02	15/11/95	10/11/00	61
		IN10GP02	20.5	12/12/95	18/11/00	164	776.4	215				
		IN09GP02	21	21/06/95	18/11/00	180		230	TP35GP02	15/04/95	10/11/00	69
		IN08GP02	20.5	19/06/95	18/11/00	179		245	TP36GP02	15/04/95	10/11/00	72

*X is the abscissa of the instrument in the global coordination system of the shiplock. Sec#17 is at X=15675.0m and Sec#20 at X=15785.0m.

Fig4.39 Survey points and inclinometers on Sec#17
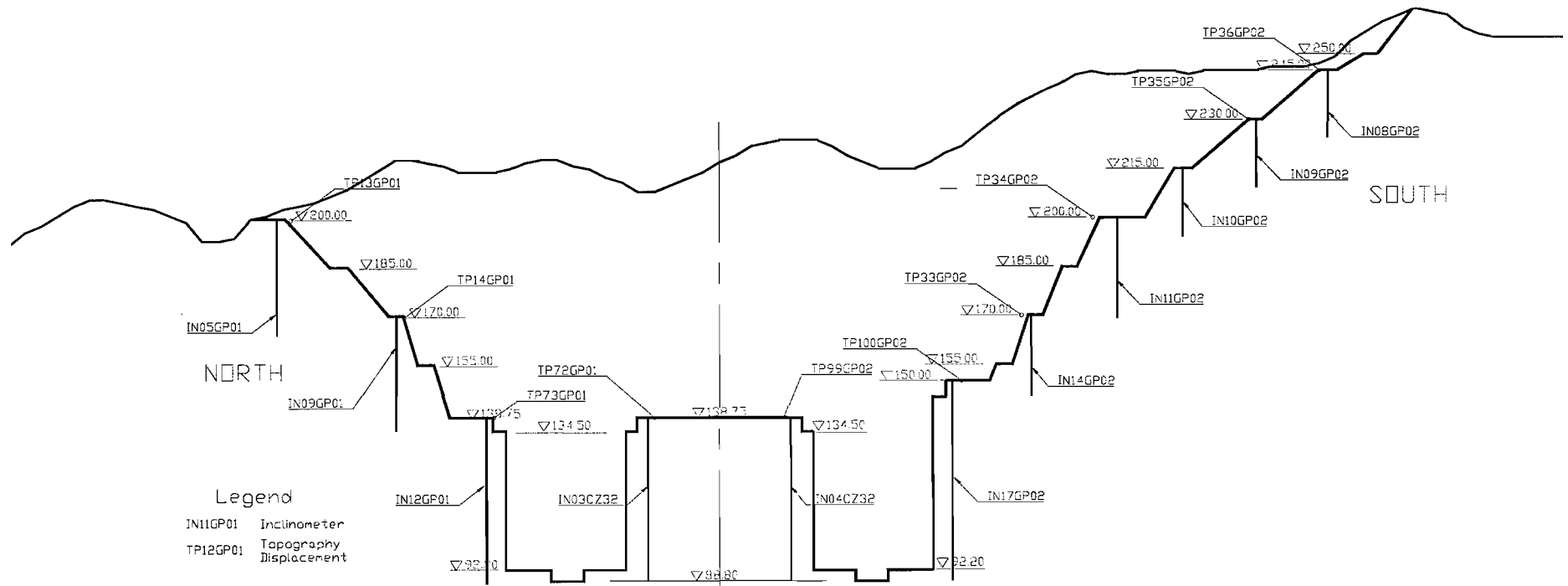
Fig4.40 Survey points and inclinometers on Sec#20
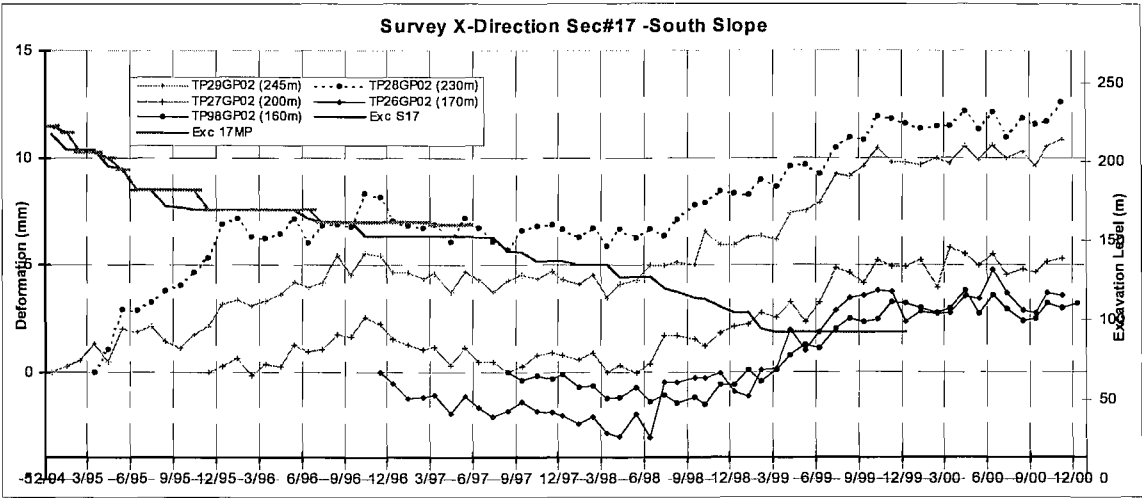
Fig4.41 x deformations of survey points on the south slope of Sec#17
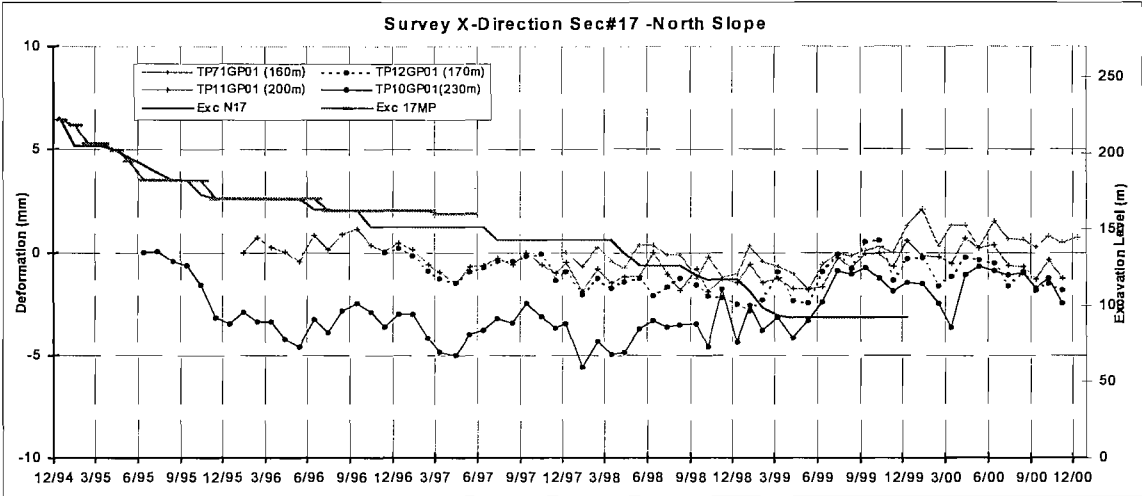
Fig4.42 x deformations of survey points on the north slope of Sec#17
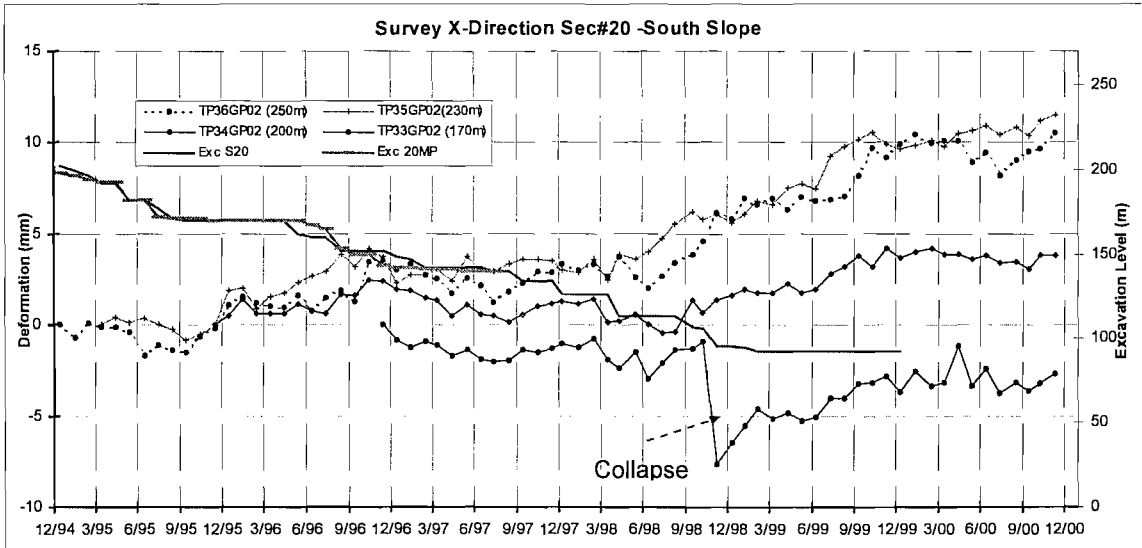
Fig4.43 x deformations of survey points on the south slope of Sec#20

92
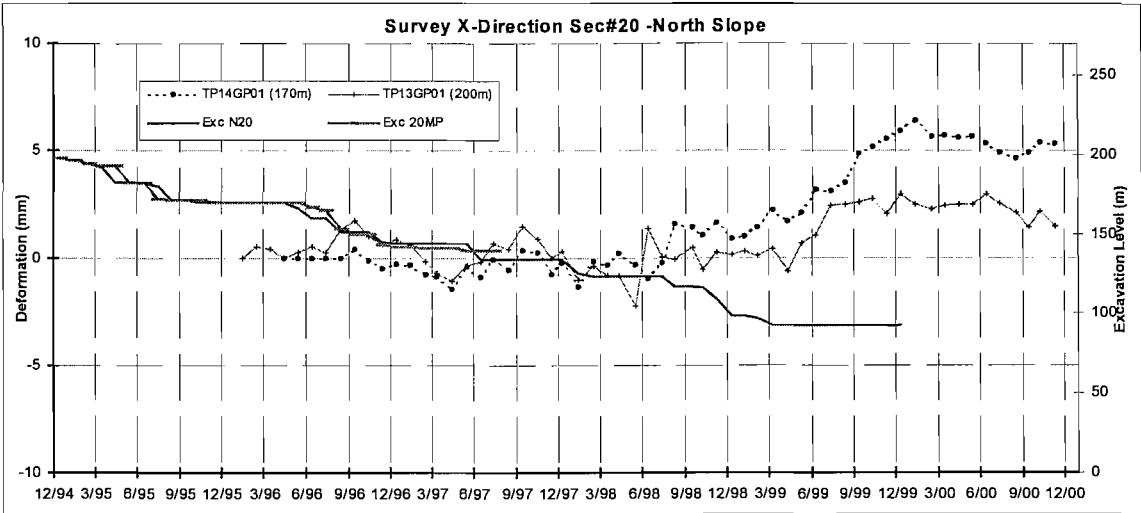
Fig4.44 x deformations of survey points on the north of Sec#20
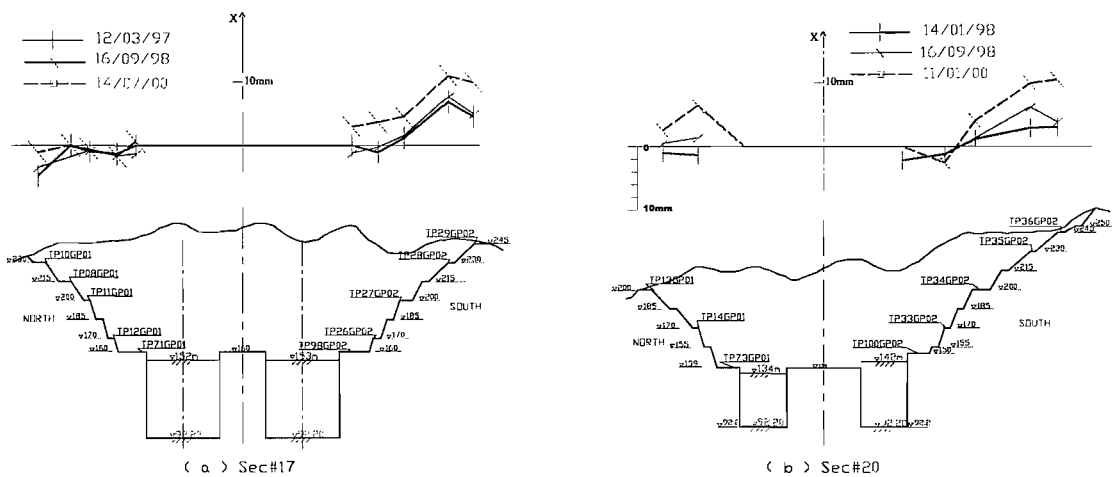
Fig4.45 x deformations of survey points on the north of Sec#20

4.3.2 y deformation

The y deformations of the survey points on slopes are shown in Fig4.46 to 4.49 with excavation levels.

On the y direction, all the survey points moved generally into the excavation gradually during excavation and stopped soon after the excavation finished around 04/99. Deformation rate was at the maximum when the excavation reached the level of each survey point (Fig4.46 to 4.49).

When the y deformations are compared with each other in terms of increments in the same period (Fig4.50 to 4.53), the survey points closer to the toes of the slope have larger

displacement than those further up on the slope. This indicates that in late stages of excavation, the slope generally responded in a sliding pattern rather than a translating or toppling pattern.

By comparing the top two points in Fig4.46 to 4.49, it can be found that the top survey point actually show lower deformation than the one below it on the slope. This could be due to either the flatter slope angle on the top or the effects of geological structures below, which puts this part of the slope into sliding pattern, or a combination of both

But in general, the points above 200m have larger total deformations than those below 200m as shown in Fig4.46 to 4.49 probably because of difference in material properties.
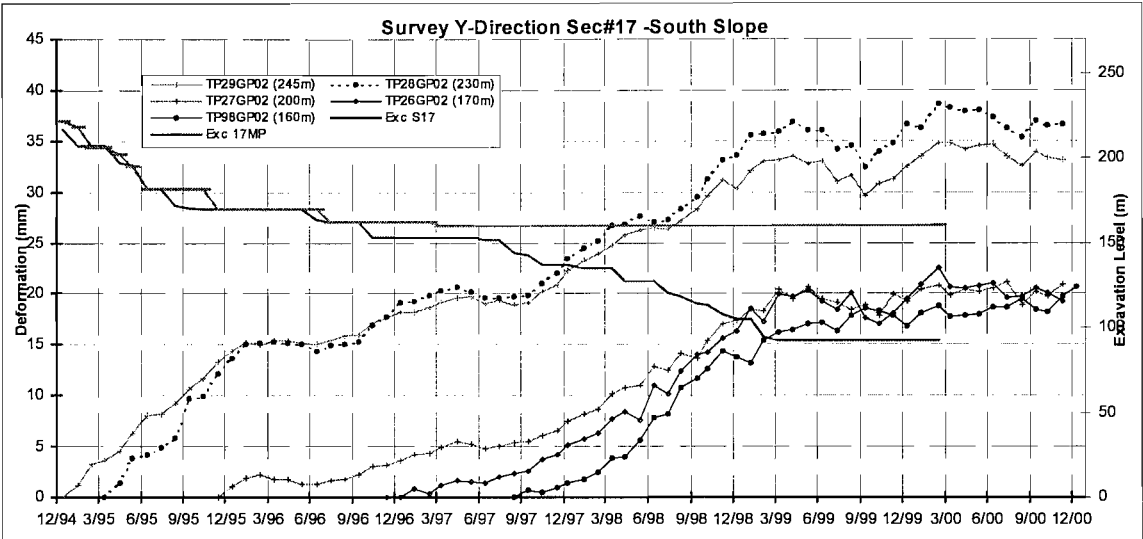
Fig4.46 y deformations of survey points on the south slope of Sec#17
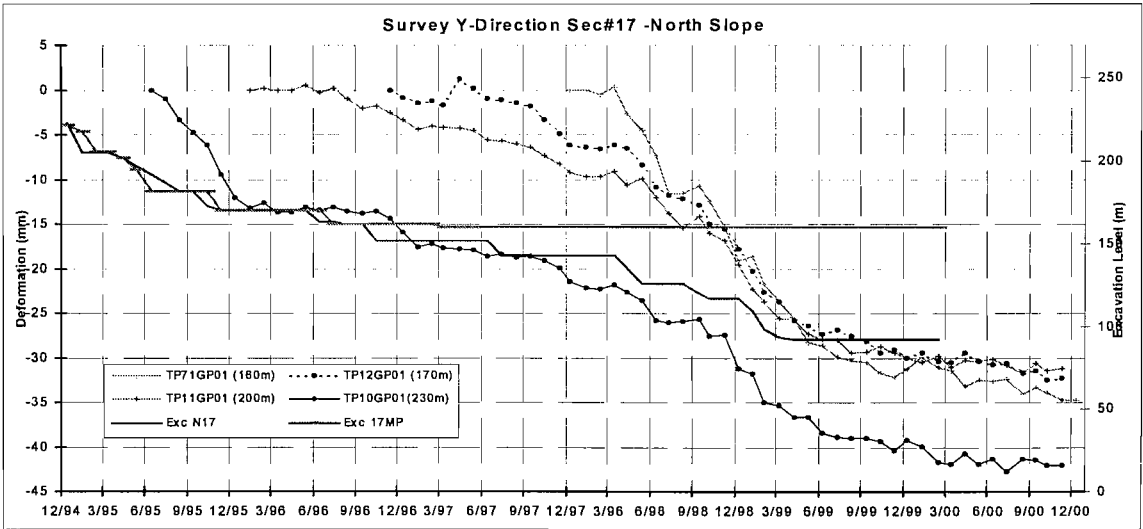
Fig4.47 y deformations of survey points on the north slope of Sec#17

94
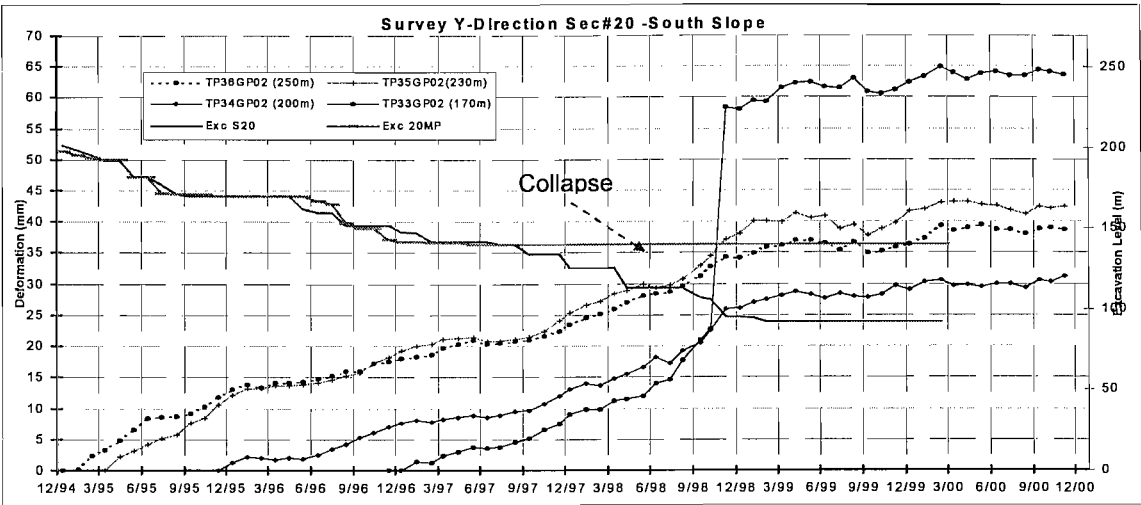
Fig4.48 y deformations of survey points on the south slope of Sec#20
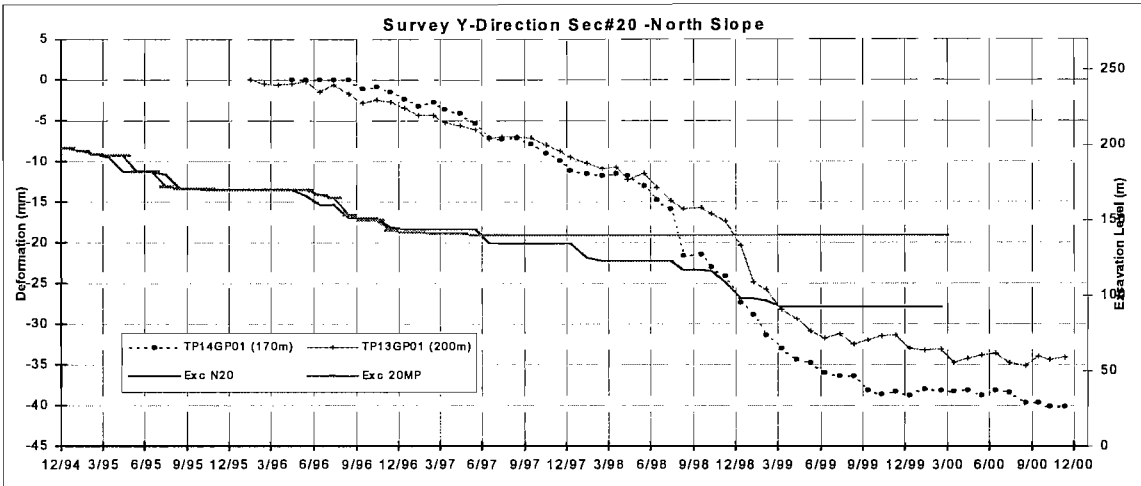
Fig4.49 y deformations of survey points on the north slope of Sec#20
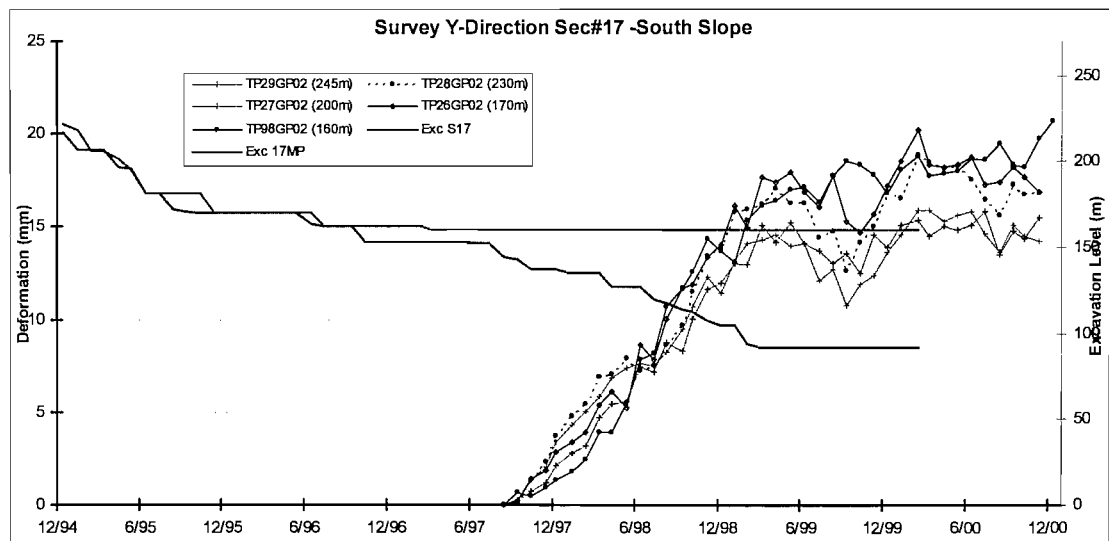
Fig4.50 Aligned y deformations of survey points on the south slope of Sec#17
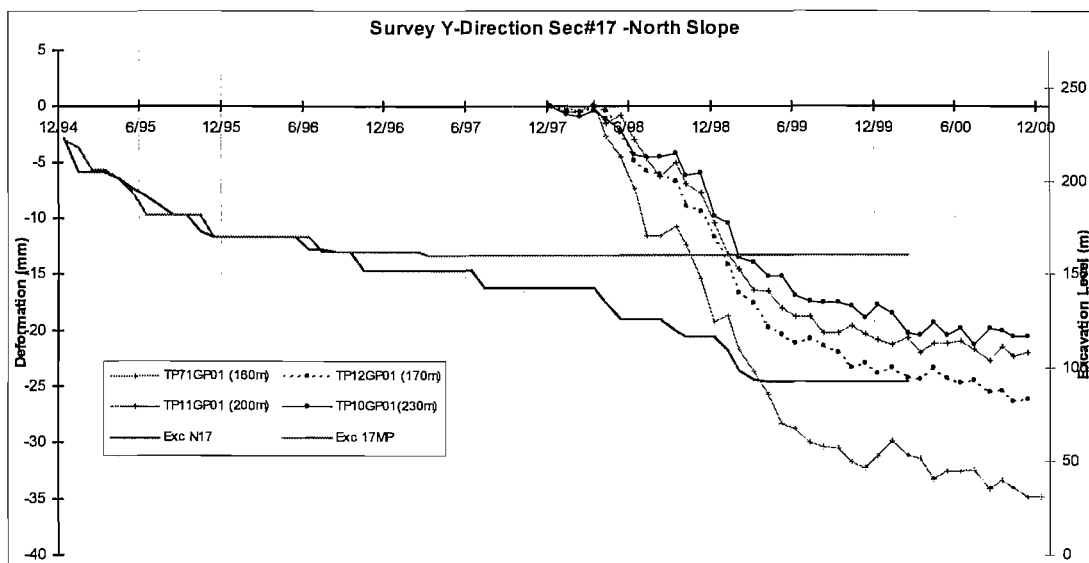
Fig4.51 Aligned y deformations of survey points on the north slope of Sec#17
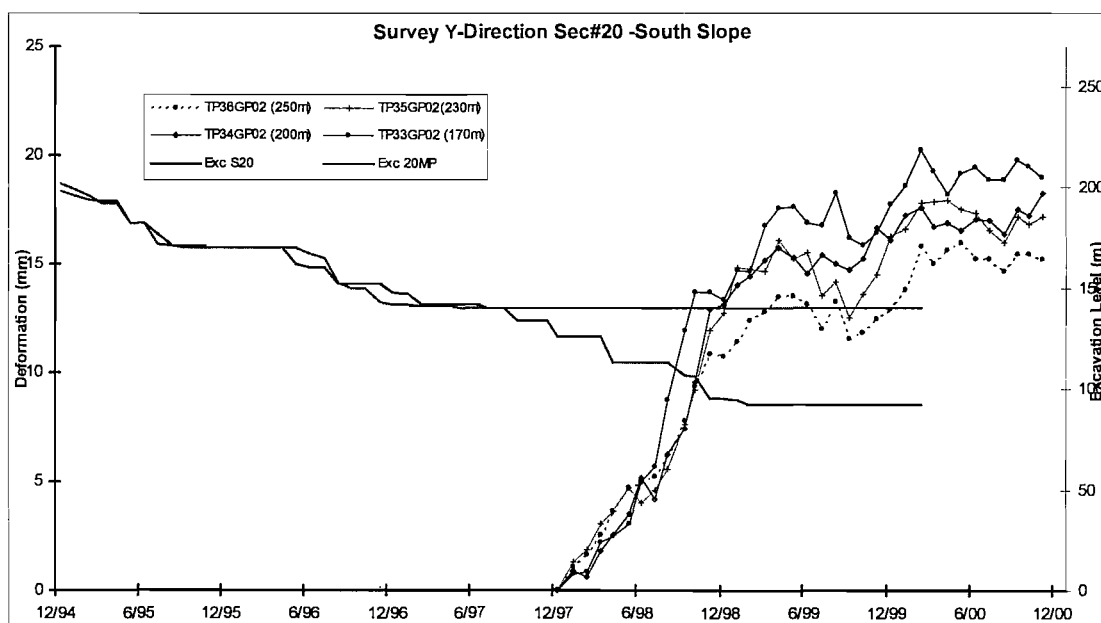
Fig4.52 Aligned y deformations of survey points on the south slope of Sec#20

96
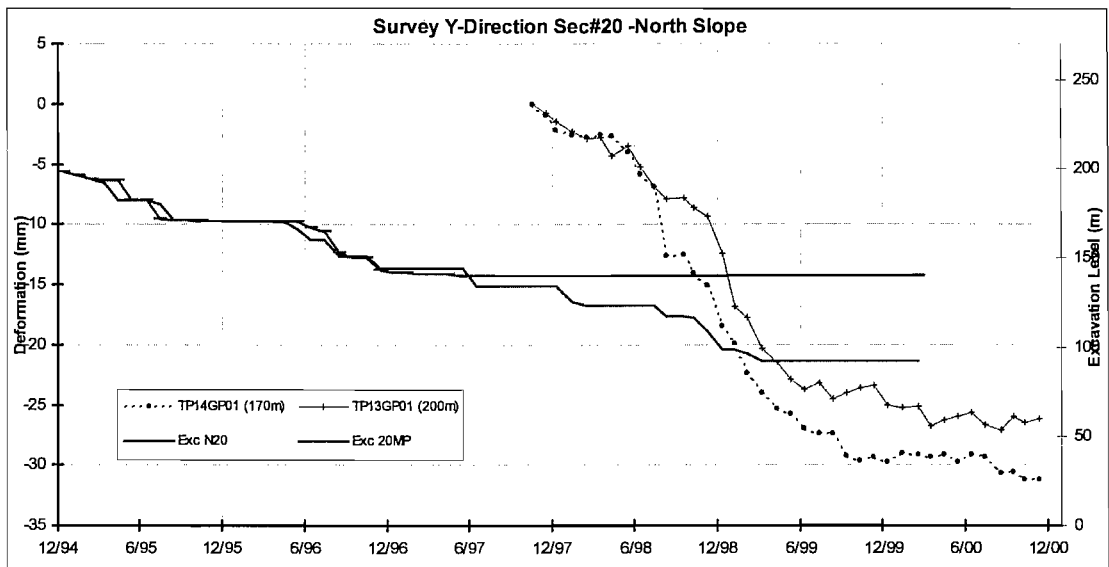
Fig4.53 Aligned y deformations of survey points on the north slope of Sec#20

4.3.3 z deformation

The z deformations of the survey points on slopes are shown in Fig4.54 to 4.57 with excavation levels.

The magnitudes of the z deformation are within 5mm for most survey point. A general trend is found that the survey points settled slightly when excavation took place close to its level.
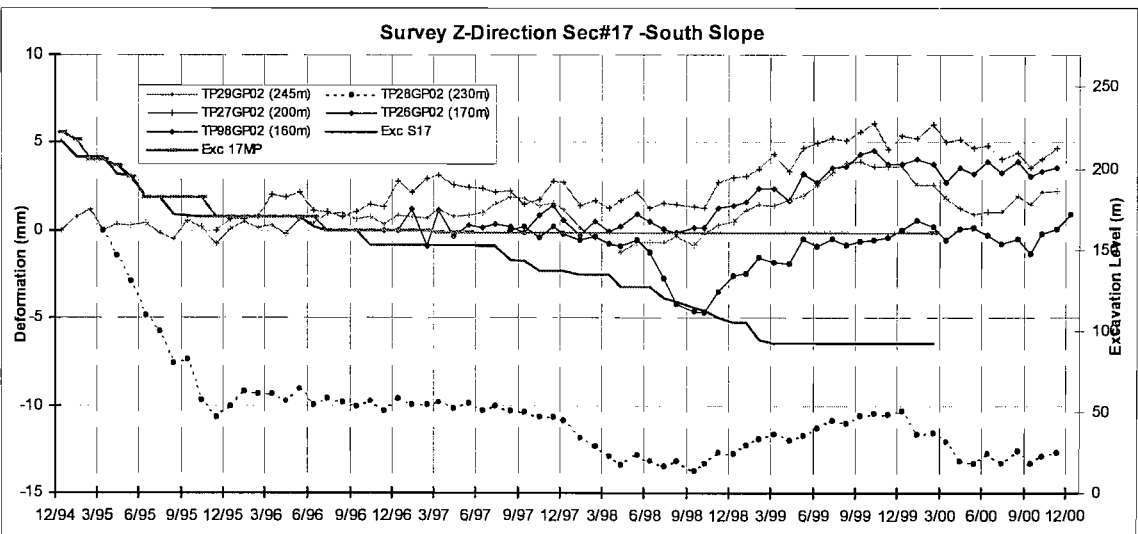
Fig4.54 z deformations of survey points on the south slope of Sec#17
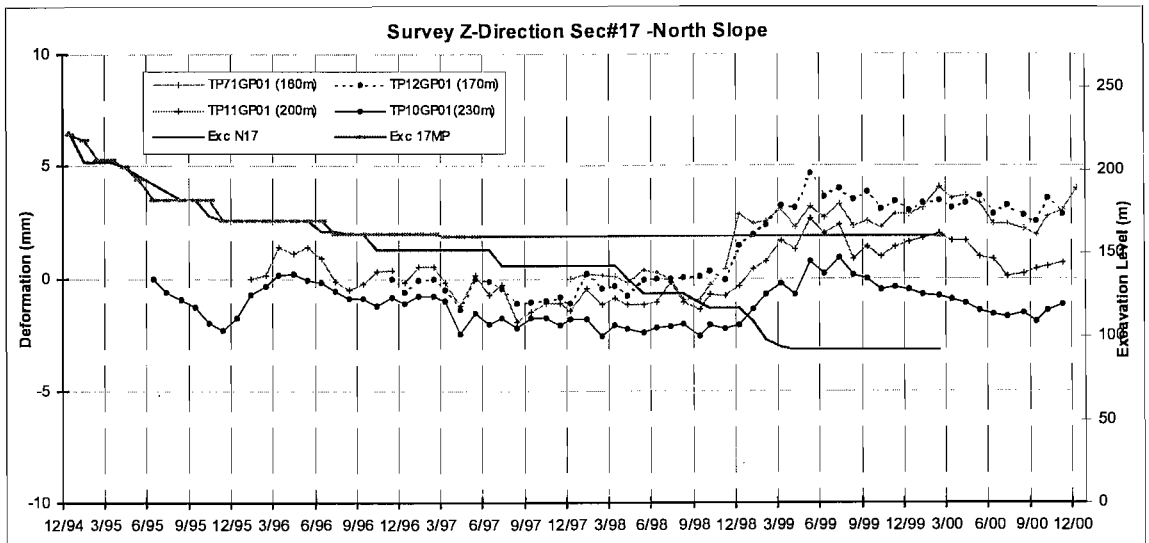
Fig4.55 z deformations of survey points on the north slope of Sec#17
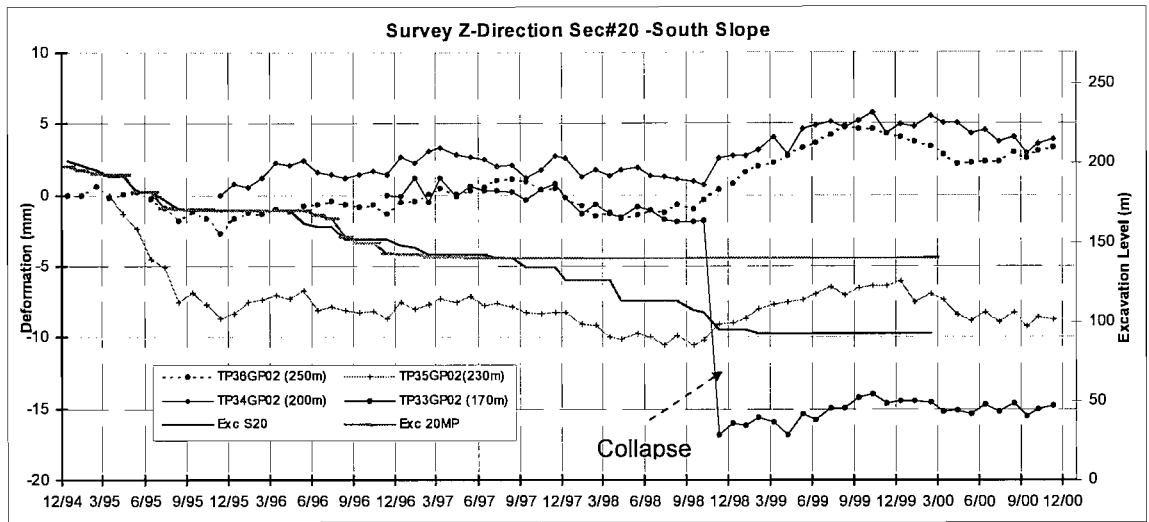
Fig4.56 z deformations of survey points on the south slope of Sec#20
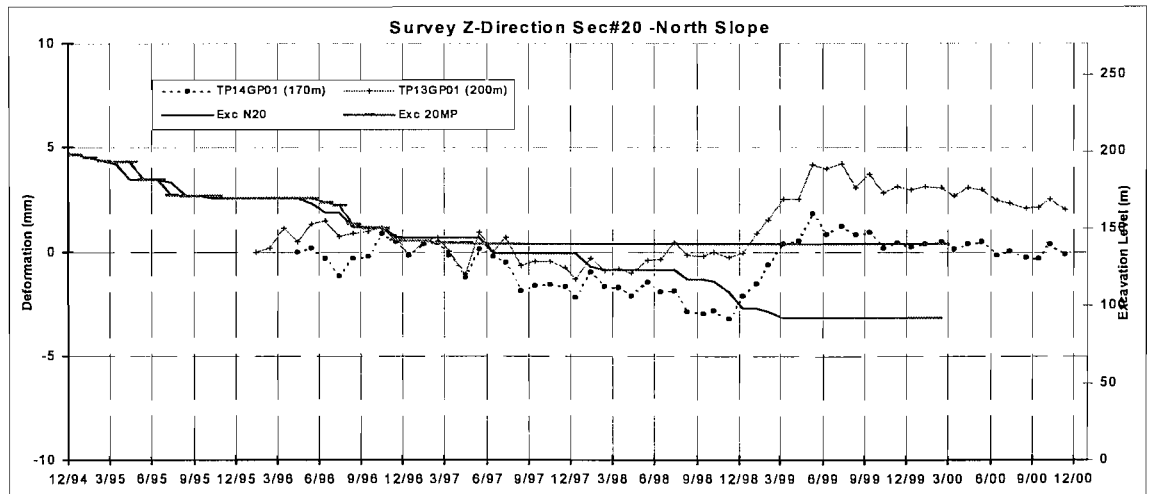
Fig4.57 z deformations of survey points on the north slope of Sec#20

98

4.4 Subsurface Deformation of Slopes

The inclinometers installed on the slopes at Sec#17 and Sec#20 are listed in Table4.8 and Fig4.39 and 4.40. The geological conditions at both sections are shown in Fig4.58 to 4.61 for the south and the north slope respectively.

Inclinometers installed on slopes are referred to in a form like "IN04GP01 (Sec#17 N-215m, L45.5m)", where "17N" means the north slope of Sec#17, "215m" is the elevation of the top of the inclinometer and "45.5m" is its length.
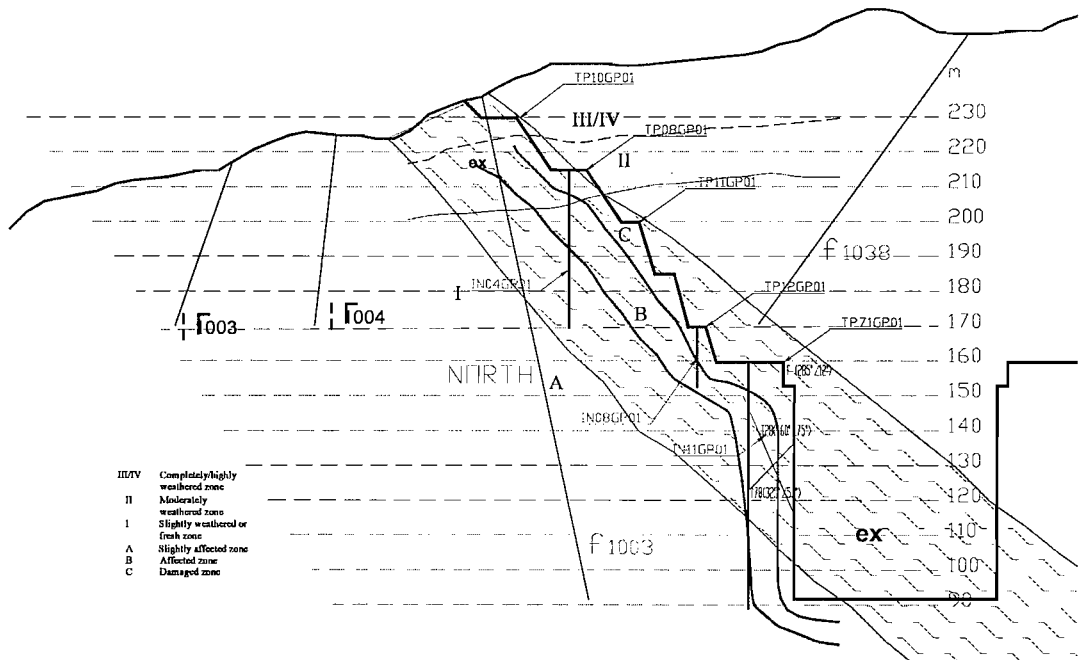
Fig4.58 Geological conditions and instrumentation on the north slope of Sec#17

Fig4.59 Geological conditions and instrumentation on the south slope of Sec#17

Fig4.60 Geological conditions and instrumentation on the north slope of Sec#20
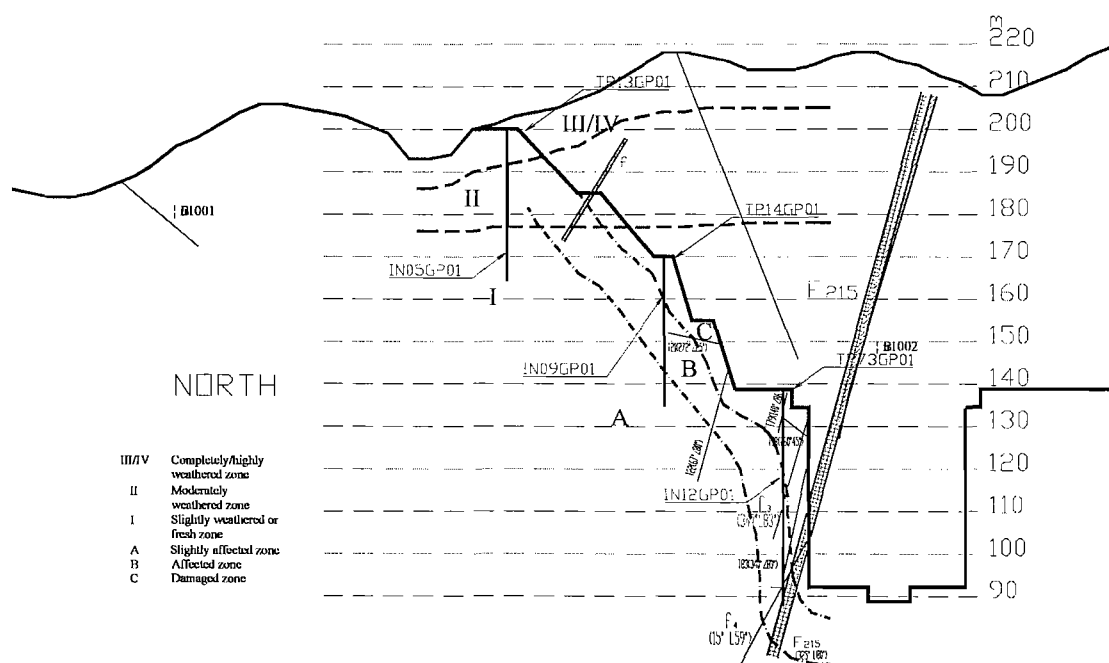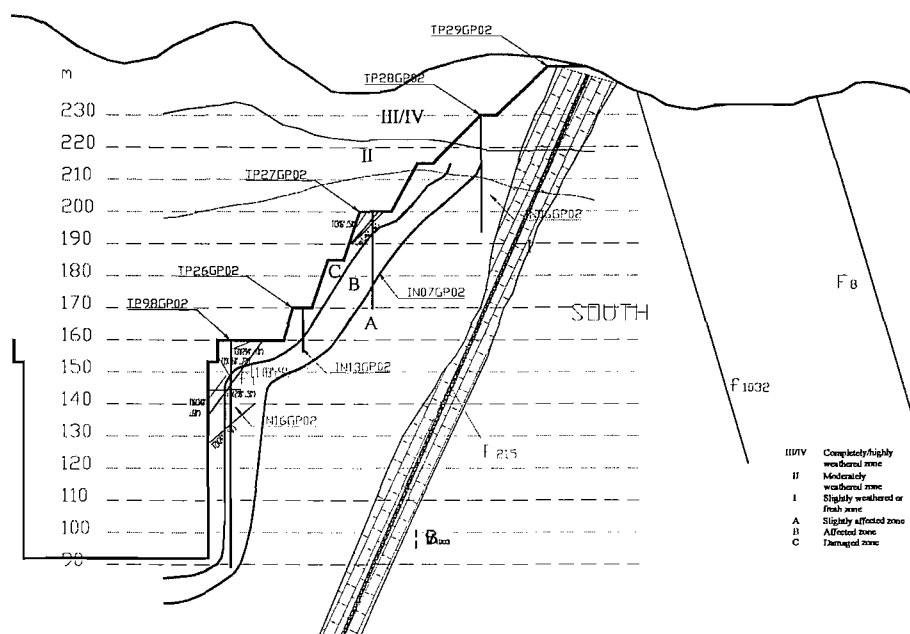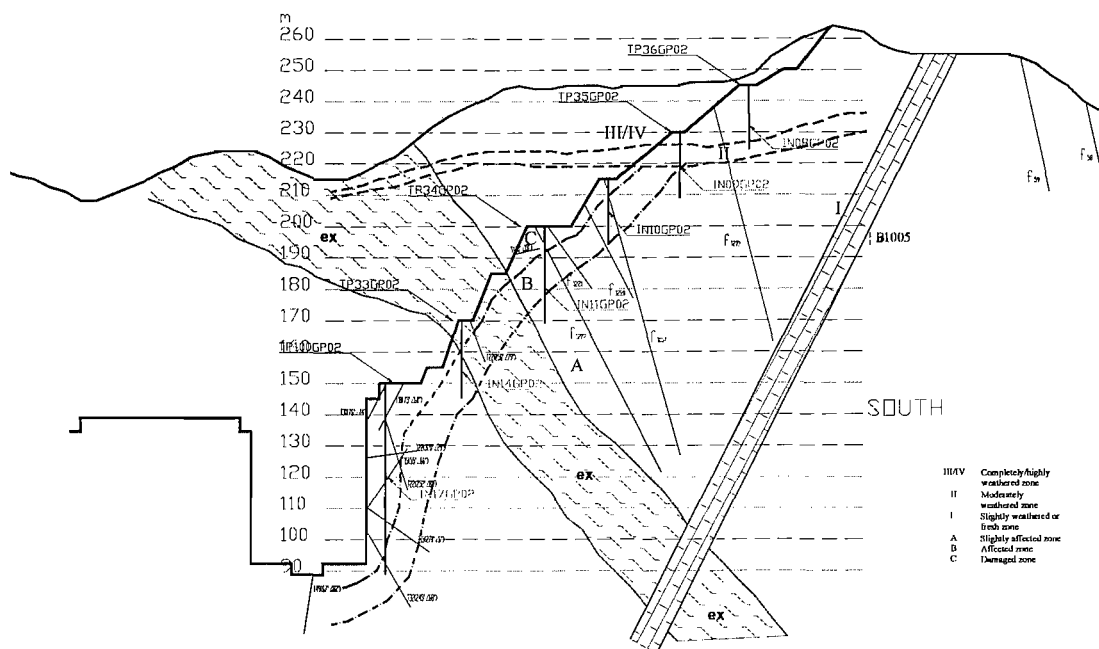
Fig4.61 Geological conditions and instrumentation on the south slope of Sec#20

4.4.1 Inclinometer data and survey data

For inclinometers installed on the slopes, it cannot be guaranteed that their toe will not move during excavation. Therefore corresponding survey data for the top of the inclinometer are used to estimate the actual subsurface deformation along its length. The available couplings of inclinometers and survey points are listed in Table4.9 and the measurements of the y deformation are compared from Fig4.62 to Fig4.73. Because the z deformations measured by inclinometers are at low magnitude and with considerable noise, it is not analyzed here.

Table4.9 List of instruments whose measurements are compared

		South Slope				North Slope	
Sec#17	Ele (m)	230	200	170	159	159	170
	Survey	TP28GP02	TP27GP02	TP26GP02	TP98GP02	TP71GP01	TP12GP01
	Inclinometer	IN06GP02	IN07GP02	IN13GP02	IN16GP02	IN11GP01	IN08GP01
Sec#20		South Slope				North Slope	
	Ele (m)	250	230	200	170	170	200
	Survey	TP36GP02	TP35GP02	TP34GP02	TP33GP02	TP14GP01	TP13GP01
	Inclinometer	IN08GP02	IN09GP02	IN11GP02	IN14GP02	IN09GP01	IN05GP01

As expected, survey data for the top points of inclinometers showed that with only two exceptions, larger deformation took place than those indicated by the measurements of the corresponding inclinometers.

The data of inclinometers at lowest elevation on Sec#17 are in good agreement with survey data shown in Fig4.65 and Fig4.66. The difference is assumed to correspond to the accuracy of the survey measurement, which is ±5mm. This proves that the bottoms of these two inclinometers are fixed (about 2m below the bottom of excavation). Although no comparison is available for the lowest inclinometers at Sec#20, it is reasonable to assume the bottom-fixity of these inclinometers on Sec#20.

The local deformation pattern along the length of each inclinometer is estimated by translating the inclinometer profile to match its top displacement to survey data (Table4.10). It can be seen that most of the ramps deformed in a toppling pattern and the sliding pattern is found at high ramps above 200m. The inferred deformation patterns are summarized in Table4.10.

Table4.10 Local deformation pattern from inclinometer data and survey data

	Characteristics	Examples
Toppling Fig4.1 (a)	Top relative deformation of inclinometer is in the same direction as the survey point	Fig4.62 and Fig4.65, Fig4.66, Fig4.69, Fig4.72 and 4.73
Sliding Fig4.1 (b)	Top relative deformation of inclinometer is in the opposite direction to survey data	Fig4.63 and Fig4.70
Translating Fig4.1 (c)	Top relative deformation of inclinometer changes very little	Fig4.64 and Fig4.67, Fig4.68 and Fig4.71
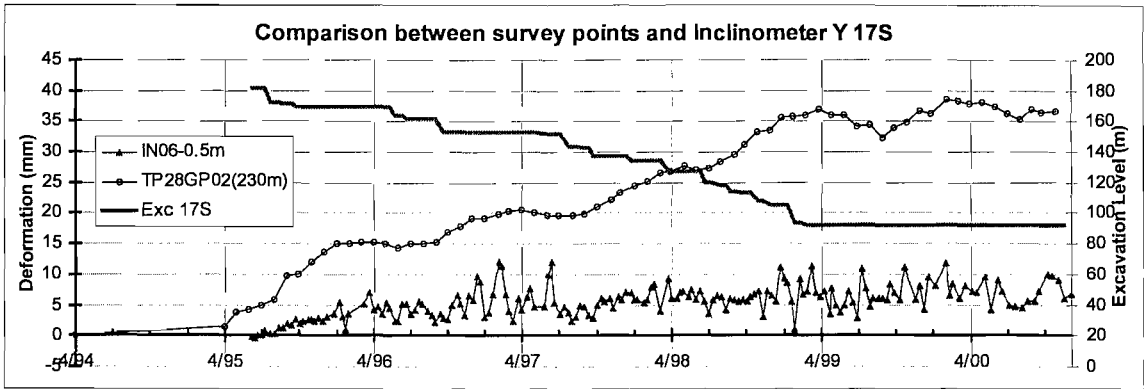
Fig4.62 y deformation comparison between inclinometer and survey (Sec#17 S-230)
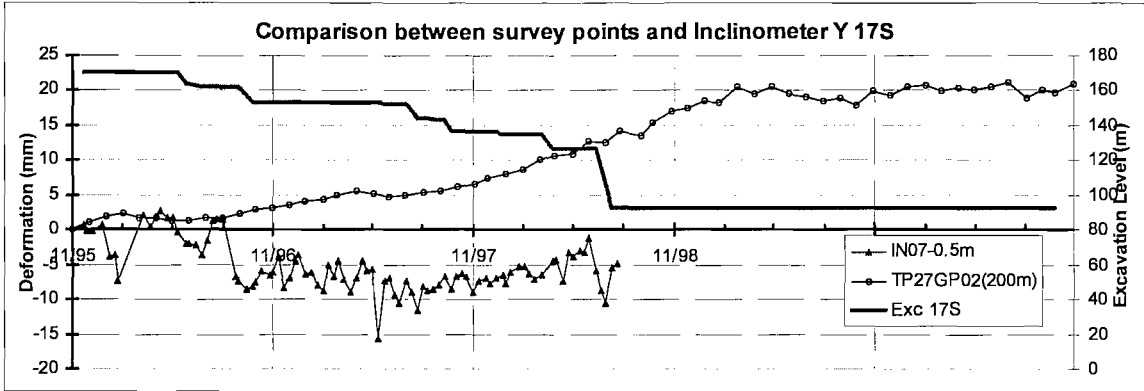
Fig4.63 y deformation comparison between inclinometer and survey (Sec#17 S-200)
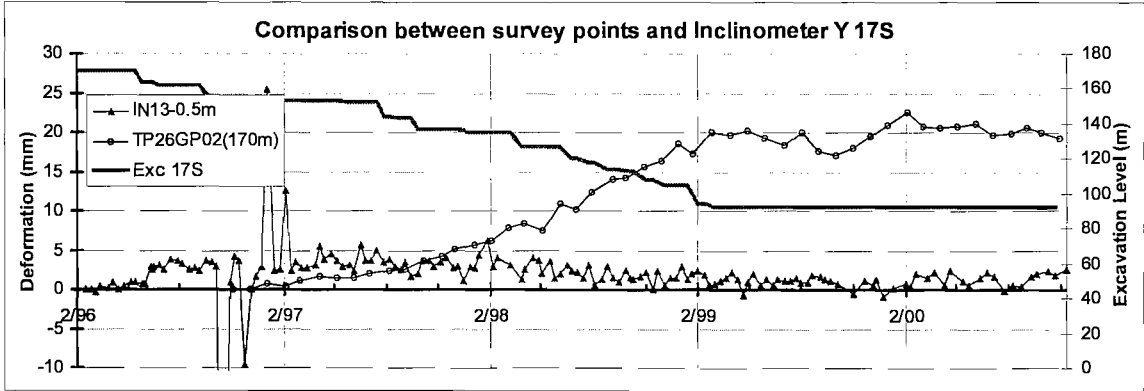
Fig4.64 y deformation comparison between inclinometer and survey (Sec#17 S-170)
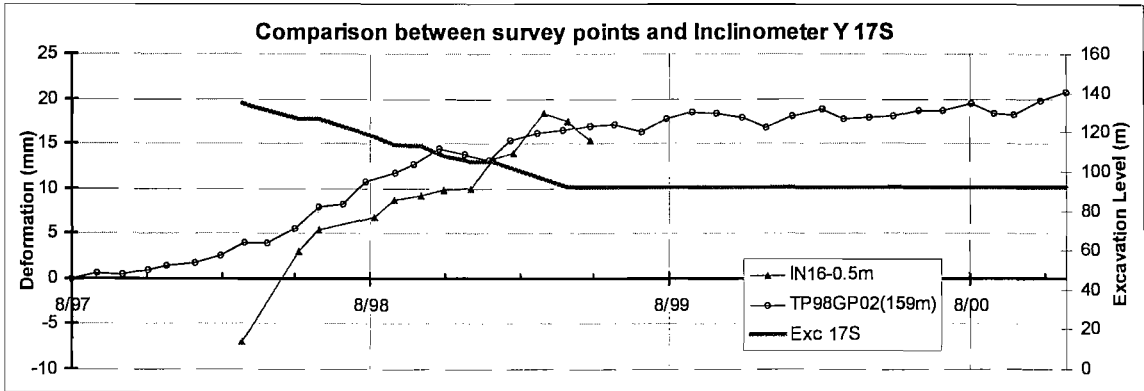
Fig4.65 y deformation comparison between inclinometer and survey (Sec#17 S-159)
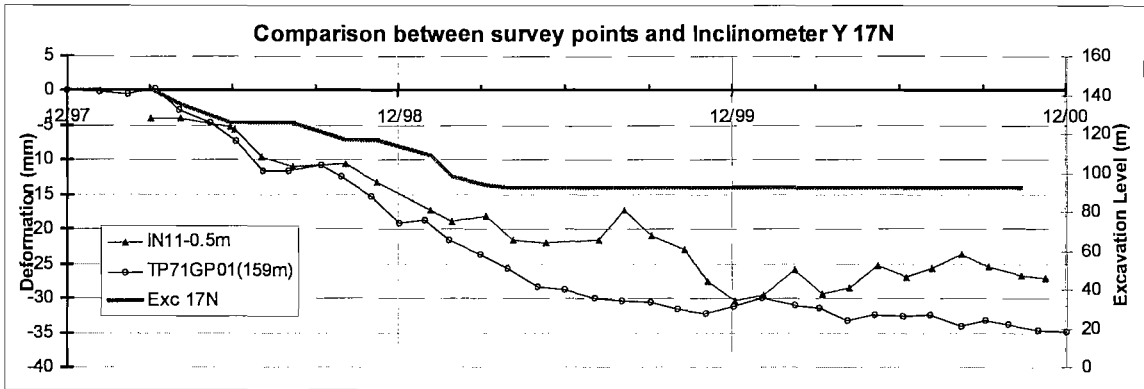
Fig4.66 y deformation comparison between inclinometer and survey (Sec#17 N-159)
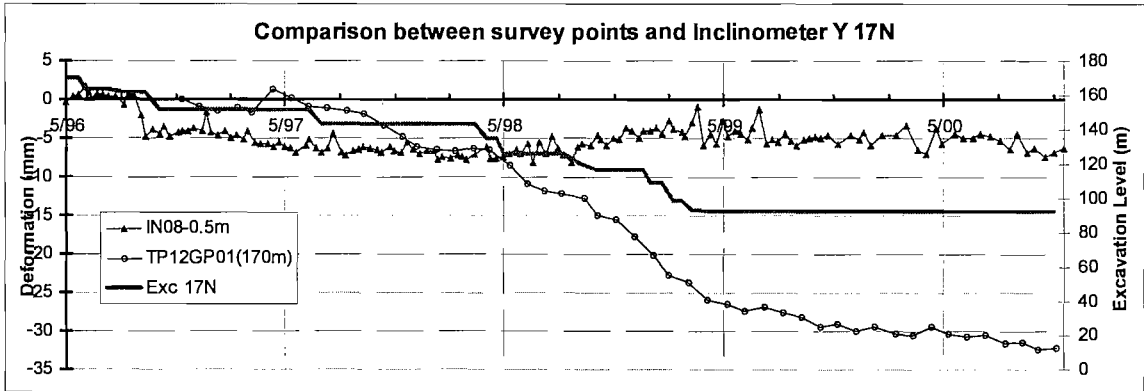
Fig4.67 y deformation comparison between inclinometer and survey (Sec#17 N-170)
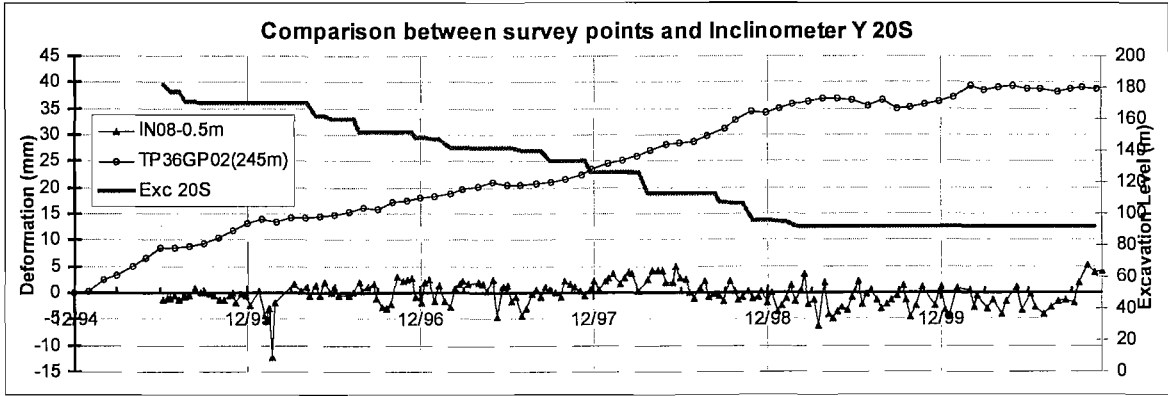
Fig4.68 y deformation comparison between inclinometer and survey (Sec#20 S-245)
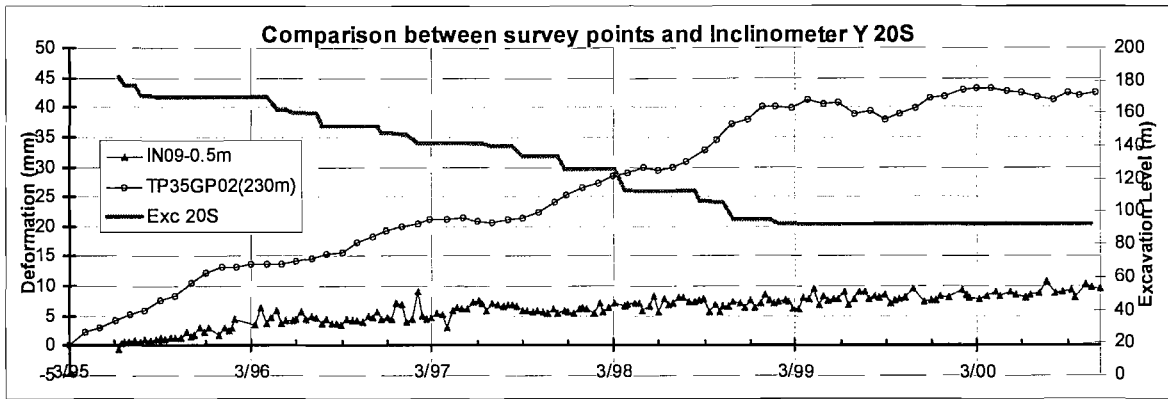
Fig4.69 y deformation comparison between inclinometer and survey (Sec#20 S-230)
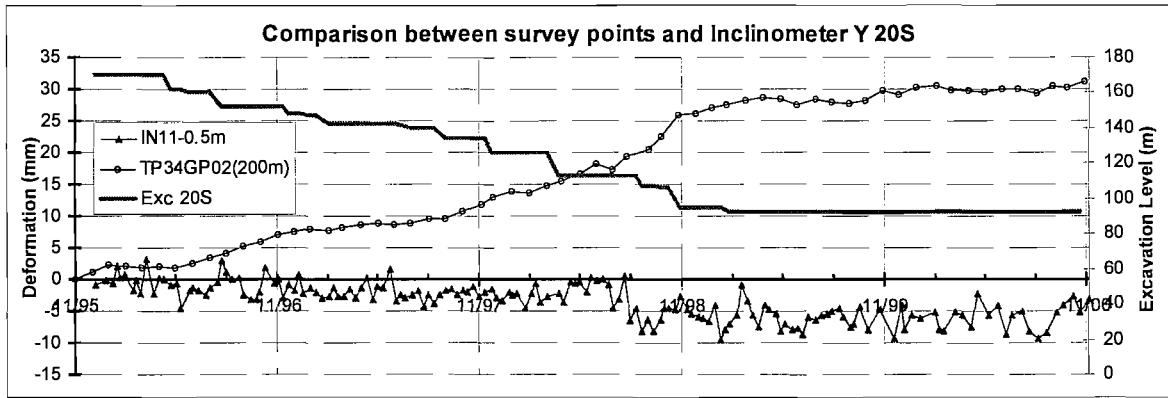
Fig4.70 y deformation comparison between inclinometer and survey (Sec#20 S-200)

105
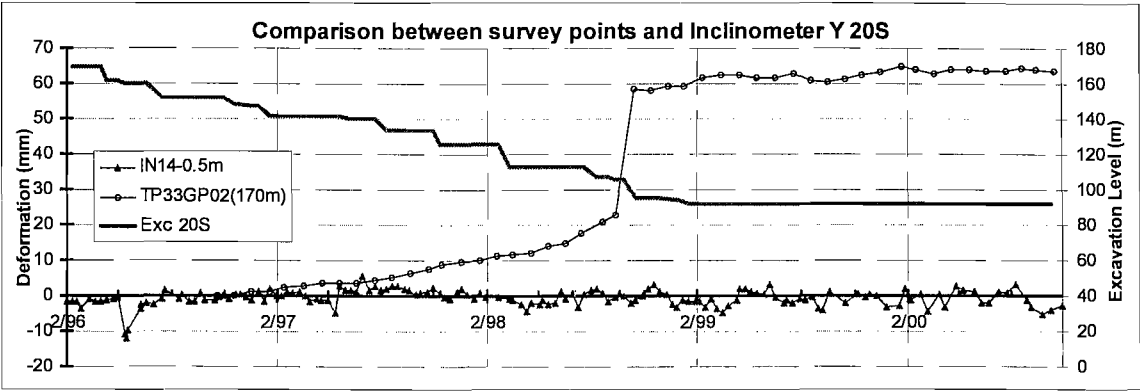
Fig4.71 y deformation comparison between inclinometer and survey (Sec#20 S-170)
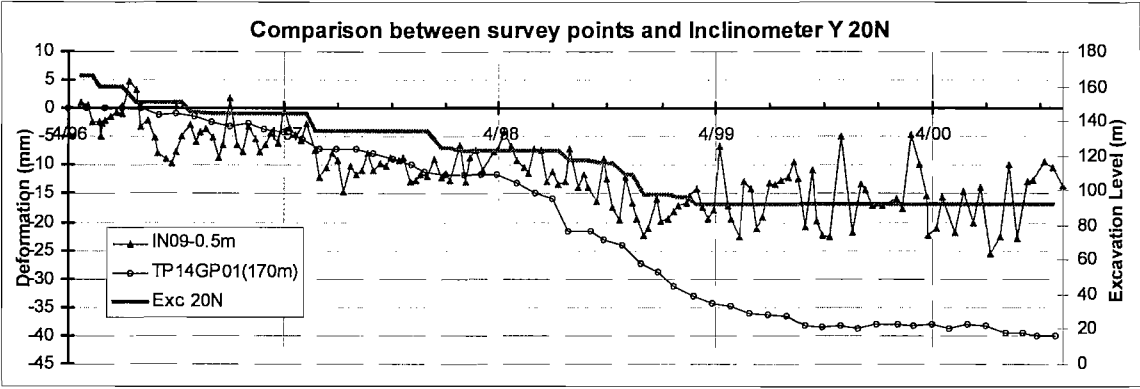
Fig4.72 y deformation comparison between inclinometer and survey (Sec#20 N-170)
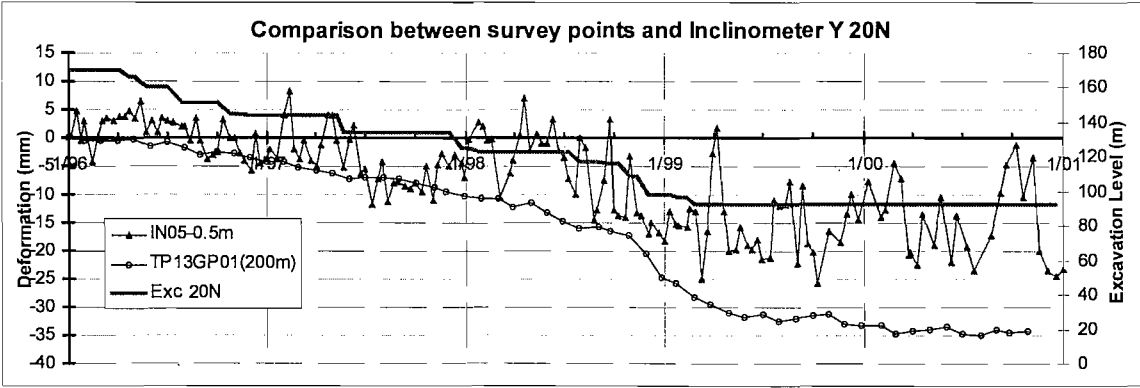
Fig4.73 y deformation comparison between inclinometer and survey (Sec#20 N-200)

4.4.2 Slips on inclinometer profiles

As for the Middle Pier, the same classification and threshold (? mm/0.5m) described in section 4.1.4 are used to identify slips on profiles of inclinometers on the slopes.

For inclinometers not lying on the section of interest, it is necessary to correct the depths of intersection with discontinuities and other geological features by the method presented in section 4.1.4. The actual depths at which each inclinometer intersects geological features are listed in Table4.11.

Compared to the chamber walls on the Middle Pier, inclinometers on the north and south slopes are subject to more influencing factors such as slope profiles and weathered zones.

The slopes of the shiplock consist of a series of ramps of different inclinations connected by benches with a width of either 5m or 15m. These benches provide much more confinement to the rock below than above, which is similar to the restriction effect of excavation levels on profiles as shown in Fig4.74. It is possible that the existence of these benches causes changes or even jumps on inclinometer profiles at these levels, e.g. slips shown in Fig4.2.

The inclinometers close to the original ground surface (Fig4.58 to 4.61) may be affected by the existence of weathered zones, as they have different material properties. Because the weather zones extend horizontally along the shiplock axis to such a distance that the interfaces between weathering zones are at the same level within the distance between the inclinometer and section of interest. Therefore, the intersection depths of inclinometer with weathered zones can be measured directly from the geological section maps and are listed in Table4.11.

The EDZ subzones due to excavation may cause turning points or slips in inclinometer profiles for the same reasons for the weathered zones of different material properties.
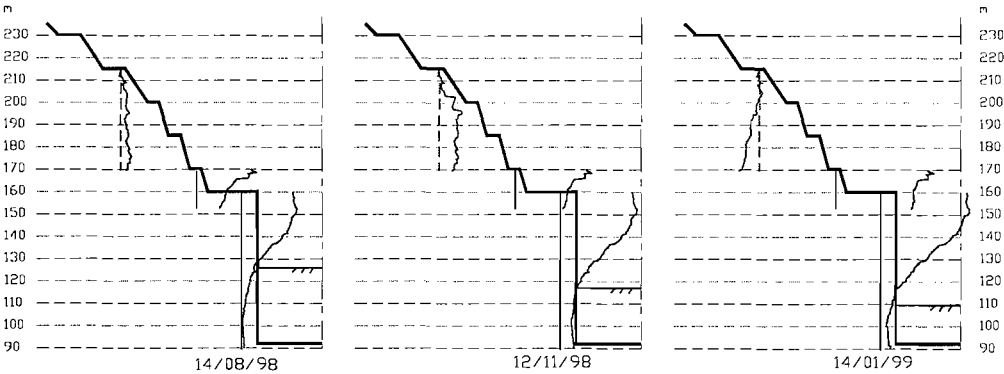
Fig4.74 Profiles of inclinometers on the north slope of Sec#17, on various dates

Table4.11 Depth of intersection of inclinometers with discontinuities and zone boundaries

Sec#17					Sec#20			
Inclinometer	Intersecting discontinuity or weak zone	dx (m)	Depth (m)		Inclinometer	Discontinuity or weak zone	dx (m)	Depth (m)
	North Slope					North Slope		
IN04GP01	BC	5.1	6.8		IN05GP01	III/II	-9.0	8
	II/I	5.1	9.9			II/I	-9.0	22.6
	AB	5.1	22.5					
					IN09GP01	T21 (272 ∠25?	-7.6	20.8
IN08GP01	BC	0.9	9.7			AB	-7.6	10
	T52(250 ∠70?	0.9	1.1			BC	-7.6	27
IN11GP01	T28 (260 ∠75?	-6.7	34.4		IN12GP01	T79 (140 ∠86?	-2.6	-27.1
	T78 (325 ∠53?	-6.7	44.4			T98 (260 ∠45?	-2.6	8.8
	ex-lower		44			f3 (340 ∠83?	-2.6	40.9
	North Slope					T83 (340 ∠80?	-2.6	54.2
IN16GP02	T31 (294 ∠78?	-2.4	14.0			f4 (15 ∠59?	-2.6	46.5
	T16 (340 ∠60?	-2.4	12.7			F215 (325 ∠80?	-2.6	61.2
	T19 (260 ∠72?	-2.4	17.6			AB	-2.6	18
	F1 (13 ∠56?	-2.4	14.5			North Slope		
	T15 (298 ∠50?	-2.4	18.2		IN17GP02	T30 (76 ∠74?	-2.4	-5.9
	T21 (265 ∠60?	-2.4	30.0			T18 (75 ∠68?	-2.4	6.2
						T22 (252 ∠81?	-2.4	22.8
IN13GP02	AB	-0.4	9			T22 (320 ∠29?	-2.4	24.2
						T15 (55 ∠66?	-2.4	28.5
IN07GP02	f1213 (340 ∠50?	5.3	-1.2			T15 (270 ∠6?	-2.4	44.0

		dx	Depth				dx	Depth
	AB	5.3	7.1			T32 (245 ∠68?	-2.4	62.9
	BC	5.3	23			AB	-2.4	53.5
IN06GP02	III/II		10.4		IN14GP02	ex-low	-0.1	10.8
	AB		15			AB	-0.1	9.3
	II/I		19.4					
					IN11GP02	f1221(260 ∠70?	-9.2	20.2
						f1222(247 ∠71?	-9.2	24.9
						AB	-9.2	8.3
						BC	-9.2	22.1
					IN10GP02	f1007 (260 ∠80?	-9.6	51.3
						f1007 (260 ∠80?		58.9
						f1220 (250 ∠70?	-9.6	33.5
						BC	-9.6	5.6
						AB	-9.6	20.5
					IN09GP02	III/II		4
						II/I		11
						AB		11.9
					IN08GP02	f1219 (260 ∠82?		35.4

Notes:

*AB/BC: boundary between zone B (affected zone) and zone A (slightly affected zone)/ C (damaged zone) ;

*III/II or II/I: boundary between zones III (completely/highly weathered), II (moderately weathered) or I (slightly weathered or fresh zone);

*ex-low: lower boundary of xenolith "ex".

* Depth: positive: downwards from top of inclinometer; negative: no intersection with inclinometer;

*dx: difference between the x coordinate of the inclinometer and the x coordinate of Sec#17 or Sec#20.

4.4.3 Subsurface deformation of the north slope at Sec#17

The geological conditions on the north slope of Sec#17 are shown in Fig4.58. The anchorage installed on the north slopes around Sec#17 is shown in Fig3.16 and the prestressed cables are listed in Table3.8. The slope surface is almost fully embedded in the xenolith "ex" (Fig4.58).

On the north slope of Sec#17 (Fig4.40), only the measurements of IN08GP01 (170m) are adjusted using survey point data. Inclinometer IN11GP01 (160m) is considered bottom-fixed because Fig4.66 shows IN11GP01 (160m) is in agreement with the respective survey point and its bottom extends around 3m below the bottom of the excavation. At elevation about 215m, there is no suitable survey point to compare IN04GP01 (215m) measurements to (Table4.8).

4.4.3.1 General deformation

Inclinometer data (Fig4.75) agree with survey data that the slope moved to the south gradually as excavation progressed.
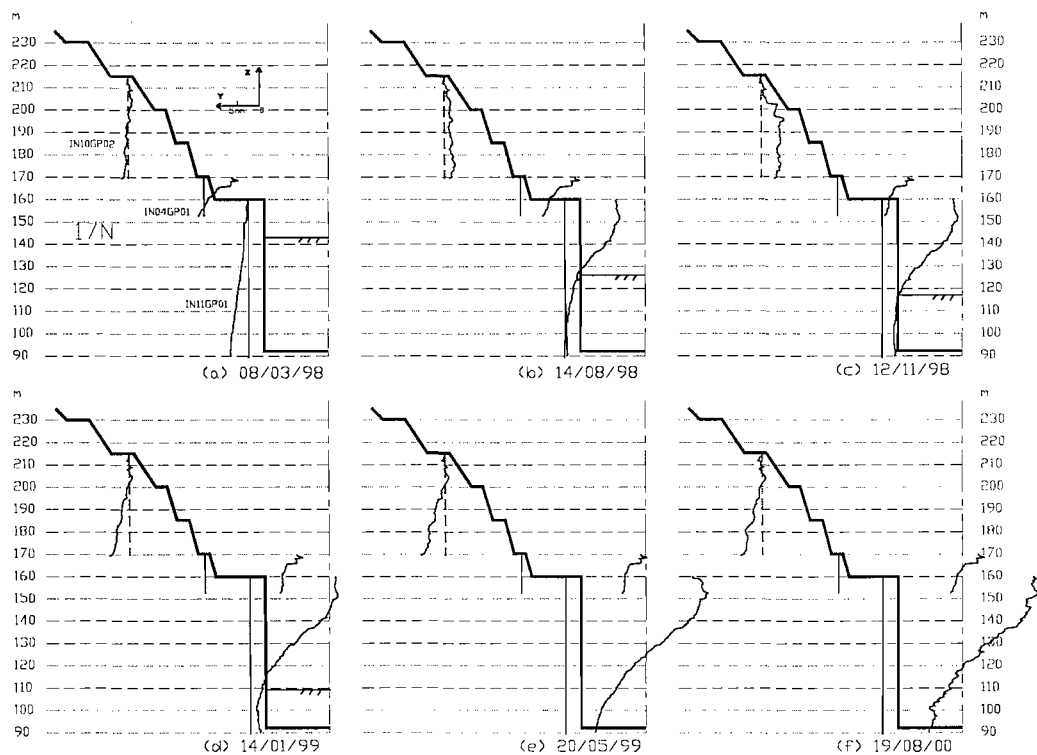
Fig4.75 Profiles of inclinometers on the north slope of Sec#17

All three inclinometers on the north slope of Sec#17 showed a toppling deformation pattern (Fig4.75). Within the length of each inclinometer, the top of inclinometers moved more into the excavation than the bottom because of more restrictions at the bottom.

110

The deformation profiles of the inclinometers related closely to the excavation levels (Fig4.75 (b-e)). This is particularly apparent on the inclinometer profiles of IN11GP01 (170m, Fig4.75).

The maximum displacement of 37mm occurred at elevation of 170m. The top of the vertical wall (160m elevation) moved south to the excavated chamber around 27mm.

4.4.3.2 Slips on the inclinometers

(1) IN04GP01 (Sec#17 N-215m, L45.5m)

This inclinometer is located in the xenolith "ex" and does not intersect any known discontinuities. However, there are two similar slips at depth of 36m-36.5m and 42m-42.5m along IN04GP01 as shown in Fig4.76. Both slips show the upper part moved into the excavation (the south). Relative displacement of slips started to increase in 03/98 and accelerated from when excavation was nearly completed (04/99). The large variations of relative displacement between 09/99 and 12/99 and after 06/2000 are difficult to explain on the basis of available information and are perhaps due to measurement errors.

(2) IN08GP01 (Sec#17 N-170m, L17.5m)

This inclinometer is located in the xenolith "ex" and does not intersect any known discontinuities. There are two slips at depth of 1.5m-2m and 4m-4.5m along IN08GP01. The upper layers moved to the south relative to the lower layers as shown in Fig4.77 and Fig4.78. Most of the relative displacement of the slip between 2m-1.5m occurred when excavation reached that depth, with particularly no relative displacement occurring afterwards.

There is a turning point at a depth of 9m on the profile of IN08GP01, which can be attributed to the effect of the slope geometry (Fig4.78). It developed in 09/96 when excavation reached that depth (162m), removing the mass of rock that restricted the deformation of the lower part of IN08GP01.

(3) IN11GP01 (Sec#17 N-160m, L70m)

This inclinometer intersects the lower edge of the xenolith "ex" at a depth of around 44m and fissures T_{28} and T_{78} at depths of 34.4m and 44.4m respectively. A number of slips are observed along IN11GP01 (Fig4.79) with the relative displacement shown in Fig4.80 to 4.82. Some slipping layers are formed by slips (a) and (b), (e) and (f), (h) and (i) in Fig4.79.

The slip around depth of 44m (Fig4.79 (g)) can be related to fissure T_{78} and xenolith "ex" that both intersect the inclinometer at this level but with different dipping directions (Fig4.79 (b)).

Most of the relative displacement along slips varied significantly between 19/10/99 and 16/07/2000 after excavation (Fig4.80 to 4.82). These variations cannot be related to the installation of any prestressed cables. It seems more likely due to measurement errors considering the simultaneous changes at multiple levels.
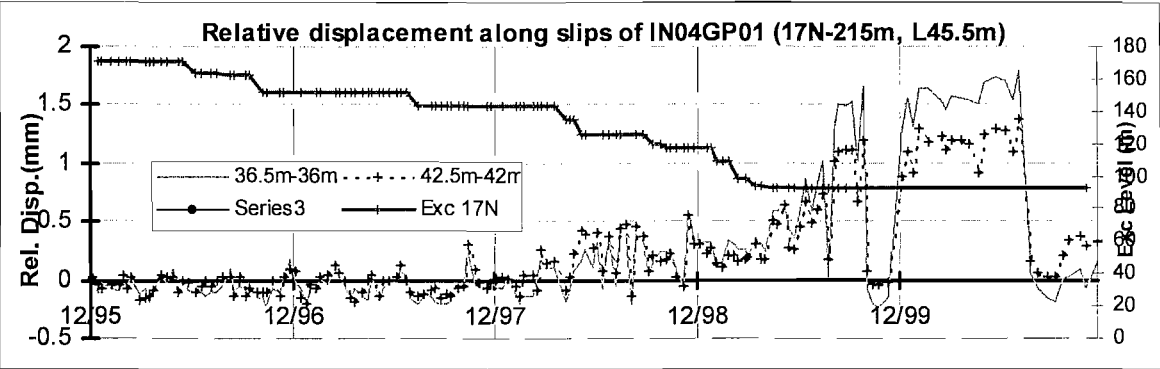
Fig4.76 Relative displacement of slips on IN04GP01 (Sec#17N)
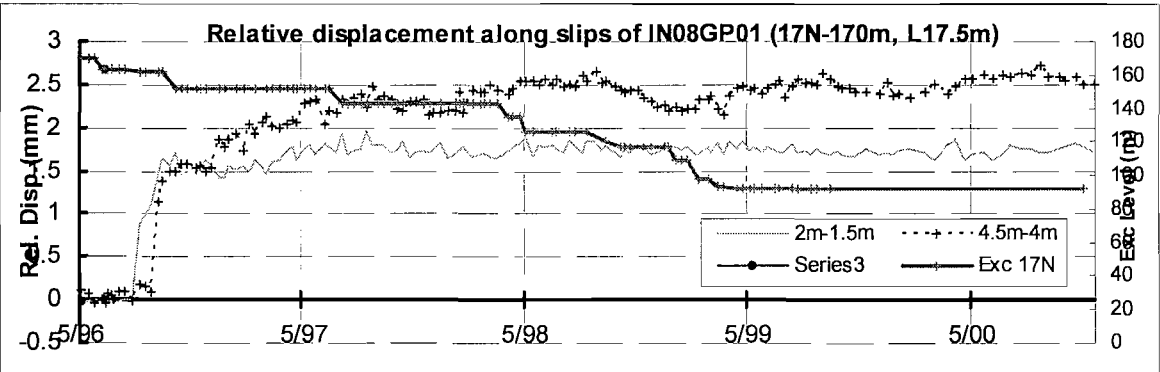
Fig4.77 Relative displacement of slips on IN08GP01 (Sec#17N)

(a) Profile on 25/08/96
(Sec#17N Slope)

(b) Profile on 05/09/96
(Sec#17N Slope)
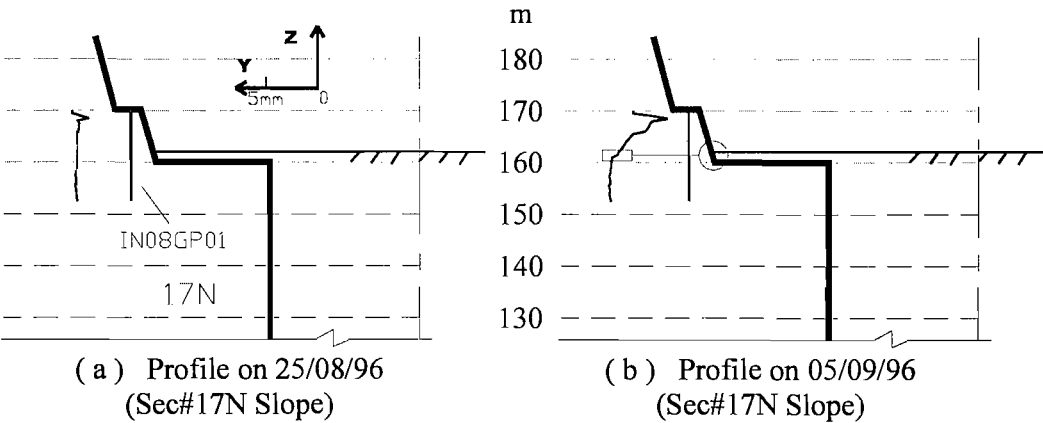
Fig4.78 Effect of excavation level on IN08GP01 (Sec#17 N70)

112

(a) Profile of 12/09/99　　　　　　(b) Typical profile during 23/10/99 ~
　　　　　　　　　　　　　　　　　　　　　　21/06/00

Fig4.79 Slips on IN11GP01 (Sec#17 N159)
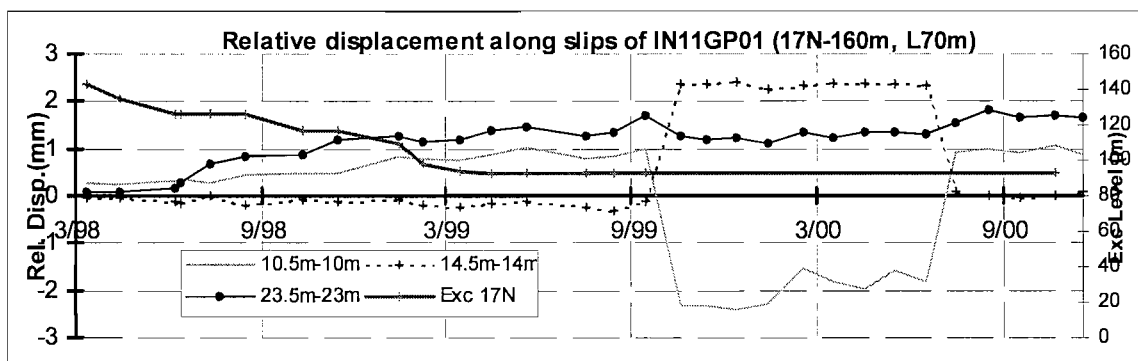
Fig4.80 Relative displacement of slips on IN11GP01 (Sec#17N-1)
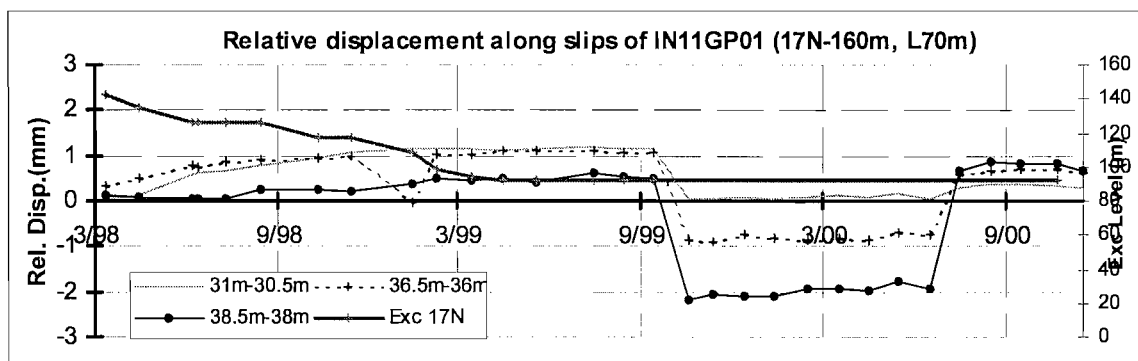
Fig4.81 Relative displacement of slips on IN11GP01 (Sec#17N-2)

Relative displacement along slips of IN11GP01 (17N-160m, L70m)
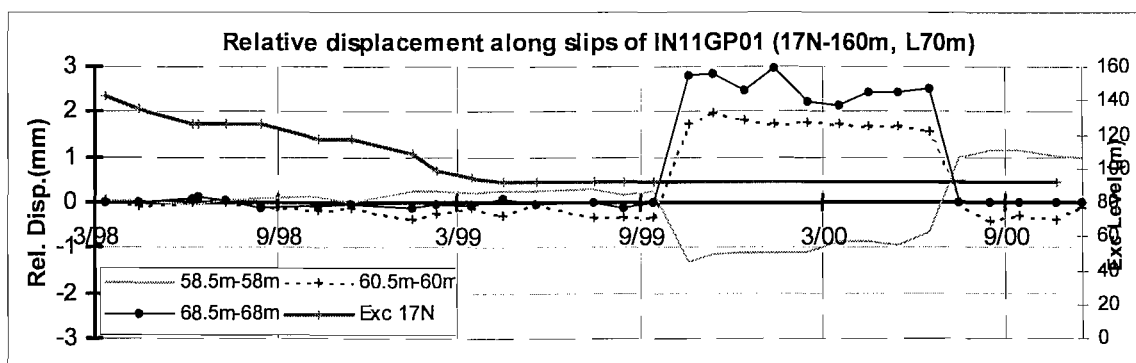
Fig4.82 Relative displacement of slips on IN11GP01 (Sec#17N-3)

4.4.4 Subsurface deformation of the north slope at Sec#20

The geological conditions on the north slope of Sec#20 are shown in Fig4.60. The anchorage installed on the north slopes around Sec#20 is shown in Fig3.16 and the prestressed cables installed are listed in Table3.9.

On the north slope of Sec#20 (Fig4.40 (b)), the measurements of IN05GP01 (200m) and IN09GP01 (170m) are adjusted using survey point data. There is no corresponding survey point available for IN12GP01 (139m) (Table4.8).

IN12GP01 (139m) was damaged during the installation of an anchorage in 11/98. Therefore, data from IN12GP01 have been discarded after 11/98.

4.4.4.1 General deformations

Inclinometer data (Fig4.83) agree with survey data that the slope moved to the south gradually as excavation progressed.

All three inclinometers on the north slope of Sec#17 show a toppling deformation pattern (Fig4.83). Within the length of each inclinometer, the top of the inclinometer moved more into the excavation than the bottom because of more restriction at the bottom.

Both IN09GP01 (170m) and IN12GP01 (139m) show a typical pattern of toppling deformation.

IN05GP01 (200m) initially deformed in a sliding pattern, but later switched to a toppling one, probably due to the toppling pattern of the overall slope when excavation reached the bottom (Fig4.83).

114

It can be seen that the tops of IN09GP01 (170m) and IN05GP01 (200m) show considerably larger deformations than IN12GP01 (139m) before 11/98 (Fig4.83). This is consistent with the survey point data (Fig4.49).
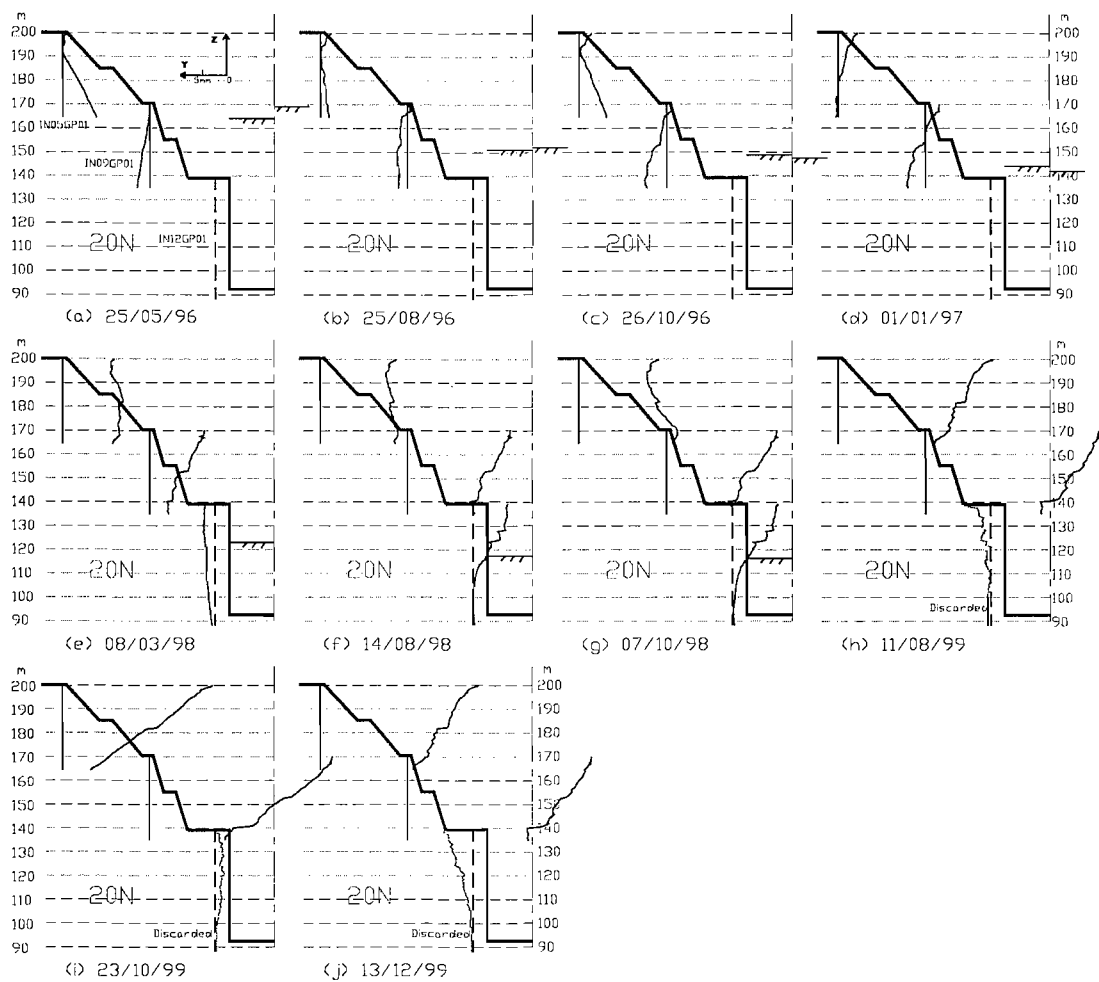
Fig4.83 Profiles of inclinometers on the north slope of Sec#20

4.4.4.2 Slips on the inclinometers

(1) IN05GP01 (Sec#20 N-200m, L35.5m, 15775.6m)

A slip occurred between at a depth of 18.5-18m of IN05GP01, which is close to the boundary of completely/highly weathered zone (22.6m, Table4.11). The relative displacement increased steadily before the end of excavation in 05/99 and did not develop further after that (Fig4.84).

(2) IN09GP01 (Sec#20 N-170m, L35m, 15777.4m)

Two slips are observed at depths of 17.5m-17m and 30m-29.5m.

Fissure T_{21} intersects IN09GP01 at a depth of about 20.8m (Table4.11). This could be related to the slip at 17.5m-17m because the relative displacement of the slip started to increase from 08/96 when the fissure T_{21} was exposed by the excavation (Fig4.85) and the orientation of T_{21} (272 ∠25? also coincides with the slip pattern. The relative displacement developed between 09/96 and 07/97, when the excavation approached the level of the top of the Middle Pier. It did not develop further afterwards.

The slip at depth 30m-29.5 is clearly related to the wide bench at the elevation of 140m, which restricted the deformation below it (Fig4.2 and Fig4.83 (e)). Another contributing factor could have been the boundary between the affected zone and the damaged zone that intersects IN09GP01 at 27m depth (elevation 143m, Table4.11) (Fig4.60).

(3) IN12GP01 (Sec#20 N-139m, L51m, 15782.35m)

Three slips are observed on IN12GP01 with relative displacements shown in Fig4.86. The relative displacements of the slips between 11.5m-11m and 16m-15m did not change after the end of excavation in 11/99. The third slip (between 6.5m-6m) started to develop in 11/99, after excavation finished.

The slip at 16m-15m coincided with a fissure at a depth of 15m-15.2m found by borehole exploration. The exposed fissure was partly filled with mud, which is likely to encourage the development of a slip.

The slip of 6.5m-6m may relate to fissure T_{98} that intersected IN12GP01 at depth of around 8.8m (Table4.11).
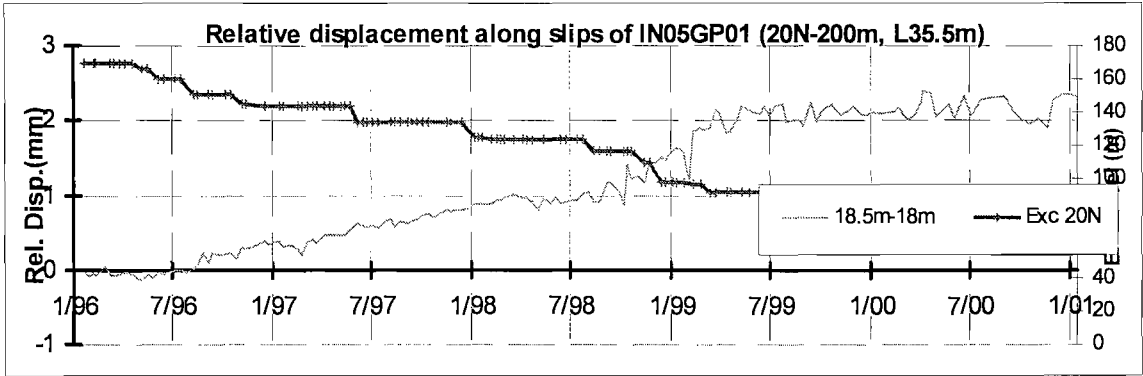
Fig4.84 Relative displacement of slips on IN05GP01 (Sec#20N-1)
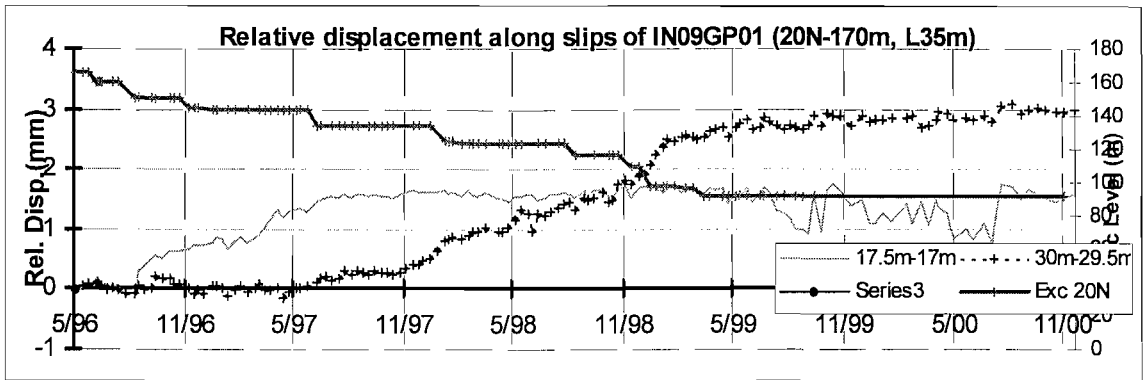
Fig4.85 Relative displacement of slips on IN09GP01 (Sec#20N-2)
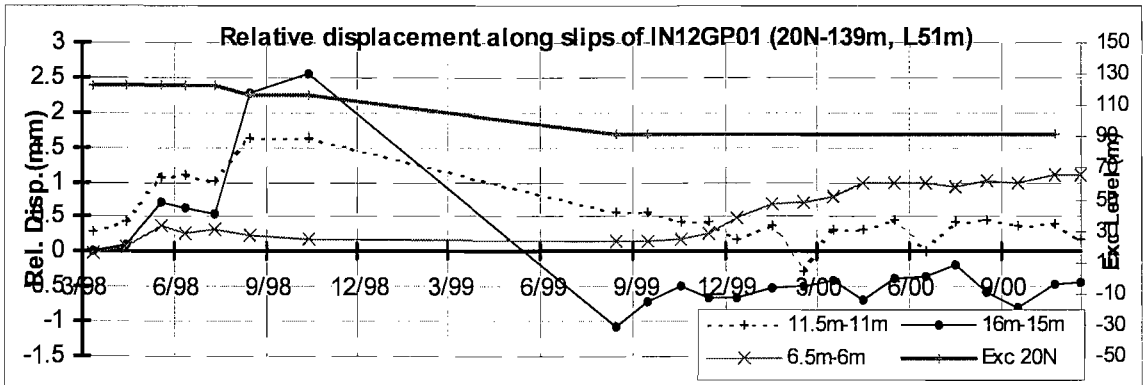
Fig4.86 Relative displacement of slips on IN12GP01 (Sec#20N-3)

4.4.5 Subsurface deformation of the south slope at Sec#17

The geological conditions on the south slope of Sec#17 are shown in Fig4.59. The anchorage installed on the south slopes around Sec#17 is shown in Fig3.16 and the prestressed cables installed are listed in Table3.10.

On this slope, the measurements of inclinometers IN13GP02 (170m), IN07GP02 (200m) and IN06GP02 (230m) are adjusted using the data of their corresponding survey point (Table4.9) (Fig4.87).

There are no measurements for IN06GP02 (230m) after 05/99 due to the damage to the inclinometer that occurred during anchorage installation.

117
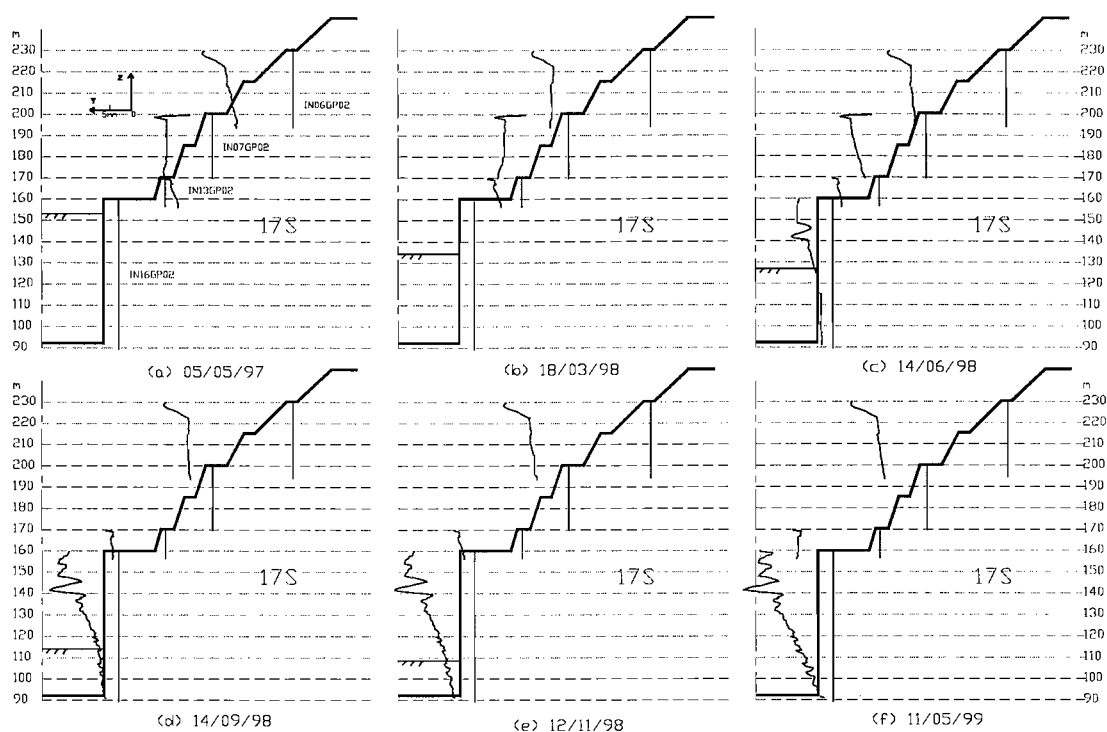
Fig4.87 Profiles of inclinometers on the south slope of Sec#17

4.4.5.1 General deformations

Inclinometer data on the south slope of Sec#17 confirm the general deformation pattern shown by survey data (Fig4.87). All the inclinometers on the slope moved to the north as excavation progressed. The deformations at bench levels increased with height. However deformations are close for points below 200m elevation as shown in survey data (Fig4.46).

Inclinometers on this slope do not show obviously either a toppling pattern or a sliding pattern.

4.4.5.2 Slips on the inclinometers

(1) IN16GP02 (Sec#17S-160m, L69m)

The inclinometer profiles show a noticeable "Z" shape between depths of 11.5m and 20.5m (Fig4.88 to Fig4.90). The point at 14.5m relates to f_1 and T_{31} that intersected IN16GP02 at about 14.5m depth and the point at 18.5m relates to T_{15} that intersected IN16GP02 at depth around 18m (Fig4.90 (b)).

Two more slips developed at depths 6.5m-6m and 55m-54.5m, which deformed in a similar way (Fig4.89). The decrease of relative displacement during 05/98 may have been the result of prestressed cables installed before 05/98 (Items 1 to 4 in Table4.12).

118

Other apparent slips cannot be related to any known geological conditions or slope geometry and could be linked with anchorage.

Most of the relative displacements increased between 06/98 and 08/98 when excavation was taking place about 40m below the top of the inclinometer, and changed very little afterwards (Fig4.4.88 and Fig4.88).

(2) IN13GP02 (Sec#17S-170m, L14m)

There is one slip apparent at IN13GP02 between depths 1m-0.5m (Fig4.91 and Fig4.92), which could be attributed to an excavation-induced fracture close to excavation surface.

(3) IN07GP02 (Sec#17S-200m, L30.5m)

Two slips are apparent at depths of 1.5m-0.5m and 2.5m-1.5m as shown in Fig4.92. They might relate to fault f_{1213}, which intersected IN07GP02 at a depth about 2m. The relative displacements developed between 15/08/96 and 13/09/96 and did not change afterwards (Fig4.93).

(4) IN06GP02 (Sec#17S-230m, L36.5m)

One apparent slip is found at a depth of 7.5m (Fig4.92), which cannot be related to known discontinuities.
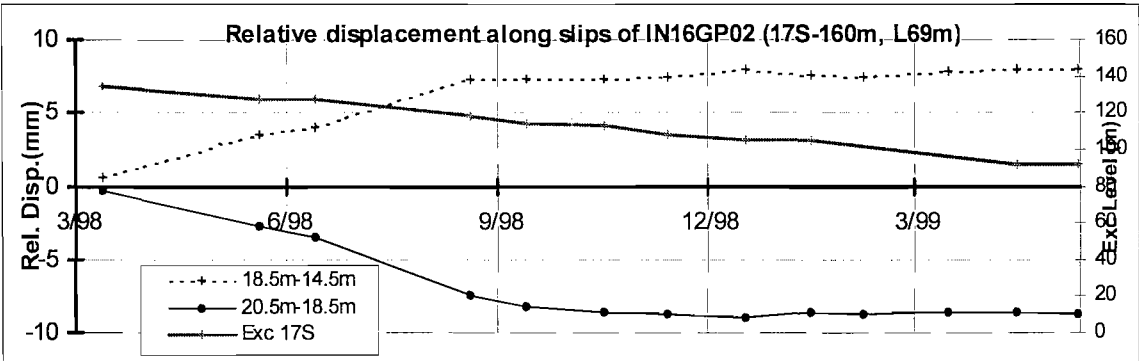
Fig4.88 Relative displacement of slips on IN16GP02 (Sec#17S-1)
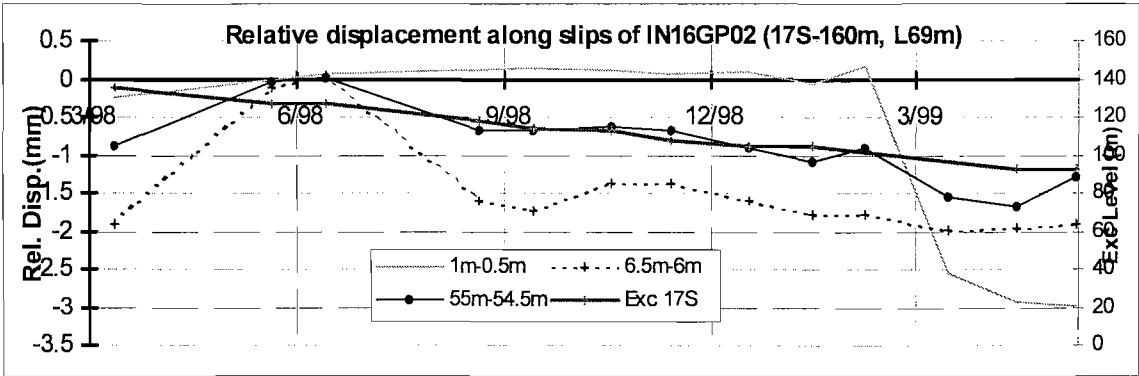
Fig4.89 Relative displacement of slips on IN16GP02 (Sec#17S-2)

119

(a) Profile of IN16GP02 on 14/06/98   (b) Profile of IN16GP02 on 11/05/99
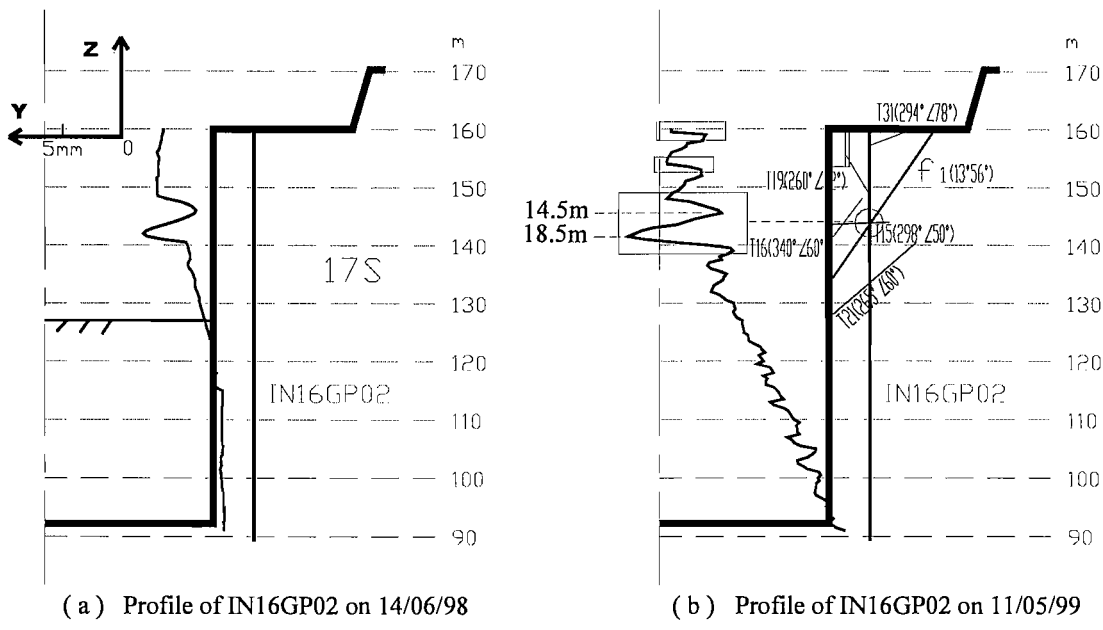
Fig4.90 Deformation profiles of IN16GP02 and slips on upper IN16GP02
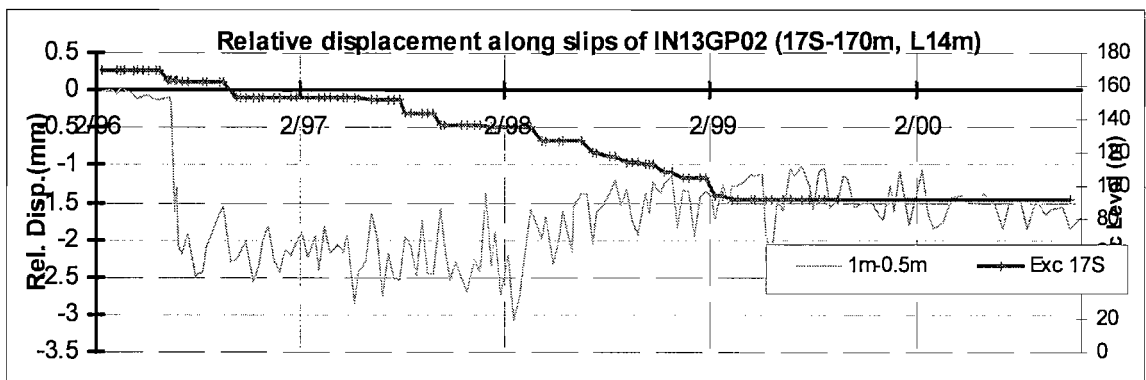
Fig4.91 Relative displacement of slips on IN13GP02 (Sec#17S)

(a) Profiles on 17/05/96 (Sec#17 South Slope)   (b) Profiles on 25/06/98 (Sec#17 South Slope)
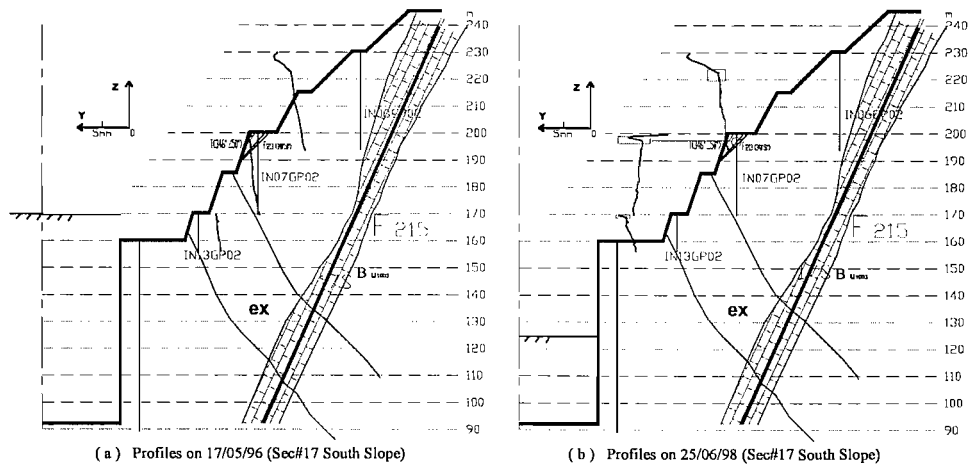
Fig4.92 Deformation profiles on the south slope of Sec#17 and the slip at 199m elevation
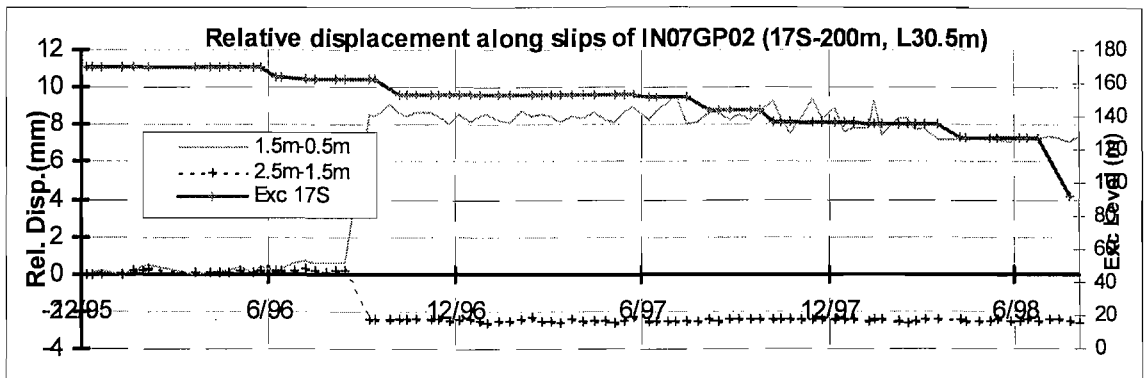
Fig4.93 Relative displacement of slips on IN07GP02 (Sec#17S)

4.4.6 Subsurface deformation of the south slope at Sec#20

The geological conditions on the south slope of Sec#20 are shown in Fig4.61. Most of the major discontinuities are dipping to the south. The anchorage installed on the south slope around Sec#20 is shown in Fig3.16 and the prestressed cables installed are listed in Table3.11.

On this slope, IN14GP02 (170m), IN11GP02 (200m), IN09GP02 (230m) and IN08GP02 (245m) are adjusted using survey point data (Table4.8). There is no survey point available for IN10GP02 (215m). The measurements at the top point of IN14GP02 (170m) (0.5m) are discarded because the instrument was hit in a site accident, while the data for depth below 0.5m are consistent and retained.

4.4.6.1 General deformations

All the inclinometers deformed to the north gradually as excavation progressed and registered very little deformation after the excavation was completed. The average deformation of the inclinometers increased with height in general (Fig4.94).

IN17GP02 (150m) and IN09GP02 (230m) show a toppling pattern while IN11GP02 (200m) and IN10GP02 (215m) eventually adopted a sliding pattern. The profile pattern of IN14GP02 (170m) was significantly affected by excavation below the elevation of 150m (Fig4.94 (c-e)). IN08GP02 (245m) presented an "S" shape profile (Fig4.94), which could be related to the slope geometry and the varying material properties of the weathered zones that the inclinometer penetrates.

There was a collapse at elevation of around 170m during 10/98 and 11/98 that resulted in a significant increment on IN14GP02 (170m) and IN17GP02 (150m) (Fig4.94 (e-f)) corresponding to that of survey point TP33GP02 (170m) (Fig4.48).

121
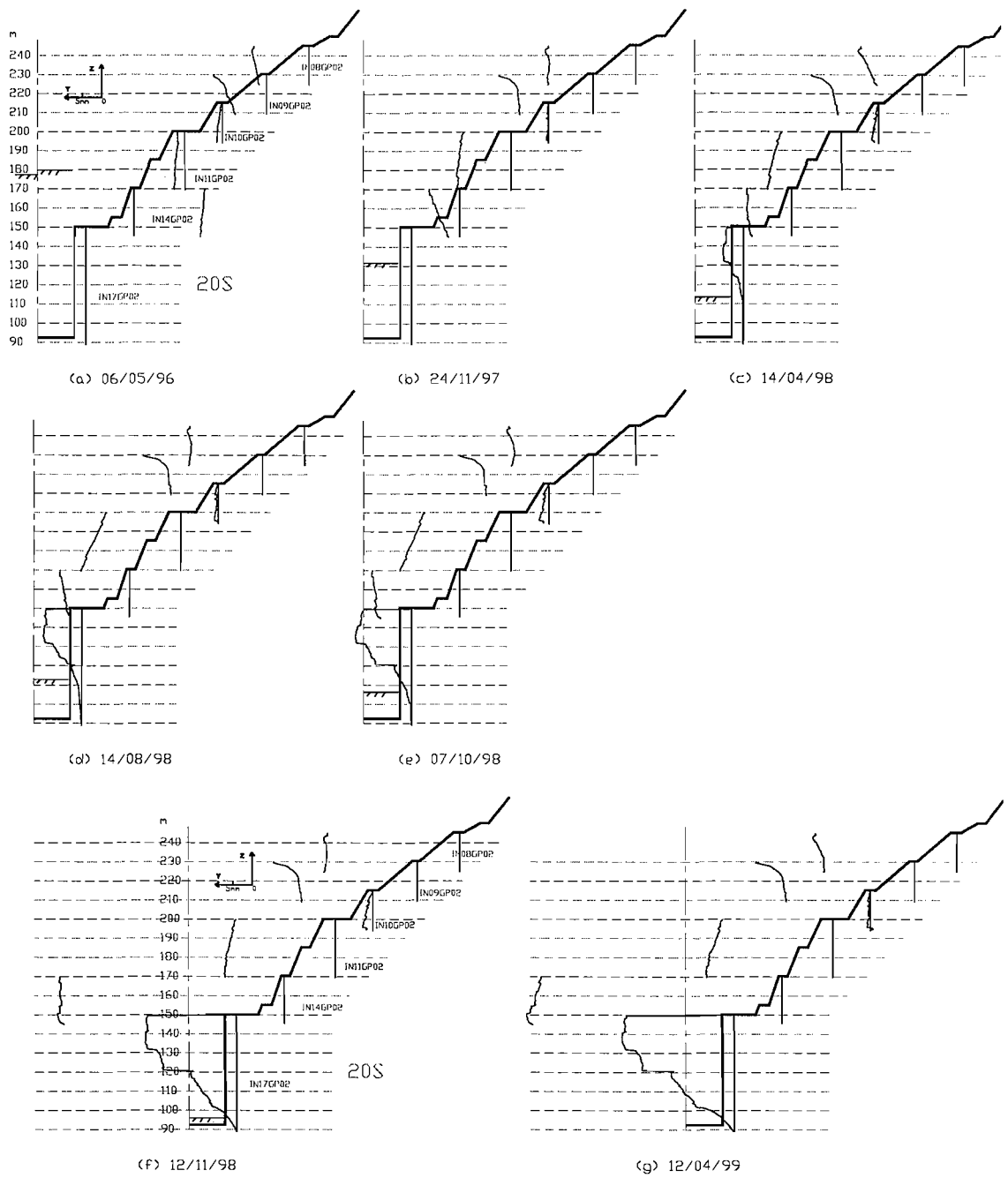
Fig4.94(a-g) Profiles of inclinometers on the south slope of Sec#20
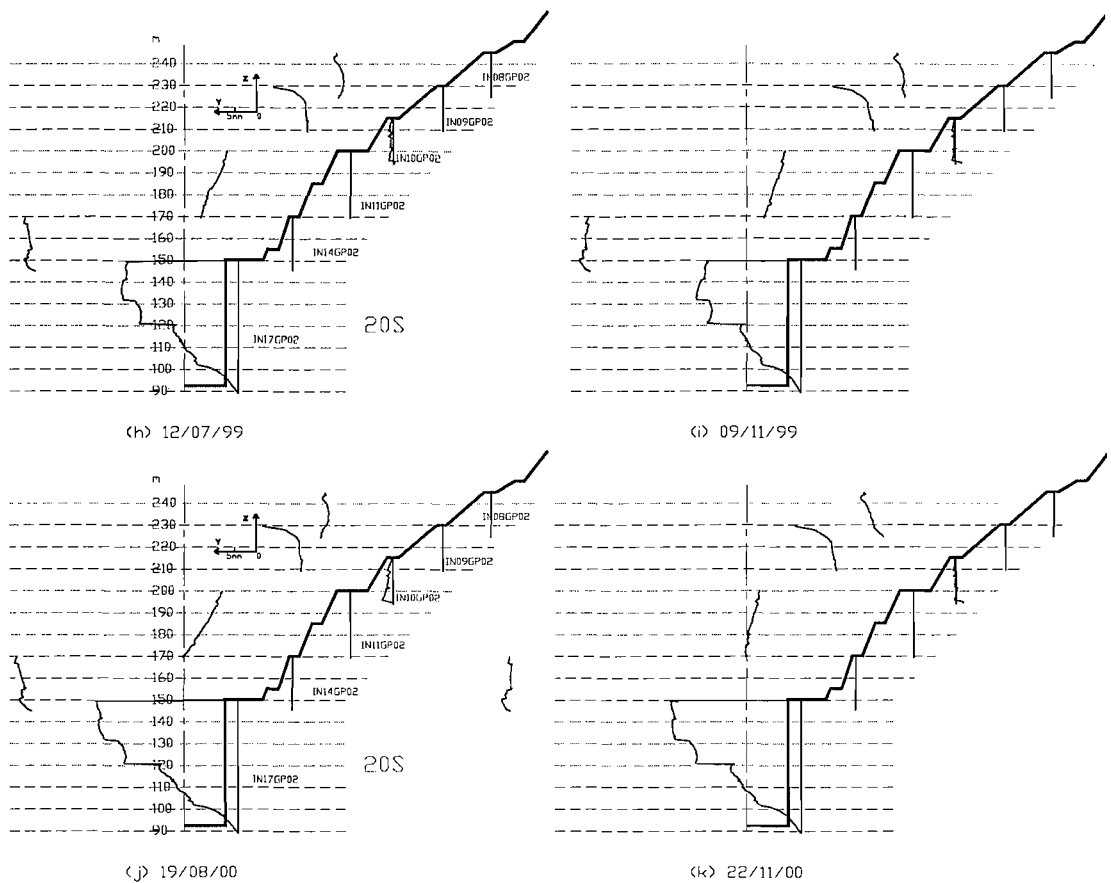
Fig4.94(h-k) Profiles of inclinometers on the south slope of Sec#20

4.4.6.2 Slips on the inclinometers

(1) IN17GP02 (Sec#20S-150m, L61m, 15782.61m)

IN17GP02 is intersected by a number of discontinuities (Fig4.61). Two slips are observed at depths of 18.5m-18m and 29.5m-29m. Both slips developed gradually during excavation and changed little after that (Fig4.95).

The slip at 29.5m-29m can be related to fissure T_{15} that intersected IN17GP02 at about 28.5m (Table4.11). The relative displacement started to increase significantly from 06/98 when T_{15} was exposed on the vertical wall (Fig4.95) and changed little afterwards. The slip coincides with an unstable block of $27m^3$ located below elevation 135m as reported in the field construction report. The block was reinforced by anchors (Fu, 1999).

(2) IN14GP02 (Sec#20S-170m, L25m, 15784.87m)

There are two similar slips observed at depths of 15.5m-15m and 19.5m-19m. Their relative displacements developed during the last period of excavation (Fig4.96). The lower slip may be related to the interface between xenolith "ex" and rock.

123

(3) IN11GP02 (Sec#20S-200m, L30.5m, 15775.75m)

There are no jumps in the deformation profiles of IN11GP02.

(4) IN10GP02 (Sec#20S-215m, L20.5m, 15776.36m)

Two continuous slips at 19.5m-19m and 20.5m-19.5m depth form a layer protruding to the south. It may relate to the fault f_{1221} that intersected the inclinometer at a depth of about 20m (Table4.11). There were large variations of relative displacement after excavation was completed in 03/99 (Fig4.97).

The behaviour of these two slips resembles the slips at depth of 36.5m-36m and 42.5m-42m on IN04GP01 (Sec#17 N-215m, L20.5m) during the same period.

(5) IN09GP02 (Sec#20S-230m, L21m,)

The top part of IN09GP02 moved to the south significantly more than the lower part (Fig4.94). This could be attributed to two reasons: (a) top part is in the weaker materials of weathered zone or EDZ that have lower modulus; and (b) the low part is much farther horizontally from the excavated slope surface, which apparently resulted in less deformation.

(6) IN08GP02 (Sec#20S-245m, L20.5m,)

A slip is found close to the bottom of IN08GP02 (19.5m-19m) with small relative displacement (Fig4.98). No related discontinuity is identified. It has a similar large variation in the relative deformation after the end of excavation, as those on IN04GP01 and IN10GP02 (Fig4.98).

It is difficult to explain these abnormalities on the basis of available information.
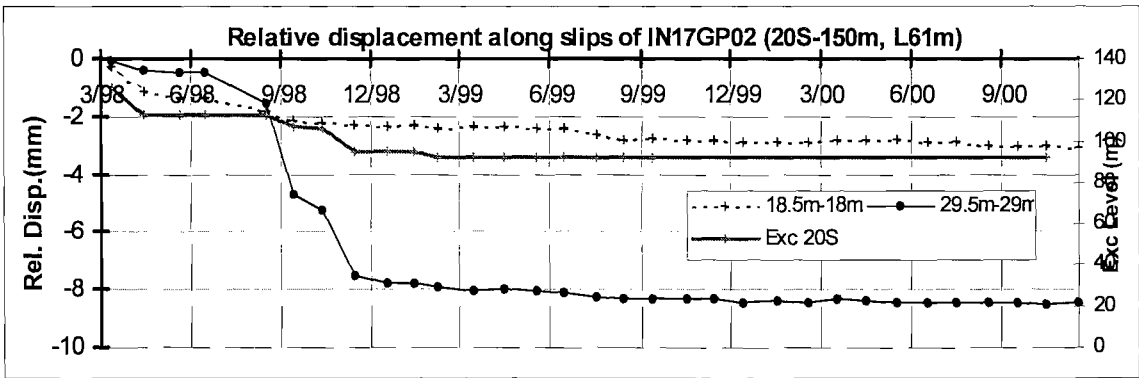
Fig4.95 Relative displacement of slips on IN17GP02 (Sec#20S)
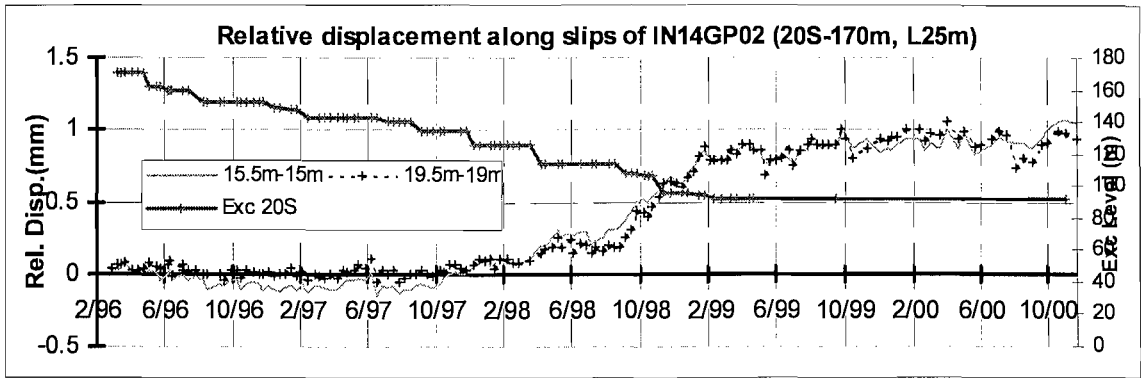
Fig4.96 Relative displacement of slips on IN14GP02 (Sec#20S)
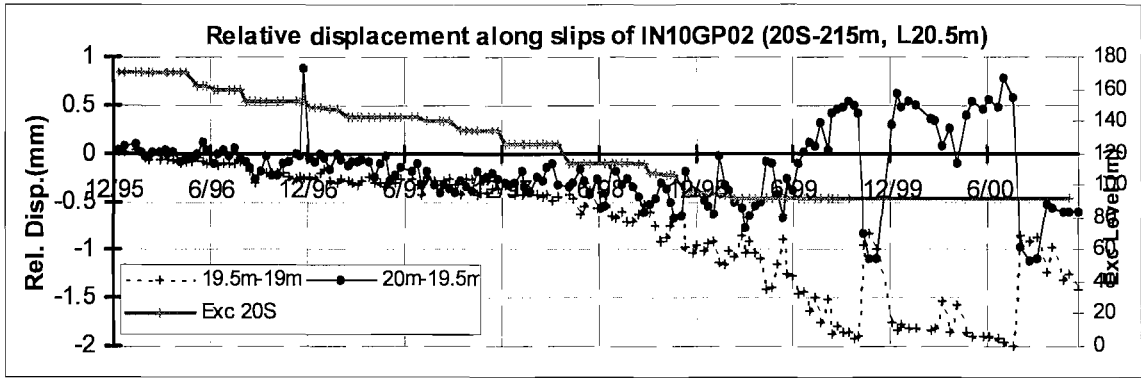
Fig4.97 Relative displacement of slips on IN10GP02 (Sec#20S)
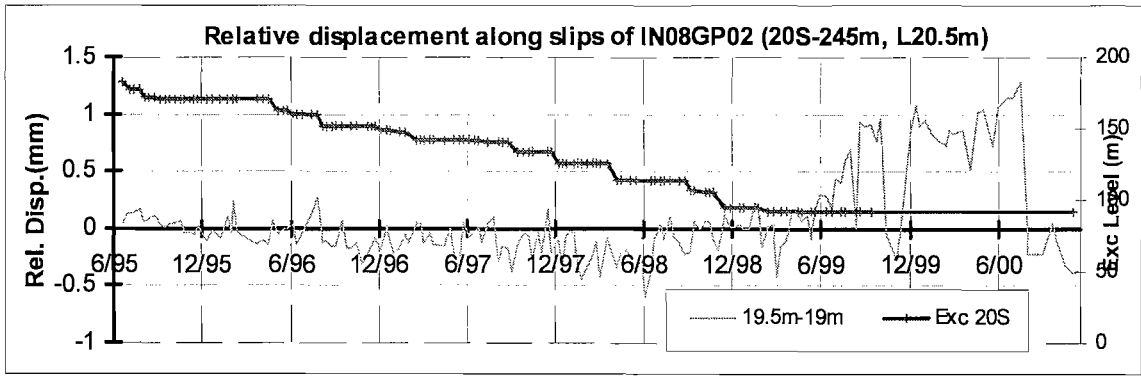
Fig4.98 Relative displacement of slips on IN08GP02 (Sec#20S)

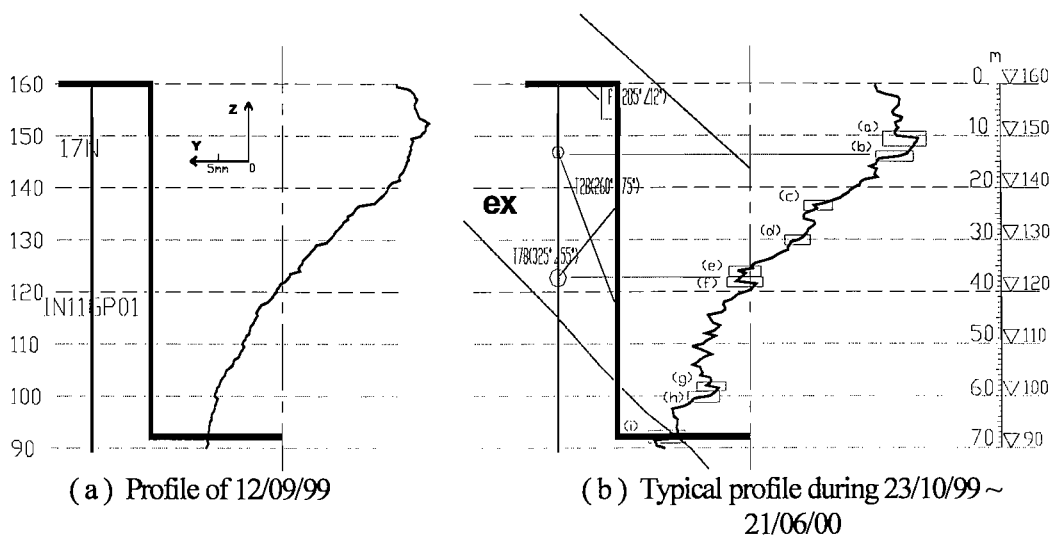## 4.5 Conclusions on the Deformations of the TGP

The case study of the field data investigated the deformation pattern of the excavated slopes and identified and evaluated the various.

The study shows that a combination of survey and inclinometer data can provide good insight into the surface and subsurface deformations of the slopes. Also, inclinometers are effective in identifying slips and changes of the deformation profiles deep in the rock.

In general, the slopes deform towards the excavated space gradually with excavation. Some small movements are observed after the excavation finished in limited areas.

On the Middle Pier at Sec#17, vertical walls of the chamber are influenced by the excavation level in the other chamber because of the limited width of the Middle Pier. As a whole, the Middle Pier inclined to the north under the influence of geological conditions. Excavation on one side of the Middle Pier has less effect on the deformation of the other side of the pier when the pier width increases. As a result, the Middle Pier at Sec#20 expanded even on both sides, increasingly with rising elevation. Therefore the intermediate discontinuities on the Middle Pier at Sec#20 are less important to the overall behaviour pattern of the pier beside their respective effects on the nearside chamber wall. Field data show that the deformations at the bottom of inclinometers, which are effectively 2-3m below the excavation bottom, are very small.

The analysis of field data of the Middle Pier shows that geological features (e.g. joints and weather zones), excavation sequence and proximity of multiple-stage excavations have an influence on the deformation pattern.

Both the north and south slopes behaved in a toppling pattern as a whole. The major discontinuities are found to influence the deformation pattern of slopes.

However, different deformation patterns, namely toppling, sliding and translating are observed locally on different parts of the slopes, due to the combined influence of factors like slope geometry, discontinuity pattern, reinforcement, formation of EDZ and geological features. There is little evidence in the field measurements to indicate that single minor discontinuities, or the majority of single intermediate ones, affect the overall deformation pattern. Prestressed cables through the Middle Pier have a strong restriction on expansion of the pier locally. Systematic bolts that spread along full slope surface do not have noticeable effect on deformation measurements. These suggest that the rock around the excavation behave more like a continuum more or less except for the major discontinuities.

Slips identified by inclinometer data are mostly related to existing discontinuities that slipped due to excavation-induced stress release. Slope geometry and prestressed cables may result in slips on inclinometer profiles as well.

Inclinometer data have shown that the excavation damaged/disturbed zones (EDZ) have important effects on deformation of rocks in the relevant zones and they are sometimes related to changes of deformation profile implicitly. However, it is difficult to extract quantitative information of their ranges and effects from inclinometer data due to the uncertainties involved. Numerical modelling may help to assess the EDZ to a certain degree, e.g. by plasticity in material, with proper material properties and material models. After all,, the geophysical methods such as the Acoustic Emission discussed in the literature review would be the most useful tool.

Chapter 5 Construction and Validation of a Numerical Model for the Shiplock

5.1 Introduction

In order to investigate appropriate methods of modelling and analysis of excavations in discontinuous rock, it is important to find out what are the major influencing factors and their effect on the behaviour of discontinuous rock.

As demonstrated in the literature review and by the analysis of the field data in the previous chapter, the major factors influencing the behaviour of discontinuous rock include rock quality, discontinuities and the geometry and the sequence of excavation. The quality of rock mass affects directly their deformations. Strong rock masses tend to cause lower deformation than weak rock mass under similar conditions. The effects of discontinuities vary from changing deformation pattern in a large extent to local slips along the discontinuities, which are both observed in field data. Excavation is the direct cause of deformation in rock mass, which determines the deformation profile both in space and in time series. As a consequence of excavation induced stress release, the excavation damage/disturbed zone (EDZ) is another important factor for deformation magnitude and profile around the excavation. However what the literature search and field data analysis present is a comprehensive picture of the combined results of various factors, e.g. strength and modulus of rock and discontinuities, discontinuity patterns, properties of EDZ and excavation sequence etc. In order to simulate the complex discontinuous system correctly and effectively, it is helpful to ask questions like how many discontinuities need to be modelled and how much EDZ can influence the behaviour of rock mass etc. Therefore a parametric study of these properties is needed to identify quantitatively which ones matter for discontinuous rock, which gives guidance on how to incorporate them into model.

As shown both in literature theoretically and in field data, all of discontinuities, excavation and EDZ are of three-dimensional characteristics in space and/or time sequence. However because of the complexity associated with three-dimensional modelling, it is rational to check how well a two-dimensional model can simulate these effects. Therefore a comparative study between 2D and 3D modelling will be carried out after the parametric study.

In the modelling, the Sec#20 is selected because it represents a more general case of the shiplock formation and geological conditions than the Sec#17. It suits better the purpose of modelling excavations in discontinuous rock.

The distinct element packages 3DEC and UDEC introduced in Chapter 2 are used to model the shiplock around Sec#20 in 3D and 2D dimension respectively.

5.2 Program of numerical analysis

The whole program of numerical analysis consists of four parts: model building and validation, modelling discontinuities and excavation damaged/disturbed zone, parametric sensitivity study and comparative study between 2D and 3D modelling. The tasks carried out in the program are presented as follows.

(1) The geometry and extent of the model were determined on the basis of geological conditions and the geometry of the shiplock. The model was validated by comparing to field data.

(2) The discontinuities that need to be modelled explicitly were identified, while equivalent continuum solutions were used to take into account the remaining discontinuities in the model including EDZ.

(3) The sensitivity of the model to discontinuity properties was firstly studied. A further parametric study was carried out on the properties of rock blocks of equivalent rock continuum and the properties and ranges of EDZ subzones.

(4) A comparative study between 2D and 3D modelling was carried out to investigate the suitability of 2D modelling. The possible influences of different modelling solutions on the deformation were studied.

The first part of the research, model construction and validation are introduced in this chapter, whereas the others are presented in Chapter 6.

In this chapter, the basic parameters and geological conditions modelled in the analysis are described in section 5.3. The methods used to interpret numerical results are presented in section 5.4. The validations of the model geometry and extent are presented in sections 5.5 and 5.6.

5.3 Geotechnical parameters and geological conditions

A number of previous studies on geotechnical parameters and geological conditions of the Three Gorges Project site have been introduced in Chapter 3. The relevant information used in numerical modelling is presented in this section.

5.3.1 Material properties

The geotechnical parameters were summarized from results of field tests carried out at the shiplock site and laboratory tests on samples from the site. According to their conditions, the material properties of discontinuities fall in 4 categories (JMat1, Jmat2, JMat3 and JMat4) in numerical modelling. The basic discontinuity properties are selected from Table3.2 and publication by Zhang & Zhou (1999) as listed in Table5.1. Based on the structure of rock mass in fresh/slightly weathered and moderately weathered zones from site investigation, the material properties for rock in these zones, shown in Table5.2, were selected according to the properties recommended in Table3.3. As the completely weathered zone at the top was very thin and its depth varied considerably at different locations, it was modelled as a part of the highly weathered zone, which had an average depth of around 22m.

Table5.1 Material properties for discontinuities in models

Discontinuity type	Joint Mat no	Weathered Zones	Cohesion C	Friction f	Normal stiffness	Shear stiffness
			MPa	(°)	MPa/m	MPa/m
Hard	JMat1		0.2	35.0	690	240
Soft	JMat2	Fresh /Slightly	0.18	31.0	280	96
	JMat3	Moderately/Highly	0.12	21.8	280	96
F215 interfaces	JMat4		0.1	18	280	96

Table5.2 Material properties for rock blocks in models

Weathered zones or filling		Fresh/ slightly	Moderat ely	Highly	*F215* Filling
		BMat1	BMat2	BMat3	BMat4
Unit weight	γ (kN/m^3)	27.0	26.8	26.5	25.4
Elastic modulus	E (GPa)	32	10	1.0	0.75
Poisson's ratio	ν	0.22	0.24	0.3	0.2
Friction	f (°)	59	50	45.0	18
Cohesion	C (MPa)	1.8	1.0	0.35	0.1
Dilation angle	Ψ (°)	na	na	na	na
Residual friction	f' (°)	52.4	47.7	42.0	na
Residual cohesion	C' (MPa)	0.7	0.35	0.15	na
Tensile strength	T (MPa)	1.5	1.0	0.5	na
Compressive strength	(MPa)	100.0	50.0	20.0	na

- For the xenolith "ex": the properties of the part in fresh/slightly weathered zone were close to the properties of moderately weathered zone; the properties of the part in moderately and highly weathered zones were close to the properties of the highly weathered zone.

- BMat1/2/3/4 denote block material numbers for different rock materials in the model .

5.3.2 Classification of discontinuities

In terms of their scale of geological exposure (Fig3.8 and Fig3.9) and their relevance to the section of interest, discontinuities considered at different parts of the model can be classified into three groups: major discontinuities, intermediate discontinuities and minor discontinuities according to their scales, as listed in Table5.3.

The major discontinuities generally ran through the whole of the shiplock area and were thought to have significant influence on the behaviour of the cut slopes. These discontinuities

included the xenolith "ex", and most of the veins and large faults (Table5.3). Some of them were filled with weak materials. It was decided that the major discontinuities would be modelled explicitly.

The intermediate discontinuities located on the cut slopes were expected to have important influence on the local deformation of a slope. They were possible to model explicitly either as individuals if in a limited number or as generalised fault sets if presenting certain patterns. Considering their limited number, in the preliminary stage of the study intermediate discontinuities were modelled individually.

The third group consisted of a large number of predominantly small scale discontinuities. They were impossible to model individually, although they could still be modelled explicitly as they could be generalised statistically into a number of discontinuity sets. Alternatively, they could be taken into consideration by using an equivalent continuum approach. The statistical information for minor discontinuity sets close to the excavation is listed in Table5.4 and was available from relevant publications (Chen et al., 1996 and Zhang &. Zhou, 1999). The persistence of these fissure sets was estimated at 56% for the upper part of the slopes and at about 25% for the lower part.

However except for major discontinuities and pervasive fault sets, discontinuities far away from the excavation were not modelled explicitly because firstly they are too far to make a lot of difference to the deformation around the excavation; secondly not enough information was available about them, and thirdly also for reasons of computational efficiency. The equivalent continuum method was adopted to take into consideration these discontinuities.

Table5.3 Classification of discontinuities

Type	Position	Discontinuities
Major		F215, ex, Bu1003, Bu1005, Bu1002, Bu1001
Intermediate	South slope	f1219, f1220, f1221, f1222, f1007
	North slope	f3, f4, f1005, f10
Minor		Remaining faults and fissures

Table5.4 Statistical parameters of dominant fissures around Sec#20

Position	Group	Dip Dir (°)	Dip (°)	Spacing (m)
Middle Pier	NWW/NE	358	67	1.91
	NEE/NW	324	74	1.58
	NNW/NE	50	63	0.93

	NNE/NW	269	63	2.50
South Slope	NNW	235	59.2	2.10
	NNE	193.7	69.36	2.50
	NEE	320	71.2	2.41
North Slope	NNE	283.9	68.9	4.8
	NEE	323	77.5	2.1
*Dipping direction following the shiplock coordination system				

5.3.3 In situ stress

The in situ stress in the highly or completely weathered zones (generally within 20m from ground surface) was derived by gravity.

Based on field tests, the in situ stress field was described by a series of formulae defining each stress component magnitude (unit in MPa) as a linear function of depth from the original ground surface (Feng & Zhang et. al., 2000). These are given in Equation (5-1).

$$S_{xx} = -4.3867 - 0.01184 \cdot H$$
$$S_{yy} = -1.4629 - 0.03031 \cdot H$$
$$S_{zz} = -4.5344 - 0.01129 \cdot H$$
$$S_{xy} = 0.849 - 0.00073 \cdot H$$
$$S_{xz} = 0.4142 - 0.00028 \cdot H$$
$$S_{yz} = -0.04623 - 0.00002 \cdot H$$

$$(5\text{-}1)$$

Here "H" (unit in meters) is the vertical distance from the ground surface. Equation (5-1) is valid for $H>20$m. The depth "H" is defined according to general topography in a relatively large area around the section, since it was difficult to calculate H according to topographic details. "H" could be expressed in the shiplock coordination system in the region around Sec#20 by

$$H = 218 - 0.214x - y - 0.398z \qquad (5\text{-}2)$$

The in situ stress field can be derived from Equation (5-1) and (5-2) listed in Table5.5.

Table5.5 Original in situ stress field

	Stress at (0,0,0)	Stress gradient (MPa/m)		
Components	(MPa)	x	y	z
Szz	-6.96782	0.00253	0.01184	0.00471

Syy	-8.07048	0.00648	0.03031	0.01206
Sxx	-6.99562	0.00241	0.01129	0.00449
Syz	0.68986	0.00015	0.00073	0.00029
Szx	0.35316	0.00005	0.00028	0.00011
Sxy	-0.05059	0.00000	0.00002	0.00000
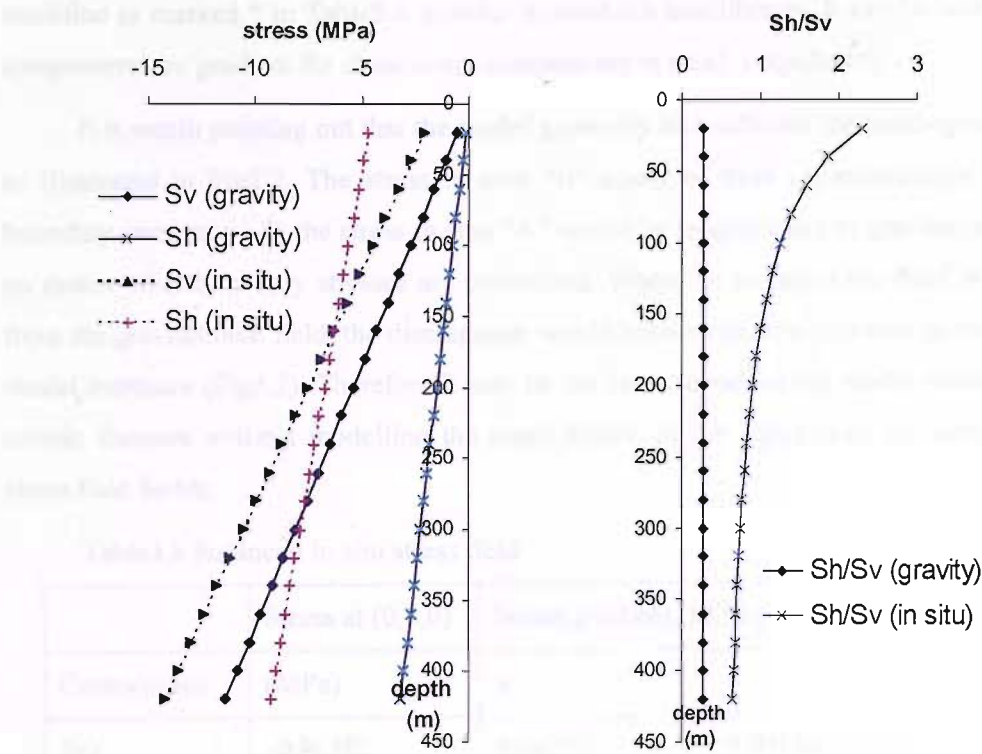
Fig5.1 In situ stress vs gravity-induced stress in elastic medium (a) horizontal stresses and vertical stresses and (b) the ratios between horizontal stresses and vertical stresses

The in situ stress field was compiled from measurements of about 62 segments in 8 deep boreholes and 5 shallow boreholes around the whole shiplock area. Both the piezomagnetic overcoring method and the hydro fracturing method were used. Apart from the field measurements, the topography and the tectonic history of this area were also taken into consideration through back analysis and statistical regression (Gong, 1995, Feng & Zhang et. al., 2000). Most of the parameters describing the in situ stress profile bear a good confidence. Therefore the stress profile is considered applicable to the area around the section of interest. The proposed in situ stress, which is very different from the gravitational one, obviously has an influence on model results. However it is difficult to verify how representative of the real stress condition due to the lack of information.

The formulae revealed that the in situ stress level was higher than the level of in situ stress that gravity alone would induce (Fig5.1 (a)) and the ratio between the tectonic horizontal stress and vertical stress was much higher than of the one gravity would induce in an elastic medium. Therefore the tectonic stress in the shiplock area is significant and cannot be ignored.

However, because the formulae were compiled from measurements at different locations with different confidence for each component independently, they describe a stress field that is not in equilibrium. Therefore, the in situ stress components with the lowest confidence were modified as marked * in Table5.6 in order to establish equilibrium. It can be seen the modified components are gradient for shear stress components in small magnitudes.

It is worth pointing out that the model geometry also affected the build-up of in situ stress as illustrated in Fig5.2. The stress in area "B" could be built up accordingly by prescribed boundary stresses while the stress in area "A" would be largely close to gravitational stress field no matter what boundary stresses are prescribed. When the in situ stress field is very different from the gravitational field, the discrepancy would become more significant as the extent of the model increases (Fig5.2). Therefore it may be desirable to extend the model horizontally from a certain distance without modelling the exact details of the topography in order to model the stress field better.

Table5.6 Balanced in situ stress field

| | Stress at (0,0,0) | Stress gradient (MPa/m) | | |
Components	(MPa)	x	y	z
Szz	-6.96782	0.00253	0.01184	0.00471
Syy	-8.07048	0.00648	0.03031	0.01206
Sxx	-6.99562	0.00241	0.01129	0.00449
Syz	0.68986	0.00015	-0.002595*	-0.000225*
Szx	0.35316	-0.003085*	0.00028	-0.000225*
Sxy	-0.05059	-0.003085*	-0.002595*	0.00000
	Note: "*" marks the components of low confidence and modified			
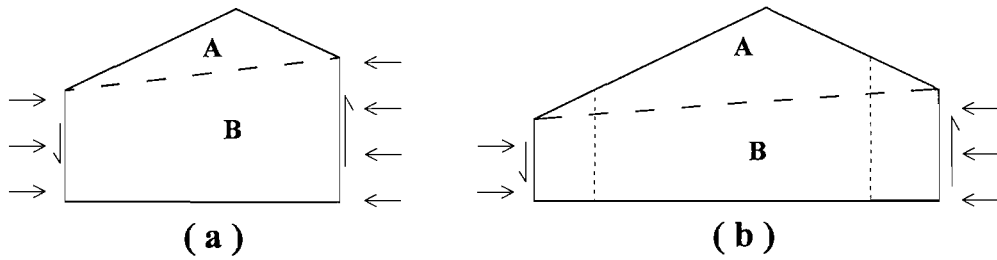
Fig5.2 Model geometry and in situ stress field

In numerical modelling, there are two ways of establishing the in situ stress in the model: (a) Specify stress boundary conditions and initialize stress in the model, then step the model to equilibrium; and (b) Specify only stress boundary conditions then step the model to equilibrium, i.e. allow the stress in the model to develop automatically.

In theory, given the appropriate boundary conditions (e.g., fixed bottom, roller side boundaries), the model will generate its stress field compatible with the applied boundary conditions and gravity if specified in either way. But this second method is inefficient and it may be only applicable to simple elastic continuous models as it may result in erroneous results in other cases. Generally in discrete element modelling like 3DEC, it is recommended to initialise the zones and contacts with stresses consistent with those applied at stress boundaries (Itasca, 1998).

There are two reasons for the above. Firstly, because the zones are normally not the same size in the blocks. For static analysis, 3DEC tries to keep the timestep equal for all zones, so it increases the inertial mass for the gridpoints of the smaller zones to compensate for their size. These gridpoints then accelerate more slowly than those of the larger zones. Consequently, the slower acceleration may result in slow build-up of horizontal stress. In reality, a large amount of plastic flow could occur because the confining stress does not build up immediately. Second, the horizontal stresses depend on the dynamics of the process. This will have unexpected abnormalities in a material that is path-dependent. Therefore the best solution is to initialise the stresses in the zones and contacts with values conforming to the desired stress conditions.

Nevertheless, it is very difficult to determine whether the stress state installed in a jointed model is representative of the in-situ state of stress because of the difficulty in obtaining detailed field data.

5.3.4 Model construction in 3DEC

Construction of the 3DEC model starts from cutting a single block to fit the dimensions and geometry of the problem. Any shape of features modelled has to be approximated by one or a series of joint planes. Divided blocks may be deleted if required. A joint plane is defined either by three points on the plane, or by a point on the plane, its dip direction and dip angle. Creating a joint set requires parameters of joint spacing and number of joints in the set. Discontinuous or non-persistent discontinuities require the parameter of persistence that defines the percentage of blocks lying in the joint plane that will be split on average. Statistical variation is possible for these parameters.

It is noted that 抯oints? in a 3DEC model do not necessarily represent actual discontinuities. Apart from discontinuities modeled individually, they could be 抴ctitious joints? used for model construction purposes, e.g. to form the topography, model boundaries, precut excavation geometry, boundaries between different materials, zones of different mesh density.

Eventually, a 3DEC model consists of a number of blocks connected through discontinuities (or contacts) via point contacts. A contact may be considered a boundary condition that applies external forces to each of the blocks that share it. Each block is discretized into tetrahedral finite-difference zones, in which the mechanical response (e.g., stress/strain) is calculated. Normally the area of interest will have the finest mesh and mesh density will reduce toward the far-field. Each contact is divided into sub-contacts for both rigid and deformable blocks. The density of subcontact depends on the zone density of blocks forming the contact. Interaction forces between blocks are applied at sub-contacts.

All the blocks/zones and contacts in the model are assigned with a constitutive model and corresponding material properties. Then the boundary conditions and in situ conditions are prescribed and the model is allowed to step to equilibrium under the initial conditions before any excavation or change is made.

5.3.5 Excavations and stages

Once initial equilibrium has been established in the model, a multi-stage excavation is executed.

For excavations in a general elastic stable system, the final deformation is always towards the excavation and the magnitude depends primarily on the excavation volume and the stress

level. However different excavation sequences could result in different shapes of the deformation vs time curve. This is illustrated in Fig5.3 where the expected deformation vs time curves of two different points are shown qualitatively. These points, A and B, are in identical conditions before excavation.
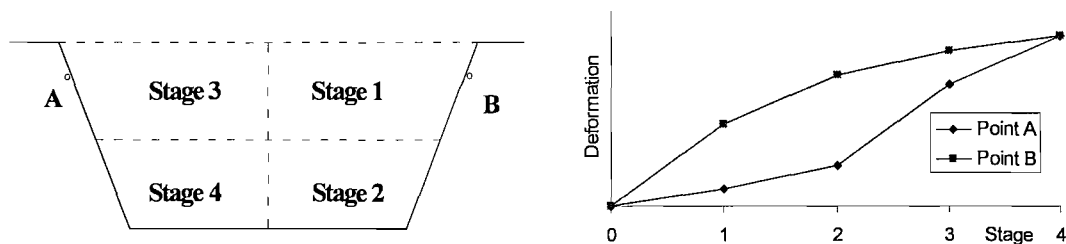
Fig5.3 Different deformation curves by excavation sequences

Analysis of field data has shown that each excavation step of the shiplock resulted in immediate and obvious deformations of the area close to the excavation as shown sufficiently in Chapter 4. Therefore, for analysis results to be comparable directly to field data, the way of modelling the excavation process should approximate the actual construction process as closely as possible. For this reason, a multi-stage excavation scheme was employed in the numerical analysis. Available information of excavation history along the shiplock axis was limited, but excavation stages can generally be taken as horizontal along the shiplock axis. During the construction of the shiplock, the principle of even excavation on the north and south sides was followed, therefore excavations on the section can be considered in horizontal layers. The whole excavation height of about 170m was divided horizontally into 11 steps with 13~ 20m high according to the actual excavation history (Fig5.4). The time corresponding to each excavation step was obtained by interpolating the excavation level history.

Before any excavation occurs in the model, the material properties assigned throughout are those of unexcavated rock. However, as excavation advances, an EDZ develops gradually downwards. The development of this zone is taken into account in the model by changing, after each excavation step, the material properties of the rock at the top 10m from the current excavation level. This depth is in line with the extent of the proposed influencing zone (Sheng et. al., 2000) (Fig6.5 (a)).

During excavation, the groundwater level was controlled well below the excavation level successfully by drainage systems (see section 3.4.1). For this reason, pore pressure is not included in the analysis.
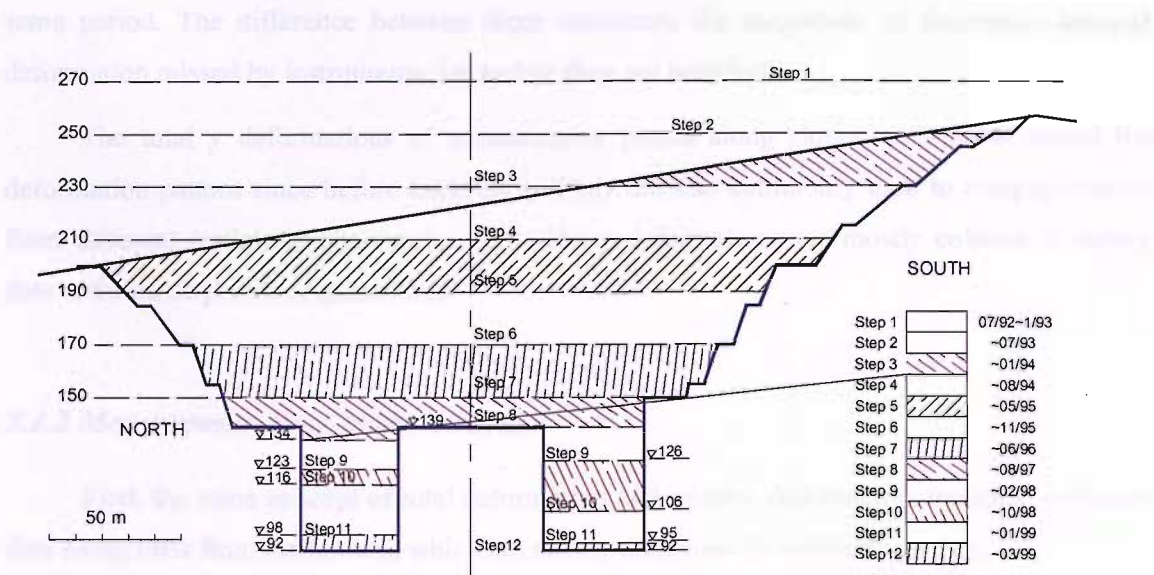
Fig5.4 Multi-stage excavation procedure

5.4 Interpretation of model results

In the following, numerical results will be extracted from the various models at points corresponding to bench level, and along vertical and horizontal lines at various excavation stages. The locations of these lines are shown along with identifications in Fig5.5 and 5.6. Deformations or stresses along these lines will be collated to field data and/or compared with each other in one of the following forms or a combination of some. Surface deformations from the models and survey points are used for model construction and validation and parametric sensitivity study. Subsurface deformations from the models are required in addition for the 2D-3D comparative study with inclinometer data in future sections.

5.4.1 Measurement points in the models

The numerical analysis is able to predict the deformation including the part corresponding to the period before instruments are installed in reality, which is useful to reveal the slope deformation pattern since its beginning.

Taking the y deformation as example, the "total y deformation" refers to the overall excavation-induced deformations throughout the whole excavation period; and the "y deformation" refers to the excavation-induced deformation occurred during the same period as the operation period of instruments (survey points or inclinometer), i.e. relative deformation roughly from when excavation reaches the level of survey point or top of inclinometer. The y deformation is directly comparable to field data since they are measuring the deformation of

same period. The difference between them represents the magnitude of excavation-induced deformation missed by instruments, i.e. before they are installed.

The total y deformations of measurement points along slopes are able to reveal the deformation pattern since before excavation. They are also commonly used to compare results from different models in parametric study. The y deformations are mostly collated to survey data at the same position against time.

5.4.2 Measurement lines in the models

First, the same concept of total deformation and relative deformation applies to extracted data along lines from the models, which are mostly compared to inclinometer data.

Deformations along vertical lines were collated to inclinometer data at the same position where available. In collation, model deformations before installation of corresponding inclinometers were subtracted. For the inclinometers with survey data available, model deformations were compared with inclinometer data in terms of the deformation increment since the installation of the inclinometer (such comparisons are marked as type I in Table5.7). For inclinometers without corresponding survey data, comparisons were made in terms of the deformation increment relative to the bottom of the inclinometer since the installation of inclinometer (such comparisons are marked as type II in Table5.7).

In reality, the top points of the inclinometers were not necessarily identical to the locations of the survey points where the corresponding surface deformations were obtained; therefore some difference between the reported deformations may exist. However, the difference was generally within the accuracy of survey data.

Table5.7 Vertical lines and corresponding inclinometers and survey points

	Slope/ MP	Top Ele (m)	With inclinometer	With survey	Comparison type
Line1	N	200	Yes	Yes	I
Line2	N	185	No	No	
Line3	N	170	Yes	Yes	I
Line4	N	155	No	No	
Line5	N	139	Yes	No	II
Line6	MN	139	Yes	Yes	I

Line7	MN	139	No	No	
Line8	MS	139	No	No	
Line9	MS	139	Yes	Yes	I
Line10	S	150	Yes	No	II
Line11	S	170	Yes	Yes	I
Line12	S	185	No	No	
Line13	S	200	Yes	Yes	I
Line14	S	215	Yes	No	II
Line15	S	230	Yes	Yes	I
Line16	S	245	Yes	Yes	I
Line17	S	250	No	No	

Notes:(i) N: north slope; S: south slope; MN/MS: north/south side of the Middle Pier. (ii) I: comparison with survey and inclinometer; II: comparison with inclinometer only.
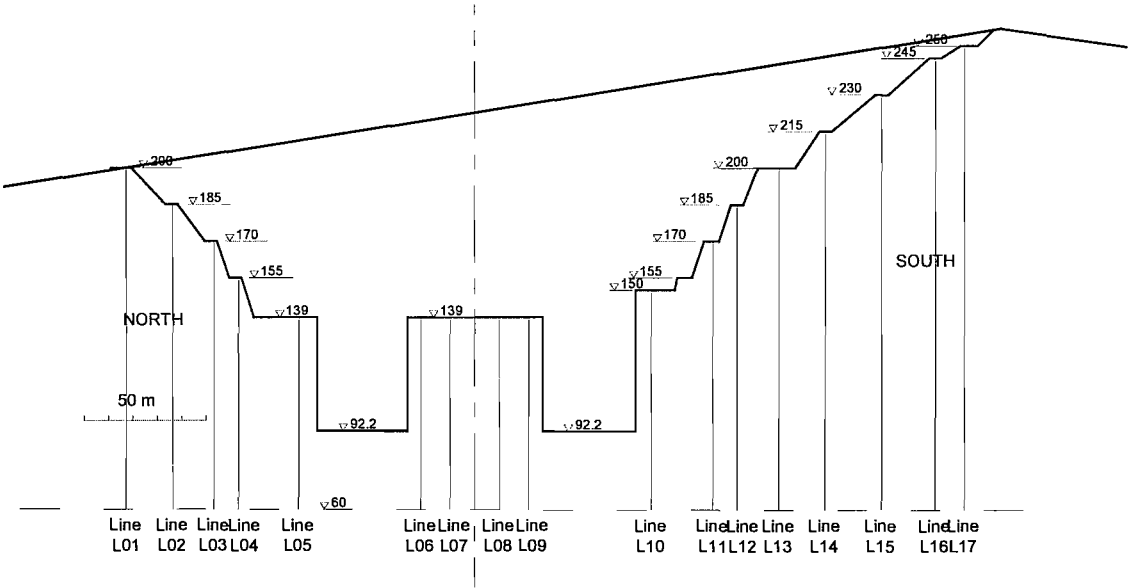
Fig5.5 Vertical lines for excavation and interpretation of model results
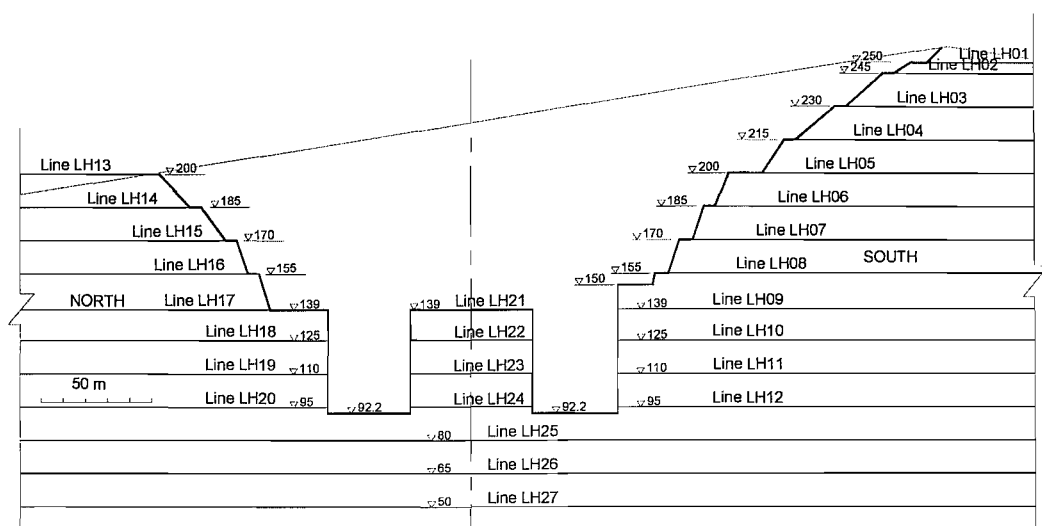
Fig5.6 Horizontal lines for excavation and interpretation of model results

5.5 A first model for Sec#20

The shiplock was constructed in a strip-shape, with similar cross sections along the shiplock axis. Therefore, a simple model representing a slice along the shiplock axis around the section of interest is first attempted. This model will be referred to in the following as the "slice model".

5.5.1 Model geometry and mesh

Taking into account the actual length of the third shiplock (about 110m) and the excavation depth around Sec#20 (about 160m), it was decided that the slice modelled should extend 50m upstream and 50m downstream from Sec#20. The bottom of the model was located at an elevation of -100m, which was 192m below the bottom of the 3rd shiplock (Fig5.7). The in-plane width of the model was 600m (Fig5.8).

The ground surface was approximated using two intersecting planes (Fig5.9). This is a reasonable approximation, as can be seen by the original geological map (Fig5.8). Along the shiplock axis (x axis), the slope of the approximated ground surface was 0.31 (Fig5.10). The excavation geometry and excavation steps along the x axis follow the scheme indicated in Fig5.4.

The material properties used are given in Table5.1 and Table5.2.

The discontinuities introduced in the model included the major and intermediate discontinuities as categorized in section 5.3.2. The rock blocks divided by discontinuities were discretized into finite difference elements/zones by assigning the dimension of the elements.

142

The zone density was greatly limited by model volume and computational efficiency. On the central section, the area surrounding the excavation had the finest zone mesh with average zone length at 4~8m. The zone density decreased away from the excavation, as illustrated in Fig5.11. Similarly along the shiplock axis, the zone density decreased toward both upstream and downstream from the central section.

The discontinuity planes in the model were also discretized into subcontacts, to take into account variations of stress and displacement conditions along the discontinuity plane. Thus variation of conditions along single discontinuities was possibly modelled.
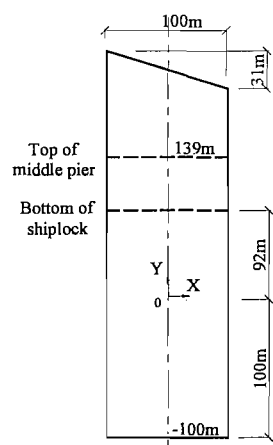
(a) Side view

Fig5.7 Longitudal section of the slice model (elevation)
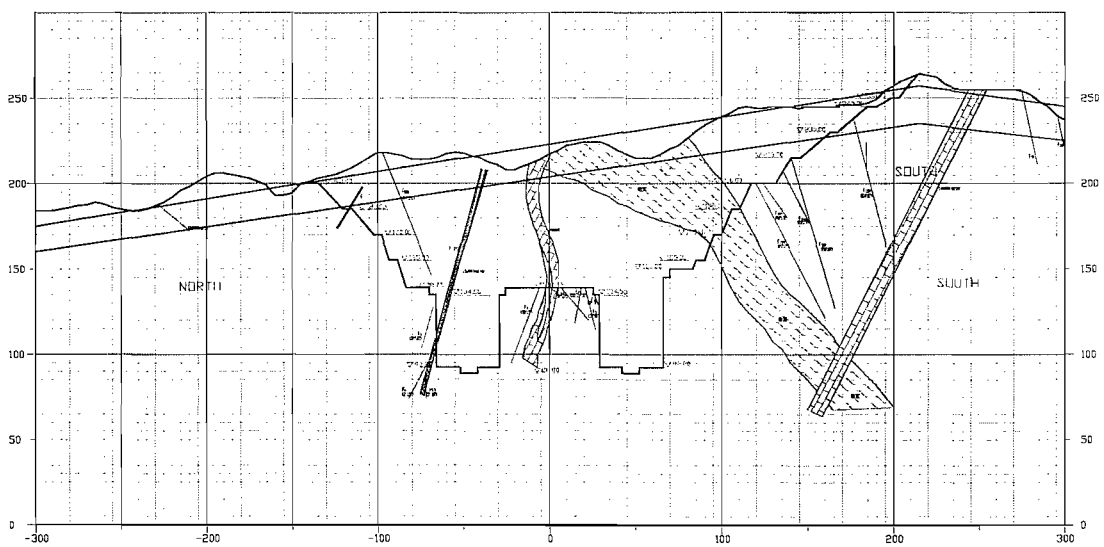
Fig5.8 Model dimension at Sec#20
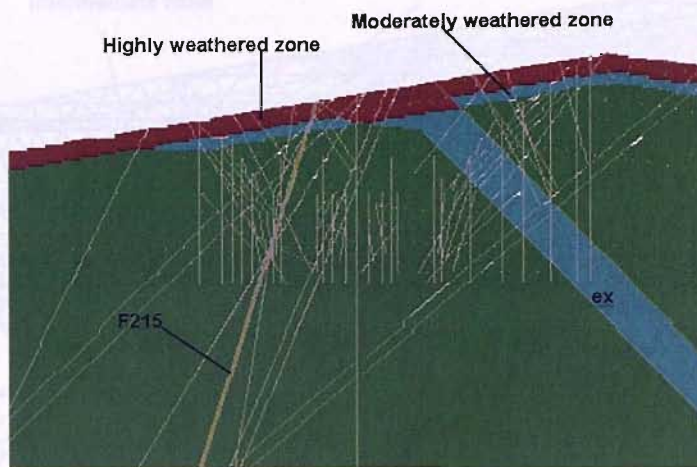
Fig5.9 Central cross-section of the slice model
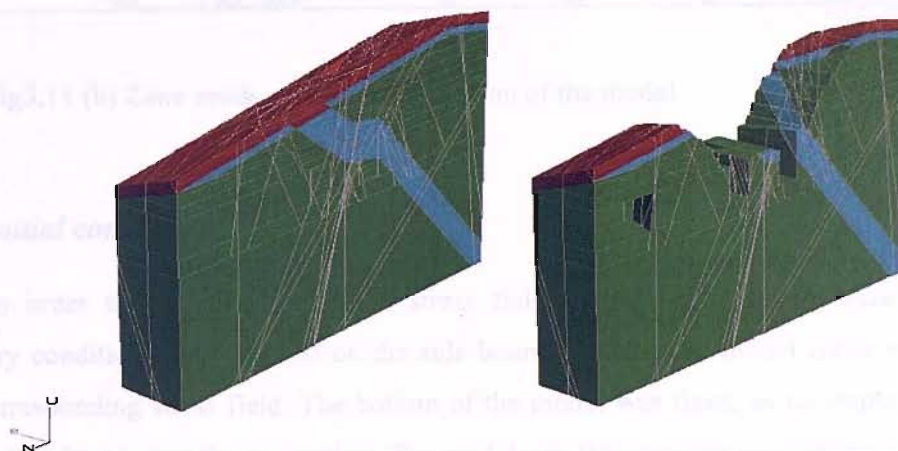
Fig5.10 Perspective view of the slice model before and after excavation
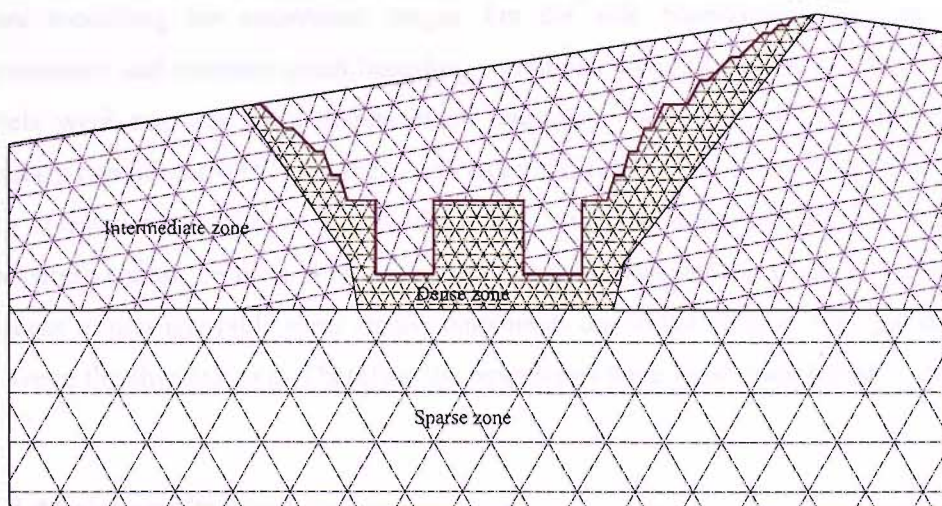
(a) Illustration of zoning strategy

144

(b)
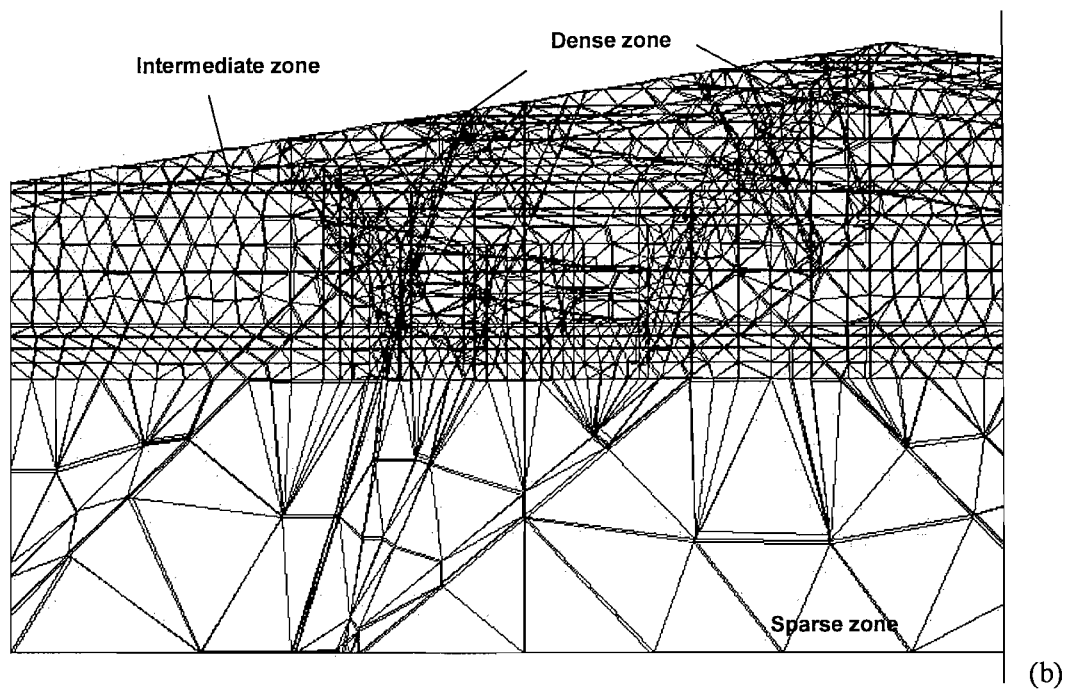
Fig5.11 (b) Zone mesh on the central section of the model

5.5.2 Initial conditions

In order to prescribe the initial stress field in the model before excavation, stress boundary conditions were applied on the side boundaries and the model zones was initialized with corresponding stress field. The bottom of the model was fixed, as no displacements were expected so deep below the excavation. The model was then brought to equilibrium.

After equilibrium was reached, the side boundaries along the y direction were fixed before modelling the excavation stages. On the side boundaries along the x axis, both displacement and constant stress boundary conditions were applied in two separate cases. Two models were run, one with displacement boundary condition (MTS1) and one with stress boundary condition (MTS2) on the x-end faces respectively, to evaluate the effects of different types of boundary conditions. For model MTS1, roller boundary conditions that could not take shear stress cannot be used because in situ stress measurement in Chapter 3 has indicated the existence of non-ignorable shear stress components due to the oblique principal stress directions relative to the shiplock axis. Therefore the boundaries were fixed completely in model MTS1.

5.5.3 Model results

The model MTS1 was run with x-end faces fixed completely and yielded very small deformations compared to field measurements after excavation. This shows that the fixed

145

boundaries were too close to the section and restricted in-plane deformation. Therefore the length of the model along the x axis was insufficient to justify the fixity of the x-end faces.

The model MTS2 was run with constant stress boundaries on the x-end faces during excavation. The prescribed boundary stresses were derived from in situ stress conditions described in section 5.3.3. This model showed excessive deformation along the x axis that was about 1-2 orders of magnitude higher than field data. The possibility that this difference was due to large displacement along discontinuities was ruled out because (a) no major slip was observed in the model; and (b) the same model but without any discontinuities showed similar, unreasonably large deformation along the x axis.

It was considered that the excessive x axis deformation resulted from imbalance of the boundary stresses applied on the x-end faces due to uneven excavation between the upstream and downstream x-end faces. When blocks on the x-end faces were excavated, the boundary stresses applied to these blocks were removed as well and consequently the boundary stresses acting on the model became out of balance along the x-end faces (Fig5.12). As the model was thin along the x axis, this imbalance caused considerable deformations (Fig5.12 (b)). Therefore the length of the model along the shiplock axis was not enough to justify constant stress boundaries.

Furthermore, it is reasonable to assume that the boundary stresses acting on the x-end faces were changing considerably during excavation, particularly for the area close to excavation. Applying constant boundary stress when the boundary is so close to the excavation can then introduce significant errors. But in reality, it is difficult to know how the stress conditions change and consequently impossible to apply such stress changes to the model.

It can be seen from the above that the slice model was not suitable regardless of the type of boundary conditions used and alterations were necessary to be introduced into the model. In particular, a greater extent of the shiplock along the x-axis should be modelled.

(a) Before excavation   (b) Imbalance of boundary
                                stresses between two sides
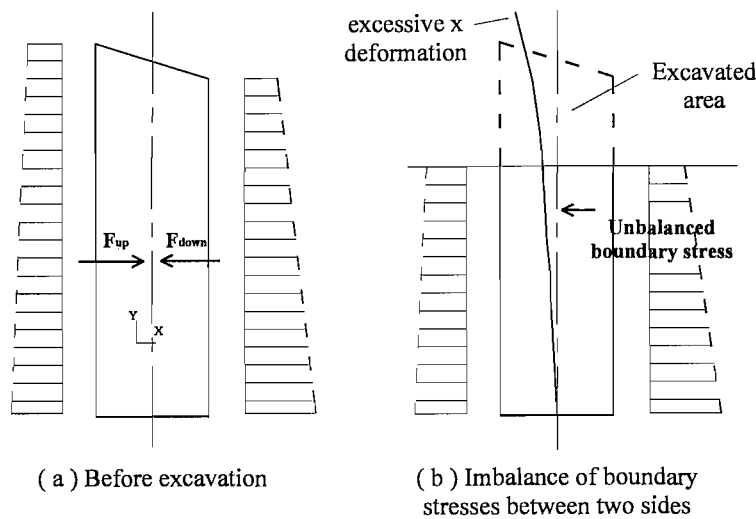
Fig5.12 Excessive x deformations due to imbalance of boundary stresses (model shown in elevation)

5.6 A refined model for Sec#20

The results of section 5.5 conclude that a larger part of the shiplock along the x axis needs to be modelled. The extent of the boundaries needs to be decided.

Generally when the model boundaries are far enough from the excavation, two assumptions may be justified: (a) the induced displacement at the boundaries by the excavation is negligible so that fixed displacement boundary can be used; or (b) the induced stress at the boundaries by excavation is negligible so that constant stress boundary can be used.

Without knowing the far-field stress conditions at boundaries, the displacement boundary was used during excavation. The principle for determination of model boundary is that the induced stress caused by excavation should not be significant. Theoretically, for a 2D cavity of radius "a" in a hydrostatic stress field, the induced stress at a distance of 2a is about 5% of the hydrostatic stress level and 1% at a distance of 3.7a. The decay of induced stress away from excavations of different shape is expected to be more rapid than for a circular hole (Itasca, 1998). Obviously the real shape of excavation is one of the major factors influencing the decay.

At what distance the excavation induced stress concentration becomes negligible is largely case-dependent. In theory, the model boundary should be set at a distance from the excavation, such that further increase of this distance has no effect on the predicted deformations. This can be achieved by either extending the model boundary far enough or limiting the extent of excavation, or both of them, which essentially decrease the dimension of

excavation relative to the whole model. It is common to extend the model boundaries in practice.

However for the shiplock, when the x boundaries are extended, further problem arises in how much details of excavation and topography along the x axis should be modelled. It is obviously unnecessary to model the whole actual excavation as when excavation occurred far away has limited effect on the section of interest. However, the extent of excavation should be adequate to simulate the effects of excavation on the section. In the case of the shiplock, the model has to simulate the actual shape of excavation within a certain distance from the section of interest, while the excavation outside could be ignored partly in a gradual way. Meanwhile excavation stages in the cross section planes of the shiplock should be modelled as accurately as possible. It is a very similar scenario for topography to model the approximated general topography within the area close to the excavation and extend horizontally outside.

5.6.1 Extension along the shiplock axis

In terms of modelling the Sec#20, it was impractical and unnecessary to model the whole shiplock, which stretched over 1600m. In order to make a displacement boundary condition applicable on x-end faces, the slice model was extended 500m upstream and 500m downstream along the shiplock axis (Fig5.13, model ML1), which was generally over three times of the excavation depth on both sides.

According to the above discussion on model extent, the excavation scheme as shown in Fig5.13 was introduced. The central part of the model followed the actual excavation shape and topography, while the excavation volume reduced gradually and the topography was simplified outside the central area.

Considering the long-strip shape the shiplock, the section of interest was much less sensitive to the model extent along the shiplock axis direction, i.e. the induced stress decayed faster in this direction. For an average excavation depth of around 170m on the section of interest (Sec#20), the 200m length of central excavation and gradually changed excavation outside (Fig5.13) was assumed enough to account for the effects that excavation shape along the shiplock would have on the deformation of the section in reality.

On the other hand, such excavation arrangement gave a boundary distance (500m) of about twice of the average excavation radius (estimated as 250m in the vertical longitudal plane), which was expected to yield less induced stress at that distance than the 5% expected from a cavity in a hydrostatic stress field.

Stress boundary conditions were used to build up the initial stress condition before excavation in the model.

The area of excavation was extended obliquely outside the central 200m, with a slope 1:2 (26.5? (Fig5.13). This served to avoid creating vertical or steep slopes that may result in unrealistic instability in the model. Each excavation stage had the depth shown in Fig3.5 but extended horizontally throughout the whole excavation volume (Fig5.13) along the shiplock axis. Not excavating any part of the boundaries also avoided the concern of imbalance the applied boundary forces similar to the case of model MTS2 (Fig5.12).

The major and intermediate discontinuities modelled run through the whole length of the extended model while minor discontinuities were limited within the central 200m along the shiplock axis. The weathered zones were extended horizontally along the shiplock axis outside the central zone. The in situ stress field in the central 200m along the shiplock axis followed the stress field described in section 5.3.3. Outside this 200m zone, the gradients of stress components along the shiplock were set to zero.
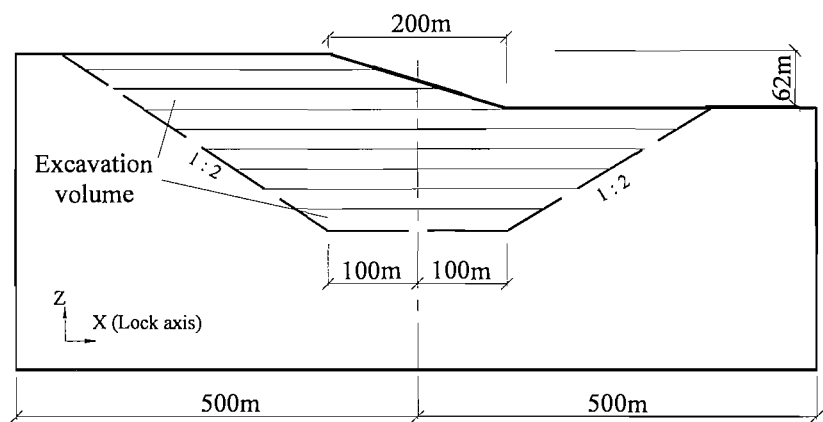
Fig5.13 Model extension along the x axis (model ML1)
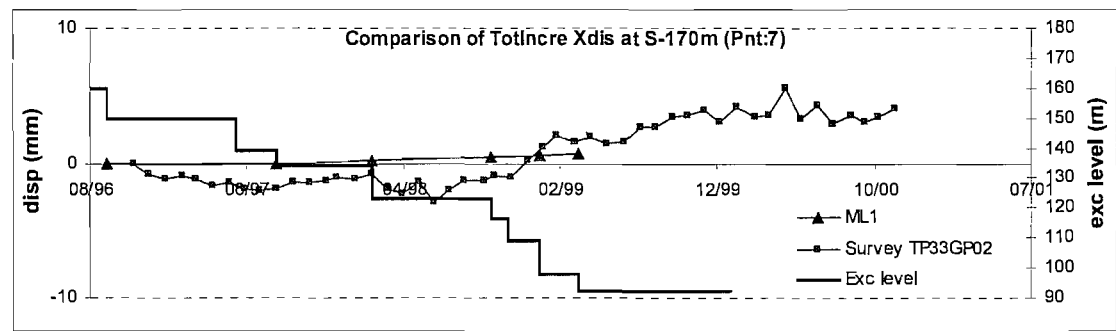
Fig5.14 X deformation at S-230m and S-170m in ML1 and field data

Results from the above model (ML1) show that it predicted more reasonable deformations along the x axis than the slice model did. Fig5.14 compares model predictions

with field data from the corresponding survey point. It can be seen that they are of the same order of magnitude.

5.6.2 Effect of model topography and excavation geometry

Although of the same order of magnitude, the results of model ML1 still showed noticeable difference of deformation from the field data.

The difference of topography and excavation geometry in the model from reality could be partly responsible for deformation discrepancies in terms of both deformation-time profile and magnitude, as discussed in section 5.3.4. The topography and excavation steps on the central section plane had been modelled reasonably close to the geological map. But little consideration was given to the topography outside the central section along the x axis.

(a) Model ML1 with boundary extensions

(b) Model ML2 with refined upstream topography

(c) Model ML3 with refined excavation geometry
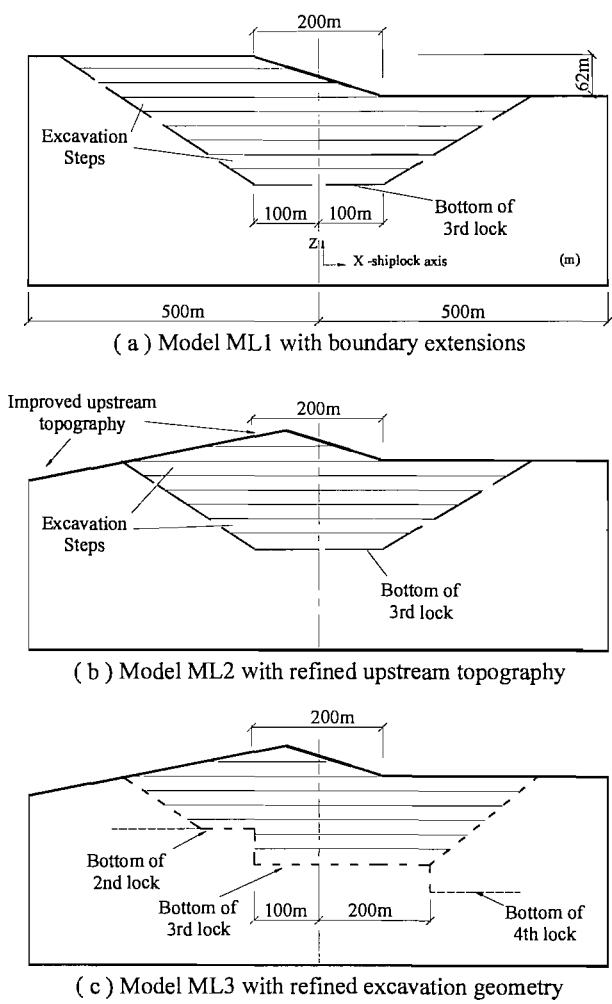
Fig5.15 Models with refined topography and excavation geometry along the shiplock axis (long section)

Using available information outside the central area along the shiplock axis, the topography and excavation geometry in the model were further refined as shown in Fig5.15. Compared to model ML1, ML2 approximates better the regional topography along the shiplock. Model ML3 goes one step further, approximating the excavation shape along the axis in a more realistic manner. The difference that modelling such details can make is shown by comparing the total x deformations of the three models in Fig5.16 and Fig5.17.

In general, most of points on the section moved upstream in the early stages of excavation and backward later as indicated in Fig5.16 and 5.17 because more volume was excavated upstream during the early stages than downstream, while at later stages the opposite was true (Fig5.15).
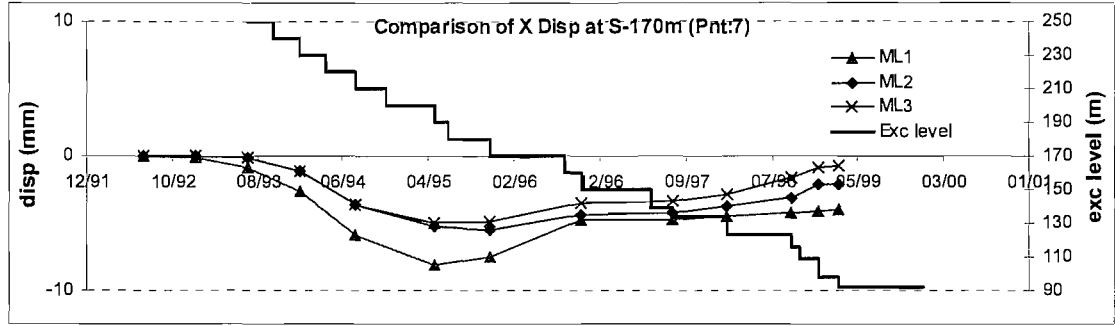
Fig5.16 Total x deformation at point N-170m in models
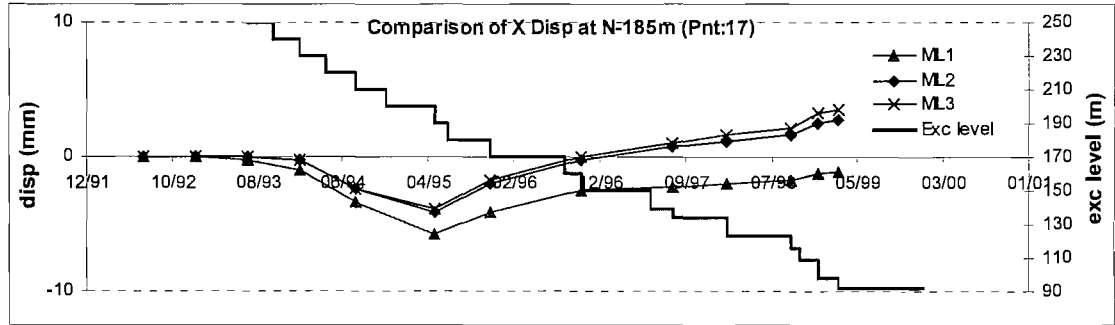
Fig5.17 Total x deformation at point S-185m in models

Compared with ML2 in which excavation geometry upstream was reduced, ML1 showed larger upstream deformation, particularly during the early stages when excavation steps were affected by reduced topography. Meanwhile ML3 showed larger downstream deformations as the ratio of downstream excavation volume vs upstream excavation volume increased.

The results of the original model ML1 and the two refined models (ML2 and ML3) are compared to field data in the following.

1. X deformation

The models with refined topography and excavation geometry showed improved x deformation as shown in Fig5.18 and 5.19. They are of the right order of magnitude and have the correct trend.
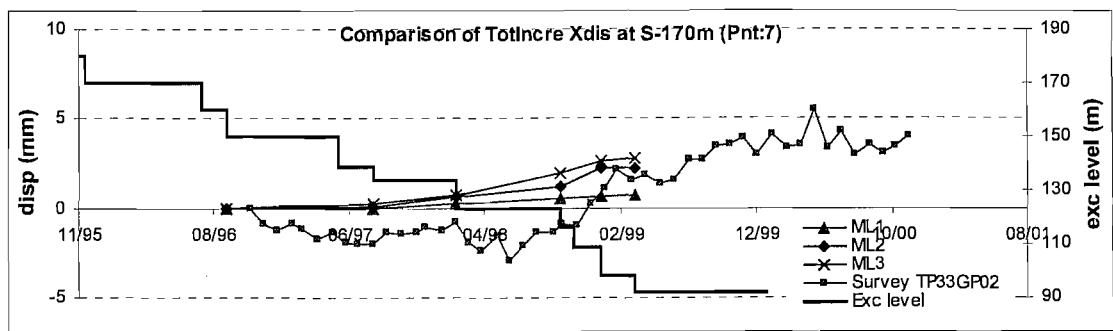
Fig5.18 Comparison of X deformation at point S-170m in models and field data
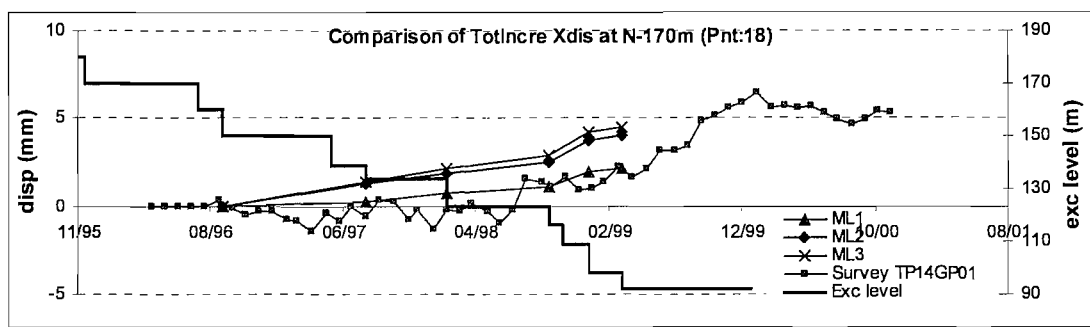
Fig5.19 Comparison of X deformation at point N-170m in models and field data

2. In-plane deformations

Compared with ML1, the models ML2 and ML3 showed improved y deformation (vertical) (Fig5.20 and Fig5.21), mostly on the south slope. The deformations changed little on the north because the improvement of the topography affected little the north slope as shown in Fig5.22. All three models showed similar deformations in the z direction, with low magnitudes as shown in Fig5.23 and 5.24.

There was very little difference between the results of ML2 and ML3 in spite that excavation volumes upstream and downstream changed. This generally indicates that changing the excavation geometry along the x axis had no particular influence on in-plane deformations on the central section.

As ML3 modelled the shiplock more closely, its configuration was chosen as a basis for future models.
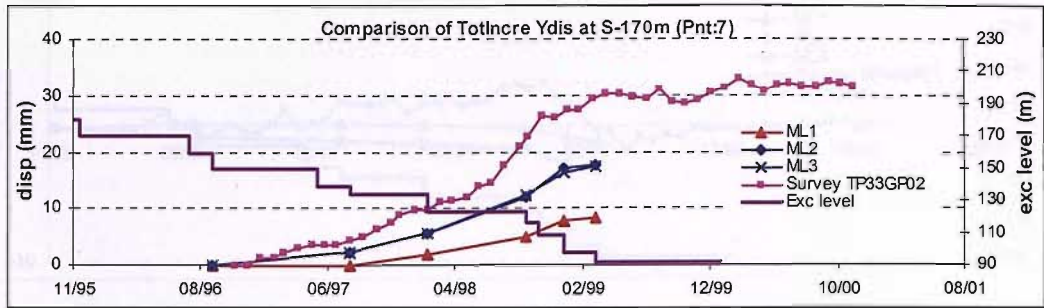
Fig5.20 Y deformation at point N-170m in models and field data
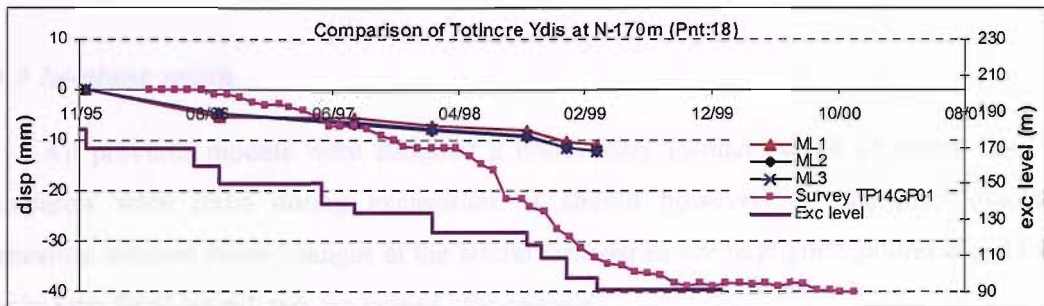
Fig5.21 Y deformation at point N-170m in models and field data
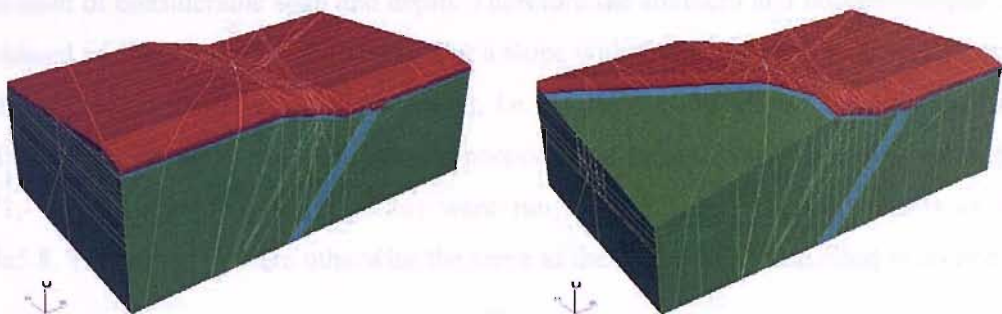
Fig5.22 Change of topography
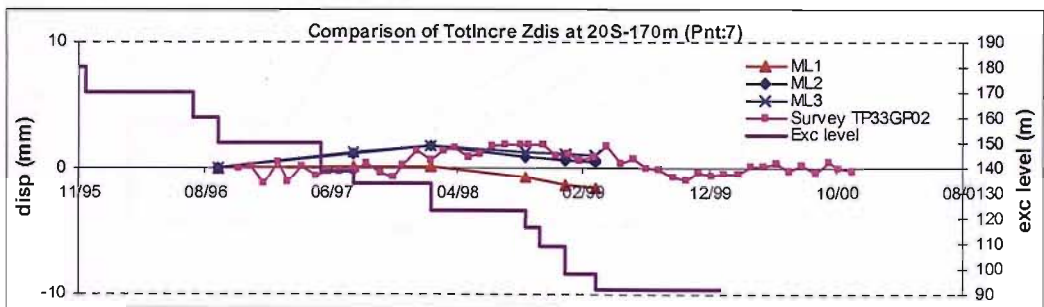
Fig5.23 Z deformation at point N-170m in models and field data
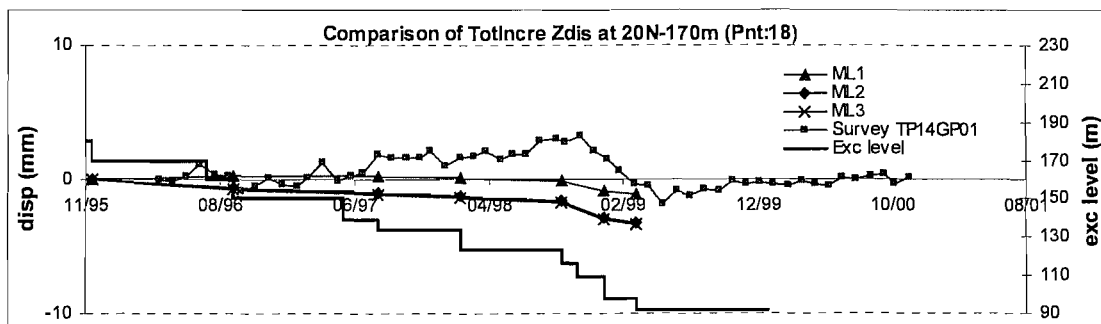
Fig5.24 Z deformation at point N-170m in models and field data

5.6.3 In-plane width

All previous models were assigned a preliminary in-plane width of 600m. The lateral boundaries were fixed during excavation. It should however be examined whether the excavation induced stress changes at the lateral boundaries are negligible as they should be, i.e. whether the fixed boundaries are indeed "far enough".

In the TGP shiplock, the southern and northern slopes were separated by a significant excavation of considerable span and depth. Therefore the southern and northern slopes could be considered as single slopes respectively. For a slope with fixed slope angle, the necessary model width can be defined in terms of the height, i.e. the ratio of model width to excavation height W/H (Fig5.25). In order to investigate the necessary boundary distance, a set of three models - MW1, MW2 and MW3 (see Fig5.26) were run with different in-plane widths as listed in Table5.8. These models were otherwise the same as the model ML3 described in section 5.6.2.
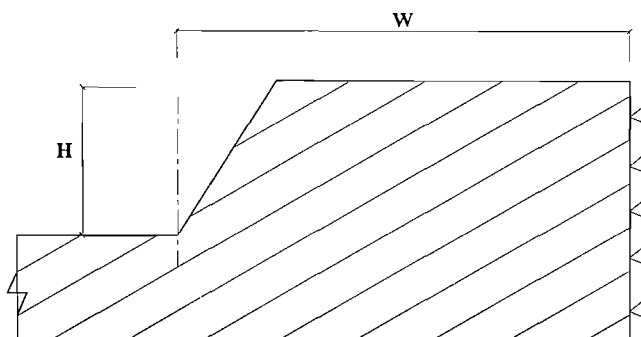
Fig5.25 Model width and excavation height

154

Table5.8 In-plane width and ratio of W/H of models

	North	$(H_1 \approx 110m)$	South	$(H_2 \approx 165m)$
Model	Width	W/ H_1	Width	W/ H_2
MW1	300m	2.7	300m	1.8
MW2	500m	4.5	500m	3.0
MW3	500m	4.5	800m	4.8

(a) Model MW1 (N300m + S300m)

(b) Model MW2 (N500m + S500m)

(c) Model MW3 (N500m + S800m)
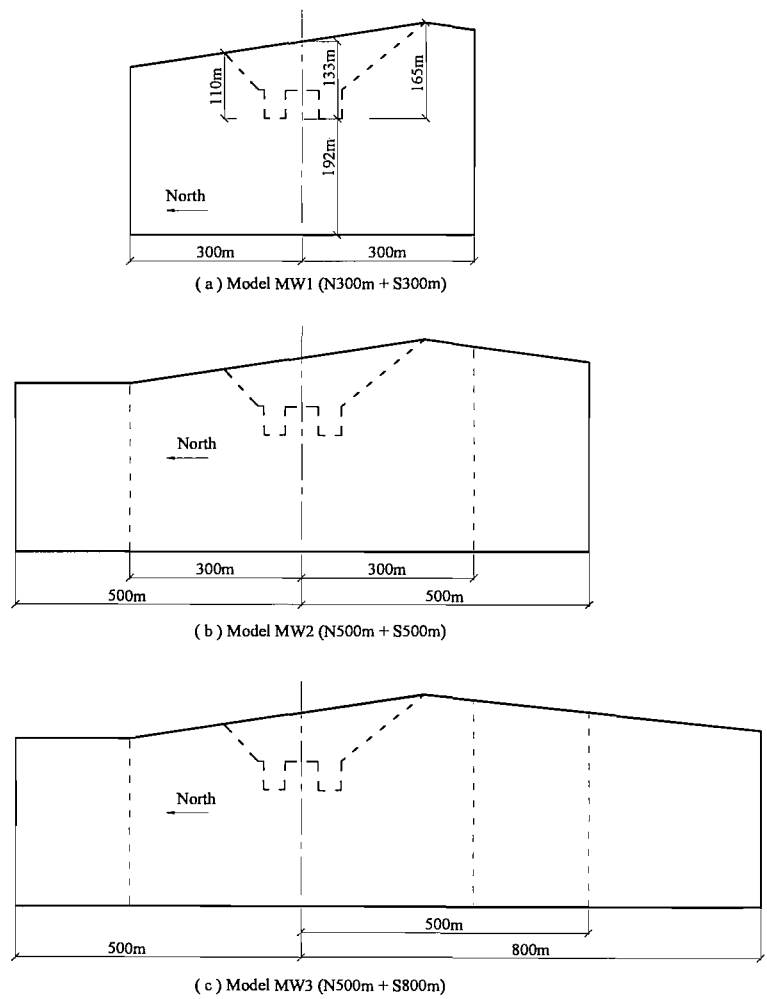
Fig5.26 The geometry of cross sections of the three models MW1, MW2 and MW3 with different width

Results of model MW1 indicated that its boundaries were not far enough as the induced stresses (stress release) at the boundary position was considerable - up to 30% of the in situ stress at the southern boundary (Fig5.27). The significant difference of deformations between

155

MW1 and MW2 (Fig5.28) also indicated that the in-plane boundaries in MW1 were not far enough.

It was noted that large variations existed at the top 20m~30m of all curves when compared with the relatively smooth curves below. This could be because a different initial stress field (gravitational field) was assigned in the highly weathered zone, which is about 22m deep from the ground surface. However the lower part of the curves presented a clear general trend, which provided enough information to assess the stress changes.
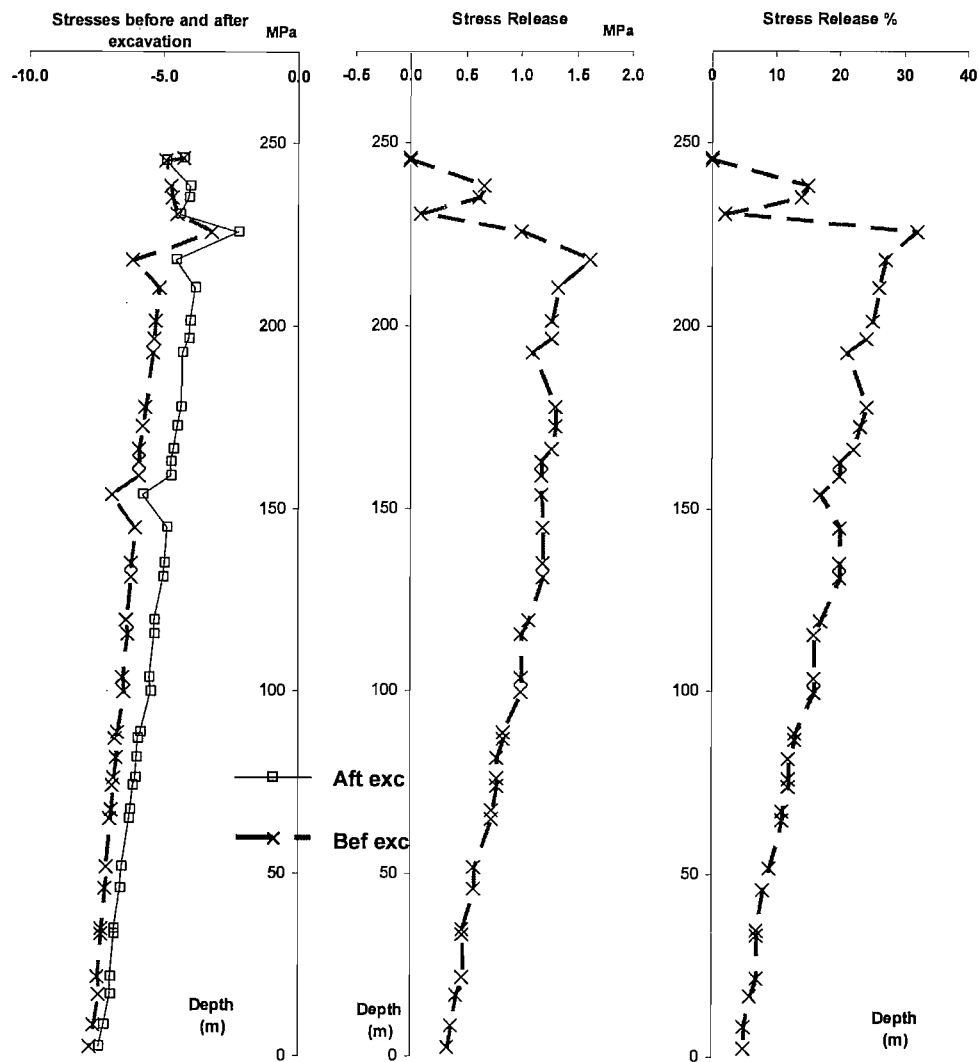
Fig5.27 Stress change (Syy) at the southern vertical boundary of model MW1
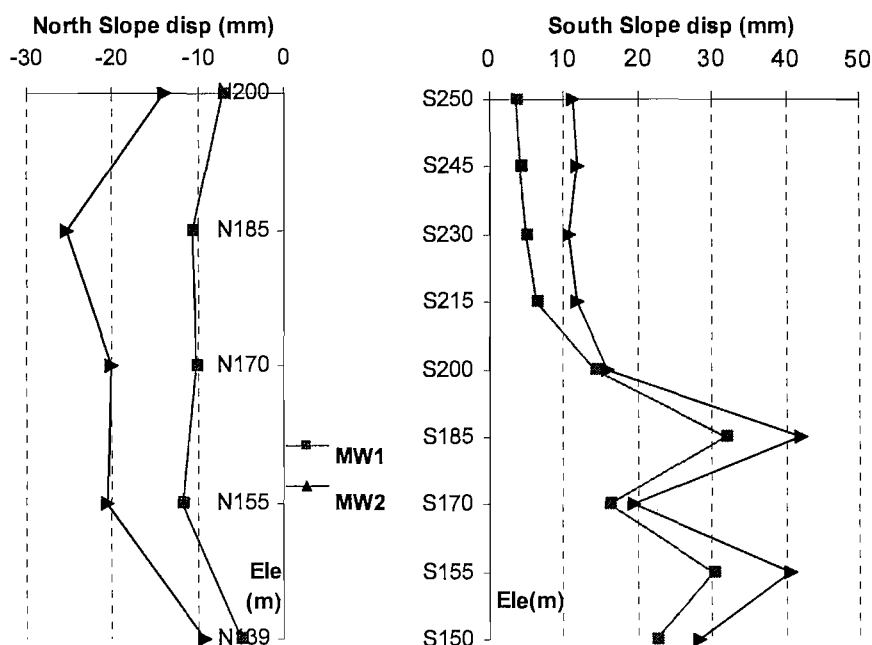
Fig5.28 Comparison of Y deformation along height of the north and south slopes for models MW1 and MW2 with different in-plane width

The stress conditions on the southern boundaries of model MW2 and MW3 are shown in Fig5.29. In both models, the induced stresses at the southern boundaries were below 10% of the original stress in the unweathered zones.

The stress conditions on the northern boundaries in MW2 and MW3 were identical since they had the same W/H ratio of 4.5 on the north side. The stress release was about 10% below the highly weathered zone as shown in Fig5.30, which is generally acceptable.

Field test of in situ stress suggested that the standard deviations of the stress components measured could range from 0.018MPa to 0.746MPa (Liu et. al., 1992). The stress releases of MW2 and MW3 (Fig5.29 and 5.30) were well within the average standard deviation of stress measurements.

Following the principle of determining boundary distance discussed in section 5.6, the difference of deformation caused by different width in model MW2 and MW3 was minimal (Fig5.31). Therefore the smaller model MW2 was considered sufficient. Furthermore it was more computationally efficient.

157
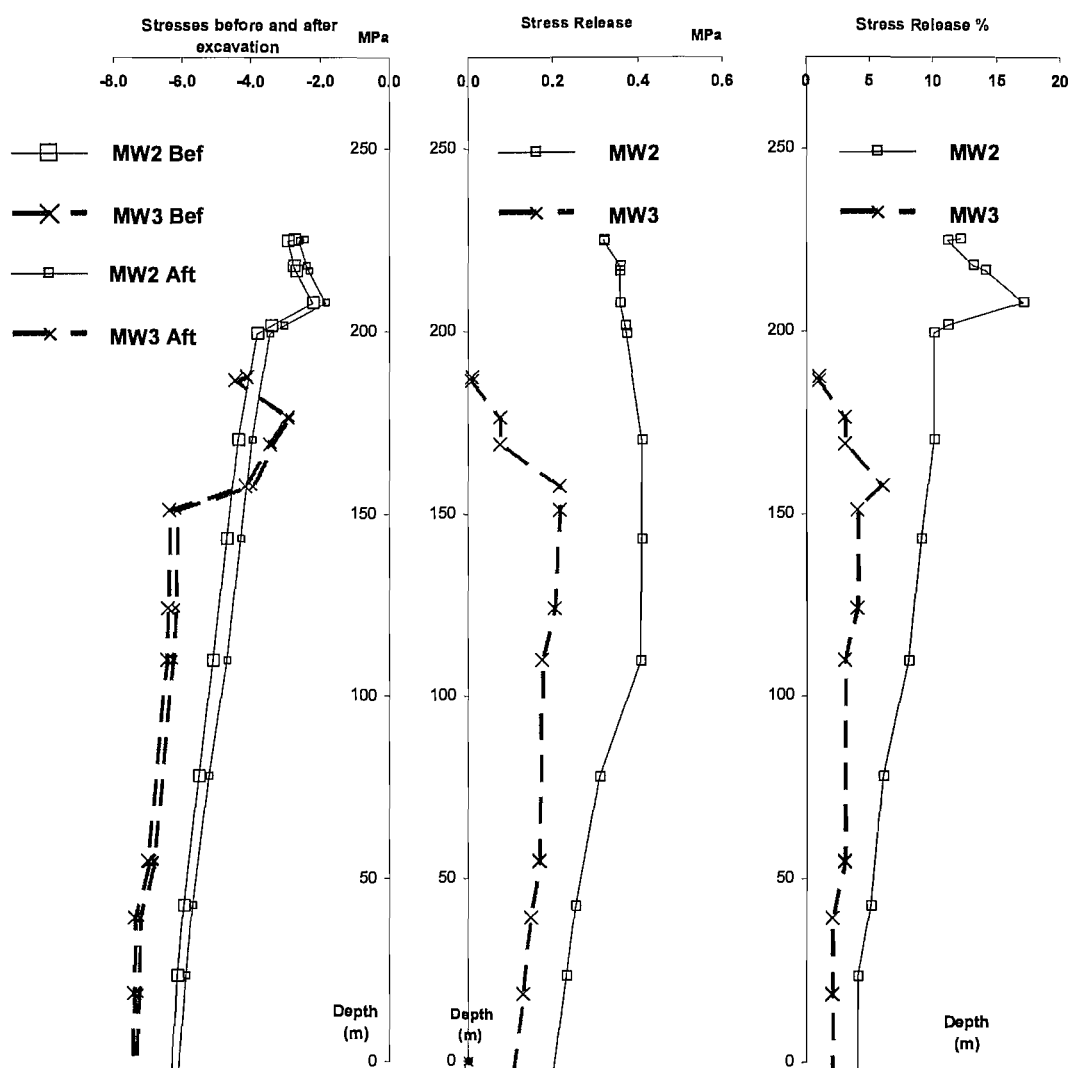
Fig5.29 Stress conditions at southern boundaries of model MW2 and MW3
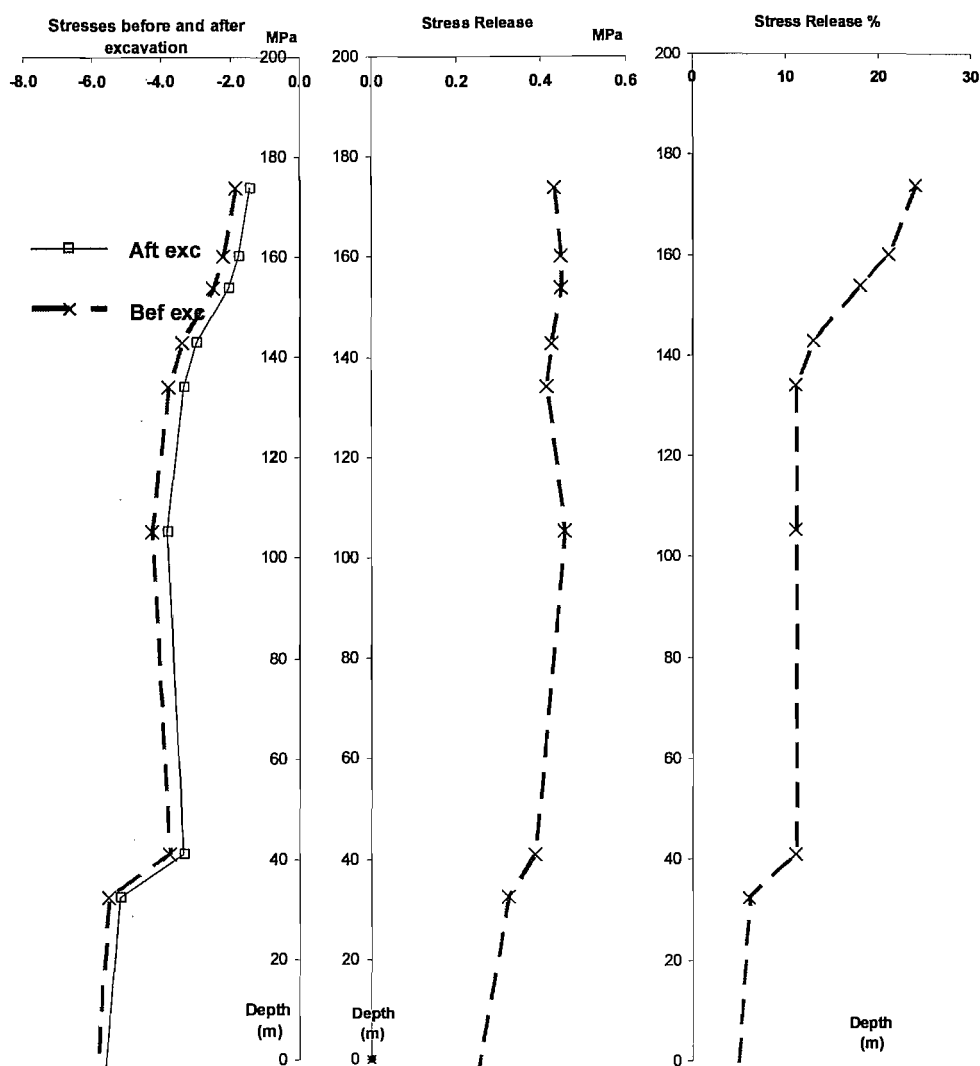
Fig5.30 Stress change (Syy) at the northern boundary of model MW2 or MW3
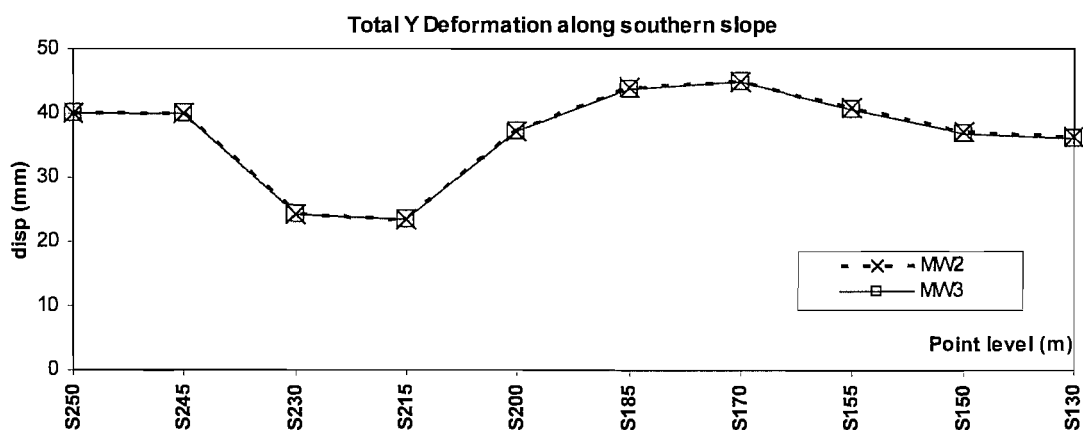
Fig5.31 Total Y deformations along south slope of MW2 and MW3, at different points

159

(a) Excavated volume

(b) Model after excavation
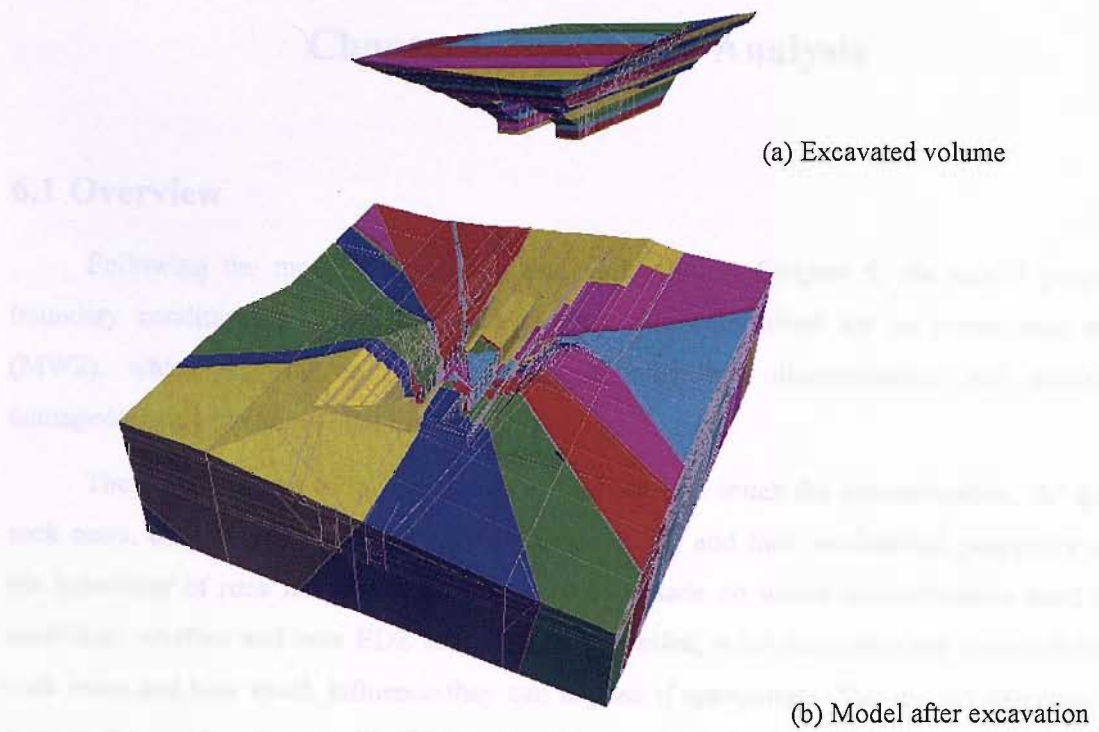
Fig5.32 Ariel view of excavated volume (a) and model ML2 after excavation (b)

Chapter 6 Numerical Analysis

6.1 Overview

Following the model construction and validation in Chapter 5, the model geometry, boundary conditions and initial stress conditions are determined for an initial base model (MW2), which will be used for exercise of modelling discontinuities and excavation damaged/disturbed zones (EDZ).

The first objective of this chapter is to find out how much the discontinuities, the quality rock mass, excavation damaged/disturbed zones (EDZ) and their mechanical properties affect the behaviour of rock mass. Conclusions are to be made on which discontinuities need to be modelled; whether and how EDZ should to be modelled; what properties are sensitive for the rock mass and how much influence they can impose if appropriate. The second objective is to answer the question how well a 2D analysis can simulate the 3D effects by comparing to 3D modelling.

This chapter is presented in three parts:

(a) The first part presents the modelling of discontinuities (section 6.2), which investigates how different category of discontinuities affect the rock deformation and which ones need to be modelled explicitly; and the modelling of EDZ (section 6.3), which illustrates the importance of taking in account of EDZ

(b) The second part presents results of a parametric study of the properties of discontinuities (section 6.4); and a parametric study of the equivalent continuum properties used to model the rock mass (section 6.5)

(c) The last part presents a comparative study of the suitability of 2D modelling compared with 3D modelling (section 6.6).

6.2 Modelling discontinuities

Discontinuities in excavations in rock mass include the pre-existing discontinuities and excavation-induced discontinuities or cracks. The excavation-induced discontinuities are normally closely related to the excavations in terms of both location and time sequence. They are difficult to be modelled explicitly because they are random in pattern, large in number and small in scale normally. It is more appropriate to take them into account by EDZ, which will be discussed in future sections. The term "discontinuity" refers to pre-existing ones unless stated otherwise.

In order to identify the discontinuities that need to be modelled individually, a study was carried out to investigate the effects of different kinds of discontinuities on the deformations predicted by the model.

As discussed in section 5.3.2, the discontinuities were classified into three groups: major, intermediate and minor ones. The major and intermediate discontinuities were identifiable on geological maps, so it was possible to model them individually. Most of the minor discontinuities were not possible to identify, with the exception of those exposed and recorded after excavation. Therefore, two separate numerical studies were carried out: one for major and intermediate discontinuities; and one for minor discontinuities.

Considering most of rock materials are fresh or slightly weathered granite in the model, elastic models are used for the rock blocks in the models for simplicity and computational efficiency. This should not affect the sensitivity of the models to discontinuities.

6.2.1 Major and intermediate discontinuities

In order to investigate the necessity of modelling the major and intermediate discontinuities, three models were run with different discontinuity configurations: (a) no discontinuities; (b) with only major discontinuities included and (c) with both major and intermediate discontinuities included.

The y deformations (horizontal in-plane deformation) predicted by these three models are compared in Fig6.1. They are also compared with field data in Fig6.2 and Fig6.3.

In following context, the measurement points along slopes and walls of the Middle Pier will be referred to by its position id (N/S for the north/south slope; MN/MS for the north/south vertical wall of the Middle Pier) followed by its elevation, e.g. N170 or N-170m for the point at 170m elevation on the north slope.
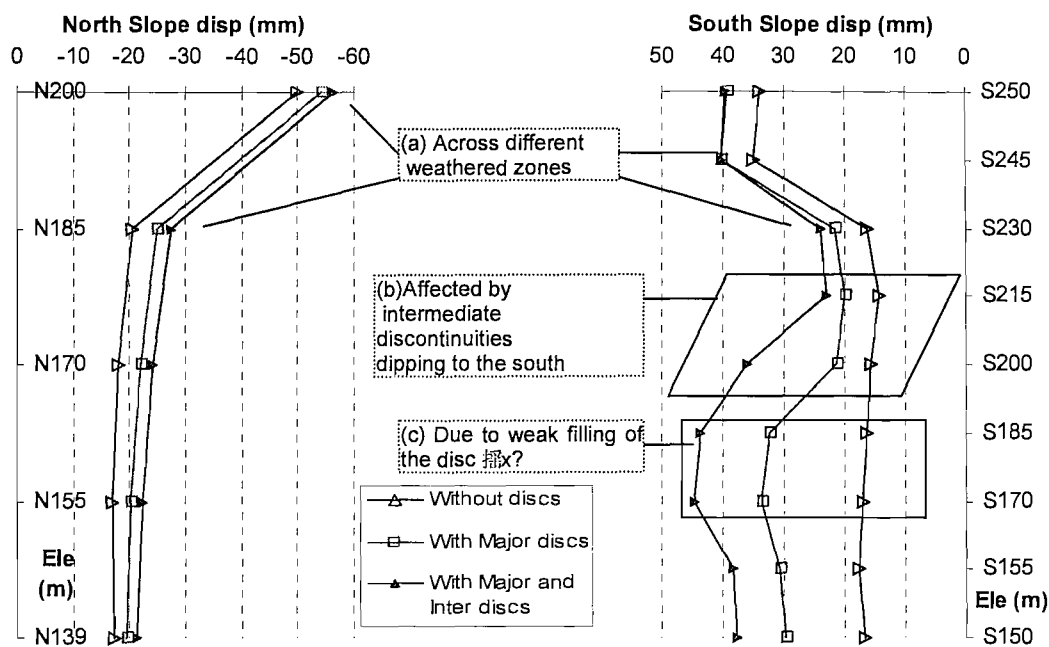
Fig6.1 Comparison of total Y deformations along height of slopes predicted by models with different discontinuity configurations
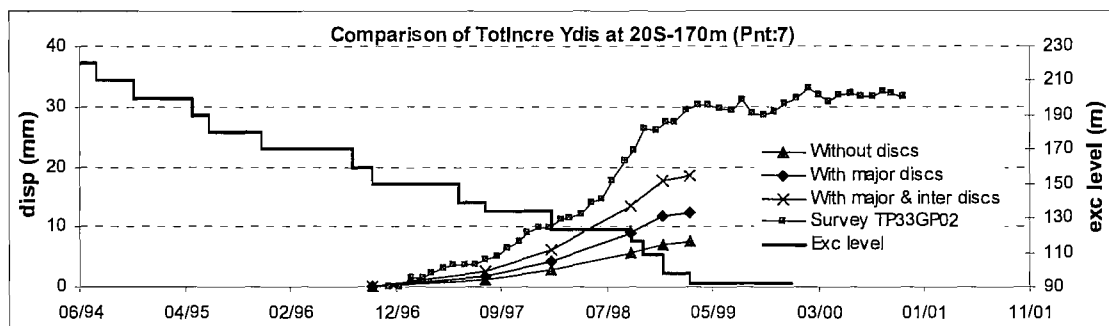
Fig6.2 Y deformation vs time at point 7 (S-170m)
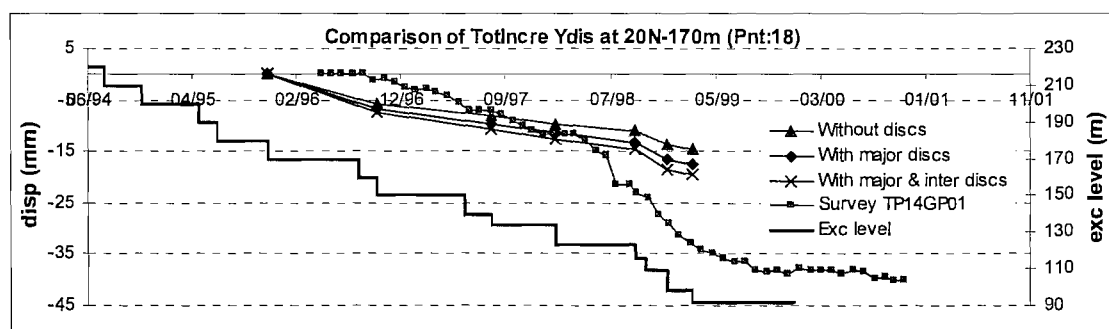
Fig6.3 Y deformation vs time at point 18 (N-170m)

163

The presence of major and intermediate discontinuities has a significant contribution to the predicted deformation (Fig6.1). One obvious example can be seen at S170 (for point at elevation 170m on the south slope) on the south slope. The initial deformation of S170 (18mm) was almost doubled (32mm) when major discontinuities were included in the model, and increased further (45mm) when the intermediate discontinuities were further considered.

The effect of major discontinuities is clearly illustrated in Fig6.1 (c), where a localized large increase of deformations was caused around elevations of 170m and 185m by the major discontinuity xenolith ex. The deformation increase outside this elevation range was related to the other major discontinuities, for example βu1005 on the south slope that is below most of the south slope.

A number of intermediate discontinuities on the south slope resulted in an even increase of deformation for elevation below 215m (Fig6.1 (b)). It is also noted that the part of the slope above 215m did not show the same deformation increase caused by the inclusion of intermediate discontinuities, as the part below215m did. This could be the result of: a) most of the intermediate discontinuities were dipping into the slope (to the south) as shown in Fig4.61, i.e. the upper part above the intermediate discontinuities tended to "slip" into the slope along the general orientation of the intermediate discontinuities; and b) there was fewer discontinuities above 215m elevation on the south slope to develop deformation.

The deformation profiles of the north slope predicted by the three models were similar. These profiles show that the north slope probably translated due to deformations occurring along discontinuities located below 139m elevation, e.g. F215, f3, f4 (Fig3.9).

It is also shown that model results compare better to field data when both major and intermediate discontinuities are taken into account (Fig6.2). The model reproduces the observed deformation mechanism and gives deformation of the correct order of magnitude. However, it is noted that all models underestimated deformations compared with field data. The reasons could be that elastic properties were used for rock blocks in the model and EDZ was not modelled.

From above we conclude that it is important to model the major and intermediate discontinuities explicitly. The effects of modelling these discontinuities also depends on their dipping directions relative to the excavation.

From the comparison of models with and without discontinuities presented in from Fig6.1 to Fig6.3, it can be seen that the proportion of the total deformation that takes place along the discontinuities is comparable to the proportion that is due to rock block strain.

6.2.2 Minor discontinuities

As discussed in section 5.3.2, the fissures or minor faults were difficult to model explicitly because little information was available. Alternatively, the assumed mechanical properties of the rock mass were reduced in order to account for the existence of these discontinuities. The rock block parameters are shown in Table5.2. It is not unusual in practice that these fissures or minor faults are generalised into a few joint sets statistically. Although it is possible to incorporate such generalised joint sets in distinct element models, the approach is not computationally efficient as it can result to prohibitive number of rock blocks and discontinuities. This is especially true for large scale, three-dimensional models.

During excavation, a large number of fissures were subject to opening or shearing and many new fissures or cracks developed in the area surrounding the excavation due to unloading (Shen & Barton, 1997). Such alterations would have important effects on the model behaviour. Limited information on those fissures was available from site investigation carried out after these were exposed by excavations, as compiled and generalised in Table5.4 for the TGP.

It is also important to note that these fissure sets were under the restraints of anchorage during the construction of the TGP shiplock. Unless the effect of anchorage is also considered in the model, taking into account the fissure sets would result in significant overestimation of deformations and possibly in unrealistic failure mechanisms. An example is shown in Fig6.4, which presents results from the model with both major and intermediate discontinuities presented in section 6.2.1, in which the sets of minor fissures were included. This lead to an over-prediction of deformation of the Middle Pier by an order of magnitude.

Therefore the modelling solution adopted for minor discontinuities was to reduce the equivalent continuum properties of rock mass instead of modelling minor fissures explicitly. The properties listed in Table5.2 can be considered as having included this level of discontinuity structures in the shiplock site during site investigation (Zhang & Zhou, 1999). Therefore no further consideration is needed for them.
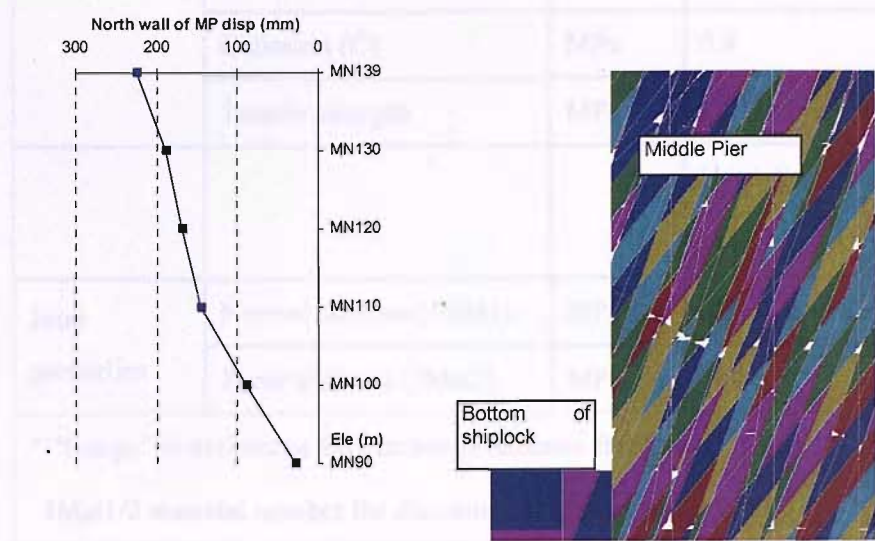
Fig6.4 Excessive deformation on the north side of MP with fissures

6.3 Modelling EDZ

Although the existence of an excavation damaged/disturbed zone (EDZ) around excavation in rock is generally recognized and there have been conferences dedicated to this subject (McEwen, 2003; NEA, 1989 and CNS, 1996 and 2002), it is very difficult to determine its extent and properties by a commonly available procedure.

EDZ can be generally divided into damaged and disturbed subzones according to the damaging extent. Field tests and numerical analyses of the EDZ of the shiplock in TGP also suggest this (Sheng et. al., 2002). The extent and properties of these subzones from field test are detailed in Table6.1. It is shown that the rock mass in the damaged zone was weakened by about 45% and 23% in the affected zone and the properties of discontinuities in the EDZ range were also reduced accordingly with discontinuity stiffness being reduced to 75% of its original values.

Table6.1 Rock and discontinuity properties for different EDZ subzones (Sheng et. al., 2002)

	Property		Damaged zone	Affected zone
	Range*	(m)	5~10	15~20
Block	Elastic modulus (E)	GPa	12	24

properties	Poisson's ratio (v)		0.25	0.23
	Friction (f)	°	45	53
	Cohesion (C)	MPa	0.9	1.4
	Tensile strength	MPa	0.8	1.2
			Hard disc. JMat1	Soft disc. JMat2
Joint properties	Normal stiffness(JMat1)	MPa	520	224
	Shear stiffness (JMat1)	MPa	190	77

* "Range" is defined as the horizontal distance from the slope surface.

JMat1/2 material number for discontinuities, see Table5.1

In order to investigate the effect caused by EDZ, a comparative study was carried out between two models without and with EDZ included, as referred to by ME1 and ME2 respectively. Both models were based on the base model MW2 in chapter 5, which included major and intermediate discontinuities. The only difference between the two models is ME2 modelled the EDZ using lower mechanical properties presented above while ME1 did not. Mohr-Coulomb model was assigned to rock blocks in both models. Because the EDZ is considerably weakened and is subject to significant stress release, Mohr-Coulomb model is considered more appropriate for models with such rock blocks.

The EDZ subzones modelled in ME2 are shown in Fig6.5 (a) following Sheng et. al. (2002). The model ME1 (which did not include an EDZ) predicted plastic zones (Fig6.5 (b)) that have a similar shape to the influence zone indicated by previous studies (Sheng et. al., 2000) (Fig6.5 (a)), which indicates that the plastic zones predicted by model without EDZ can be used to estimate the range of possible EDZ. However this is a very crude guide since the plastic zones can be easily affected by many factors and the concept and ranges of EDZ are highly subjective and indefinitive. It is noted that in order to show the plastic zones caused by excavation only, the highly weathered zones that show considerable plastic zones before excavation is not shown in Fig6.5 (b).
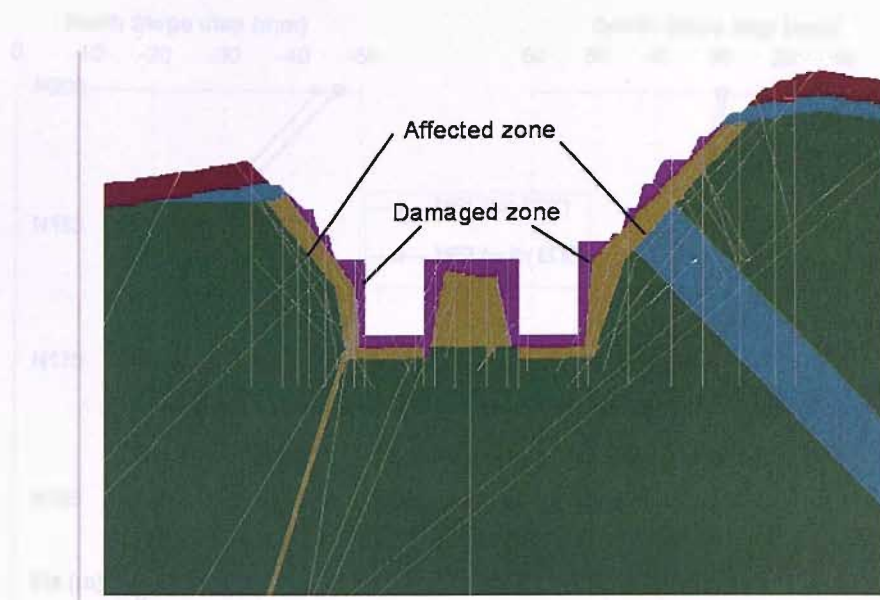
(a) EDZ subzones proposed by Sheng et. al. (2002)
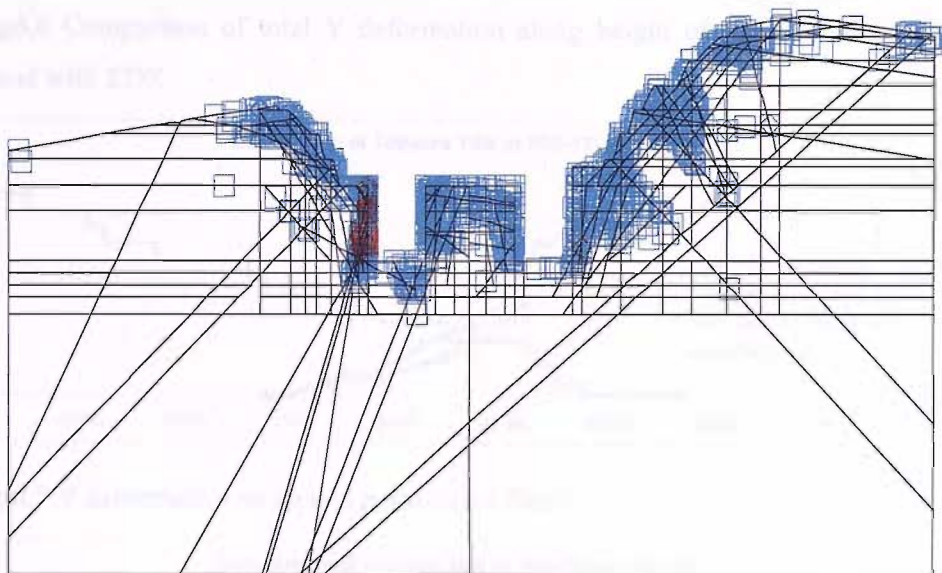
Fig6.5 (b) Plastic zone predicted by model ME1 (no EDZ)

The comparisons between deformations predicted by ME1 and ME2 are shown in Fig6.6 to Fig6.8. It is observed that the inclusion of EDZ increased the predicted deformation and improved the match to the field data. It was concluded that it is important to include the EDZ in the numerical analysis.
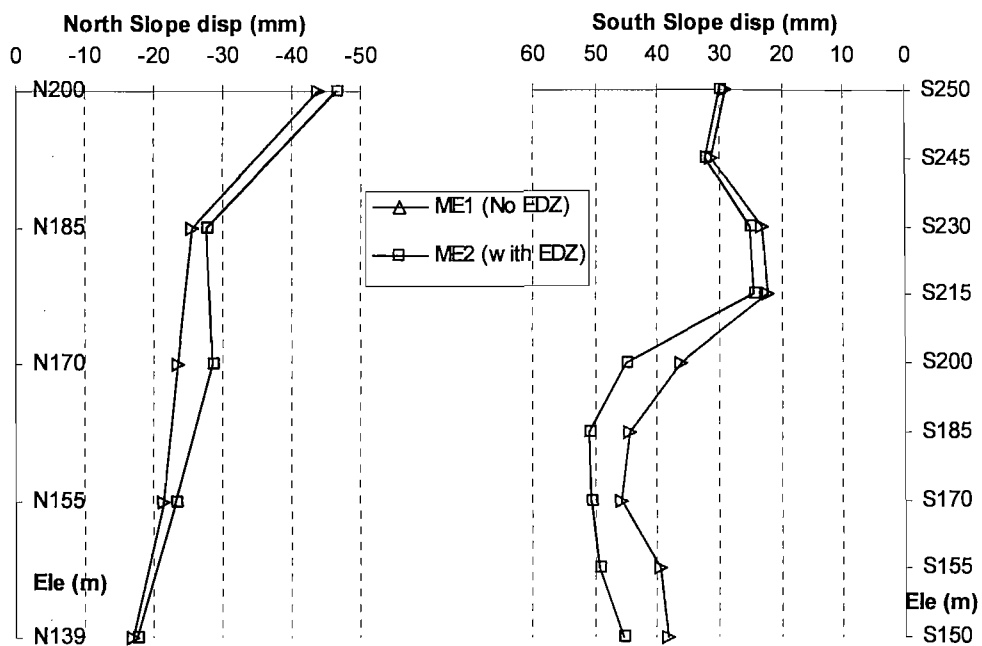
Fig6.6 Comparison of total Y deformation along height of slope predicted by models without and with EDZ
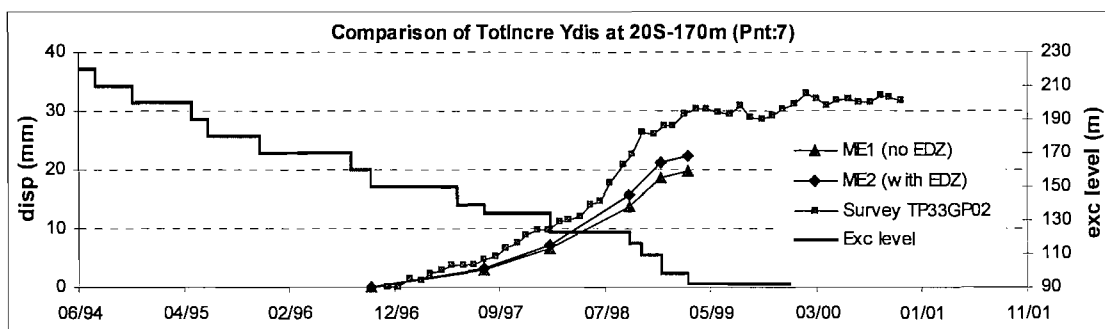
Fig6.7 Y deformation vs time at point 7 (S-170m)
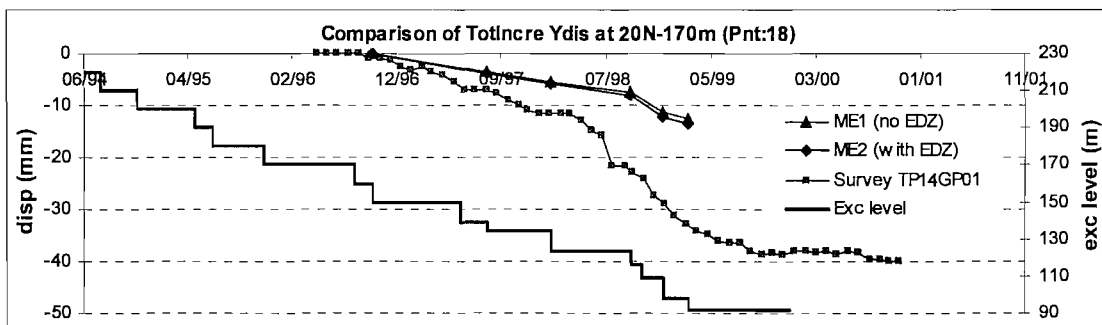
Fig6.8 Y deformation vs time at point 18 (N-170m)

169
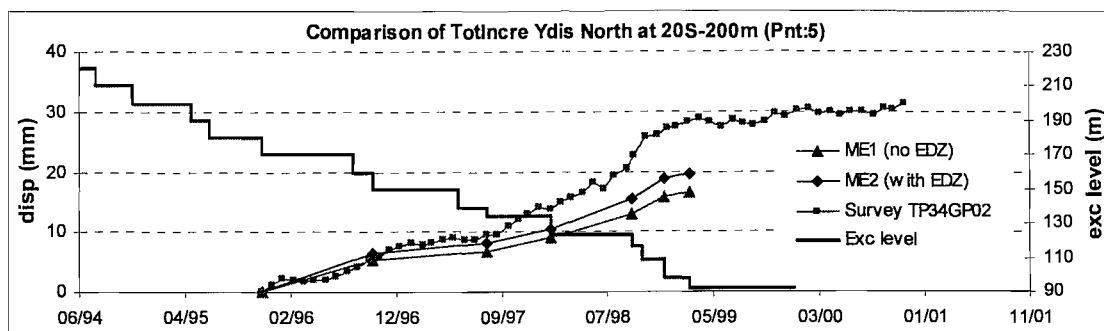
Fig6.9 Y deformation vs time at point 5 (S-200m)

6.4 Parametric study of discontinuity properties

From the modelling exercises in section 6.3, a new base model (ME2) has been developed with major and intermediate discontinuities modelled explicitly, EDZ included and elasto-plastic rock blocks. Those parameters listed in Table5.2 and Table5.3 are the base values. This model will serve as the base model for the parametric study.

In order to establish the sensitivity of the model to the parameters that define the behaviour of discontinuities, a parametric study was conducted on the joint stiffness, friction angle, cohesion and dilation angle of joints. Joint parameters were varied around the base values listed in Table5.1.

As most discontinuities were assigned with properties of joint Mat No 1 as listed in Table5.1, the effect of changes to the properties of other discontinuities was expected very limited in theory. They were included for the sake of completeness.

6.4.1 Effect of joint stiffness

Four models named MJK1 to MJK4 were run with different joint stiffnesses, among which MJK2 is the base value extracted from site investigation reports. MJK1 corresponded to significantly stiffer joints, while MJK3 and MJK4 corresponded to more compliant joints (Table6.2). The other parameters used for these models were equal to the base ones.

The comparison of results shows that the model deformation is sensitive to joint stiffnesses, particularly to decreasing stiffness. This is shown by the spatial distribution of deformation in Fig6.10 and Fig6.11, and deformation vs time curves of Fig6.12 and Fig6.13.

Because few discontinuities were present on the north slope, the influence of discontinuity stiffness on the predicted deformations was less remarkable on the north slope

than on the south slope. It is noted that all models underestimated deformations of the north slope.

Due to reduced joint stiffness, unstable wedges emerged in model MJK3. These were indicated by excessive deformations (Fig6.14).

On the south slope, models MJK1 and MJK2 underestimated the Y deformation while MJK4 overestimated considerably when compared with field data (Fig6.12). Results of model MJK3, which has 50% of the suggested values of stiffnesses, matched the field data well. This indicated that the assumption of same joint stiffness for majority of discontinuities is a gross one, which requires more detailed information for reliable modelling.

Table6.2 Parametric study of joint stiffnesses – value and changes

Model	Kn (MPa)	Ks (MPa)	Values of parameters (%)	Average change of predicted deformation %	
				South	North
MJK1	7500	3000	1000% of MJK2	-29%	-12%
MJK2	690	240	100%	0%	0%
MJK3	345	120	50% of MJK2	34%	11%
MJK4	140	48	20% of MJK2	122%	49%

It can be concluded that the deformation predicted by numerical models is sensitive to the value of joint stiffness used. Deformation of the north slope appeared less sensitive than the south slope to joint stiffness used since there were fewer discontinuities on the north (Fig6.11). The average deformation change in percentage on the south caused by varying joint stiffness is over twice of that on the north (Table6.2).

It is also noted that using too low stiffness can result in local instabilities where many discontinuities intersect each other.
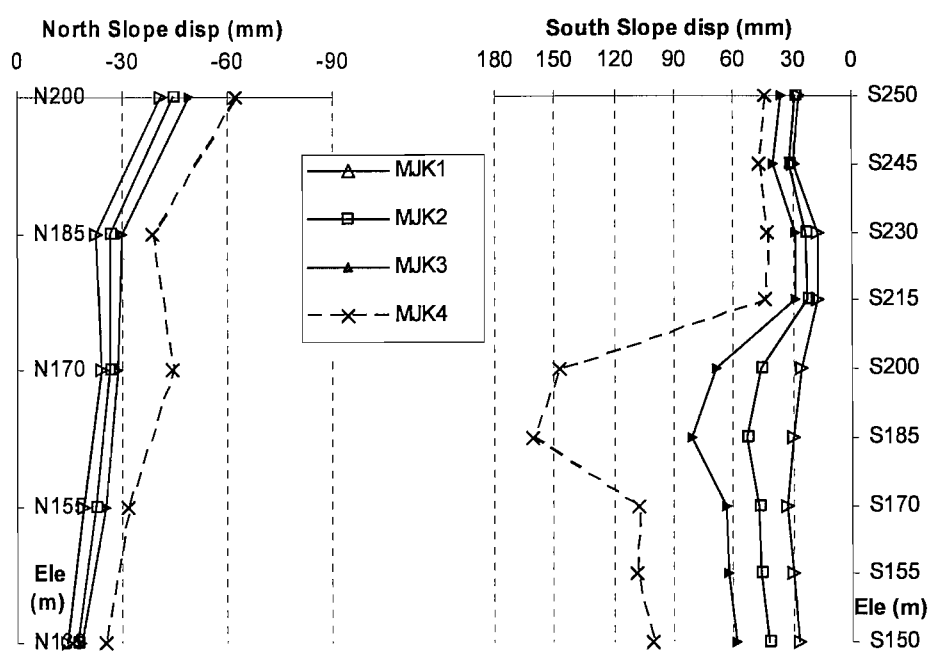
Fig6.10 Comparison of total Y deformations along height of slopes predicted by models with different joint stiffnesses
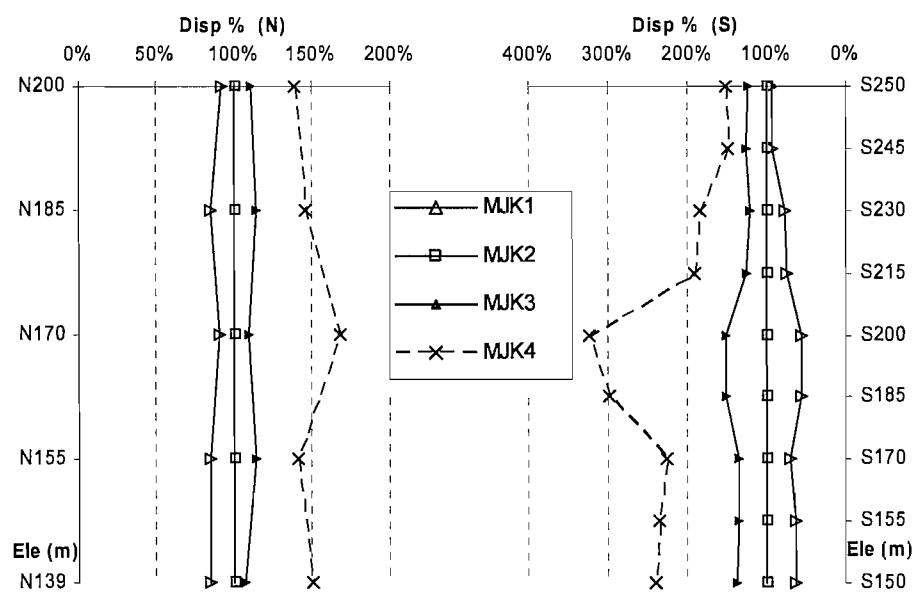
Fig6.11 Comparison of total Y deformations along height of slopes predicted by models with different joint stiffnesses relative to MJK2 in percentage
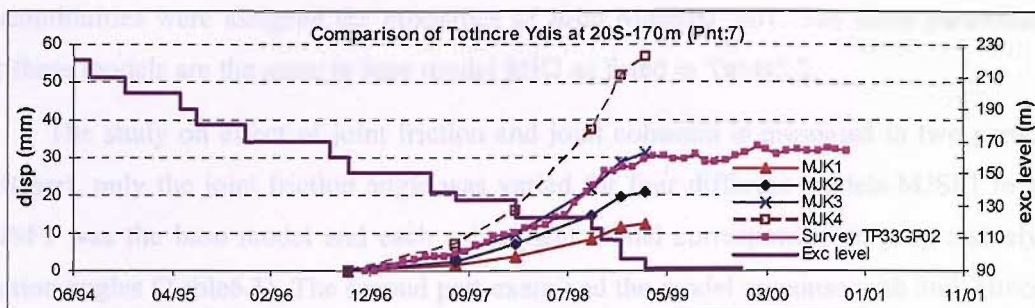
Fig6.12 Y deformation vs time at point 7 (S-170m)
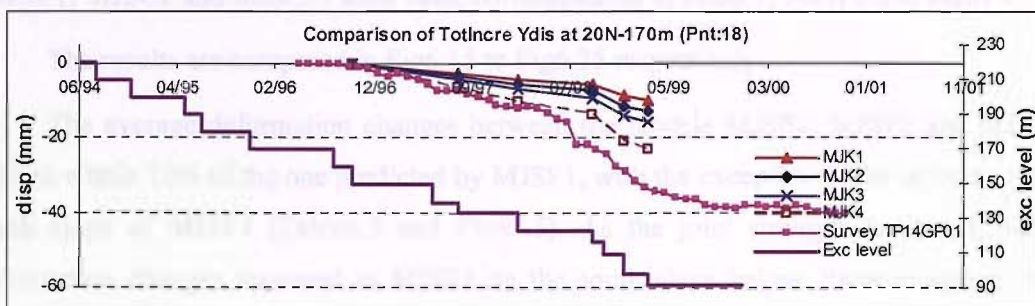
Fig6.13 Y deformation vs time at point 18 (N-170m)
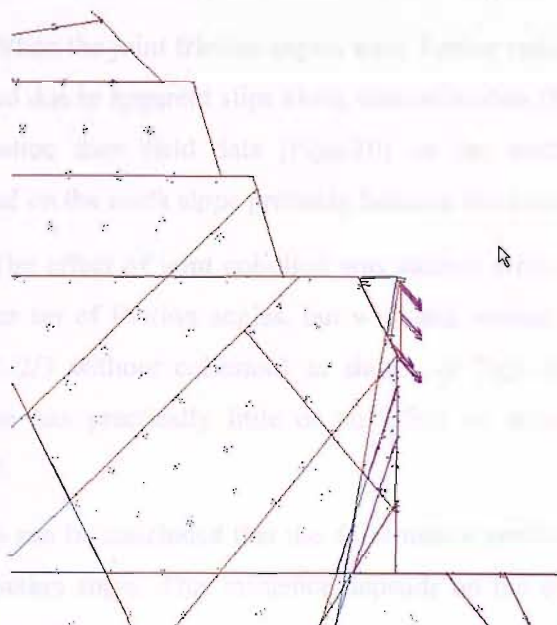
Fig6.14 Unstable wedges on the vertical walls of the north slope (model MJK3)

6.4.2 Effect of joint friction angle and cohesion

Based on the base model ME2, a number of models were run with different values for the friction angle and the cohesion of discontinuities (Table6.3). Various joint properties were used

173

for different discontinuities as introduced in section 5.3 (Table5.1), while the majority of discontinuities were assigned the properties of Joint Material No1. The other parameters used for these models are the same to base model ME2 as listed in Table5.2.

The study on effect of joint friction and joint cohesion is presented in two parts. In the first part, only the joint friction angle was varied for four different models MJSF1 to MJSF4. MJSF1 was the base model and each subsequent model corresponded to progressively lower friction angles (Table6.3). The second part examined the model response with and without joint cohesion under different joint friction angles (Table6.3). Three zero-joint-cohesion models (MJSC1, MJSC2 and MJSC3) were used, corresponding to MJSF1, MJSF2 and MJSF3.

The results are compared in Fig6.15 to Fig6.25 respectively.

The average deformation changes between the models MJSF1, MJSF2 and MJSF3 was limited within 10% of the one predicted by MJSF1, with the exception of the deformation of the south slope of MJSF4 (Table6.3 and Fig6.15). As the joint strength decreased, noticeable deformation changes appeared in MJSF3 on the south slope below 200m elevation, where a considerable number of discontinuities were present. This is considered an indication of more discontinuities at failure over there.

When the joint friction angles were further reduced (MJSF4), excessive deformation were observed due to apparent slips along discontinuities (Fig6.15). The model predicted much lower deformation than field data (Fig6.20) on the south slope. However, little difference was observed on the north slope probably because there are much fewer discontinuities there.

The effect of joint cohesion was studied with comparisons made between models using the same set of friction angles, but with and without cohesion (MJSF1/2/3 with cohesion and MJSC/1/2/3 without cohesion) as shown in Fig6.19, Fig6.23 and Fig6.25. In general, joint cohesion has practically little or no effect on deformation except for a single occasion in Fig6.19.

It can be concluded that the deformation predicted by the numerical model is sensitive to joint friction angle. This influence depends on the overall discontinuity orientation relative to the excavation. On the other hand, the deformation predicted by models appears to be insensitive to joint cohesion.

Table6.3 Parametric study of joint strength

Model	Friction f (°)	Cohesion C (MPa)	Average change of predicted deformation %	
	JMat 1 / 2 / 3	JMat 1 / 2 / 3	South	North

MJSF1 (base)	35 / 31 / 21.8	0.2 / 0.18 / 0.12	0%	0%
MJSF2	30 / 25 / 20	0.2 / 0.18 / 0.12	7%	4%
MJSF3	25 / 20 / 15	0.2 / 0.18 / 0.12	7%	-3%
MJSF4	15 / 12 / 8	0.2 / 0.18 / 0.12	35%	-4%
MJSF1 (base)	35 / 31 / 21.8	0.2 / 0.18 / 0.12		
MJSC1	35 / 31 / 21.8	0 / 0 / 0		
MJSF2	30 / 25 / 20	0.2 / 0.18 / 0.12		
MJSC2	30 / 25 / 20	0 / 0 / 0		
MJSF3	25 / 20 / 15	0.2 / 0.18 / 0.12		
MJSC3	25 / 20 / 15	0 / 0 / 0		
* The friction angles and cohesions corresponded to discontinuity material JMAT1, 2 and 3 in Table5.1 and 5.2.				
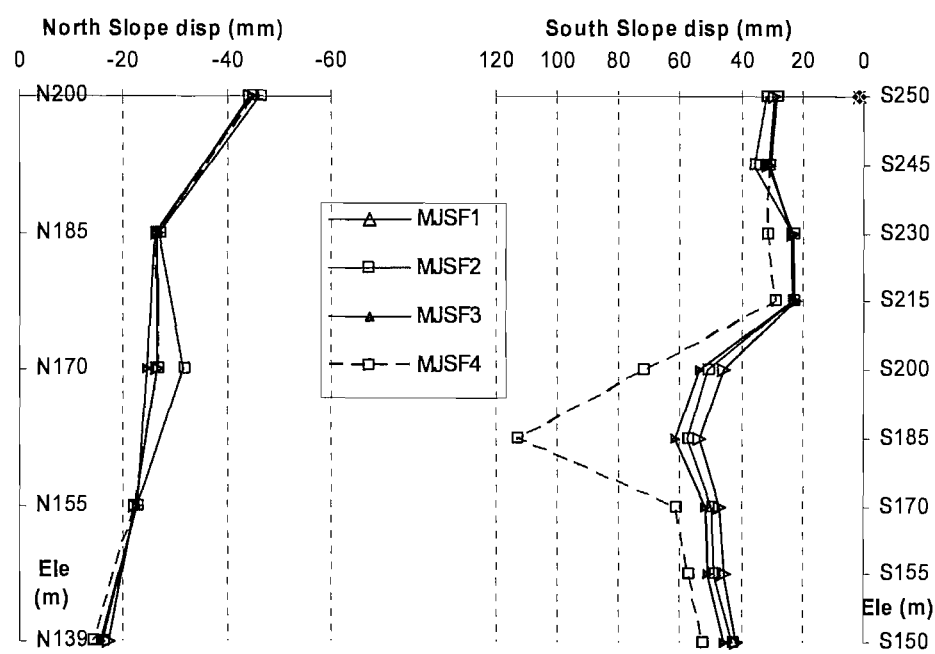
Fig6.15 Comparison of total Y deformations along height of slopes predicted by models with different joint frictions (base model - MJSF1)
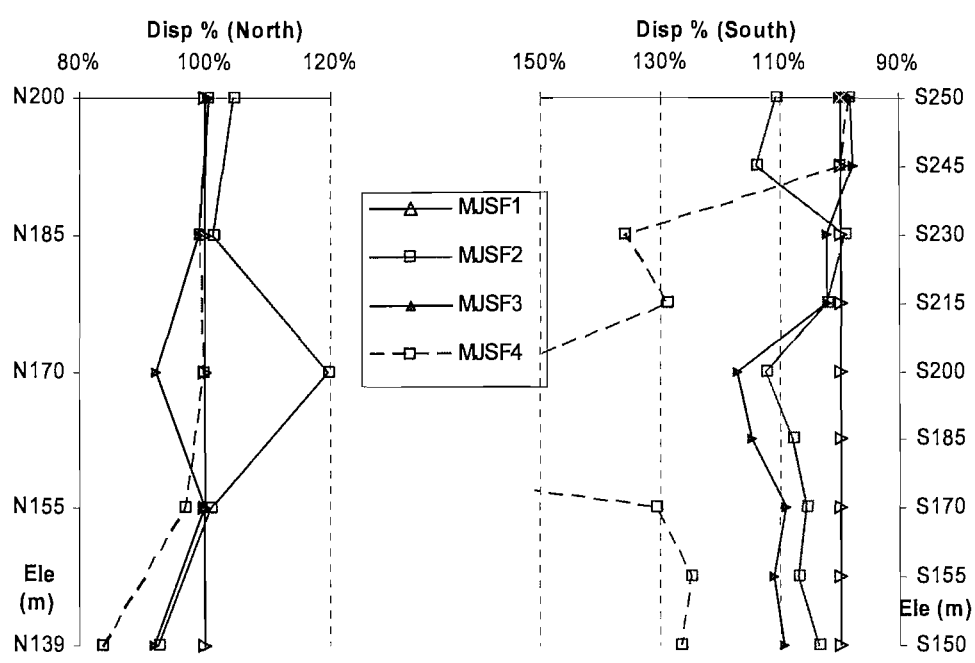
Fig6.16 Comparison of total Y deformations along height of slopes predicted by models with different joint frictions and deformation change relative to MJSF1 in percentage
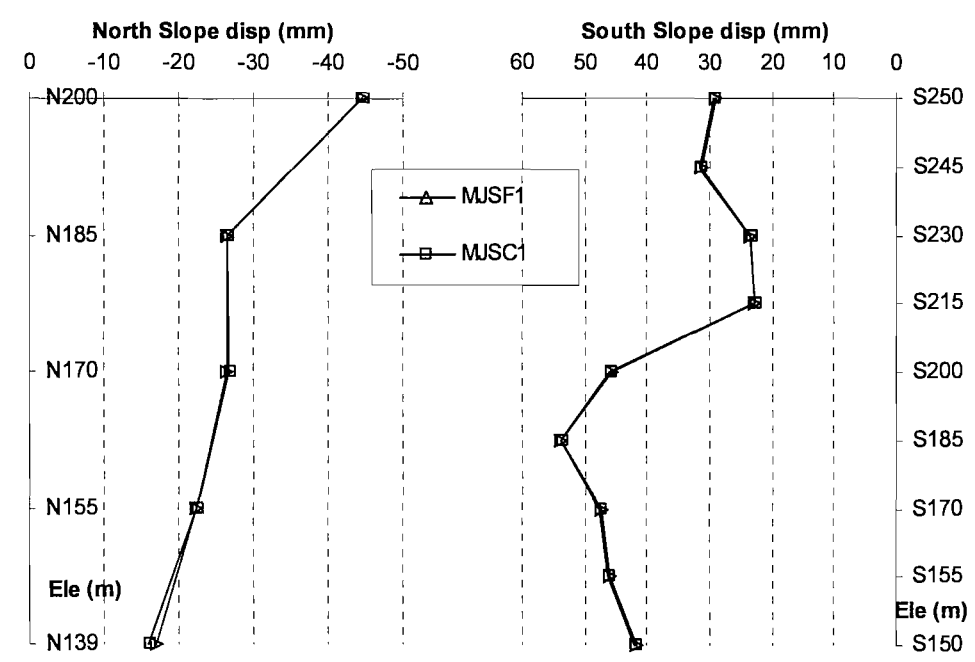
Fig6.17 Comparison of total Y deformations along height of slopes predicted by models with and without cohesion with same joint friction angle of 35?31?21.8? for JMat1/2/3 (Table6.3)

176
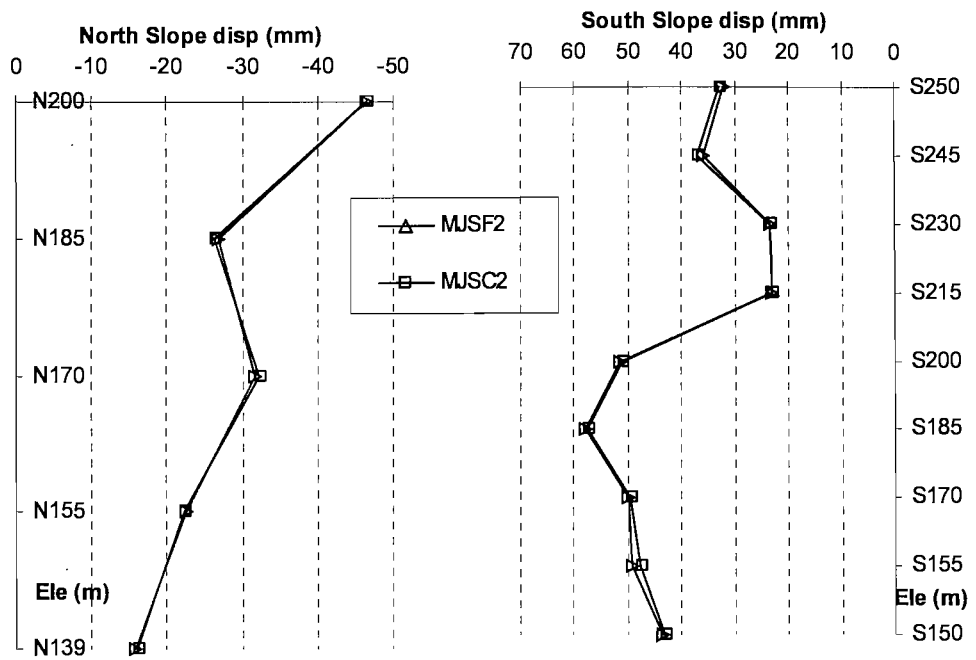
Fig6.18 Comparison of total Y deformations along height of slopes predicted by models with and without cohesion with same joint friction angle of 30?25?20?for JMat1/2/3 (Table6.3)
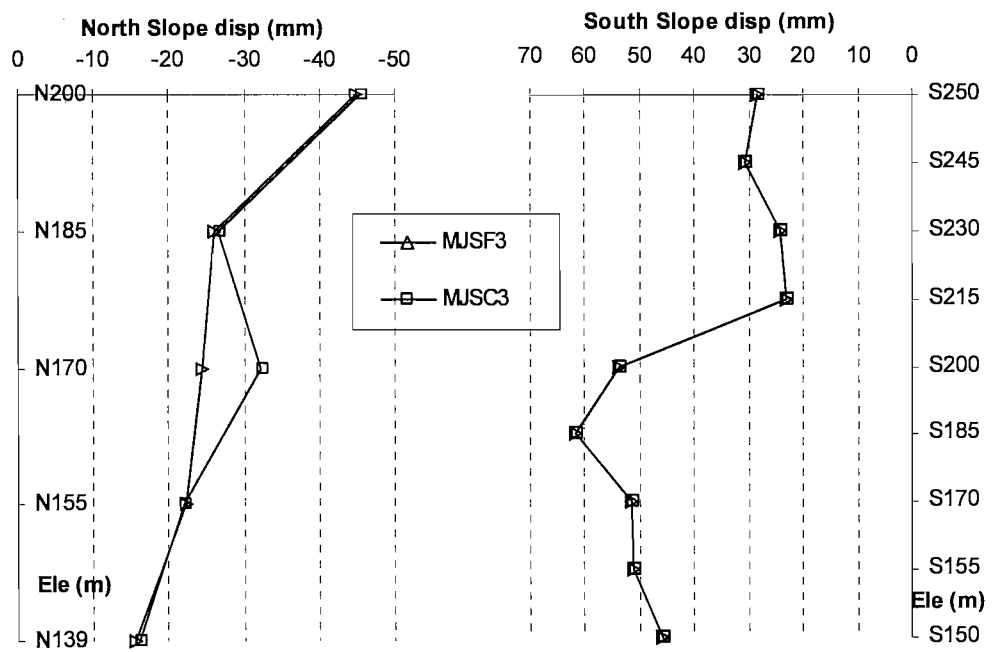
Fig6.19 Comparison of total Y deformations along height of slopes predicted by models with and without cohesion with same joint friction angle of 25?20?15?for JMat1/2/3 (Table6.3)
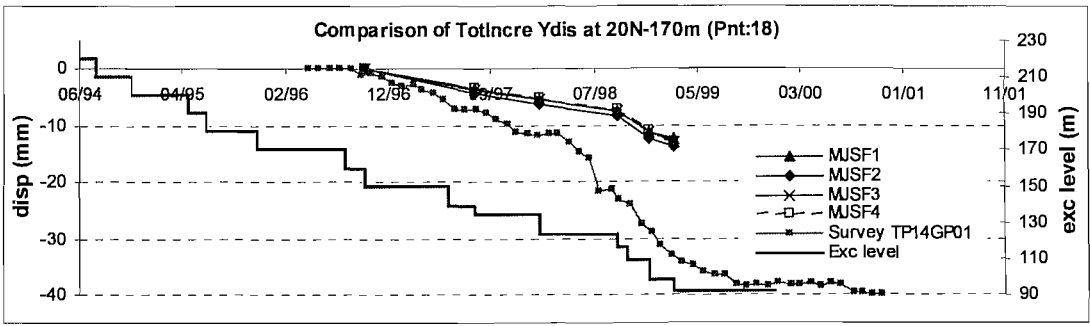
Fig6.20 Y deformation vs time at point 7 with different joint frictions (S-170m) (MJSF1 to MJSF4 in Table6.3)
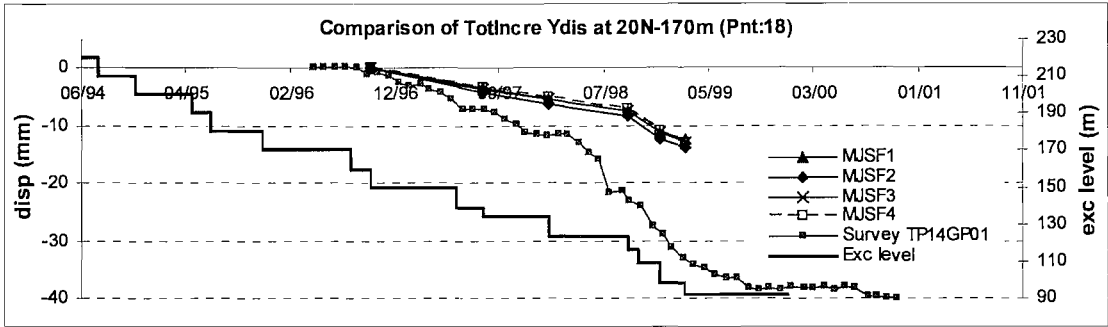
Fig6.21 Y deformation vs time at point 18 with different joint frictions (N-170m) (MJSF1 to MJSF4 in Table6.3)
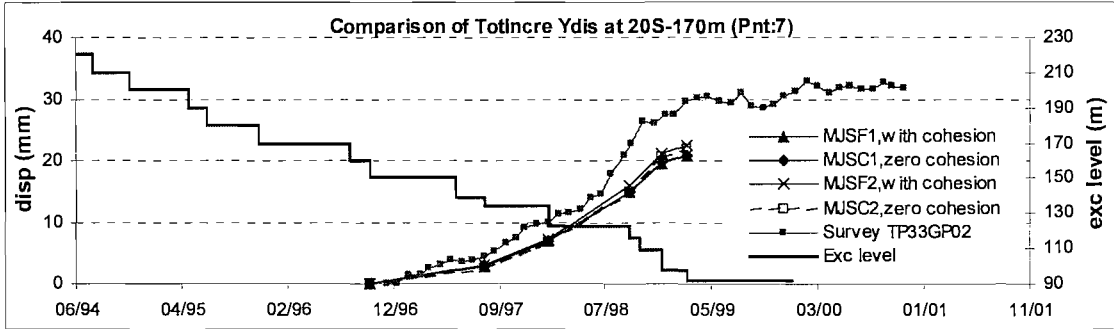
Fig6.22 Y deformation vs time at point 7 (S-170m) with and without cohesion, joint friction angles JMat1/2/3 of 35?31?21.8? for MJSC1 and MJSC2 and 30?25?20? for MJSC3 and MJSC4 (Table6.3)

178
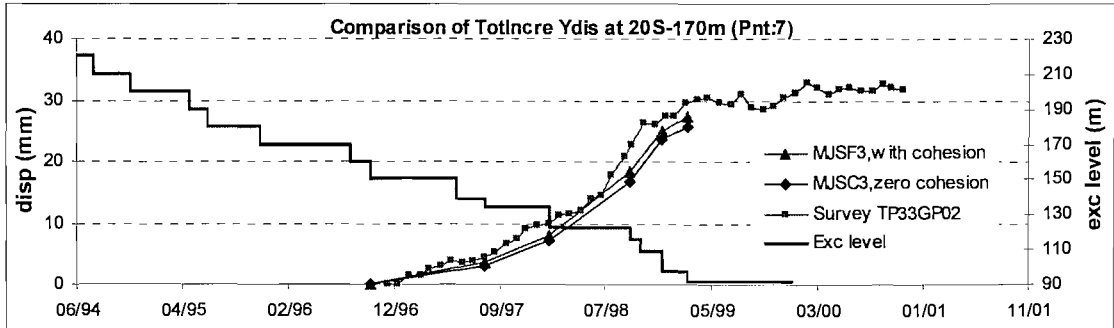
Fig6.23 Y deformation vs time at point 7 (S-170m) of model with and without joint cohesions (MJSC5 to MJSC6)
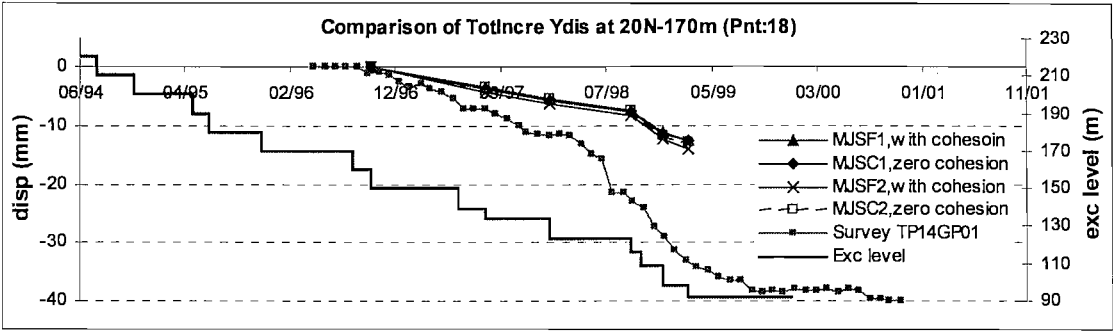
Fig6.24 Y deformation vs time at point 18 (N-170m) of model with different joint cohesions MJSC1 to MJSC4
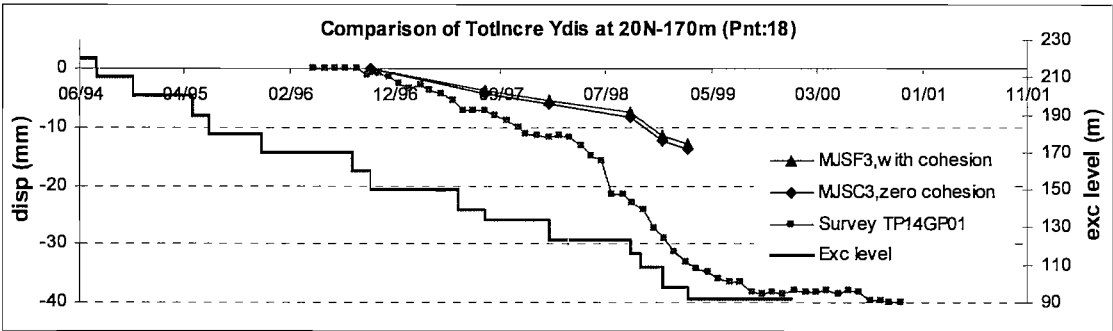
Fig6.25 Y deformation vs time at point 18 (N-170m) of model with different joint cohesions MJSC5 to MJSC6

6.4.3 Effect of joint dilation angle

When discontinuities are clay-filled, or planar, or exhibit signs of earlier shearing, their dilation angle can be assumed to be zero. If the discontinuities are nonplanar, unfilled, and not presheared, their trend to dilate when sheared will increase the available shear strength. When the dilation is prohibited, the effective normal stress across the relevant joints will increase and consequently the shear strength will increase (Barton & Choubey, 1976). This could serve as a stabilising factor to the discontinuities and consequently the excavation.

To investigate the effect of the dilation angle, two models based on the base model ME2 were run with different dilation angles as listed in Table6.4. The other parameters used for these models are listed in Table5.2. In the base model, the dilation for joints were set to zero due to lack of information.

The results were compared with those of the model MJD1, which used zero joint dilation. Fig6.26 shows joint dilation affected the deformation very little, even when discontinuities were assigned with high dilation angles, equalling to the respective friction angles (MJD3) (Fig6.26). The average deformation change due to the introduction of non-zero joint dilation angles is listed in Table6.4. This was within 5% on the south and slightly higher on the north. It is worth noting that increasing joint dilation tends to increase predicted deformation. This was probably due to the dilation of those discontinuities undergone shearing during excavation, which counteracted the restraining effect of increased joint strength. But in this case, the magnitude is trivial.

It was concluded that the joint dilation angle was an insensitive parameter.

Table6.4 Parametric study of joint dilation

|	Dilation angles	Average change of predicted deformation %	
	JMat 1/2/3	South	North
MJD1 (base)	0 / 0 / 0		
MJD2	5 / 5 / 3	2%	6%
MJD3	30 / 25 / 20	1%	1%
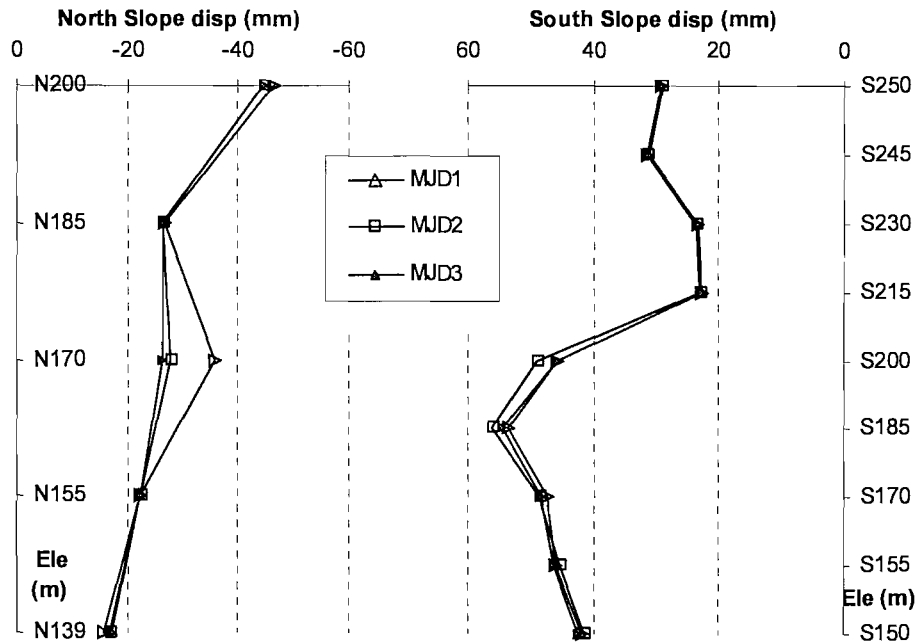
Fig6.26 Comparison of total Y deformations along height of slopes predicted by models with different joint dilations

6.4.4 Continuously yielding joint model

The Coulomb model in 3DEC could not simulate the post failure characteristics of discontinuities. As introduced in section 2.5.3.3, a continuously yielding model is provided in 3DEC that can account for non-linear behaviour such as joint shearing damage, normal stiffness dependence on normal stress, and decrease in dilation angle with plastic shear displacement (Itasca, 1998).

In the continuously yielding model, the joint stiffnesses can be described as exponential function of stress level in the joint. However, it has been noted by Itasca (2002) that variation of parameters for the model represent larger deformation than different constitutive models. In practice great difficulties are encountered in determination of the exponent in the equation, which governs the effects of stiffness variation (for details see 3DEC Manual by Itasca (1998)). To make the comparison meaningful and avoid the problem of obtaining practical value of the exponents in the functions, the joint stiffness is considered here as constant, with the same values as the one used for the Mohr-Coulomb model.

A parameter that is needed for the continuously yielding model is the joint roughness parameter R, which denotes the amount of joint normal opening when the asperities are sheared off. No relevant data were available for TGP. However a parametric study showed that the numerical results were not sensitive to the value of R in the range between 1e-4m to 1e-2m, within which the value of R is normally assumed to fall. It was decided to used a value of 1e-2m for the computations presented here.

Another parameter needed is the joint residual friction angle. The values used were taken from Zhang & Zhou (1999) as listed in Table6.5.

Table6.5 Discontinuity initial friction and residual friction (Zhang & Zhou, 1999)

Discontinuity type	JMat	Friction (°)	Residual friction (°)	R (m)
Hard	1	35.0	31	1e-4 ~1e-2
Soft	2	31.0	26.6	
	3	21.8	19.2	
F215	4	18	15	

Compared with the model with Mohr Coulomb discontinuities, the model with the continuously yielding discontinuities predicted larger deformation (Fig6.27) and matched the

field data better (Fig6.28 to Fig6.30), though it was more computationally expensive. The effect on the north slope was again not significant, since there are fewer discontinuities there.

The results show that by considering the post-failure behaviour of discontinuities, the simplified continuously yielding model predicted the behaviour of discontinuities better than the Mohr-Coulomb model. It is concluded that the continuously yielding joint model should be used instead of the Mohr-Coulomb model where computational efficiency is not an issue, and where the relevant parameters can be identified.
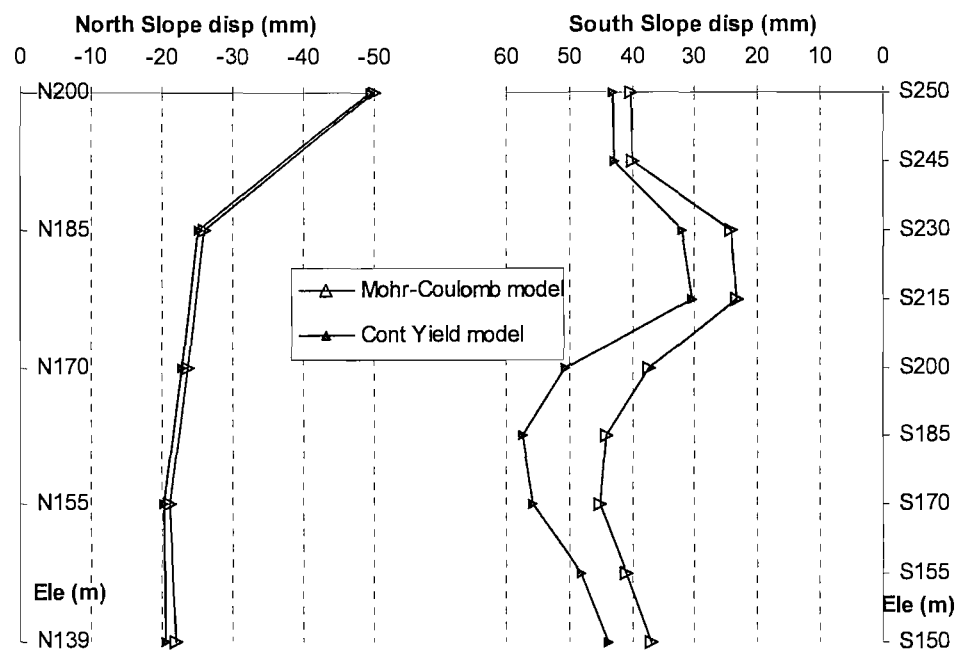
Fig6.27 Comparison of total Y deformations along height of slopes predicted by models with Mohr-Coulomb model and continuously yielding model for discontinuities
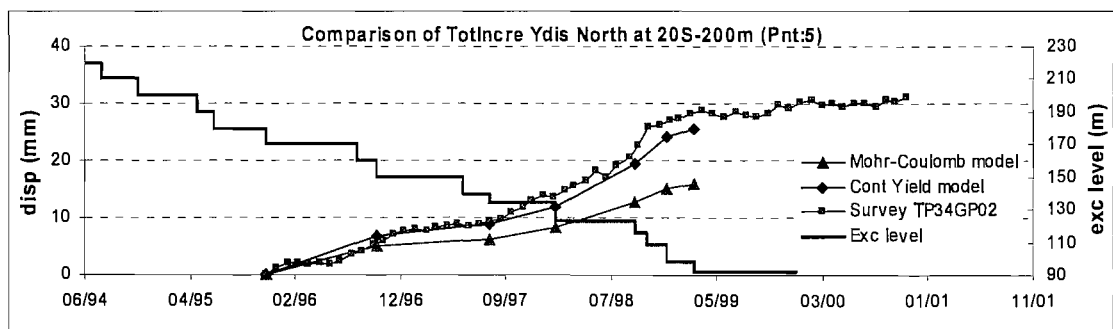
Fig6.28 Y deformation vs time at point 5 (S-200m)
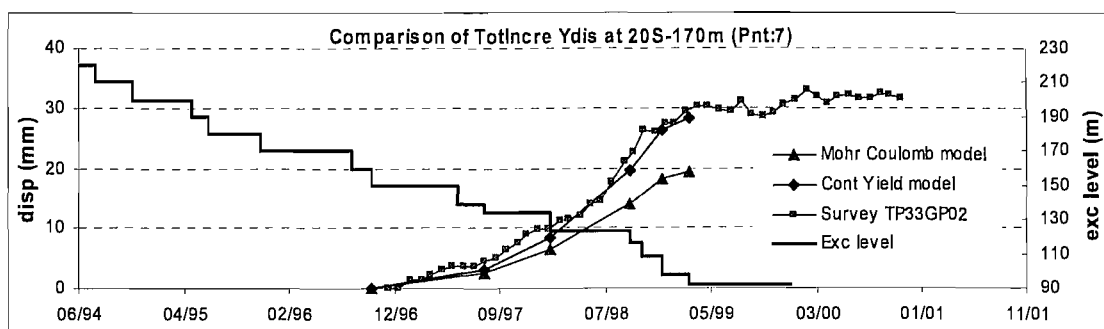
Fig6.29 Y deformation vs time at point 7 (S-170m)
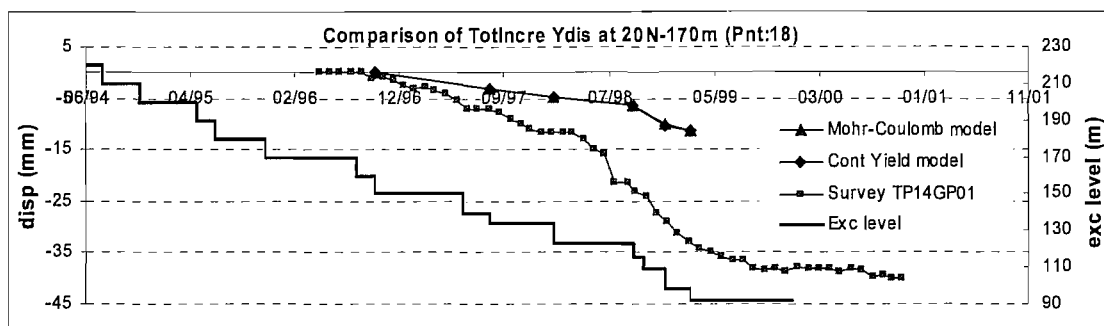
Fig6.30 Y deformation vs time at point 18 (N-170m)

6.5 Parametric study of equivalent continuum properties

As discussed in section 6.2, when some discontinuities are impossible to model explicitly, e.g. minor discontinuities, the equivalent continuum approach is used in numerical analyses. As the region for which the equivalent continuum approach is used may spread over a large area or even the whole model, the influence of the material properties used could be significant to numerical results. The extent to which material properties must be reduced to take into account the existence of discontinuities is usually decided empirically, assisted by site investigation.

As discussed in section 6.2, the excavation-induced discontinuities are taken into account by assuming the existence of an EDZ around the excavation, with reduced material properties.

In this research, a parametric study was carried out on the material properties of rock blocks and the EDZ. The study looked into the sensitivity of predicted deformation to block modulus, constitutive models, strength parameters, dilation angles and effect of EDZ properties.

6.5.1 Effect of block modulus

In order to investigate the effect of rock block modulus, a series of models based on the base model ME2 (MBM1, MBM2, MBM3 and MBM4) were run with different rock modulus (Table6.6). Rock blocks of different quality (BMat1, BMat2, BMat3 and BMat4) were assigned with correspondent material properties as listed in Table5.2. The block moduli used were selected based on a scale of 125%, 100%, 75% and 50% of the modulus of the base model MBM2. However, only the values of block models BMat1 and BMat2, which consist of majority of the blocks, were varied. The effect of varying values for model BMat3 (for the highly weathered zone) was very limited because only a few blocks were assigned with this model. That the value of BMat3 remained unchanged also helps to avoid unexpected instability outside of the area of interest.

Table6.6 Parametric study of rock modulus and change of deformation caused

	Young's Modulus (GPa)			Average change of predicted deformation %	
	BMat1 /2 /3 /4	EBMat1/2*	%	South	North
MBM1	40 /12.5 /1/0.75	15/ 30	125%	-8%	-15%
MBM2(base)	32 /10 /1/0.75	12/ 24	100%	0%	0%
MBM3	24 /7.5 /1/0.75	9/ 18	75%	21%	25%
MBM4	16 / 5 /1/0.75	6/ 12	50%	59%	73%
* EBMat1/ 2 are block material numbers the damaged and affected subzones of EDZ.					

The total y deformations increased with decreasing rock modulus as shown in Fig6.31 while the percentage of deformation changes relative to the base model MBM2 is shown in Fig6.32. It is shown that the model is very sensitive to the value of block modulus. The deformation on the north slope was affected more than the south slope because the existence of fewer discontinuities on the north means that a larger portion of total deformation is due to rock block strain. It is worth noting that the magnitude of deformation change is very even along the slopes (Fig6.31). This indicates that the overall deformation mechanism was not affected.

The comparison between predicted deformation and field data shows that predictions improved with decreasing block modulus while deformation vs time curves kept the same trend (Fig6.31 to Fig6.34). In general, models MBM1, MBM2 and MBM3 underestimated deformations while MBM4 overestimated deformations at most points. The effects on the z deformation are similar but less significant.

The model results have shown that the model was sensitive to the block modulus. It is not unreasonable to use lower block moduli by a figure between 25% to 50% to match field data.
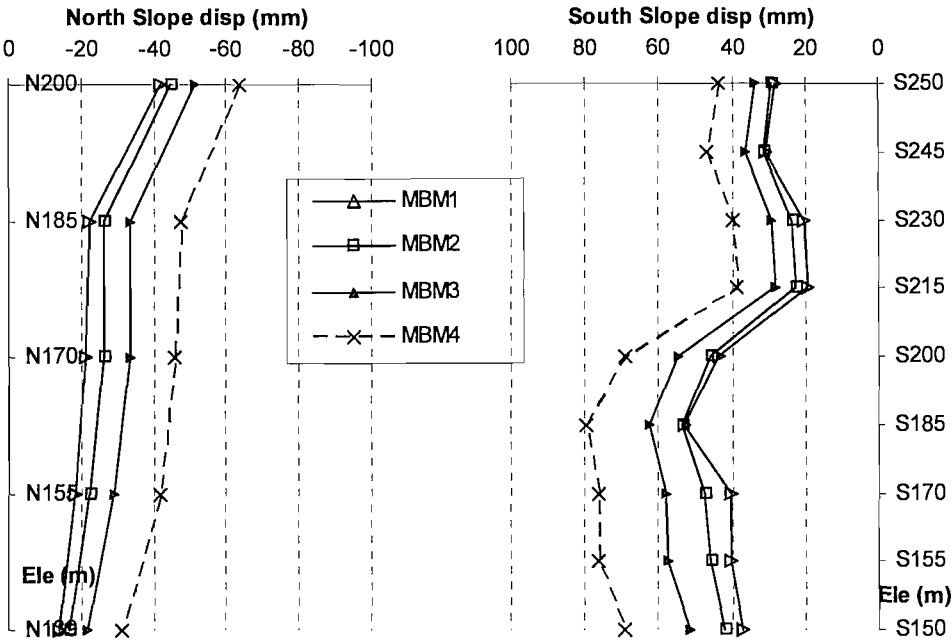
Fig6.31 Comparison of total Y deformations along height of slopes predicted by models with different block moduli
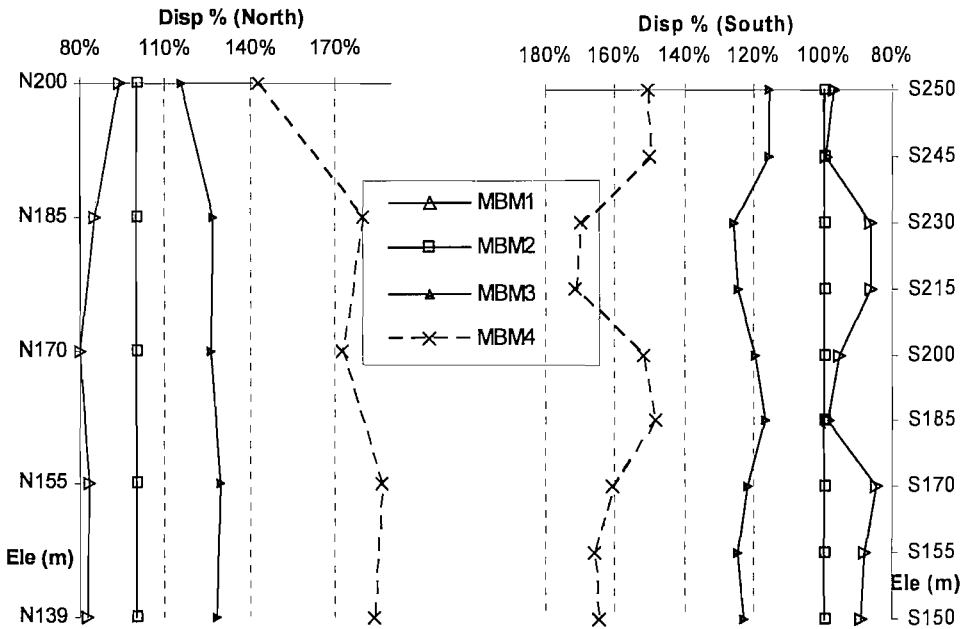
Fig6.32 Comparison of total Y deformations along height of slopes predicted by models with different block moduli in percentage relative to model MBM2

Fig6.33 Y deformation vs time at point 7 (S-170m)

Fig6.34 Y deformation vs time at point 18 (N-170m)
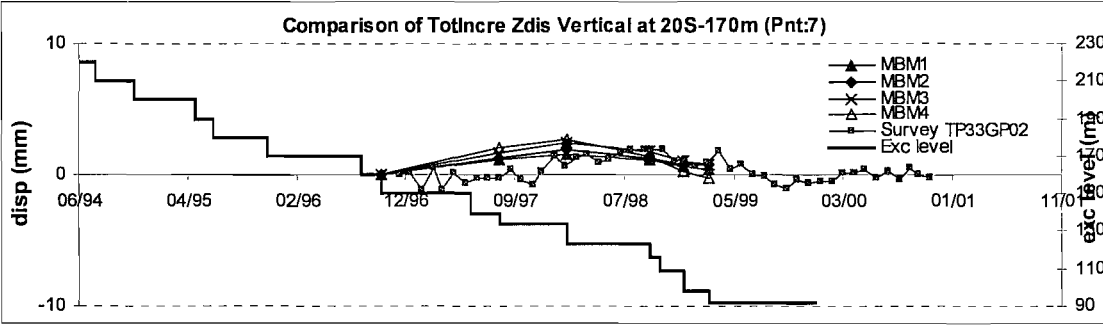
Fig6.35 Z deformation vs time at point 7 (S-170m)

Fig6.36 Z deformation vs time at point 18 (N-170m)

6.5.2 Constitutive model for the rock blocks

It has been discussed in section 6.3 that the elasto-palstic Mohr-Coulomb model is more appropriate for rock blocks in EDZ than an elastic model. To further investigate the effects of the constitutive models for rock block in the whole model, two models based on the base model ME2 were run with elastic block model (MBC1) and elasto-plastic (Mohr-Coulomb) block model (MBC2) respectively with same material properties listed in Table5.1 and 5.2. Results are compared in Fig6.37 to Fig6.39.

The comparison between the deformations predicted by the two models showed that the elastic model (MBC1) predicted larger deformation in the weathered zone and lower deformation in the unweathered zone (Fig6.37). Apparently this is related to the different conditions of rock materials of varying strength before and after excavation.

Weak materials in the highly and moderately weathered zones, where rock materials were loaded by their self-weight and the corresponding horizontal in situ stress (see section 5.3.3), may have already failed under the initial stress conditions before excavation because of poor material strength. This was shown by extensive failure observed in the highly or completely weathered zones in the model MBC2 before excavation. Therefore the stress level before excavation is lower in the elasto-plastic model than in the elastic model. Consequently, less deformation was predicted by the the plastic model (Fig6.37 and Fig6.39).

Strong materials like fresh/slightly weathered rock were mostly in elastic conditions under in situ stress condition before excavation thanks to higher block strength. For the rock materials that are strong enough to remain elastic during excavation, there was little difference in using either elastic model or elasto-plastic model. However, part of the rock materials may fail due to excavation-induced stress release if assigned with elasto-plastic model, e.g. EDZ. In this case, unloaded from the same stress level, the plastic model yielded larger deformation than the elastic model because of material failure.

The comparisons to field data (the y deformation) showed smaller difference between the two models (Fig6.38 and Fig6.39) than the total deformations (Fig6.37), e.g. the difference for the total y deformation at S-200m is 3.8mm (Fig6.37) and 1.9mm (Fig6.40) for the y deformation. As introduced in section 5.4, the total y deformation (e.g. Fig6.37) records the induced deformation at that position from the beginning of excavation on while the y deformation of each point (e.g. Fig6.38 and Fig6.39) records only the induced deformation at that position from when the instrumentation (survey points or inclinometers) are in place. It can be seen that a large part of the effect of different rock block models occurred before instrumentation and couldn't be fully reflected in field measurement.

It is shown that the Mohr-Coulomb model was more representative of rock block behaviour than elastic model. A sensitivity study of the model to the strength parameters of rock blocks is presented in the following section.


Fig6.37 Comparison of total Y deformations along height of slopes predicted by models with different constitutive model for blocks
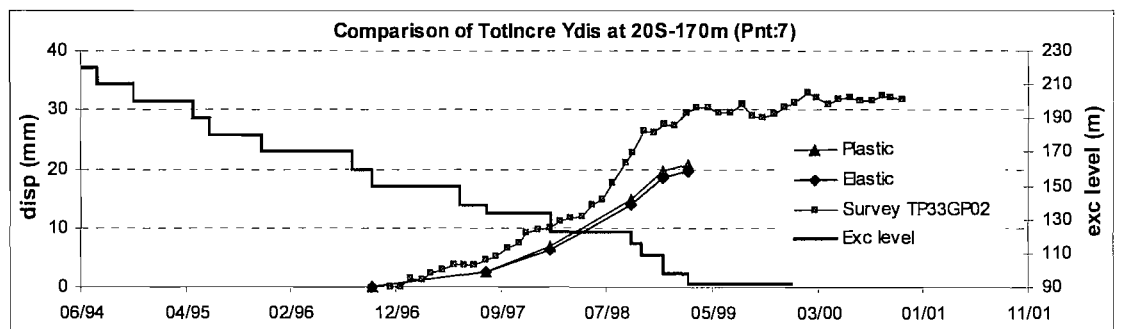
Fig6.38 Y deformation vs time at point 7 (S-170m)

Fig6.39 Y deformation vs time at point 18 (N-170m)

Comparison of TotIncre Ydis North at 20S-200m (Pnt:5)
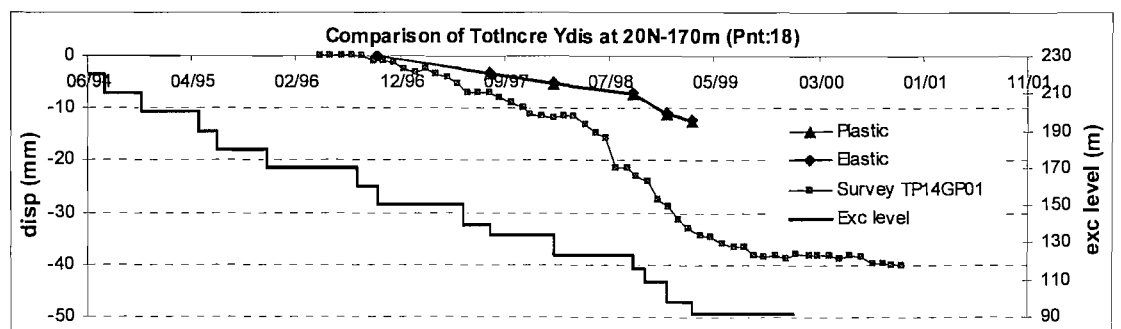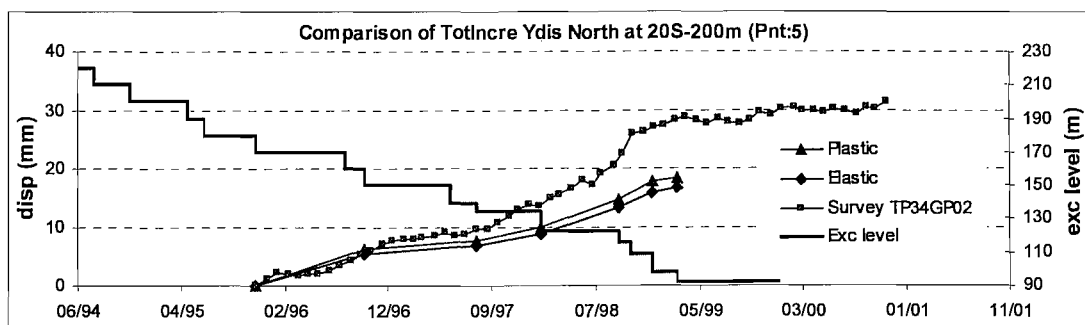
Fig6.40 Y deformation vs time at point 5 (S-200m)

6.5.3 Effect of block strength

In order to investigate the effect of rock block strength, a series of models based on the base model ME2 were run with different values for the friction angle and the cohesion of rock blocks. The models of MBSF1, MBSF2 and MBSF3 have gradually decreasing block friction and models of MBSC1 and MBSC2 have different cohesions as listed in Table6.7. Models MBSF1 and MBSC1 were the base model for varying parameters. The effect of values for BMat4 is considered negligible. Therefore only the values of strength parameter for materials BMAT1/2/3 were varied.

The results are compared in Fig6.41 and Fig6.42. It can be seen that different friction angles and cohesions affected mostly the deformation in weaker zones. The model with lower block strength predicted less deformation. This is similar to the case in section 6.5.2. The weak materials were in failure under the in situ stress condition and lower material strength resulted in low stress level, as a result, less deformation after excavation-induced stress release (Fig6.43).

The rock blocks in the unweathered zones remained in similar conditions (elastic or plastic) in spite of decreasing strength. From blocks in the unweathered zones, it may be noted that the stress conditions before and after excavation may have more significant effects on their state than the block strength does.

As can be seen from Fig6.44 and Fig6.45, varying friction angle and cohesion of rock blocks generally had no impact on how well the numerical predictions match field data.

From the above, it can be concluded that with the exception of the weak material in the weathered zone, numerical results were generally insensitive to the friction angle and the cohesion of rock blocks.

189

Table6.7 Parametric study of rock friction and cohesion

Models	Friction angle (°)		Cohesion (MPa)	
Material	BMat1 /2 /3 /4	%	BMat1 /2 /3 /4	%
MBSF1 (base)	61 / 52.4 / 45 / 18	100%	1.8 / 1.0 / 0.35 / 0.1	100%
MBSF2	45 / 39 / 33 / 18	60%	1.8 / 1.0 / 0.35 / 0.1	100%
MBSF3	36 / 31 / 27 / 18	45%	1.8 / 1.0 / 0.35 / 0.1	100%
MBSC1 (base)	61 / 52.4 / 45 / 18	100%	1.8 / 1.0 / 0.35 / 0.1	100%
MBSC2	61 / 52.4 / 45 / 18	100%	1.1 / 0.6 / 0.35 / 0.1	45%
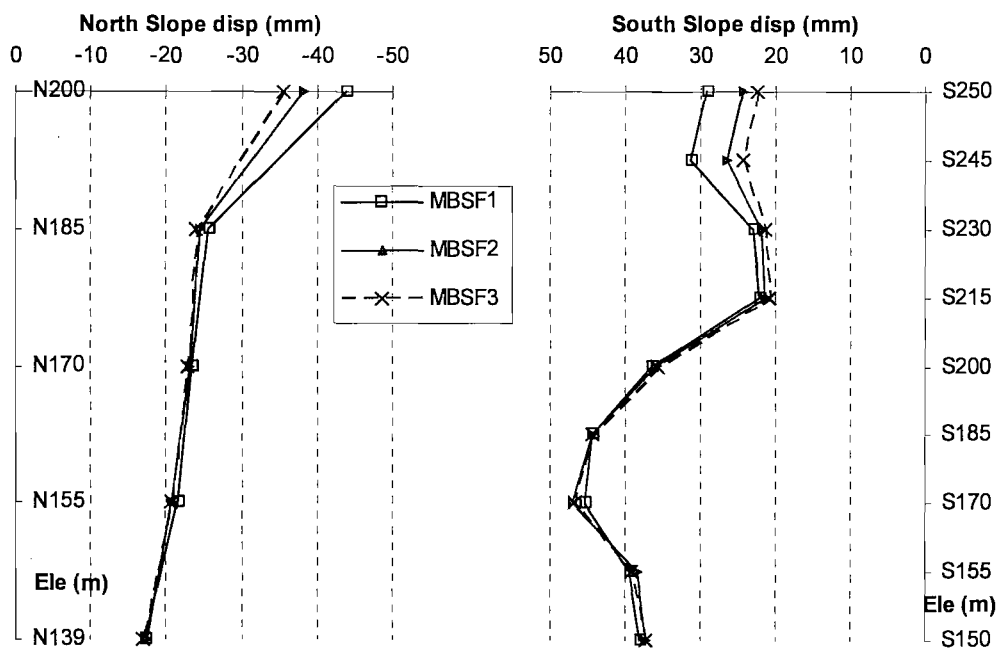
Fig6.41 Comparison of total Y deformations along height of slopes predicted by models with different friction angles of rock
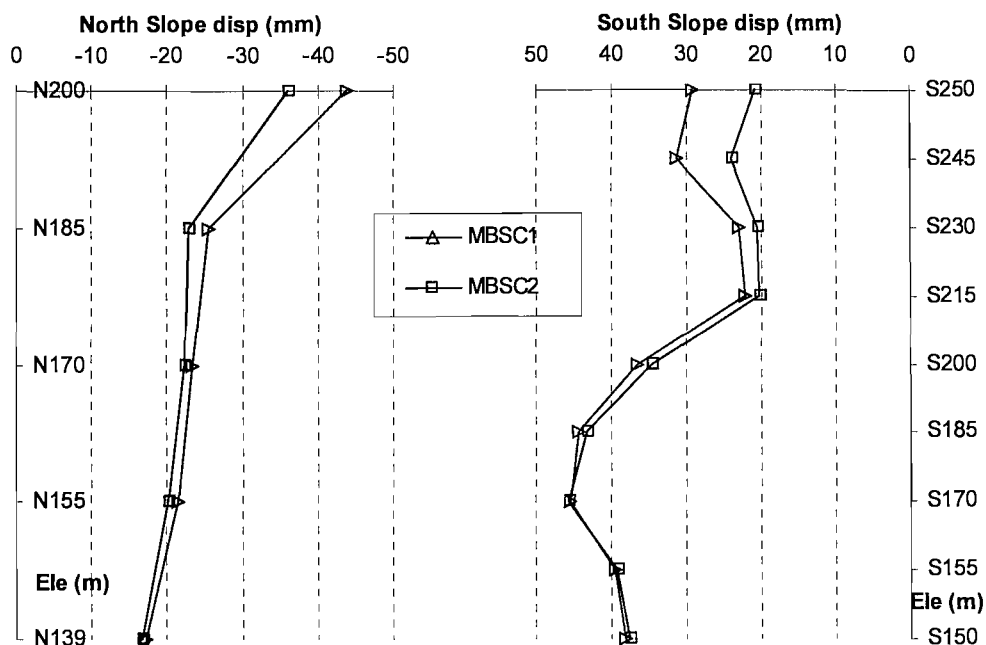
Fig6.42 Comparison of total Y deformations along height of slopes predicted by models with different cohesions of rock
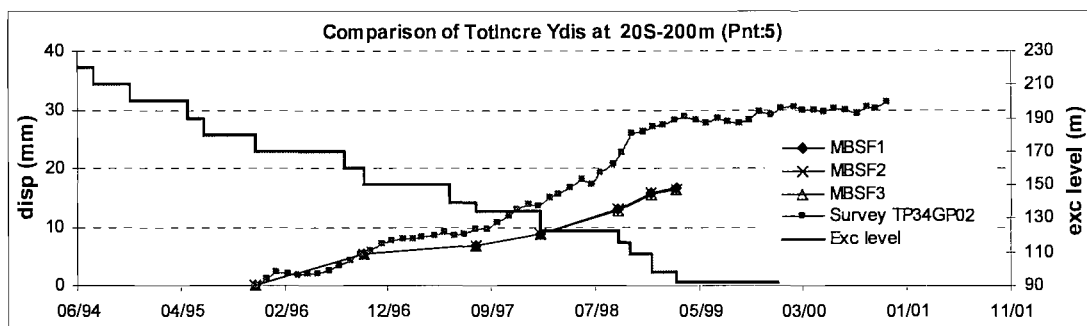
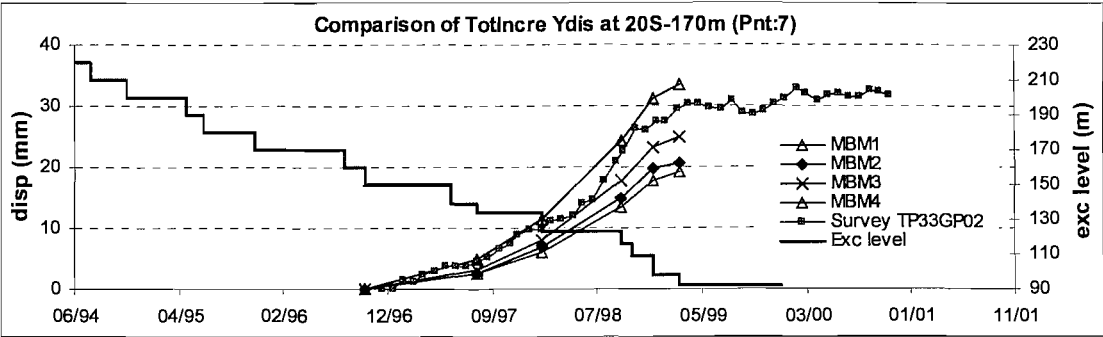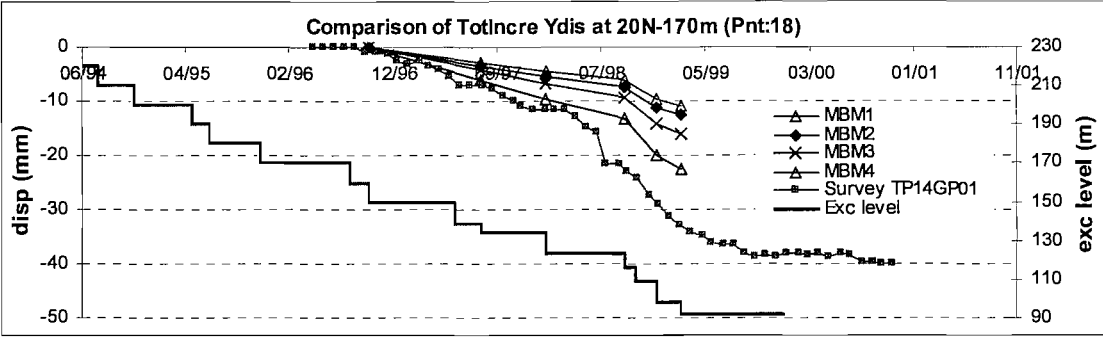Fig6.43 Y deformation vs time at point 5 (S-200m)
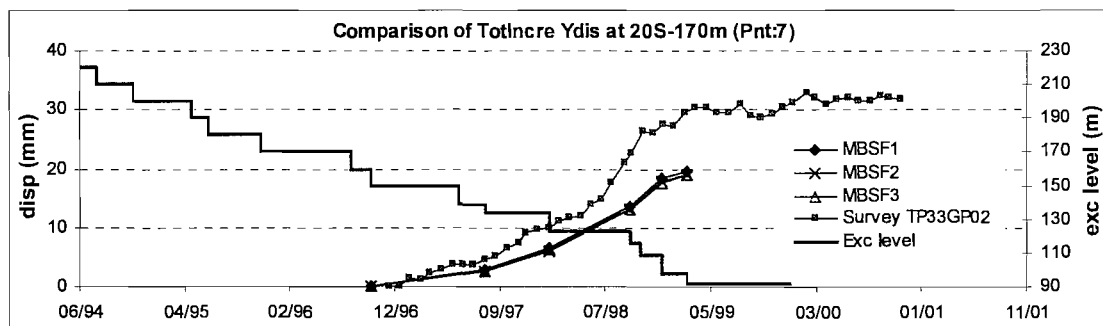
Fig6.44 Y deformation vs time at point 7 (S-170m)
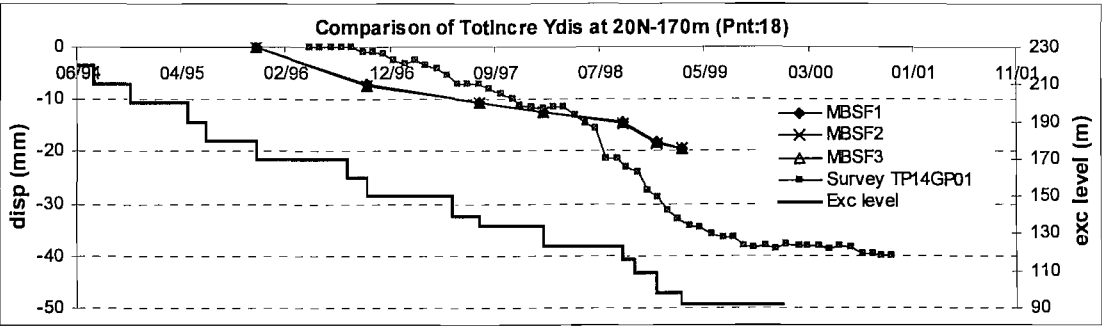
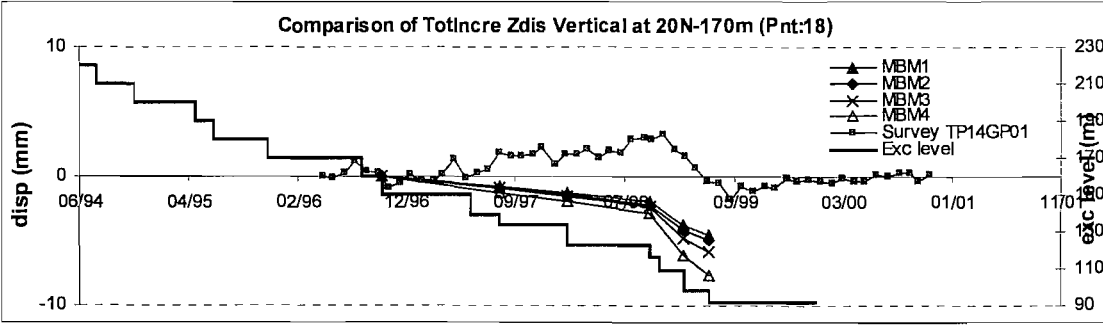Fig6.45 Y deformation vs time at point 18 (N-170m)

6.5.4 Effect of rock dilation angle

Little information is available for rock dilation angle in the TGP from the literature research. Based on the base model ME2, two models with different block dilation angles (MBD1 and MBD2, Table6.8) were compared. Since weak materials are normally considered as zero dilation angle material, only materials BMat1 and BMat2 were assigned dilation angles.

The model MBD2 predicted very similar results to the base model with zero dilation angles (Fig6.46 to Fig6.48). It can be concluded by theory that further increase of dilation angles is not going to make more difference of deformation.

Therefore, the dilation angle of block is an insensitive parameter to the model.

Table6.8 Parametric study of rock dilation angle

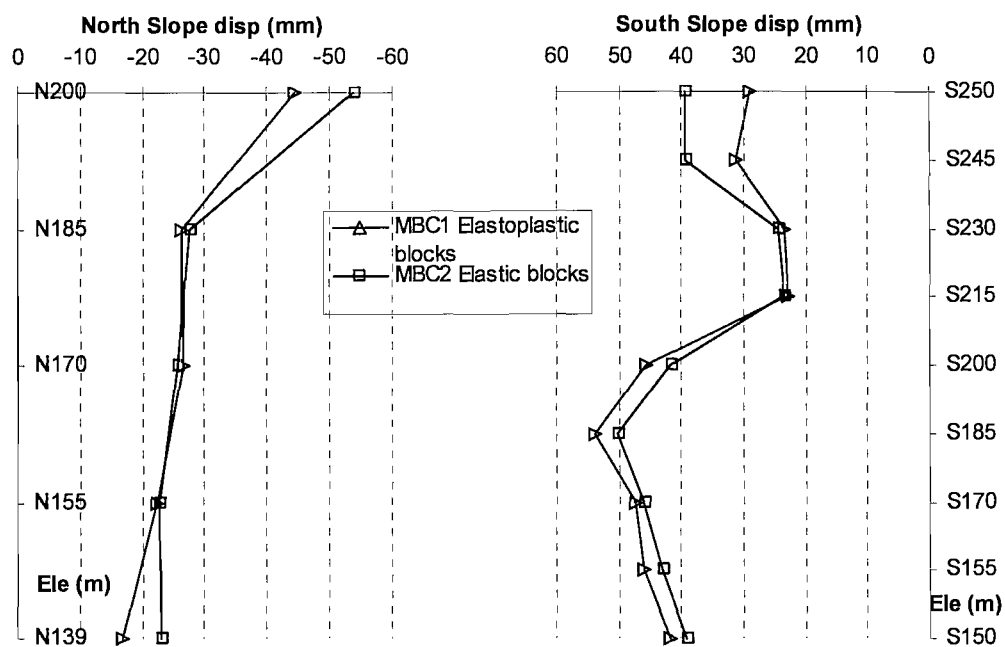| Models	Dilation angle (°)
	BMat1 /2 /3 /4
MBD1 (base)	0 / 0 / 0 / 0
MBD2	15 / 7 / 0 / 0
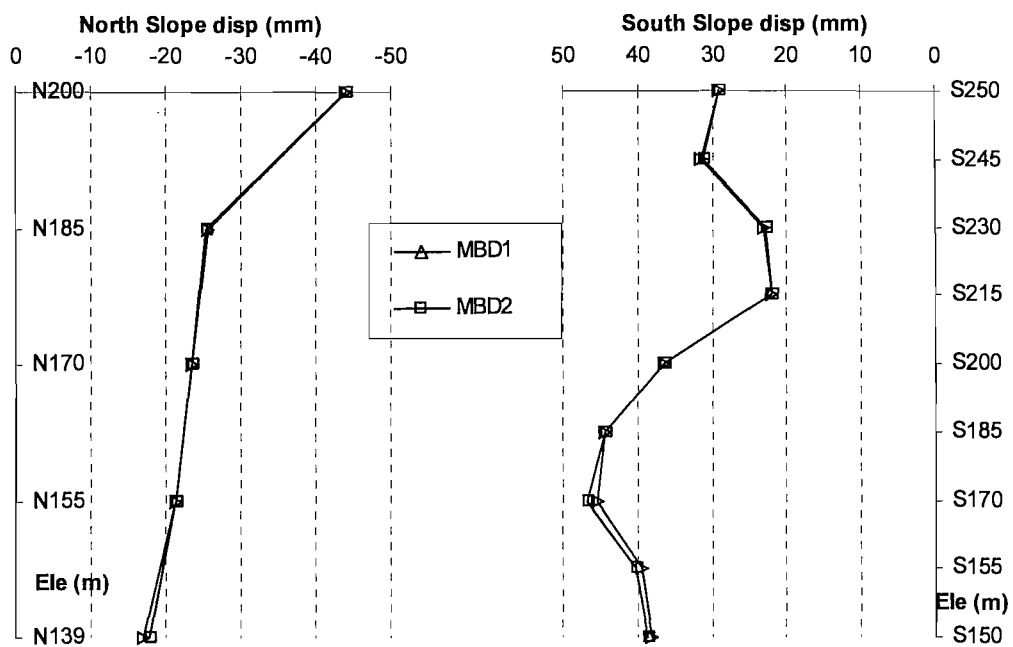
Fig6.46 Comparison of total Y deformations along height of slopes predicted by models with different dilation angles for rock blocks
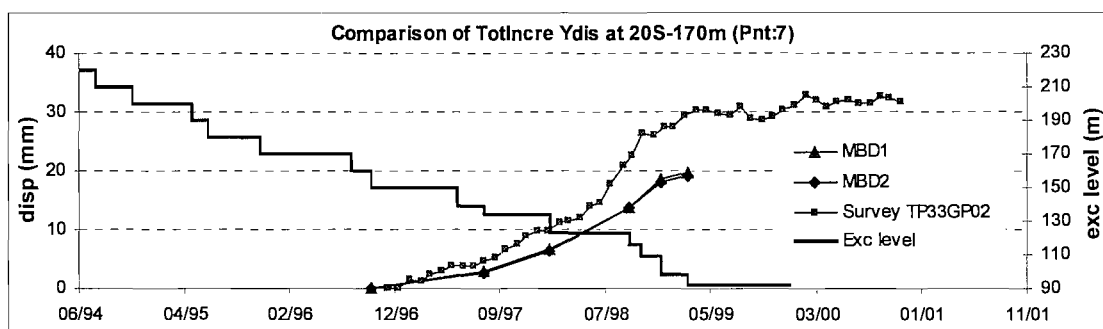
Fig6.47 Y deformation vs time at point 7 (S-170m)
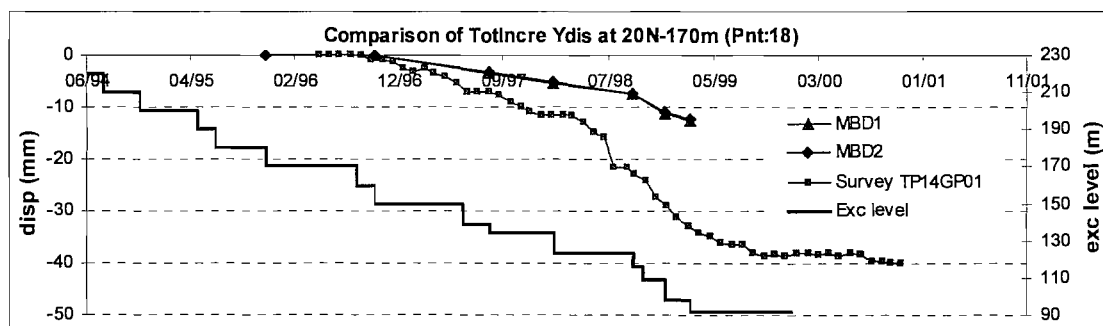
Fig6.48 Y deformation vs time at point 18 (N-170m)

193

6.5.5 Conclusion of parametric study of material properties

Among the properties of rock blocks, the block modulus appears to be the most sensitive parameter of the model.

The elasto-plastic model is more representative of the behavior of rock blocks than elastic model. The effect of different models may be not fully reflected in match to field data because a large part of the difference probably occurred before the record of field data.

The model is generally insensitive to the friction angle and the cohesion of rock blocks with the exception of the weak material in the weathered zone. Block dilation angle is an insensitive parameter to the model.

6.5.6 Parametric study of EDZ properties

As discussed before, there are considerable uncertainties regarding the material properties and range of the EDZ. In this section, the effect that these factors have on predicted deformation is investigated.

6.5.6.1 Discontinuities in the EDZs

There were a number of discontinuities existing in or across the extent of the EDZ. As discussed in section 6.3, these discontinuities or the part of them within the range of the EDZ were considerably weakened by excavation. Their stiffness could be reduced to 75% of its original value (Sheng et. al., 2002) as listed in Table6.1. From the parametric study on discontinuity properties, we know the joint stiffness is the most influential factor for the model. In order to find out how much this affected the rock behavior, a model with normal joint stiffness (ME3) was further run to compare with the base model ME2, in which the discontinuities in the EDZ were assigned with the weakened stiffness as listed in Table6.1. The other material properties used in the models are listed in Table5.1 and 5.2 for range outside of EDZ and in Table6.1 for EDZ properties.

The results are compared in Fig6.49 to Fig 6.92. By reducing the joint stiffness for the discontinuities in the EDZ range, the model ME2 predicted improved deformation. The difference of the total y deformation was at an average of 4mm to 5mm on the south slope. The difference was less on the north slope because of the presence of fewer discontinuities.

It can be seen that the discontinuities in the EDZ had an important effect on predicted deformation. It is concluded that it is important to model major and intermediate discontinuities in EDZ individually and to assign them with weakened properties.
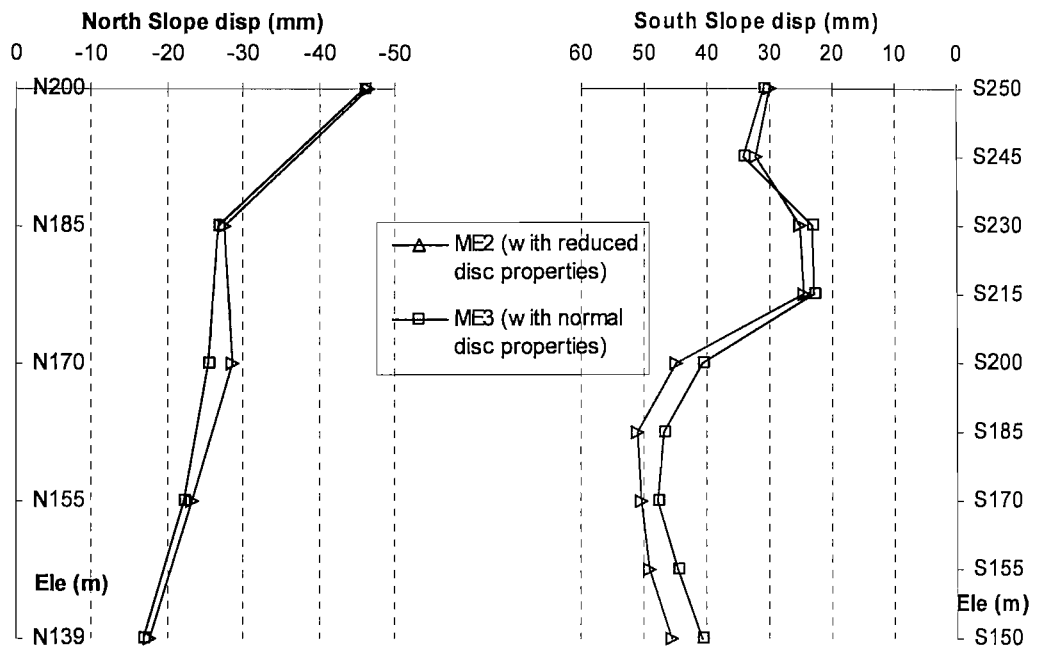
Fig6.49 Comparison of total Y deformations along height of slopes predicted by models with and without considering discontinuities in the EDZ
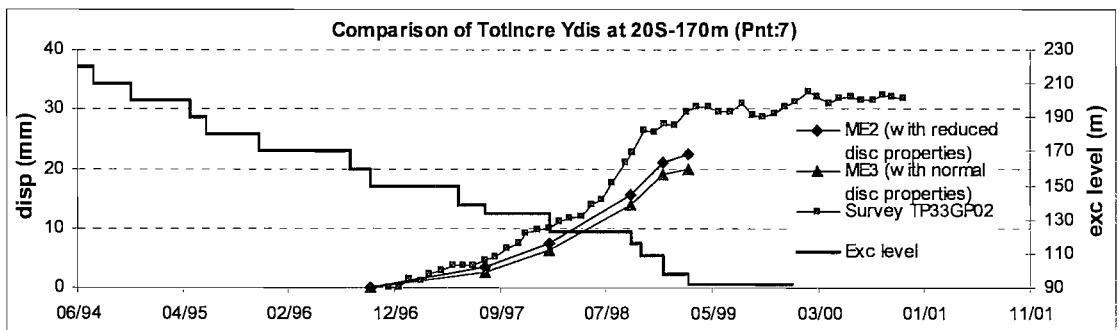
Fig6.50 Y deformation vs time at point 7 (S-170m)
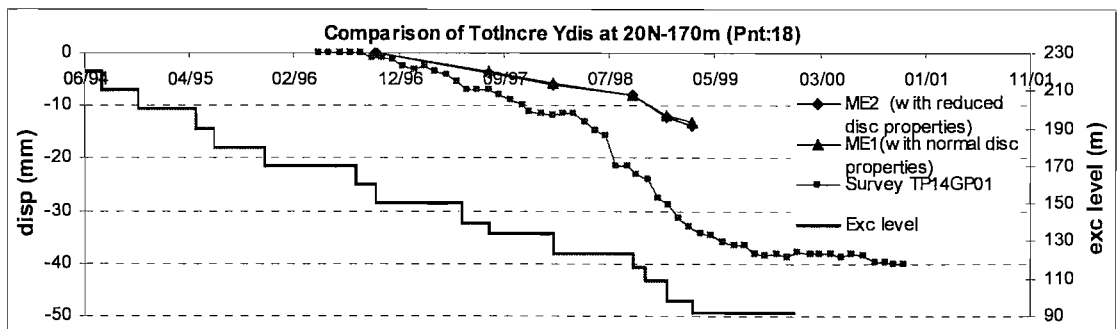
Fig6.51 Y deformation vs time at point 18 (N-170m)

6.5.6.2 The range and block properties of the EDZ

To investigate the effect of the range and properties of the EDZ, a further model ME4 based on model ME3 was run with the excavation affected subzone switched to excavation damaged subzone, which ranges from 15 to 20m from excavation (Fig6.5). The excavation damaged subzone has weaker material properties than the excavation affected subzone. The EDZ in ME4 was further weakened compared with ME2 because it has a damaged zone at the combined range of damaged zone and affected zone in ME3. Both models have normal joint properties for discontinuity in the EDZ (Table6.1). Because EDZ did not extend into the highly and moderately weathered zone (Fig6.5), the material properties for these weathered zones were not changed.

With the increased range of the damaged subzone, the model ME4 has shown increased deformation of between 2mm-4mm at most locations (Fig6.52). The largest difference occurred at points S-150m and S-155m on the south slope. There was little difference on the points in weak materials, e.g. S-170m in the xenolith "ex" (Fig4.61), because the material was weak in both models. The distribution of the deformation difference was quite even in changed areas along slopes. This indicates it was more of effect of reduced block modulus rather than plastic deformation.

These results are largely in line with the results of previous parametric study on block properties. For unweathered rock, numerical results are insensitive to block strength, therefore the deformation change was mostly due to reduced block modulus.

However, little difference is made on the match to field data (Fig6.53 and Fig6.54), because such difference occurred before history of field data as shown in Fig6.55.

Apparently the effect of EDZ range and block properties is also largely dependent on the assumed extent of the EDZ. Considering the limited scale of the EDZ, it is reasonable to assume the range and properties of EDZ are slightly sensitive parameters of the model. This may not be the case if a large scale of EDZ is present.
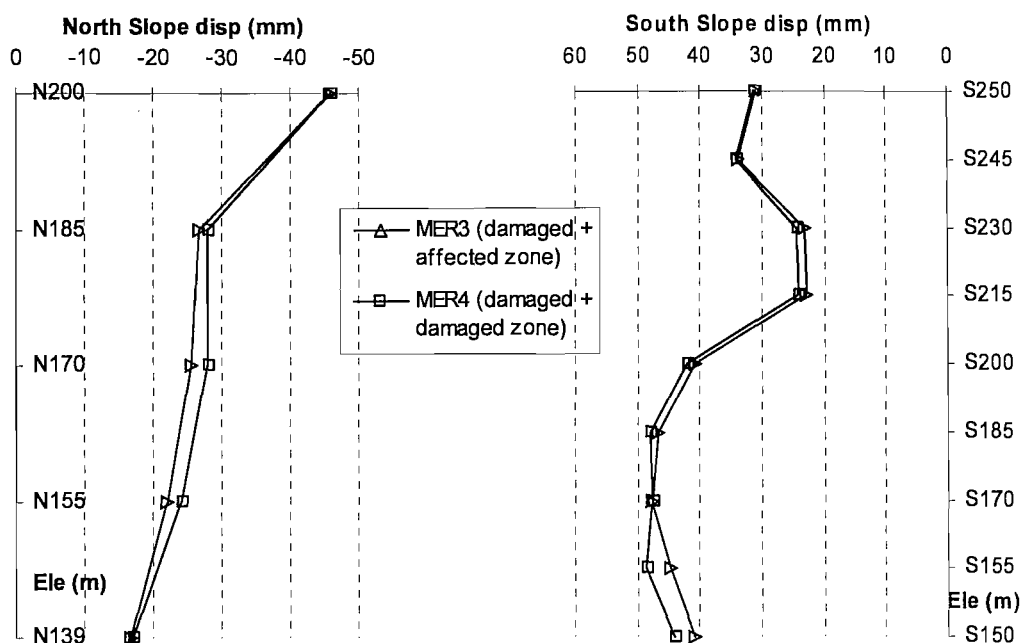
Fig6.52 Total Y deformations of models with different EDZ subzones
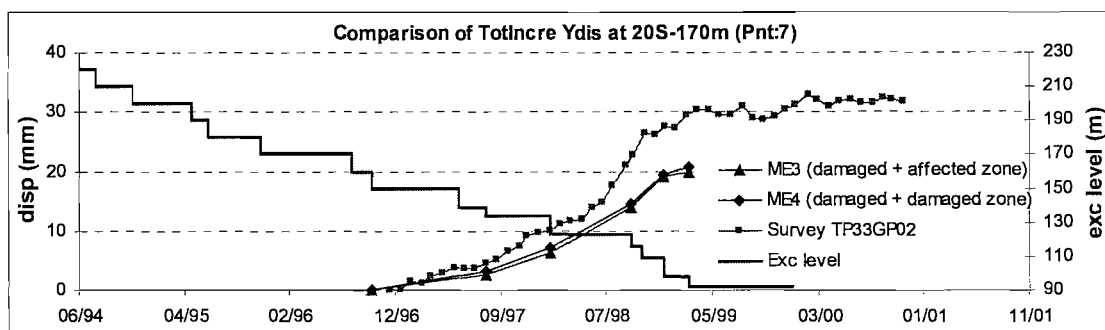
Fig6.53 Y deformation vs time at point 7 (S-170m)
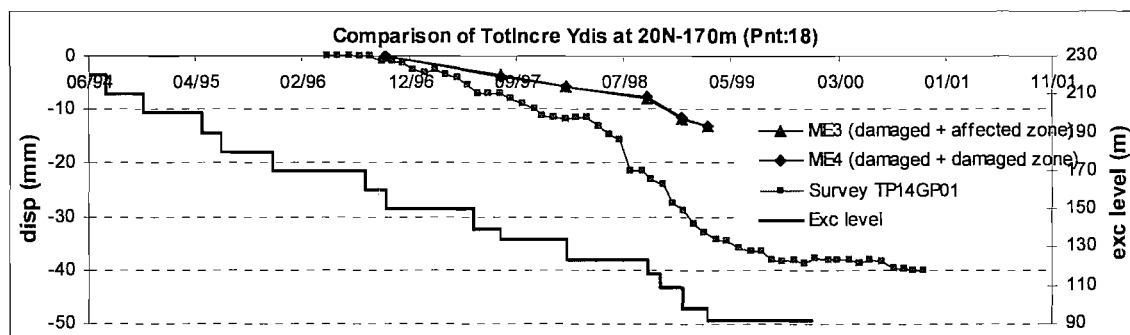
Fig6.54 Y deformation vs time at point 18 (N-170m)
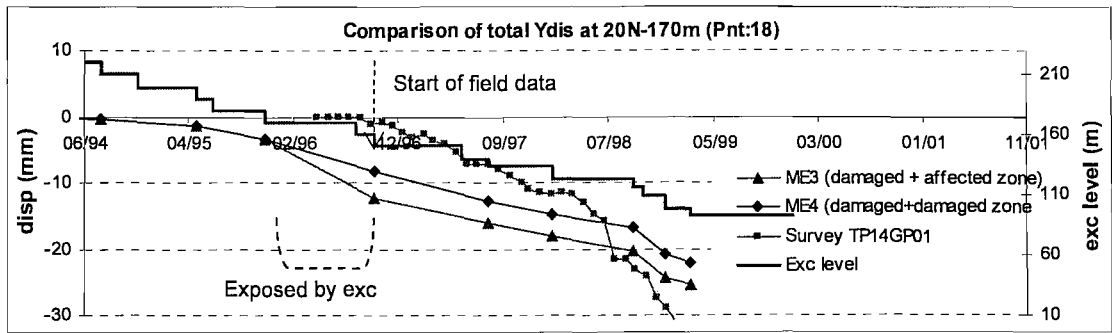
Fig6.55 Time of differential deformation and field data at point 7 (S-170m)

6.6 A comparison between 2D and 3D modelling approaches

In principle 3D analyses are superior to 2D analyses in approximating reality. However this advantage comes with a price, as 3D analyses require more detailed input information and more computational effort. As a result, 2D analyses are more commonly used.

A structure of relatively constant cross section, whose dimensions are much smaller than the length of the structure, can be considered to deform in 2D plane-strain if it is only subject to loads that are constant along the x axis and perpendicular to it. Then all cross sections perpendicular to the x axis remain in the same plane during deformation. Stresses, strains and displacements are functions of y and z only, while $\varepsilon_x = 0$; $\tau_{xy} = \tau_{xz} = 0$ and $\gamma_{xy} = \gamma_{xz} = 0$.

True plane-strain conditions are rare in practice. However, 2D plane-strain simulations give a good approximation to the behaviour of structures such as long retaining walls, bore holes, horizontal tunnels etc. In general, such 2D analyses differ from reality or a 3D analyses in the following aspects.

Firstly, there is no out-of-plane shear stress in the model, i.e. $\tau_{xy} = \tau_{xz} = 0$, which have an effect on the in-plane deformation. This also implies that the x axis is a principal direction of the in situ stress which might not be necessarily the case in reality.

In a 3D model, the blocks in the in-plane section are bonded with material outside with normal rock block strength if the effect of discontinuities is discarded. Therefore the behaviour of the in-plane blocks is restrained by material continuity. But for the 2D model, such bondage does not exist since there is no out-of-plane shear stress allowed to exist, i.e. the 2D model is cut off from the 3D entity by zero strength discontinuities parallel to the in-plane.

Secondly, the increments of out-of-plane normal stress cannot be prescribed, as they depend on the increments of in-plane stress components through the constitutive relations of the material.

Thirdly, in a 2D model discontinuities are usually represented by their traces on the section plane, which in most cases have different strikes and lower dip angles than the discontinuities themselves.

These differences can lead to different behaviour, or even different deformation mechanisms between 2D and 3D analyses, or between a 2D analysis and reality.

Comparisons between 2D and 3D models of the same problem have been carried out in slope stability analysis (Duncan, 1996; Stark & Eid, 1998; Chugh, 2003), tunnelling in soil (Dasari et. al., 1996) and strutted excavations in soils (Lee et. al., 1998). The literature shows that 2D analyses generally yield conservative estimates for the factor of safety, or larger deformations than 3D analyses. The lack of out-of-plane shear stresses has an important influence on the difference. Stark & Eid (1998) pointed out that, when the side resistance of a slide mass is not included in a 3D analysis, the calculated factor of safety is close to the average factor of safety given by 2D analyses. Stallebrass et. al. (1994) proposed a reduction of 34% of nodal forces in a 2D plane-strain analysis of an excavation in clay in order to match field measurements, to which 3D analysis yielded a close match.

Overall, a detailed investigation of the difference between the results of 2D and 3D analyses is still lacking. In this section, a comparative study was carried out to investigate the suitability of 2D analyses and the difference between 2D and 3D results obtained using UDEC and 3DEC analyses. The investigation is presented in three parts: comparison of predicted deformations and field data, effect of out-of-plane boundary conditions and effect of discontinuity orientations. In the first part (section6.6.1), the 2D and 3D predictions are compared in terms of surface deformation and subsurface deformation. The comparisons with field data arrive at the conclusion which model yields better results. In the second and third part (section6.6.2 and 6.6.3), the individual factors contributing to the difference between 2D and 3D models are examined in more details.

The 2D model, run in UDEC, had identical geometry, geological features and construction stages to the central section of the 3DEC model. Only the in-plane stress components (Syy, Szz and Syz) of the in situ stress field could be applied as boundary conditions while the out-of-plane normal stresses Sxx may only be initialized in order to accelerate reaching equilibrium of the initial conditions. However the distribution of Sxx at equilibrium depends on the in-plane stresses and the constitutive parameters.

Same to the case of 3D models in 3DEC, the 2D models were prescribed with stress boundary conditions before excavation (Fig6.56 (a)). The lateral in-plane boundaries and the bottom were fixed during excavation (Fig6.56 (b)).

An perfectly plastic Mohr-Coulomb model was used for the rock blocks and the discontinuities of all 2D models. The material properties used are listed in Table5.1 and 5.2 except where stated otherwise. The configuration of the EDZ subzones is shown in Fig6.5 and is the same as the one used for 3D models.

The 2D model predictions and 3D model predictions are compared with each other and field data. The comparisons are discussed.
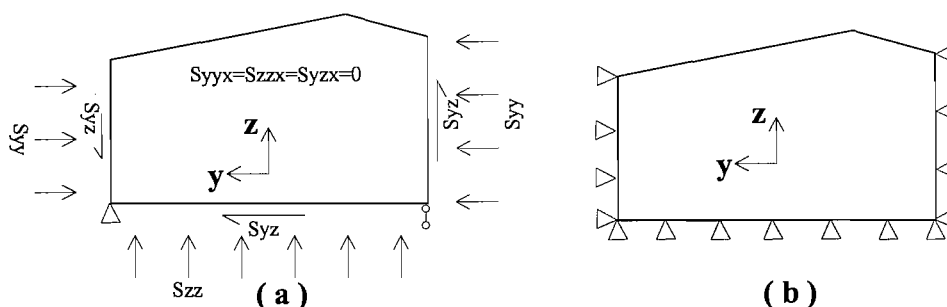
Fig6.56 Boundary conditions for in-plane boundaries

6.6.1 Surface and subsurface deformation

6.6.1.1 Comparison of surface deformation

In this section, in-plane surface deformations from the 2D and 3D models are compared to field survey data. The material properties used are listed in Table5.1 and 5.2.

Fig6.57 to Fig6.59 show that both models produced similar mechanisms and trend of deformation vs time curves and underestimated the in-plane horizontal deformations. But the 2D model predicted closer deformation to field data in the y direction. On the other hand, the vertical deformations in 3D model (Fig6.60 to Fig6.61) matched the survey data within the considered accuracy of the latter.

The 2D model yielded larger deformation than the 3D model (Fig6.57 to Fig6.62). This was consistent with the conclusions of the majority of literature. It was a similar case for the trends of vertical deformations.

It can be seen that both 3D and 2D model predicted the trend of field data well but underestimated the deformation. The 2D model predicted larger overall deformation that was closer to the field data.
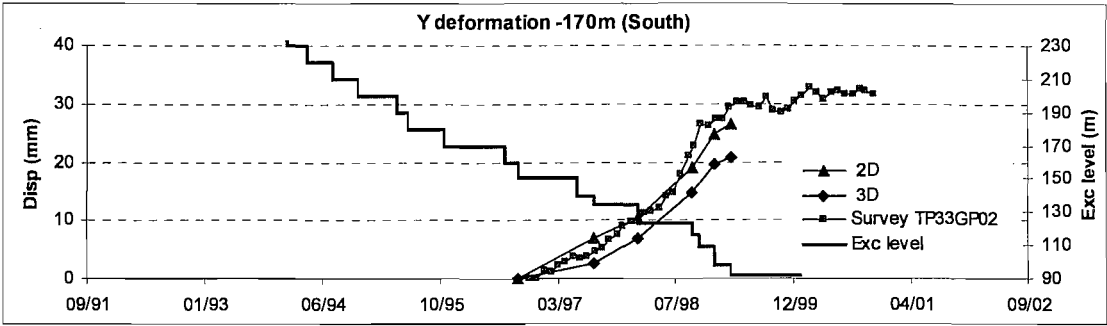
Fig6.57 Y surface deformation comparison at point S-170m
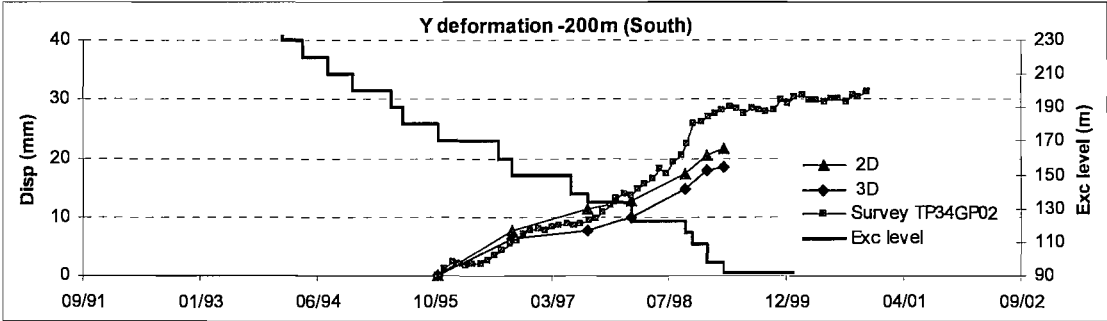
Fig6.58 Y surface deformation comparison at point S-200m
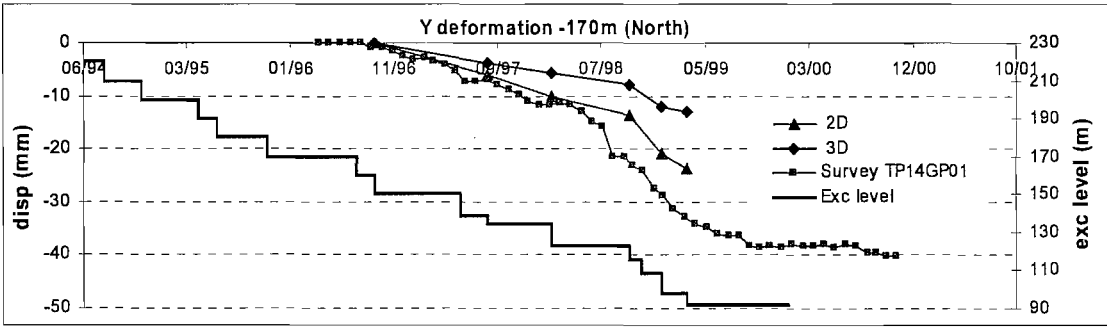
Fig6.59 Y surface deformation comparison at point N-170m
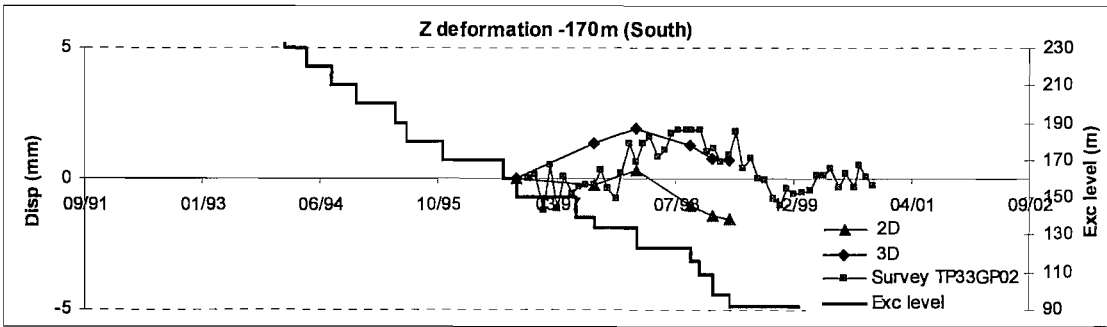
Fig6.60 Z surface deformation comparison at point S-170m
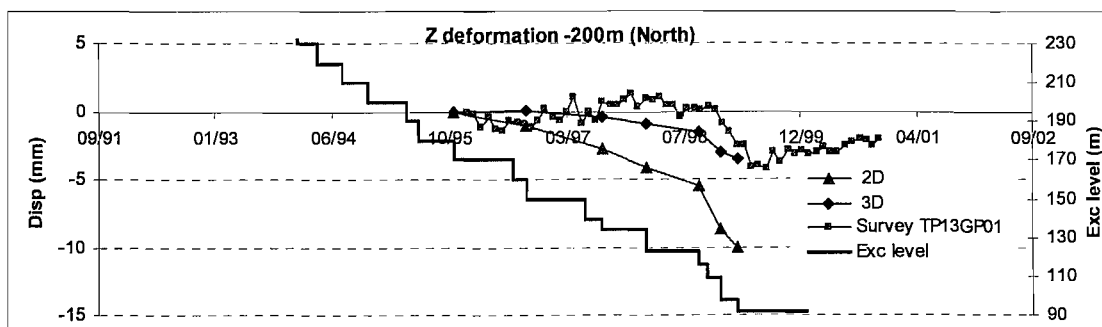
Fig6.61 Z surface deformation comparison at point N-200m
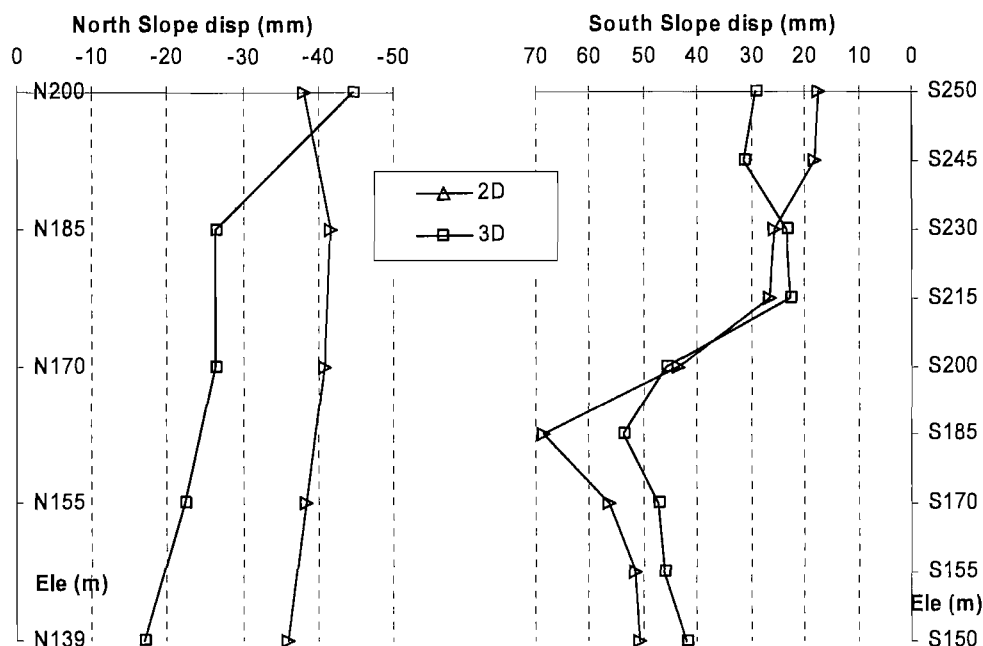
Fig6.62 Comparison of total Y deformations along height of slopes predicted 2D and 3D models

6.6.1.2 Comparison of subsurface deformation

Inclinometer data were not available for each vertical line set out in section5.4. Comparisons of deformations along these lines were divided into two types (type I and II, Table5.7) depending on the availability of corresponding inclinometer data and survey data.

For lines where inclinometer data are available with survey data, the 2D and 3D model predictions were compared with inclinometer data in terms of the deformation increment since the installation of the inclinometer (comparison type I, Fig6.63 to Fig6.70). If there were no survey data available for the inclinometer, the 2D and 3D model predictions were compared with inclinometer data in terms of the deformation increment relative to the bottom of the inclinometer since the installation of inclinometer (comparison type II, Fig6.71 to Fig6.73). In

all comparisons, the field data are denoted by the inclinometer id, measurement time and corresponding excavation elevation in the legend.

Between the 2D and 3D predictions, all three cases can be found in the comparison: (1) 3D model showed better matches to the inclinometer data, e.g. Fig6.67 and Fig6.69; (2) 2D and 3D model predictions were of the same quality, e.g. Fig6.72, and (3) 2D model showed better matches to the inclinometer data, e.g. Fig6.65.

Overall, the comparison did not show an overwhelming advantage of 3D results over 2D results, and on some locations, 3D and 2D analysis gave predictions of equal quality. However, when 3D model predictions were better than the predictions of the 2D model, they were much better, e.g. Fig6.67 and Fig6.69. On the other hand, when 2D model predictions were better, they were only marginally better, e.g. Fig6.64 and Fig6.65. In particular, the 2D model presented unstable wedges (Fig6.74) that were not evident in the survey data. This can be attributed to the lack of lateral shear resistance and the fact that all the dipping direction of discontinuities was diverted into the section plane.

6.6.1.3 Summary on model deformations

The comparison on surface and subsurface deformations has shown a consistency with the literature in that the 3D model yielded lower deformation than the 2D model. The 2D model predicted more unstable wedges that were not evident in the survey data. Both observations can be attributed to the lack of shear resistance and the fact that the true orientation of the discontinuities cannot in general be modelled.

The 2D model yielded the closest surface deformation magnitudes to the field data. However subsurface deformation profiles suggested that the 3D model predicted the overall deformation mechanism better.
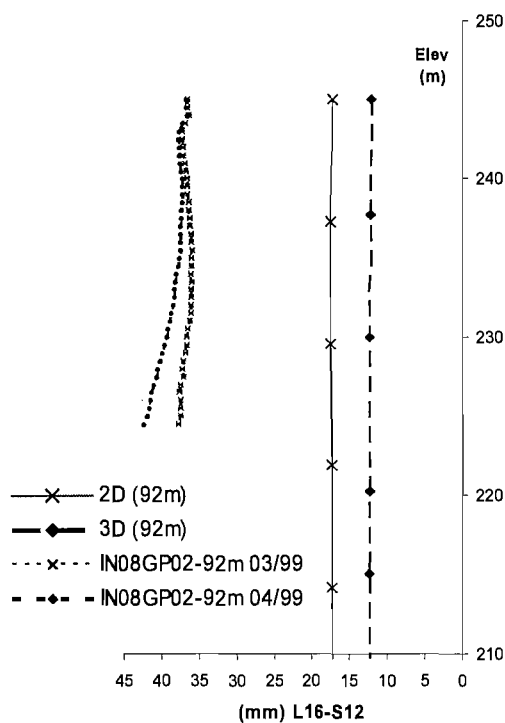
Fig6.63 Subsurface comparison of type I, S-245m
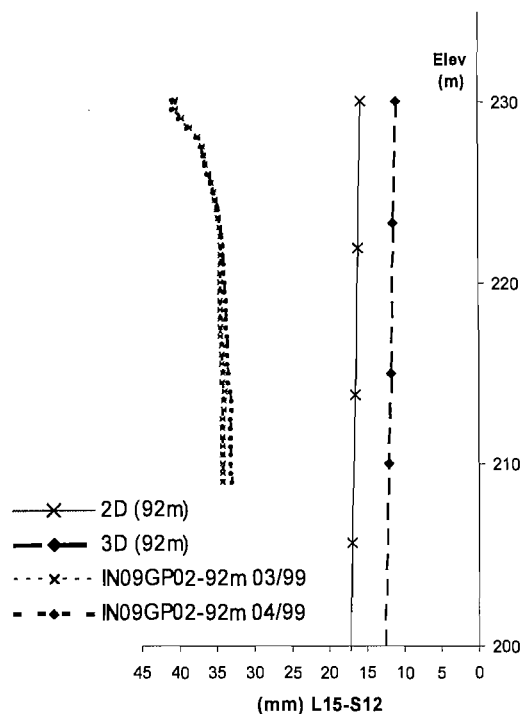
Fig6.64 Subsurface comparison of type I, S-230m
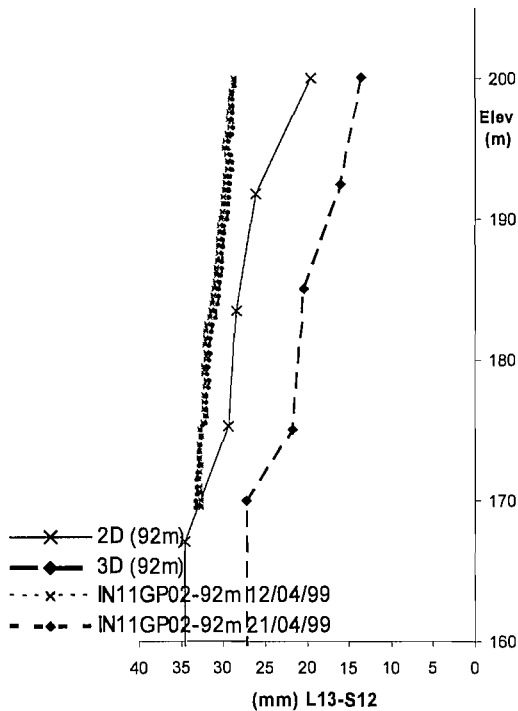
Fig6.65 Subsurface comparison of type I, S-200m
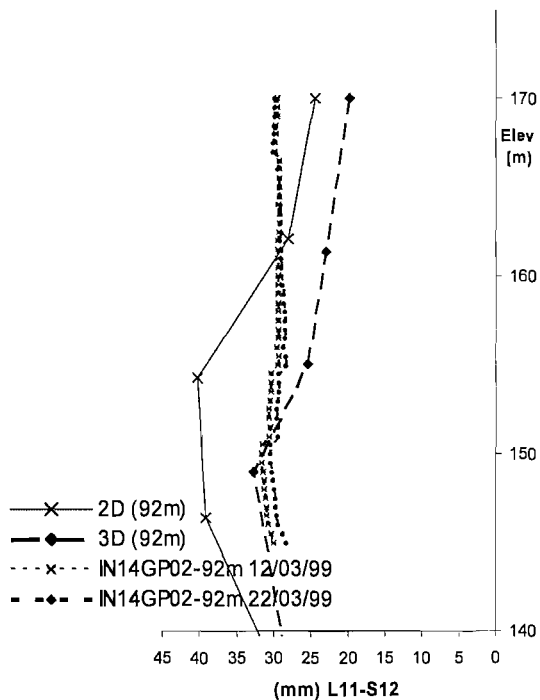
Fig6.66 Subsurface comparison of type I, S-170m
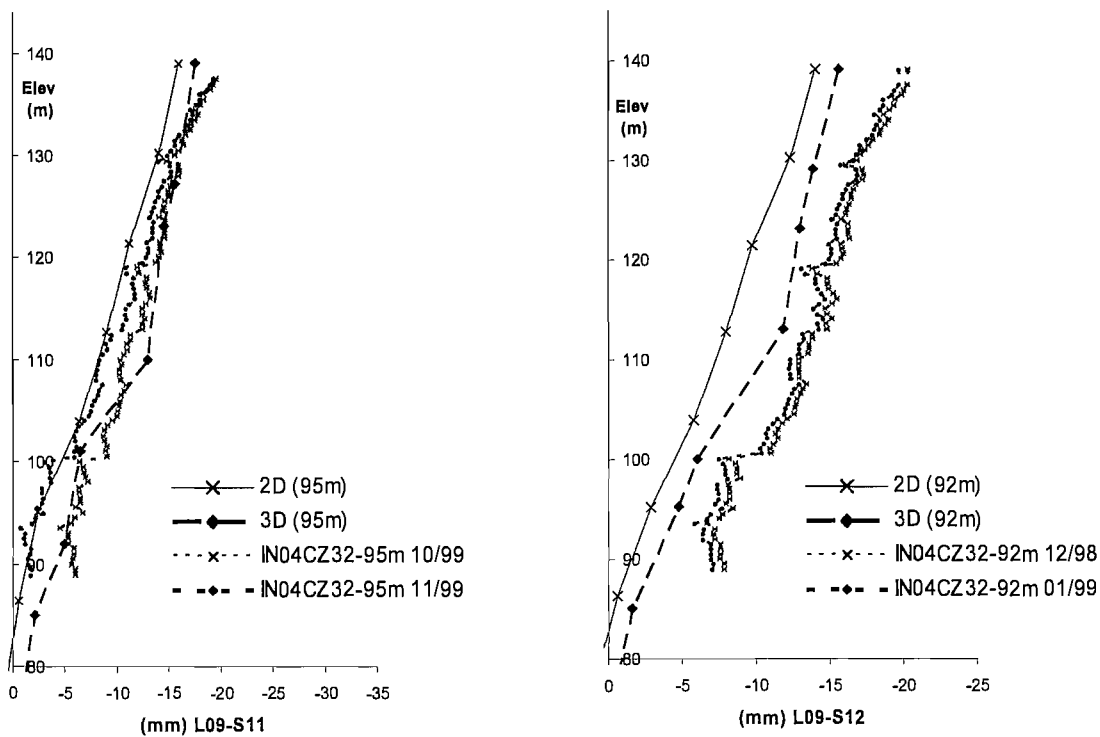
Fig6.67 Subsurface comparison of type I, MS-139m
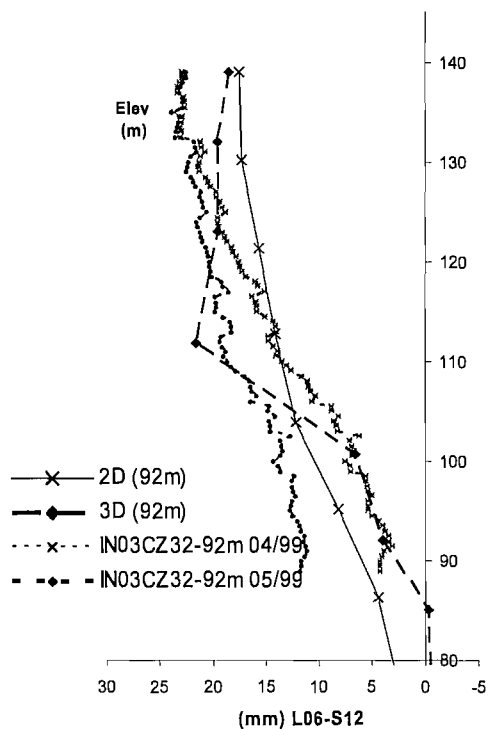
Fig6.68 Subsurface comparison of type I, MN-139m
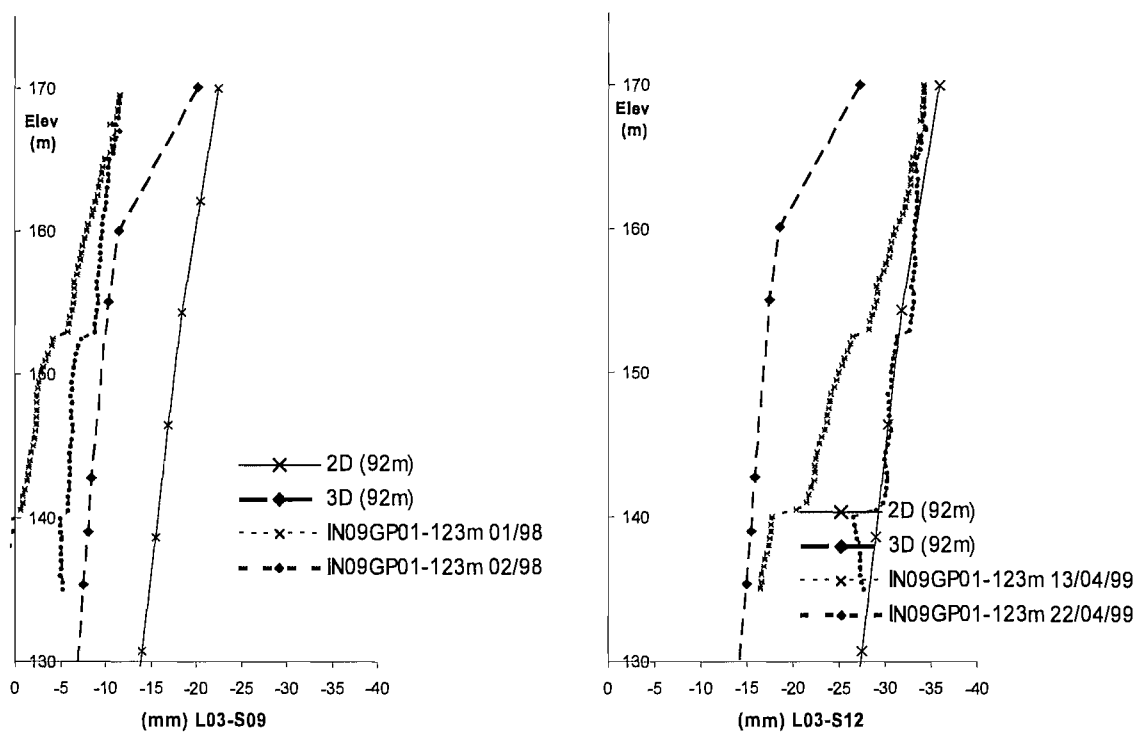
Fig6.69 Subsurface comparison of type I, N-170m
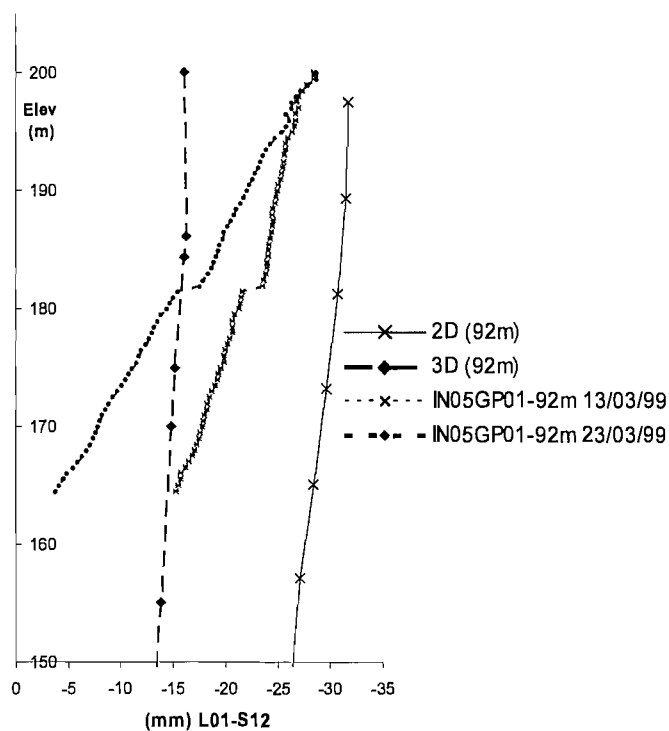
Fig6.70 Subsurface comparison of type I, N-200m
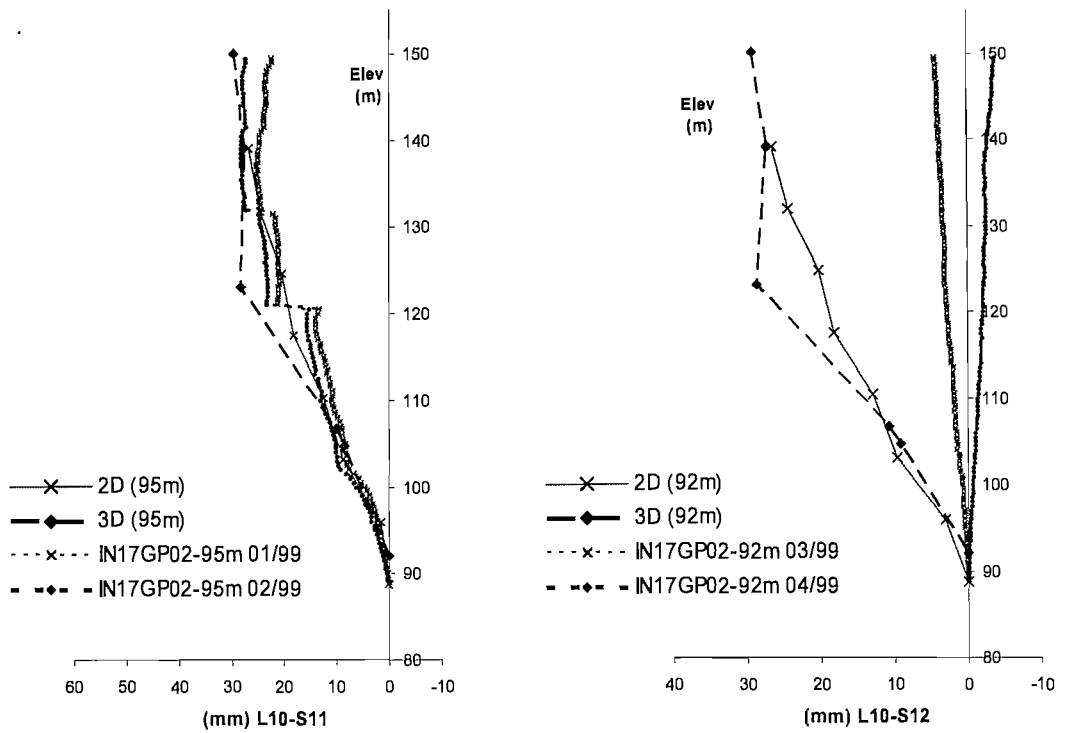
Fig6.71 Subsurface comparison of type II, S-150m
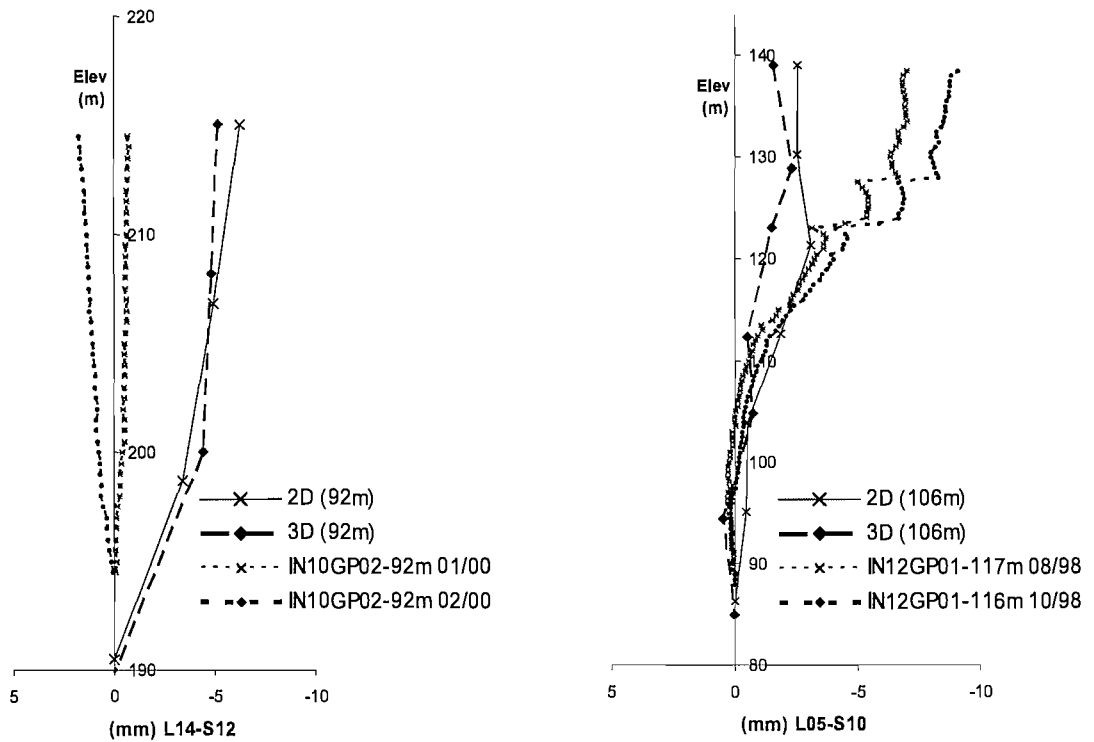
Fig6.72 Subsurface comparison of type II, S-215m

Fig6.73 Subsurface comparison of type II, N-139m (no further valid field data available after 10/98)

207
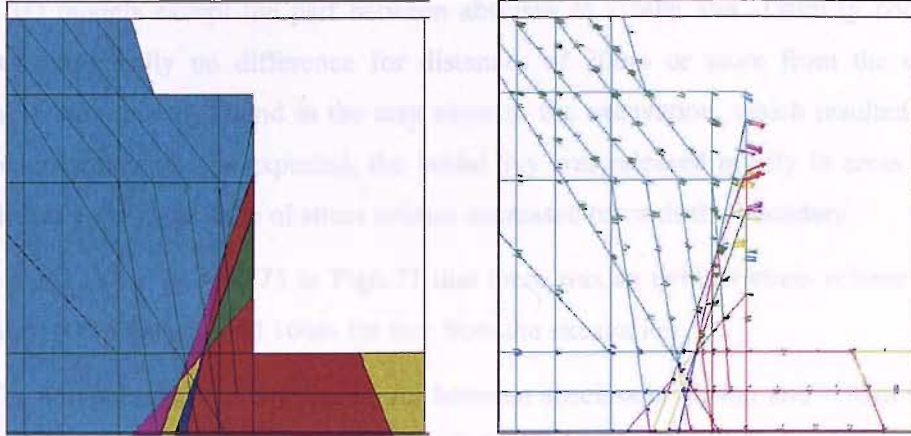
Fig6.74 Blocks and displacement along L05 (N-139m) in the 2D model

6.6.2 Stress conditions

The difference in the predictions seen between 2D and 3D models is expected to be reflected in their prediction for the stress conditions. To investigate this, predicted changes of stress due to excavation were compared for the two models.

This section presents numerical predictions of the stress along a horizontal line on the south slope at height of 139m, shown as line LH09 in Fig5.6. The line LH09 is selected because (a) its level is well above the excavation bottom line (about 40m), so excavation should cause significant stress change there; (b) the larger number of discontinuities on the south slope enables better investigation into effect of discontinuities on stress field and (c) it is one of the longest across the south slope, hence will provide more information in the model.

The sign conventions used are set out in section 3.5.2.

6.6.2.1 In-plane stress conditions

In-plane stresses, i.e. Syy, Syz and Szz in the model coordination system where the z axis is vertical and the y axis is in-plane horizontal, can exist in both 2D and 3D models. The comparison of Syy before and after excavation for the two models is shown in Fig6.75. The magnitudes of stress release of Syy and Syz due to excavation are compared in Fig6.76 and Fig6.77 respectively. The release of in-plane shear stress Syz is compared in Fig6.77.

Before excavation, the stress condition of Syy in the two models was very close as shown in Fig6.75. After excavation, the stress level of Syy dropped close to zero adjacent to the excavation. Except for the part close to the excavation, the profile of the stress curves of the two models remained similar after excavation.

Both Fig6.76 and Fig6.77 indicate the curves of stress release had similar shapes in the 2D and 3D models except the part between abscissa of -160m and -180m (y coordinations). There was practically no difference for distances of 200m or more from the central axis. Differences were mainly found in the area close to the excavation, which resulted to different predicted deformations. As expected, the initial Syy was released mostly in areas close to the excavation and the magnitude of stress release decreased towards the boundary.

It can be seen in Fig6.75 to Fig6.77 that there was an evident stress release zone which ranges about 65m for Syy and 100m for Syz from the excavation.

The abrupt changes along the curves between abscissa of -160m and -180m were closely related to the presence of discontinuities (Fig6.78). It can be concluded that modelling the discontinuities properly (i.e. in 3D) can result in local differences in the predicted stress field from what a 2D model would predict.
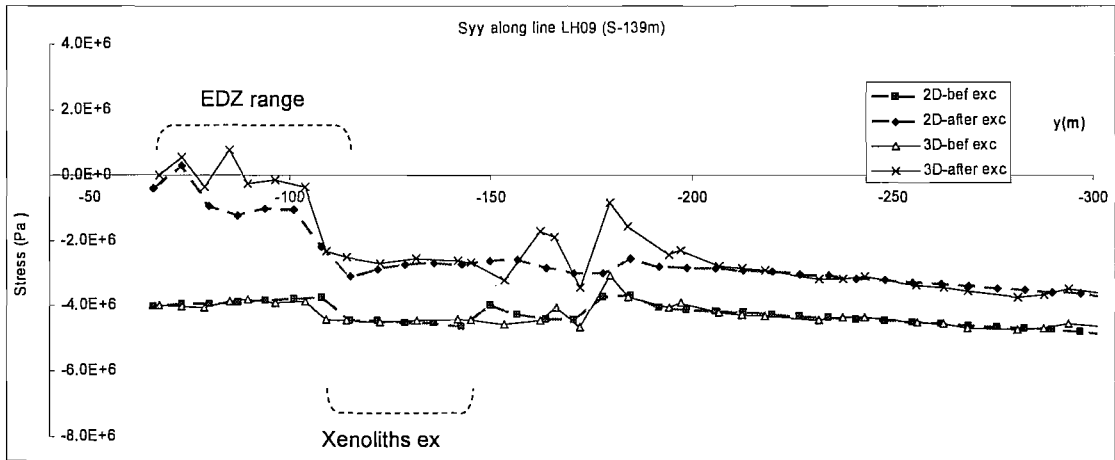
Fig6.75 Horizontal stress Syy before and after excavation in the 2D and 3D models (sign: "-" for compression and "+" for tension)
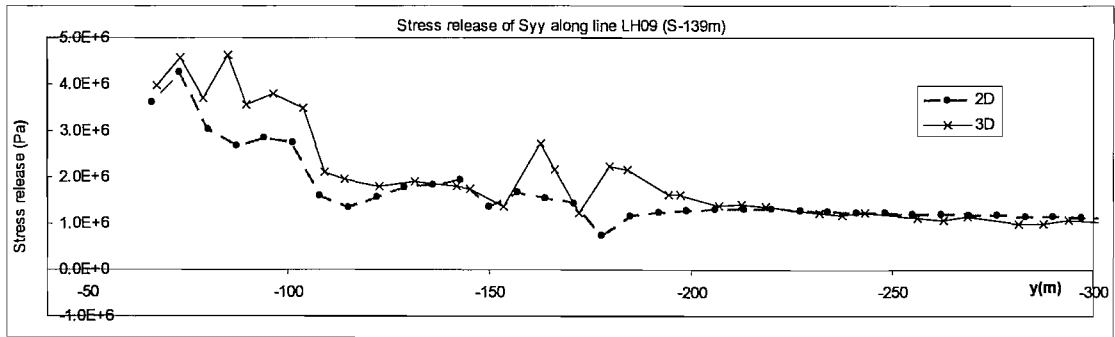
Fig6.76 Horizontal stress release of Syy due to excavation in 2D and 3D models

209
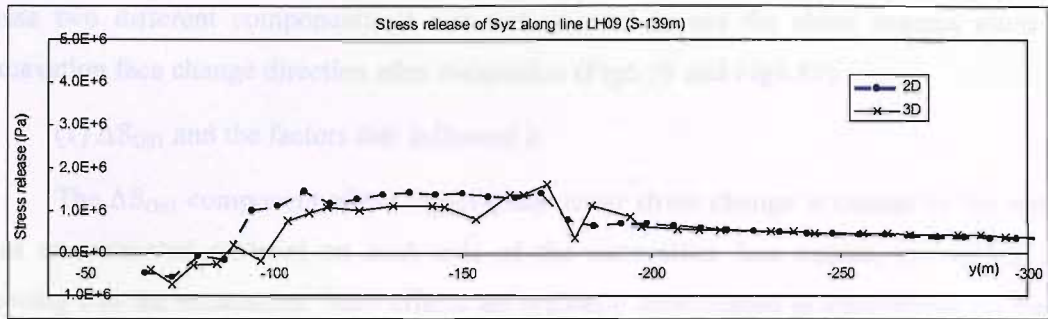
Fig6.77 In-plane shear stress release of Syz due to excavation in 2D and 3D models
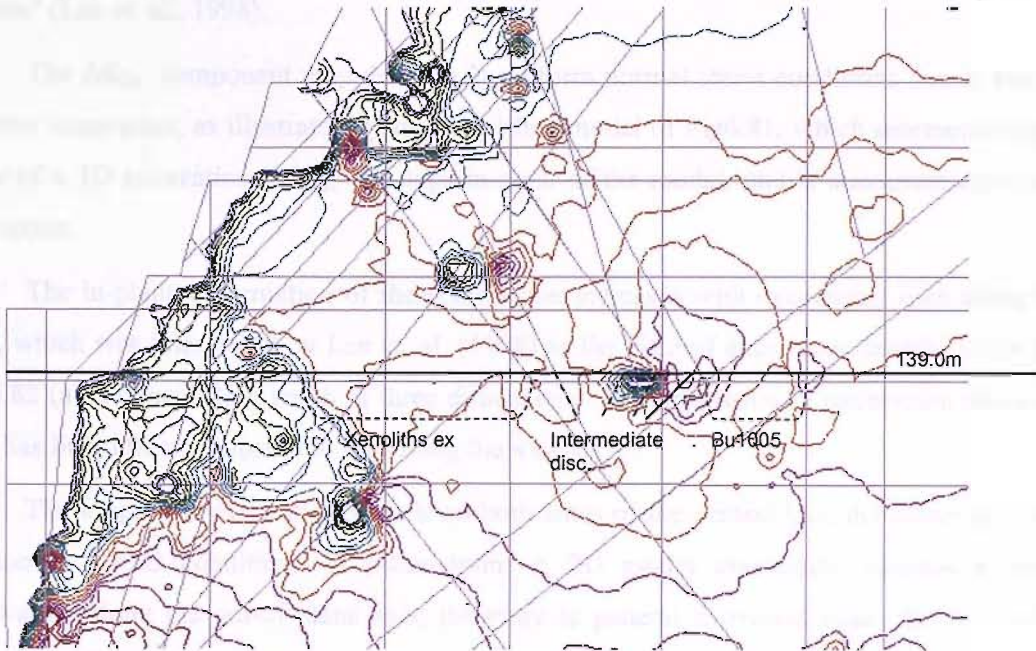
Fig6.78 Contour of Syy (horizontal in-plane) in the 2D model and discontinuities along the monitoring line

6.6.2.2 Out-of-plane shear stress conditions

The out-of-plane shear stresses Sxy and Sxz before and after excavation in the 3D model are shown in Fig6.79 and Fig6.80 respectively. In the 2D model, these stress components are identically zero.

The total change of out-of-plane shear stress due to excavation can be considered to consist of two parts: (a) ΔS_{OS1}, which corresponds to the out-of-plane shear stress that develops due to the tendency of the excavation face to move towards the excavated volume; and (b) ΔS_{OS2}, which corresponds to the reduction of the in situ out-of-plane shear stress from its original value close to the excavation, due to the excavation face being a stress-free surface. The ΔS_{OS1} and ΔS_{OS2} have different spatial distribution, as illustrated by an example of a

210

symmetric excavation in an elastic isotropic medium in two dimensions in the following. Due to these two different components, it was not unusual to see the shear stresses close to the excavation face change direction after excavation (Fig6.79 and Fig6.80).

(1) ΔS_{OS1} and the factors that influence it

The ΔS_{OS1} component of the out-of-plane shear stress change is caused by the restriction that un-excavated material on each side of the excavation face causes, preventing it from moving into the excavation. Such effects are typically encountered in excavations for basement construction in urban high-rise buildings (Fig6.81 (a)), and are commonly known as "corner effects" (Lee et. al., 1998).

The ΔS_{OS1} component may develop in uniform normal stress conditions due to any non-circular excavation, as illustrated by the simplified model of Fig6.81, which represents the plan view of a 3D excavation. ΔS_{OS1} develops in most of the model, and is maximum close to the restriction.

The in-plane deformation of the central line increases with excavation span along the x axis, which was interpreted by Lee et. al. (1998) as the ratio of excavation length (Lx or Ly in Fig6.82 (a)) to excavation depth in three dimensions. The dimension of excavation along the y axis has little effect compared to that along the x axis.

The longer the excavation span is on both sides of the central line, the closer the central section is to 2D conditions of plane-strain. A 2D model essentially assumes a through excavation along the out-of-plane axis; therefore in general it overestimates the deformation. When a section of interest represents a symmetry plane in a 3D problem, it will remain in plane-strain conditions during excavation if the in situ stress, excavation shape and boundary conditions are also symmetric. However the deformation will still be overestimated if the section is simulated as a 2D plane-strain model because the induced ΔS_{OS1} component outside the section will be ignored. In such cases, it is highly recommended to consider the ΔS_{OS1} component before adopting a 2D plane-strain model, e.g. complementary 2D analysis of the excavation in the plan view.

(2) The ΔS_{OS2} and the factors that influence it

The ΔS_{OS2} component represents the relaxation of initial out-of-plane shear stress, which is like torsion of a prismatic bar (Fig6.81 (b1 to b3)). The magnitude of ΔS_{OS2} cannot exceed the initial magnitude of the in situ out-of-plane shear stress. The ΔS_{OS2} generally resulted in tangent deformations or at an angle along the excavation boundaries (Fig6.81 (b2)), i.e. out-of-plane deformation. Along a line perpendicular to the symmetric line, the magnitude of ΔS_{OS2} increases along with distance to excavation boundary.

The effect of ΔS_{OS2} component depends on the initial magnitude that is determined by the in situ stress level and the relative orientation of the in situ principal stresses with respect to the section. In the TGP site, the out-of-plane in situ shear stress is low in magnitude and consequently little strain is caused by its relaxation. Therefore the lack of ΔS_{OS2} in 2D models is not expected to affect the difference between the deformation predicted by 2D and 3D models.

(3) Effects of out-plane-shear stress

It can be seen that mainly the ΔS_{OS1} component plays an important role in the difference between 2D and 3D models. This is shown in the Fig6.79 and Fig6.80 where Sxy and Sxz change sign at some parts after excavation due to ΔS_{OS1} since ΔS_{OS2} cannot change the directions of the Sxy and Sxz.

It is noted that the induced stress ΔSxy dissipated at the lower boundary of the xenolith "ex" at about y=104m, as a result of a slip along the discontinuity (Fig6.79). Further away from the excavation, the curve profile presents abrupt changes due to the presence of the upper boundary of the xenolith "ex", intermediate discontinuities f1007 and f1002, and vein 蓮1005 in the range of y=145m and 194m (Fig6.79). It can be seen that the distribution of induced out-of-plane stress is greatly affected by the discontinuities.

Similar observations can be made for stress Sxz, however the induced stress level was much lower (Fig6.80).
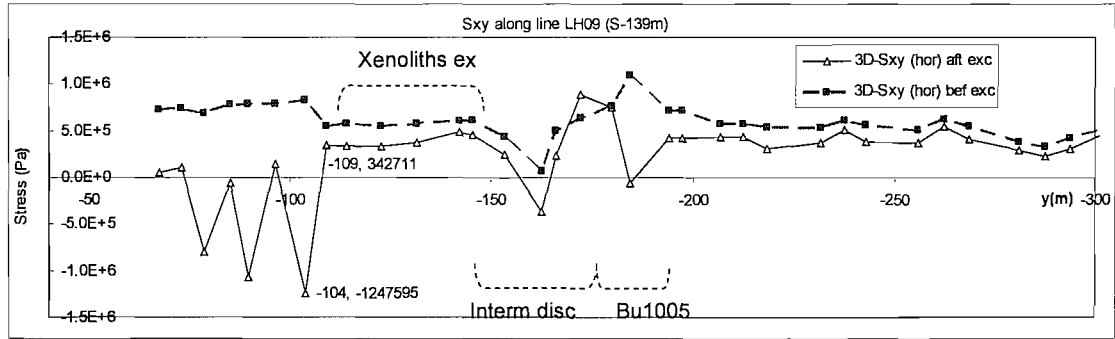
Fig6.79 Stress conditions of Sxy before and after excavation in the 3D model
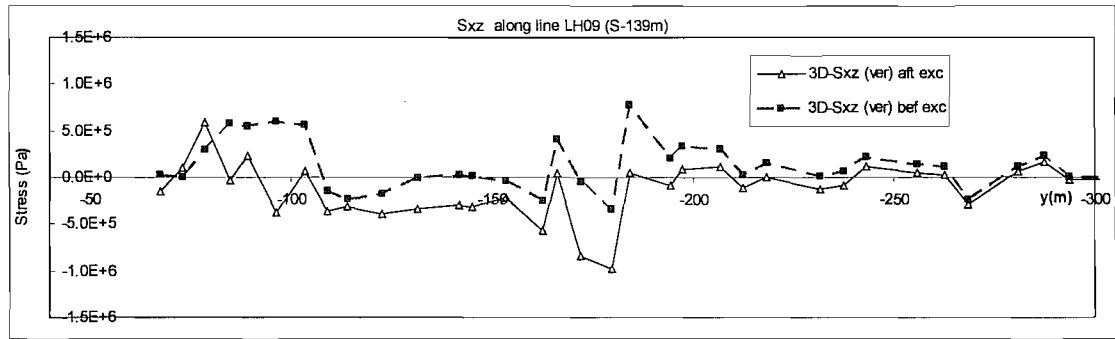
Fig6.80 Stress conditions of Sxz before and after excavation in the 3D model

(a1)   (b1)

(a2)   (b2)

(a3)   (b3)
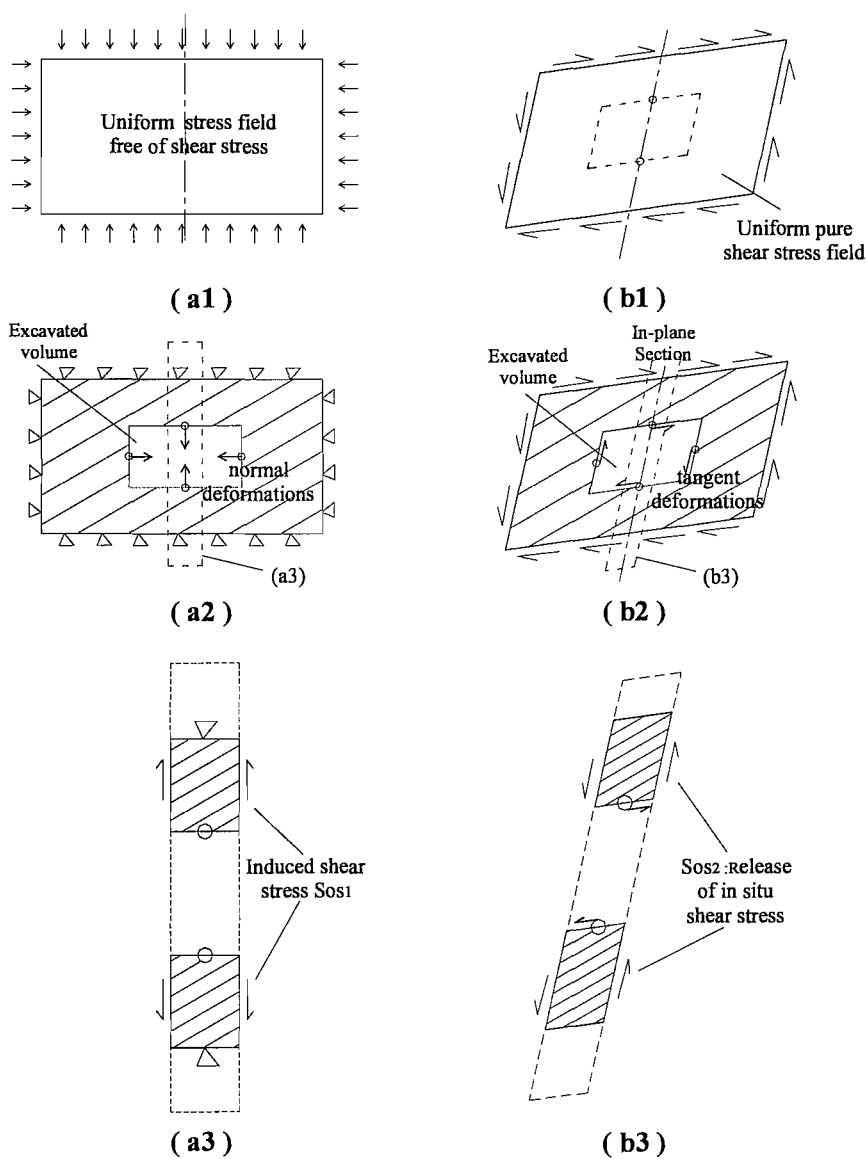
Fig6.81 Induced shear stresses in a 2D stress space (plan view)

(a)   (b)
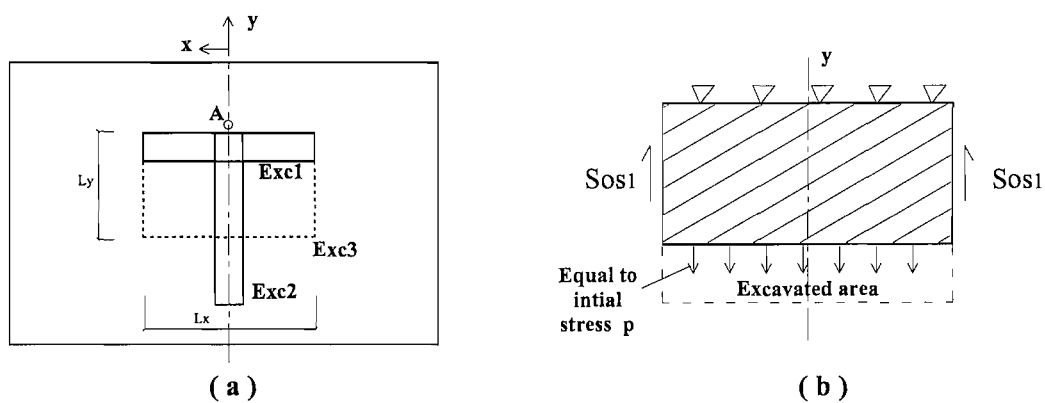
Fig6.82` Effect of excavation geometry and in situ stress on ΔS_{OS1} (plan view)

6.6.2.3 Out-of-plane normal stress conditions

As discussed in the beginning of section 6.6, the increments of the out-of-plane normal stress Sxx cannot be prescribed as they depend on the increments of the in-plane stress components through the constitutive relations of the material.

The difference of initial conditions of Sxx between the 3D and 2D model is shown in Fig6.83. The stress release of Sxx due to excavation is shown in Fig6.84 for both models.

Due to the plane-strain assumption, a 2D model predicts a different normal out-of-plane stress Sxx than a 3D model. This can consequently have implications for the predicted deformation pattern, especially if elasto-plastic material model is used. Therefore if extreme Sxx conditions are present, a 2D model should not be used.

The normal out-of-plane stress Sxx has a different effect on discontinuities in a 2D model from that of a 3D model or reality. It has little effect on the stress condition and movement along the discontinuities because the strikes of discontinuities were changed into along the x direction. Therefore if any major sliding along discontinuities towards out-of-plane is expected, 2D model should not be used.

The difference of horizontal in situ stress field between 2D and 3D models would increase when the direction of the horizontal principal stresses deviate from the section because the out-of-plane stress components is neglected in 2D increases (Fig6.85).

Therefore Sxx could be one of the reasons for the difference in predictions between 2D and 3D models. A 3D model should be used when any major out-of-plane deformations are expected on discontinuities or particularly high or low in situ Sxx exists. Otherwise a 2D analysis may be sufficient.
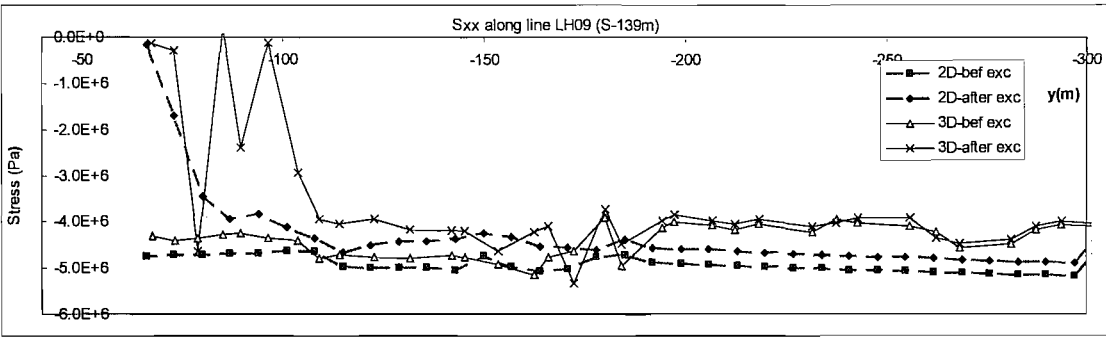
Fig6.83 Stress Sxx before and after excavation in 2D and 3D models (with plastic blocks)
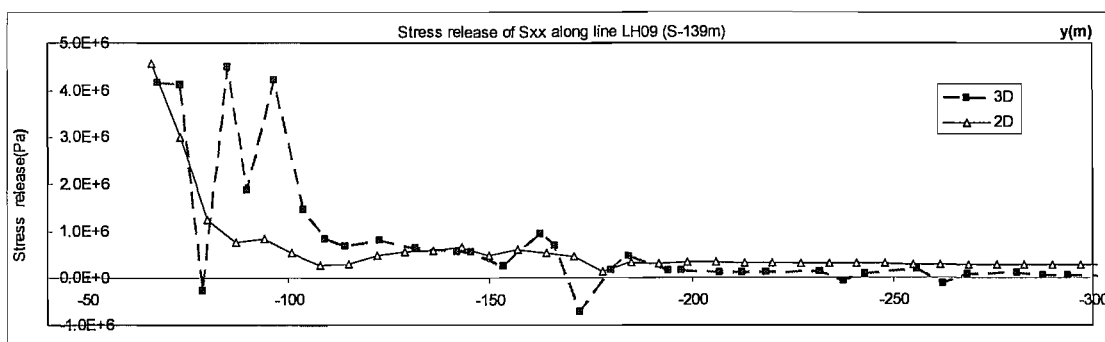
Fig6.84 Stress release of Sxx in 2D and 3D models (with plastic blocks) (res5)

(a) In situ stresses   (b) Stresses in 2D/2.5D model   (c)
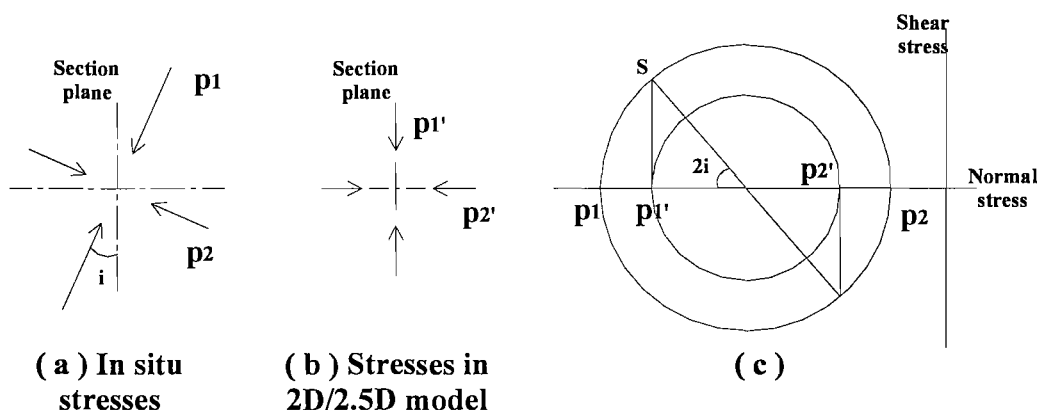
Fig6.85 Effect of orientations of horizontal principal stresses

6.6.3 Stress conditions in discontinuities and slips

The same discontinuity can behave differently in 3D and 2D models because (a) the in situ stresses prescribed and boundary conditions are different; and (b) the geometry (orientations and dip angle) of discontinuities is different.

As discussed in section 6.6.2, one of the main differences between the 2D and 3D model is the lack of out-of-plane shear restraints in the 2D model, which tends to enable blocks to slip more easily and cause more displacement along discontinuities. Additionally the behaviour of discontinuities becomes insensitive to out-of-plane normal stresses in 2D analysis, which could result in a different deformation mechanism from 3D situations.

The change of orientations and dip angle may have different effects on the model behaviour. In the 2D model, the potential slipping directions of all discontinuities are changed into the same plane by change of their strikes, which increases the probability of sliding. Thus more slips and/or larger relative displacements were observed in the 2D model and majority of them slipped downwards along the dipping directions of discontinuities.

215

The apparent dip angle in a 2D analysis is usually smaller than the actual one, which tends to stabilize the discontinuity. It is possible that a discontinuity is predicted to fail in 3D model but appears stable in a 2D analysis under same conditions. An example of this is shown in Fig6.86 (b) and (c). Therefore it is important to model the actual dip angle, particularly when the difference of apparent and true dip angles could change the condition of discontinuities.

There were cases where the 2D model predicted deformation mechanisms that were opposite to the ones predicted by 3D models and suggested by field data, e.g. (a2) and (b2) in Fig6.87 and a slip along line L05 at level of 105m (Fig6.73 and Fig6.2). This can be attributed to the difference of in situ stress conditions between the 3D and 2D models.

A notable difference between the 3D and 2D model predictions was that the latter predicted more slips and larger relative displacements along discontinuities than the 3D model (e.g. Fig6.74). The majority of them were the result of slipping downwards along the dipping directions of discontinuities. This shows that the different stress conditions and change of orientation are the dominant factors that increase the slips and deformations along discontinuities in the 2D model, as rock blocks formed by discontinuities in a 2D model have more freedom in the section plane than in a 3D model.

However, the effect of larger freedom on deformation depends largely on the general dipping directions of discontinuities relative to the excavation. Generally the deformation is expected to increase when most discontinuities dip into the excavation in the section plane, and decrease when they mostly dip into the slope. In Fig6.87, the contour of horizontal deformation on the south can be divided by two lines (line A and line B). The line A lies on the upper boundary of the region that contains the xenolith "ex" and four intermediate discontinuities dipping into the slope. As a result, the y deformation of the area above the line A is much lower than that of the area below the line A because of the overall dipping direction of the discontinuities. The contours below the line B generally run parallel along the direction of the vein 遙1005, which signals that the deformation in that area is dominated by the discontinuity. The Fig6.88 shows both cases on the south slopes in a smaller scale. The slips along vein Bu1005 that dipped to the north increased slope deformation in the 2D model (Fig6.88 (a1)) while other slips along discontinuities dipping to the south decreased slope deformation. It can be assumed that such effect would become significant for slopes with a dominant dipping direction of discontinuities in a 2D analysis.

(b) True dip

(c) Pseudo dip in 2D
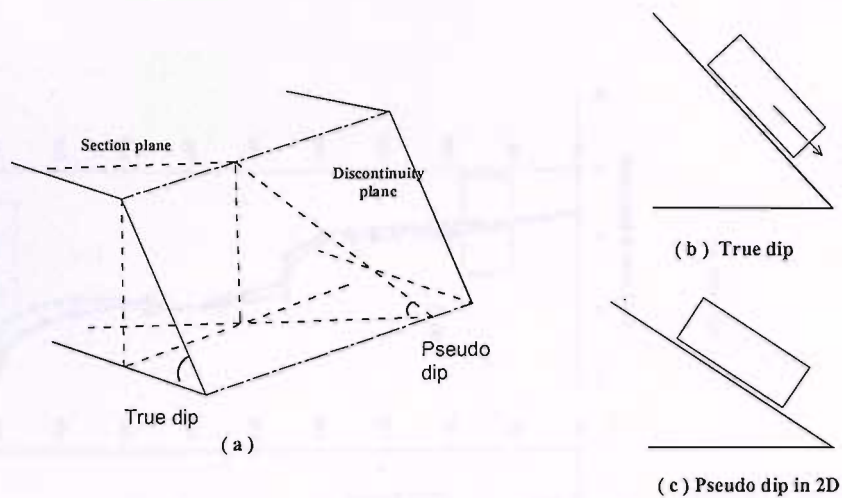
Fig6.86 Different dips change the mechanism: (b) in failure; (c) stable
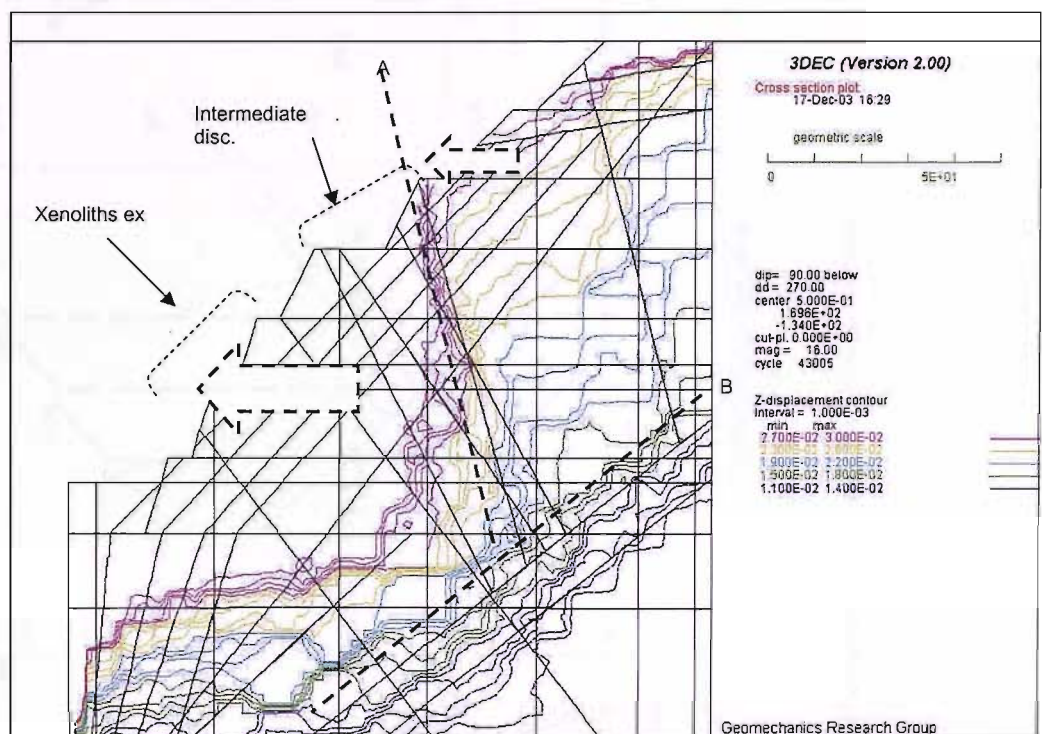
Fig6.87 Contour of y deformation in the 2D model

217
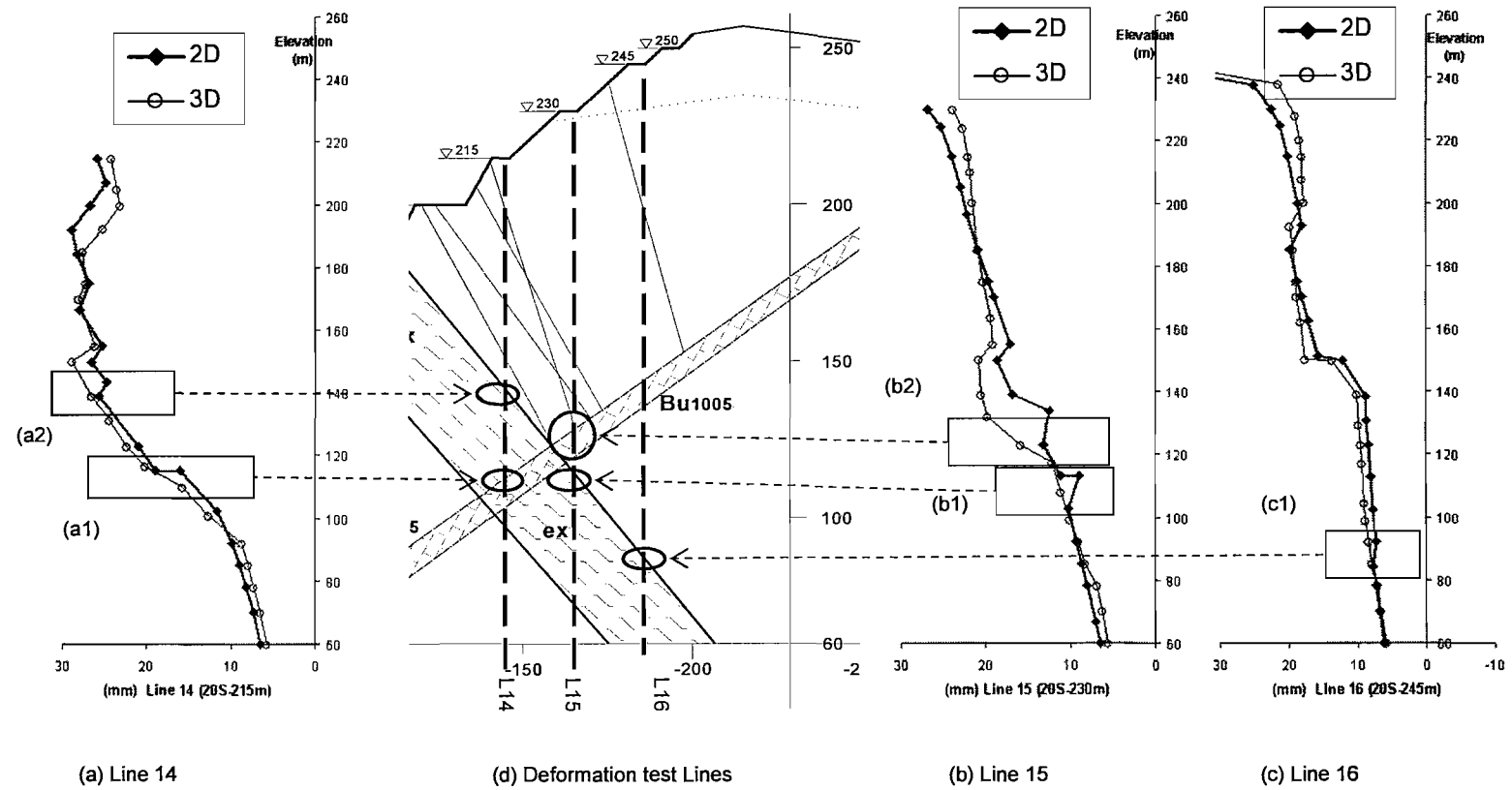
Fig6.88 Slips along discontinuities in model with elastic blocks

6.6.4 Discussion on 2D and 3D modelling

The difference in predicted deformations between the 2D and 3D models is a combined result of the following.

(1) Absence of out-of-plane shear stress ("corner effect") from 2D models

The absence of out-of-plane shear stress tends to increase the deformation predicted by 2D models. The restraints that the out-of-plane shear stresses provide depend mostly on the excavation geometry and in-plane stress level, but does not depend on the magnitude of the in situ out-of-plane shear stress.

When the excavation geometry indicates a significant corner effect, i.e. when the depth-to-length ratio is high, 2D models may not be suitable.

The out-of-plane shear stress is one of the most significant factors that results in the difference between 2D and 3D results.

(2) Lack of control of out-of-plane normal stress

A 2D model predicts a different normal out-of-plane stress Sxx than a 3D model, and could consequently predict different deformation pattern. The normal out-of-plane stress has little effect on the stress condition and movement along the discontinuities in 2D models because the strikes of discontinuities were changed into along the x direction.

A 2D model should not be used when any major out-of-plane deformations are expected on discontinuities or particularly high or low in situ out-of-plane normal stress exists.

(3) Change of orientation and dip of discontinuities

As the dipping of discontinuities are all changed into the section of interest, the possibility of sliding blocks is increased. The apparent dip angle may result in different condition of discontinuities in 2D models from 3D models.

When many discontinuities are on the verge of failure under in situ conditions, a 2D model is not suitable.

6.7 Summary of the chapter

The results of numerical modelling can be summarized as follows.

1. Major and intermediate discontinuities should be modelled explicitly. Groups of intermediate discontinuities can have significant local effects on model deformation.

2. The excavation-induced weakening of the rock surrounding the excavation can be simulated by assuming the existence of an excavation damage/disturbed one (EDZ) with lower mechanical properties than the surrounding rock.

3. The stiffness of the discontinuities was the most sensitive parameter of the model, along with joint friction angle. The model was not sensitive to the cohesion and the dilation angle of discontinuities. Joint model considering post-failure behaviour predicted better results.

4. The modulus of rock blocks was a sensitive parameter for the model deformation. Mohr-Coulomb model simulated rock behaviour better than the elastic model. However the model was not sensitive to the block cohesion or dilation. It was slightly sensitive to block friction depending on the material strength.

5. The plastic zones predicted by the model without EDZ can be used to estimate the range of the developed EDZ though not the zone properties or subzone boundaries. Models with EDZ predicted better results in matching the field data. However, as the range of EDZ is usually small compared to the size of the modelled area, the properties and ranges of the assumed EDZ do not have a very strong influence on the overall prediction.

6. 2D models predict larger deformation and more slips along discontinuities than 3D models. The differences of predicted deformations between 2D and 3D models resulted generally from the difference in stress conditions, boundary conditions and discontinuity orientations that is implicit in 2D modelling.

Chapter 7 Summary, Conclusions and Recommendations

7.1 Summary

In Chapter 2, a comprehensive review of literature on excavations in discontinuous rock was presented. The purpose of the review was to study the factors influencing the behaviour of excavations in discontinuous rock and to investigate appropriate methods for modelling excavations in discontinuous rock. The review was presented in an organized structure: the significance of discontinuities, the behaviour of a single discontinuity and discontinuous rock mass, researches on the excavation damaged/disturbed zone (EDZ) and the numerical solutions available.

In the review, the significance of discontinuities on excavations in discontinuous rock was highlighted. The pattern of discontinuity is a key factor dominating the overall behaviour of the rock masses, and therefore affects significantly the selection of modelling methods.

The behaviour of a single discontinuity was characterized and the factors influencing it were reviewed. However, it remains difficult to obtain satisfactory mechanical properties of discontinuities in field scale. Due to the complexity of discontinuity system, characterizing the behaviour of discontinuous rock masses remains one of the focal questions in rock mechanics. In many circumstances, it is appropriate and necessary to treat rock mass as a continuum with reduced strength and increased deformability compared with intact rock. In practice, it is more common and practical to derive the properties of the equivalent continuum analytically or empirically than by extensive testing program, which is expensive.

The excavation damaged/disturbed zone (EDZ) caused by the excavation activities cannot be avoided in any excavations and it imposes a huge influence on the rock behaviour. The literature shows most of the studies on EDZ in hard rock were related to deep repositories for nuclear wastes in underground rock laboratories (URL) around the world. Methods of characterization and monitoring EDZ are available in the literature. EDZ in deep repositories have been studied and understood well in comparison with those in surface/shallow excavations close to the ground. EDZ in surface/shallow excavations normally have different excavation geometry and scale, geological conditions and focuses of study. These in fact restrain the application of experience from deep repositories to surface/shallow excavations. Limited works have been reported on EDZ in surface/shallow excavations in hard rock, and fewer have taken into consideration of three-dimensional effects.

The available analysis methods for excavations in discontinuous rock were reviewed and classified in two categories according to the purpose they serve: slope stability analysis

and stress analysis. Most of the methods for slope stability analysis are based on the limit equilibrium method and provide simpler results than stress analysis methods. The methods for stress analysis are mostly realized by computer packages based on a discrete method or a continuum method or a combination of both. The choice of a discrete method or a continuum method depends mainly on the problem scale and discontinuity geometry. However, when a discrete method is chosen, the concept of equivalent-continuum may still have to be adopted to incorporate the effect of discontinuities that cannot be modeled explicitly. The computer programs 3DEC and UDEC used in this study are typical examples of discrete method. The concept and modelling capacity of 3DEC and UDEC were introduced in the review.

Finally, the difficulties in modelling excavations in discontinuous rock were summarized in three aspects: lack of information in geological conditions and material properties, lack of suitable conceptual model for rock mass and lack of information on the EDZ.

An introduction to the TGP and the permanent shiplock were presented in Chapter 3. The geological conditions, structures, reinforcement and instrumentation of the shiplock were introduced and the sections of interest were identified.

In Chapter 4, a case study on the deformation mode of the shiplock slopes was carried out based on field deformation data from the TGP. Available survey and inclinometer data provided information on the surface deformations and subsurface deformations of rock. Slips along the inclinometers were investigated. The effects of various factors on deformations were discussed.

In general, the cut slopes deformed towards the excavation gradually during excavation with influence of major discontinuities. Along the x axis (the shiplock axis), the slopes showed different deformation patterns at Sec#17 and Sec#20 due to differences in excavation geometry and geological features. The deformations of the sidewalls of the Middle Pier at Sec#17 were affected by the excavation levels in both near and far side chamber because of limited width of the Middle Pier. Meanwhile those sidewalls at Sec#20 were affected by excavation level in the near side chamber only because of larger width of the pier. The overall deformation pattern of the Middle Pier at Sec#17 was dominated by the overall dipping direction of discontinuities, which resulted in the top of the pier inclining to the north. The Middle Pier at Sec#20 expanded into excavation on both sides as the case of individual excavations. On the north and south slopes, different deformation patterns, namely toppling, sliding and translating were observed locally along slopes as a combined result of various factors including slope geometry, discontinuity pattern, reinforcement, formation of EDZ and geological features. Little evidence was found in field data signifying particular influence of minor discontinuities and some of the intermediate discontinuities on slope deformation.

A number of slips were identified by inclinometer data and they were mostly related to existing discontinuities. Slope geometry and anchorage particularly prestressed cables may also result in slips along inclinometer profiles. Reinforcement like anchorage may impose

noticeable impacts on deformations locally, e.g. the restriction of expansion of the Middle Pier by prestressed through cables. Inclinometer data also showed that EDZ and weathered zones had important effects on deformation of rocks and they result in changes of deformation profile implicitly. But it is difficult to quantify or identify such effects in inclinometer data due to the indefinitive location of these zones.

In Chapter 5, a 3DEC base model was developed and validated with field data for a detailed parametric study. A number of issues were investigated in the study including model construction, geological conditions of weathered zones, in situ stress conditions and material properties. Firstly the distance of model boundaries, particularly along the shiplock axis, and boundary conditions were investigated. It was also found the major discontinuities and intermediate discontinuities had important effects on rock deformation therefore they are needed to be modelled explicitly.

Based on the model developed, a sensitivity study was first carried out for Sec#20 in Chapter 6. The analysis studied the sensitivity of model to discontinuities modelled explicitly, constitutive model and properties of discontinuity, constitutive model and properties of blocks and EDZ subzones. The sensitive parameters identified include discontinuity stiffness, rock modulus and simulation of EDZ. The minor discontinuities were not necessary to model explicitly because counteracting reinforcement were not modelled and due to computational efficiency.

There is no doubt that the stiffness of discontinuities is a sensitive parameter for the model. The actual conditions that the discontinuities are subject to during excavation determine the sensitivity of the model to the strength properties and models of discontinuities. In cases of conditions similar to the shiplock, the model is sensitive to joint friction angle in combination with overall discontinuity orientation relative to excavation. It is not sensitive to joint cohesion or joint dilation angle. Discontinuity models considering post-failure behaviour predict better than Mohr-Coulomb model though subject to the restriction of computational efficiency. The numerical prediction could be more sensitive to the model for discontinuity than varying strength parameters in Mohr-Coulomb model for discontinuities.

Block modulus appears to be one of the most sensitive parameters for the model since it directly affects the magnitude of deformations. Elastoplastic models (Mohr-Coulomb model) for rock blocks simulate rocks better than elastic models when material failure is present. The model is generally slightly sensitive to the friction angle and insensitive to the cohesion of rock blocks with the exception of the weak material in the weathered zone. Block dilation angle is an insensitive parameter to the model.

In the second part of the Chapter, a comparative study of 2D and 3D modelling was carried out based on the 3DEC predictions and UDEC predictions of Sec#20. It was found that three-dimensional models predicted better than two-dimensional models. The reasons for the differential results between the 3D and 2D modelling were discussed and they can be

attributed to different assumptions made on stress simulation and discontinuity representation in the model. The suitability of 3D and 2D modelling was discussed for cases in practice.

7.2 Conclusions

The following conclusions are drawn from the work described in the thesis:

The deformations of the excavations are often of three-dimensional characteristics due to spatial formation of excavation and differential geological features.

In field monitoring during excavations, a combination of survey points and inclinometers provides good insight into the surface and subsurface deformation patterns of the slopes. Inclinometers provide an effective way to identify slips or changes of deformation profiles in deep rock.

The excavation activity itself, in terms of excavation geometry, spatial and temporal sequence, speed etc is one of the most influencing factors on the slope deformation pattern.

Discontinuities are another important factor influencing the deformation of rock mass. Major discontinuities were found to have strong effects on deformation pattern and therefore they need to be modelled explicitly. Intermediate discontinuities may have a large impact on deformation depending on their population and scale relative to the excavated slope. However their effect may be limited by other factors such as excavation geometry and sequence. Minor discontinuities are in some cases unnecessary to model explicitly because (a) counteracting factors such as rock bolts are not modelled; and (b) their presence is so pervasive that their influence can be easily taken into account by equivalent continuum more efficiently. The stiffness and friction angles of discontinuities modelled individually have an important effect on the behaviour of rock mass.

The study has shown that the distinct element method can simulate the excavations in discontinuous rock successfully. To achieve this, firstly it is important to determine the modelling extent and modelling elements in the model that dominate the macroscopic mechanism of model predictions. Secondly it is necessary to fine-tune the modelling elements and material properties. The parametric study provides detailed information on the sensitive parameters of the model and also gives guidance on selection of material properties in the site investigation and numerical modelling.

The excavation damaged/disturbed zone (EDZ) is an important element to include in modelling. The plastic zones predicted by the model without EDZ can be used to estimate the range of the developed EDZ though not the zone properties or subzone boundaries. The model is only slightly sensitive to varying values of materials properties of the EDZ subzones because the scale of the EDZ is usually relatively small in the model.

Three-dimensional models gave better predictions than two-dimensional models because of the different assumptions made on stress condition and discontinuity representation. Normally 2D models predicted larger deformations than the 3D models.

7.3 Recommendations

Recommendations for further study on modelling excavation in discontinuous rock are presented as follows:

Development of a conceptual model that considers the post failure effect of the discontinuities but only requires reasonable input information and computational efforts is needed for more efficient and better modelling excavation by discrete methods.

Better characterization of properties of discontinuity and equivalent continua is still expected in site investigation and parameter derivation stage.

Given the importance of EDZ, further studies on EDZ are needed to provide guidance on predicting quantitatively and modelling EDZ of excavations in discontinuous rock. Particular attention should be paid to field monitoring of the range and properties of EDZ zones. The effect of in situ stress conditions on EDZ remains another issue expecting further investigation. Although groundwater is not considered in this study, development of hydraulic-mechanical coupled analyses is expected for more practical applications.

Based on conceptual understanding of its initiation, quantitative investigation of the difference between 2D and 3D prediction will be useful, e.g. to quantify the effects of out-of-plane shear stress. Analyses and remediation techniques of the influence caused by altered discontinuity orientations in 2D modelling are expected to allow for simpler practical applications instead of 3D modelling.

References

Amadei, B. and R. E. Goodman. 1982. The influence of rock anisotropy on stress measurements by overcoring techniques. Rock Mechanics 15: 167-180.

Amadei, B. and S. Saeb. 1990. Constitutive models of rock joints, Keynote lecture, Proceedings of the International Symposium on Rock Joints, Leon, Norway.

Amadei, B. and W.Z. Savage. 1993. Effect of joints on rock mass strength and deformability, Chapter 17 in Comprehensive Rock Engineering, Vol. 1, p. 331-365, Pergamon Press, John Hudson Editor,

Bandis, S.. 1993. Engineering properties and characterization of rock discontinuities. Comprehensive Rock Engineering. Volume 1. Fundamentals (Hudson J.A, editor). p. 155-183. Pergamon Press, Oxford (UK).

Bandis, S. C. and A. C. Lumsden, et. al.. 1983. Fundamentals of rock joint deformation. International Journal of Rock Mechanics and Mining Sciences & Geomechanics Abstracts 20(6): 249-268.

Bandis, S., A. C. Lumsden, et. al.. 1981. Experimental studies of scale effects on the shear behaviour of rock joints. International Journal of Rock Mechanics and Mining Sciences & Geomechanics Abstracts; 18(1): 1-21.

Bandis, S.C.. 1990. Mechanical properties of rock joints. In Proc. Int. Soc. Rock Mech. symp on rock joints, Loen, Norway, (eds N. Barton and O. Stephansson), 125-140. Rotterdam: Balkema.

Barton, N. 1973. Review of a new shear-strength criterion for rock joints. Eng Geol; 7(4): 287-332.

Barton, N. and K. Bakhtar. 1983. Instrumentation and analysis of a deep shaft in quartzite. Proceedings of the 24th US Symposium on Rock Mechanics, Rock Mechanics: Theory - Experiment - Practice. (code 03136), College Station, TX, USA, Assoc of Engineering Geologists.

Barton, N., S. Bandis, et. al.. 1985. Strength, deformation and conductivity coupling of rock joints. International Journal of Rock Mechanics and Mining Sciences & Geomechanics Abstracts; 22(3): 121-140.

Barton, N. and S.C. Bandis. 1990. Review of predictive capabilities of JRC-JCS model in engineering practice; Rock Joints, p. 603-610.

Barton, N. and V. Choubey. 1977. Shear strength of rock joints in theory and practice. Rock Mech Felsmech Mec Roches; 10(1-2): 1-54.

Barton, N., R. Lien, et. al.. 1974. Engineering classification of rock masses for the design of tunnel support. Norg Geotek Inst, Publ(106).

Belytchko, T., Y. Krongauz, et. al.. 1996. Meshless methods: an overviewand recent developments. Comput Methods Appl Mech Eng; 1996;139:3? 7.

Bieniawski, Z.T.. 1974. Engineering classification of rock masses and its application in tunnelling; Proc. 3rd ISRM-Congress, Denver 1974, Vol. IIa, p. 27-32.

Bieniawski, Z.T.. 1978. Determining rock mass deformability: experience from case histories; Int International Journal of Rock Mechanics and Mining Sciences & Geomechanics Abstracts; Vol.15, p.237-247.

Bieniawski, Z.T.. 1979. The Geomechanics Classification in Rock Engineering Applications. Proceedings, 4th International Congress on Rock Mechanics, ISRM, Montreux. A. A. Ballkema, Rotterdam, Vol. 2:41-48.

Billaux, D, J.P. Chiles, et. al.. 1989. Three-dimensional statistical modeling of a fractured rock mass桎 n example from the Fanay-Augeres Mine. International Journal of Rock Mechanics and Mining Sciences & Geomechanics Abstracts; 26(3/4):281? 9.

Brady, B. H. and E. T. Brown. 1993. Rock mechanics for underground mining, Chapman & Hall.

Brady, B.H.G. and A. Wassyng. 1981. A coupled finite element桄 oundary element method of stress analysis. International Journal of Rock Mechanics and Mining Sciences & Geomechanics Abstracts; 18:475? 5.

Cai, M. and H. Horii. 1992. A constitutive model of highly jointed rock masses; Mechanics and Materials, Elsevier, Vol.13, p.217-246.

Canadian Nuclear Society (CNS). 1996. Designing the Excavation Disturbed Zone for a nuclear repository in hard rock, Proceedings of the EDZ Workshop, International Conference on Deep Geological Disposal of Radioactive Waste, Winnipeg, Canada, 20 September 1996, Canadian Nuclear Society.

Carranza-Torres, C. and C. Fairhurst. 1999. The elasto-plastic response of underground excavations in rock masses that satisfy the Hoek-Brown failure criterion. International Journal of Rock Mechanics and Mining Sciences; 36(6): 777-809.

Chen, E. P.. 1989. A constitutive model for jointed rock mass with orthogonal sets of joints. ASME, J. Appl. Mech; 56(3): 25-32.

Chen, H., J. Zhu, et. al.. 1996. Fractal characteristics of fracture distribution of the Three Gorges Project Permanent shiplock and its significance. Jounal of Chongqing Jiaotong Institute; 15(sup): 14-18.

Chen, X.. 2001. Some technical innovations in anchorage of Three Gorges Permanent Shiplock. China Three Gorges Construction; (1): 18-20.

Chen, Z., S. P. Narayan, et. al.. 2000. An experimental investigation of hydraulic behaviour of fractures and joints in granite rock. International Journal of Rock Mechanics and Mining Sciences; 37(7): 1061-1071.

Chugh, A.K.. 2003. On the boundary conditions in slope stability analysis. Int. J. for Num. and Analyt. Meth. in Geomechanics; (27): 905-926

Coggan, J.S. and R.J. Pine. 1996. Application of distinct element modelling to assess slope stability at Delabole slate quarry, Cornwall, England. Trans IMM, A, 105 A22-A30.

Crouch, S. L. and A. M. Starfield. 1983. Boundary element methods in solid mechanics: with applications in rock mechanics and geological engineering. London, Allen & Unwin.

Cundall, P. A.. 1977. Computer interactive graphics and the distinct element method, in rock engineering for foundations and slopes (Proceedings of the ASCE Specialty Conference, University of Colorado, 1976), Vol. 2, p. 193-199. New York: ASCE, 1977.

Cundall, P.A.. 1980. A generalized distinct element program for modelling jointed rock, Report PCAR-1-80, Peter Cundall Associates, US Army, European Research Office, London.

Cundall, P. A. 1988. Formulation Of a three-dimensional distinct element model - Part I. A scheme to detect and represent contacts in a system composed of many polyhedral blocks. International Journal of Rock Mechanics and Mining Sciences & Geomechanics Abstracts; 25(3): 107-116.

Cundall, P. A., and R. D. Hart. 1984. Analysis of block test no. 1: In elastic rock mass behavior phase 2: A characterization of joint behavior (final report). Itasca C. G., Minneapolis, Minnesota.

CWRC, 1997. Study of the permanent navigation structures of the Three Goreges Project. Wuhan. Hubei Science and Technology Press.

Cunha, P. D. (Ed.), 1990, Scale effects in rock masses. 339 p., A. A. Balkema, Rotterdam.

Damjanac, B.A.. 1996. Three-dimensional numerical model of water flow in a fractured rock mass. Ph.D. Thesis, University of Minnesota, February 1996.

Dasari, G.R.. 1996. Modelling the variation of soil stiffness during sequential construction. PhD thesis, University of Cambridge, UK

Deere, D.U.. 1968. Geologic Considerations. Chapter 1 of Rock Mechanics in Engineering Practice, K. G. Stagg and O. C. Zienkiewicz, cd., Wiley, New York.

Deng, J. H. and C. F. Lee. 2001. Displacement back analysis for a steep slope at the Three Gorges Project site. International Journal of Rock Mechanics and Mining Sciences; 38(2): 259-268.

Duncan, J.M.. 1996. Soil slope stability analysis. Landslides Investigation and Mitigation, Special Report 247, Transportation Research Board, National Academy Press, 129-173.

Duncan, J.M. and R.E. Goodman. 1968. Finite element analysis of slope in jointed rock. U.S. Army Corps of Engineers Contract Report No. S-68-3.

Dunnicliff, J. and G. E. Green. 1993. Geotechnical instrumentation for monitoring field performance. New York, Wiley.

Einstein, H.. 1993. Modern developments in discontinuity analysis, the Persistence-Connectivity Problem, Vol. 3, Chapter 9, Comprehensive Rock Engineering, (Hudson, H.A. et. al., eds.) Pergamon.

Emsley, S. et. al.. 1997. ZEDEX - A study of damage and disturbance from tunnel excavation by blasting and tunnel boring, SKB TR-97-03.

European Commission CLUSTER. 2003. Impact of the Excavation Disturbed or Damaged Zone (EDZ) on the performance of radioactive waste geological repositories. Proceedings of an EC CLUSTER Conference, Luxembourg, 03? 5 November 2003, Nuclear Science and Technology, EUR 21028 EN, 2004.

Fairhurst, C. and B. Damjanac. 1999. The Excavation Damage Zone ? An International Perspective. In Distinct Element Modeling in Geomechanics, pp. 1-26. V. M. Sharma et al., Eds. New Delhi: Oxford & IBH Publishing, 1999.

Feng, X. T., Z. Zhang, et. al.. 2000. Estimating mechanical rock mass parameters relating to the Three Gorges Project permanent shiplock using an intelligent displacement back analysis method. International Journal of Rock Mechanics and Mining Sciences; 37(7): 1039-1054.

Fossum, A. F.. 1985. Effective elastic properties for a randomly jointed rock mass. International Journal of Rock Mechanics and Mining Sciences; 22(6): 467-470.

Fu, B. Q.. 1999. Research Rep2: Study of deformation monitoring control indices for the Three Gorges Permanent Shiplock slopes. Wuhan, China, Yangtze River Scientific Research Institute.

Gao, D. and Y. Zeng. 2001. Monitoring analysis on prestress state anchor cable of high slope of the TGP permanent shiplocks. Chinese Journal of Rock Mechanics and Engineering; 20(5): 653-656.

Gerrard, C.M.. 1982. Elastic models of rock masses having one, two and three sets of joints.; International Journal of Rock Mechanics and Mining Sciences & Geomechanics Abstracts; 19: 15-23.

Giani, G.P.. 1992. Rock Slope Stability Analysis. A.A. Balkema.

Gong, et. al.. 1995. Measurement and analysis of the in situ stress in the shiplock area in the TGP. Journal of Yangtze River Scientific Research Institute; 1995(2).

Goodman, R.E.. 1976. Methods of geological engineering in discontinuous rock, West Publishing Company, St. Paul, MN.

Goodman, R.E.. 1980. Methods of geological engineering in discontinuous rock, Wiley and Sons, NY.

Goodman, R. E. and G. Shi. 1985. Block theory and its application to rock engineering. Englewood Cliffs, N.J, Prentice-Hall.

Goodman, R.E., and D.S. Kieffer. 2000. Behavior of rock in slopes. Journal of Geotechnical and. Geoenvironmental Engineering, Vol 126, No. 8, August, 2000.

Griffith, A.A.. 1924. The theory of rupture. Trans. First Intl. Cong. Appl. Mech. Delft, 55-63.

Hayward, T.. 2000. Field studies, analysis and numerical modelling of retaining walls embedded in weak rock. Ph.D. thesis, University of Southampton, UK.

Heliot, D.. 1988. Generating a blocky rock mass,. International Journal of Rock Mechanics and Mining Sciences & Geomechanics Abstracts; 25(3): 127-138.

Heuze, F. E.. 1980. Finite element models for rock fracture mechanics. International Journal for Numerical and Analytical Methods in Geomechanics; 4: 25-43.

Hocking, G.. 1992. The discrete element method for analysis of fragmentation of discontinua. Eng Comput; 9:145? 5.

Hoek, E.. 1983. Strength Of Jointed Rock Masses. Geotechnique; 33(3): 157-223.

Hoek, E.. 2002. A brief history of the development of the Hoek-Brown failure criterion. URL: www.rocscience.com/hoek/pdf/history%20of%20the%20hoek%20brown%20criterio n.pdf

Hoek, E. and B. H. G. Bray, et. al.. 1983. Rock slope engineering. Institution of Mining and Metallurgy. London,.

Hoek, E. and E. T. Brown, et. al.. 1980. Underground excavations in rock. The Institution of Mining and Metallurgy. London,

Hoek, E. and E.T. Brown. 1988. The Hoek-Brown failure criterion - a 1988 update. In Rock engineering for underground excavations, proc. 15th Canadian rock mech. symp.,(ed. J.C. Curran), 31-38. Toronto: Dept. Civil Engineering, University of Toronto.

Hoek, E. and E. T. Brown. 1997. Practical estimates of rock mass strength. International Journal of Rock Mechanics and Mining Sciences 34(8): 1165-1186.

Hoek, E., P. K. Kaiser, et. al.. 1995. Support of underground excavations in hard rock. Rotterdam, A.A. Balkema.

Hopkins, D. L.. 2000. The implications of joint deformation in analyzing the properties and behavior of fractured rock masses, underground excavations, and faults. International Journal of Rock Mechanics and Mining Sciences; 37(1-2): 175-202.

Huang considering large displacements and non strain relationships of rock joints. In: Yuan J, editor. Computer methods and advances in geomechanics, vol. 1. Rotterdam: Balkema, 1997. p. 507? 2.

International Atomic Energy Agency (IAEA). 2001. The use of scientific and technical results from underground research laboratory investigations for the geological disposal of radioactive waste, IAEA Vienna 2001. ISSN 1011-4289, IAEA-TECDOC-1243.

I.S.R.M.. 1978. Suggested methods for the quantitative description of discontinuities in rock masses. International Journal of Rock Mechanics and Mining Sciences & Geomechanics Abstracts; 15: 319-368.

Itasca Consulting Group. 1996. Universal Distinct Element Code (UDEC) - User manual. Minneapolis, Minnesota.

Itasca Consulting Group, 1998. 3 Dimensional Distinct Element Code (3DEC) - User's Guide. Minneapolis, Minnesota.

Itasca Consulting Group, 2002. Personal communication. Minneapolis, Minnesota.

Jaeger, J. and N. G. W. Cook. 1969. Fundamentals of rock mechanics, Methuen & CO LTD.

Janbu, N.. 1973. Slope stability computations. Embankment Dam Engineering, The Casagrande Volume, Wiley and Sons, NY, p. 47-86.

Jing, L.. 2000. Block system construction for three-dimensional discrete element models of fractured rocks. International Journal of Rock Mechanics and Mining Sciences; 37(4): 645-659.

Jing, L.. 2003. A review of techniques: advances and outstanding issues in numerical modelling for rock mechanics and rock engineering. International Journal of Rock Mechanics and Mining Sciences; 40: 283-353.

Jing, L. and J. A. Hudson. 2002. Numerical Methods in Rock Mechanics. International Journal of Rock Mechanics and Mining Sciences; 39: 409-427.

Jing, L., Y. Ma, and Z. Fang. 2001. Modelling of fluid flow and solid deformation for fractured rocks with discontinuous deformation analysis (DDA) method. International Journal of Rock Mechanics and Mining Sciences; 38(3): 343? 5.

Kaiser, P.K. and S. Yazici. 1992. Computerized data collection system for rockmass failures in underground openings. International Journal of Rock Mechanics and Mining Sciences & Geomechanics Abstracts; 29 (4): 431-446.

Kim, Y., B. Amadei and E. Pan. 1999. Modelling the effect of water, excavation sequence and rock reinforcement with discontinuous deformation analysis. International Journal of Rock Mechanics and Mining Sciences; 36(7): 949? 0.

Konietzky, H. and P. Marschall. 1996. Excavations disturbed zone around tunnels in fractured rock - Example from the Grimsel test site. Geomechanics '96,pp. 235-240. Z. Rakowski, Ed. Rotterdam: Balkema, 1996.

Kulahway, F. H.. 1975. Stress-deformation properties of rock and rock discontinuities; Eng Geol.; 8:327-350.

Kulatilake, P.H.S.W., H. Ucpirti, et. al.. 1992. Use of the distinct element method to perform stress analysis in rock with non-persistent joints and to study the effect of joint geometry parameters on the strength and deformability of rock masses. Rock Mechanics and Rock Engineering; 25:253-274.

Kulatilake, P.H.S.W., B. Malama and J. Wang. 2001. Physical and particle flow modelling of jointed rock block behavior under uniaxial loading. International Journal of Rock Mechanics and Mining Sciences; 38: 641-657.

Lauffer, H.. 1958. Gebirgsklassljizierung fur den Stollenbau, Geologic und Bauwesen. Vol. 24, No. 1:46-51.

Lee, F. H., Yong, K. Y., Quan, K. C., and Chee, K. T.. 1998. Effect of corners in strutted excavations: field monitoring and case histories. J. Geotech. Engrg., ASCE; 124(4): 339-349.

Leichnitz, W.. 1985. Mechanical properties of rock joints; International Journal of Rock Mechanics and Mining Sciences & Geomechanics Abstracts; 22(5):313-321.

Lemos, L.J.L., A.W. Skempton and P.R. Vaughan. 1985. Earthquake loading of shear surfaces in slopes. Proc., 11th Int. Conf. Soil Mech. And Found. Engrg. 4: 1955-1958.

Liu, Y., B. Gong, et. al.. 1992. Preliminary study of the geostress field of shiplock area of the Three Gorges Project. Journal of Yangtze River Scientific Research Institute 29(sum): 77-82.

Lorig, L.J., B.H.G. Brady and P.A. Cundall. 1986. Hybrid distinct element/boundary element analysis of jointed rock. International Journal of Rock Mechanics and Mining Sciences & Geomechanics Abstracts; 23(4):303? 12.

McEwen, T.. 2003. Review of the Conclusions of Previous EDZ Workshops, Invited lectures on A European Commission CLUSTER Conference and Workshop on EDZ in Radioactive Waste Geological Repositories Cluster03, URL: http://www.sckcen.be/sckcen_en/activities/conf/conferences/related_sck/20031103/Invited_le ctures/ILMcewen.pdf

Mohammad, N., D. J. Reddish and L.R. Stace. 1997.The relation between in situ and laboratory rock properties used in numerical modelling, International Journal of Rock Mechanics and Mining Sciences; 34(2) :289-97.

Nawrocki, P. A. and Z. Mroz. 1999. A constitutive model for rock accounting for viscosity and yield stress degradation. Computers and Geotechnics; 25(4): 247-280.

Nicholson, G. A.. 1983. In-Situ and laboratory shear devices for rock: A comparison. Technical Report GL- 83-14, U.S. Army Engineer Waterways Experiment Station, Vicksburg, MS 39180.

Nuclear Energy Agency (NEA). 1989. Excavation response in geological repositories for radioactive waste, Proceedings of an NEA Workshop, Winnipeg, Canada, 26-28 April 1988, OECD/NEA, Paris.

Nuclear Energy Agency (NEA). 2002. Characterisation and representation of the Excavation Disturbed or Damaged Zone (EDZ). Lessons learnt from a SEDE Topical Session, September 1998, Paris. NEA Report NEA/RWM (2002)1.

Olsson, R. and N. Barton. 2001. An improved model for hydromechanical coupling during shearing of rock joints. International Journal of Rock Mechanics and Mining Sciences; 38(3): 317-329.

Pan, X.D. and M.B. Reed. 1991. A coupled distinct element? nite element method for large deformation analysis of rock masses. International Journal of Rock Mechanics and Mining Sciences & Geomechanics Abstracts; 28(1):93? .

Patton, F.D.. 1966. Multiple modes of shear failure in rocks. PhD. University of Illinois.

Pratt, H.R., A.D. Black and W.F. Brace. 1974. Friction and deformation of jointed quartzite diorite, Proc. 3rd Cong. of Intl. Soc. Rock Mech., Denver, v. I.A, 243-317. .

Pusch, R.. 1989. Alteration of the hydraulic conductivity of rock by tunnel excavation. International Journal of Rock Mechanics and Mining Sciences & Geomechanics Abstracts; 26(1): 71? 3.

Pusch R.. 2003. Lessons Learned with Respect to EDZ in Crystalline Rock, CLUSTER03.

Pyrak-Nolte, L. J. and J. P. Morris. 2000. Single fractures under normal stress: The relation between fracture specific stiffness and fluid flow. International Journal of Rock Mechanics and Mining Sciences; 37(1-2): 245-262.

Read, R. S.. 2004. 20 years of excavation response studies at AECL担Underground Research Laboratory, International Journal of Rock Mechanics and Mining Sciences; 41:1251-1275.

Saeb, S. and B. Amadei. 1992. Modelling rock joints under shear and normal loading. International Journal of Rock Mechanics and Mining Sciences & Geomechanics Abstracts; 29(3): 267-278.

Sarma, S. K.. 1973. Stability analysis of embankment and slopes. Geotechnique; 23:423-433.

Sellers, E.J. and P. Klerck. 2000. Modelling of the effect of discontinuities on the extent of the fracture zone surrounding deep tunnels. Tunnelling and Underground Space Technology, Vol. 15, pp. 463-469.

Sharma, V.M., K.R., Saxena, et. al.. 1999. Distinct element modelling in geomechanics. Rotterdam, Balkema.

Shen, B., N. Barton 1997. The disturbed zone around tunnels in jointed rock masses. International Journal of Rock Mechanics and Mining Sciences; 34: 117-125.

Sheng, Q., et. al.. 2002. Estimating the excavation disturbed zone in the permanent shiplock slopes of the Three Gorges Project, China, International Journal of Rock Mechanics and Mining Sciences; 39(2): 165-184.

Shi, A. and X. Huang. 1997. Characteristics of underground water in the area of shiplock of TGP and its engineering measures. Renmin Changjiang; 28(6).

Singh, B.. 1973. Continuum characterization of jointed rock masses. Part I-The constitutive equations. International Journal of Rock Mechanics and Mining Sciences & Geomechanics Abstracts; 10: 311-335

Sitharam, T.G., J. Sridevi, et. al.. 2001. Practical equivalent continuum characterization of jointed rock masses. International Journal of Rock Mechanics and Mining Sciences; 38(3): 437-448.

Skinas, C.A., S.C. Bandis and C.A. Demiris. 1990. Experimental investigations and modelling of rock joint behaviour under constant stiffness. In Proc Rock Joints, Loen, Norway, 1990. p. 301.

Souley, M., F. Homand and A. Thoraval. 1997. The effect of joint constitutive laws on the modelling of an underground excavation and comparison with in-situ measurements. International Journal of Rock Mechanics and Mining Sciences & Geomechanics Abstracts; 34(1): 97-115.

Stallebrass, S.E., V. Jovicic and R.N. Taylor. 1994. The influence of recent stress history on ground movements around tunnels. Pre-failure Deformation of Geomaterials (Shibuya, Mitachi and Miura eds), p 615-620, Balkema, Hotterdam, ISBN 905410399.

Stark, T.D. and H.T. Eid. 1998. Performance of three-dimensional slope stability methods in practice. J. Geotech. Geoenviron. Engr., ASCE, 124:11, 1049-1060 (1998).

Stephansson, O., et. al.. 1985. Fundamentals of rock joints proceedings of the International Symposium on Fundamentals of Rock Joints, Bjorkliden, 15-20 September 1985. Lulea, Centek.

Terzaghi, K.. 1946. Rock defects and loads on tunnel support. Rock Tunneling with Steel Support. R. V. Proctor and T. White, Commercial Shearing Co., Youngstown, OH: 15-99.

Thomas, A., A. Pienau and J.-L. Blin-Lacroix. 1987. Determination of a spatial fracture network. International Journal of Numerical and Analytical Methods in Geomechanics, 11, 381? 90, 1987.

Toledo, P.E.C. and M.H. Freita. 1993. Laboratory testing and parameters controlling the shear strength of filled rock joints. Geotechnique XLIII(1): 1-19.

Tsang, C.F., F. Bernier and C. Davies. 2005. Processes in the excavation damaged zone in crystalline rock, rock salt, and indurated and plastic clays, International Journal of Rock Mechanics & Mining Sciences; 42(1): p. 109-125, LBNL-55700.

USACE. 1994. Rock foundation. Engineer Manual: EM 1110-1-2908, Department of the Army, U.S. Army Corps of Engineers.

Wei, L, and J.A. Hudson. 1988. A hybrid discrete束continuum approach to model hydromechanical behaviour of jointed rocks. Eng Geol; 49:317? 5.

Wei, Z.Q. and J.A. Hudson, 1986. The influence of joints on rock modulus. Proceedings of the International Symposium Rock Engineering. in Complex Rock Formations. Beijing, China: Science Press, 1986. p. 54? 2.

Weissbach, G.. 1978. A new method for the determination of the roughness of rock jointsin the laboratory. International Journal of Rock Mechanics and Mining Sciences & Geomechanics Abstracts; 15: 131-133.

Wickham, G. E., H. R. Tiedemann and E. H. Skinner. 1972. Support determinations based on geologic predictions. Proceedings, First Rapid Excavation and Tunneling Conference, Chicago, VOII.

Wibowo, J.L. 1997. Consideration of secondary blocks in key-block analysis. International Journal of Rock Mechanics and Mining Sciences; 34(3/4), Paper No. 333.

Xu, N., X. Yu, et. al.. 2001. Design of the underground drainage system and its effect verification for high slope of the TGP permanent shiplock. Chinese Journal of Rock Mechanics and Engineering; 20(5): 738-741.

Yang, Z.Y., J.M. Chen, et. al.. 1998. Effect of joint sets on the strength and deformation of rock mass models. International Journal of Rock Mechanics and Mining Sciences; 35(1): 75-84.

Yoshida, H. and H. Horii. 1998. Micromechanics-based continuum analysis for the excavation of large-scale underground cavern. Proc. of SPE/ISRM Rock Mech. in Petro. Eng., 8-10 July 1998, Trondheim, Norway, 1 (1998) 209-218.

Zhang, X. and M.W. Lu. 1998. Block-interfaces model for non-linear numerical simulations of rock structures. International Journal of Rock Mechanics and Mining Sciences; 35(7): 983-990.

Zhang, X., W. Powrie, et. al.. 1999. Estimation of permeability for the rock mass around the shiplocks of the Three Gorges Project, China. International Journal of Rock Mechanics and Mining Sciences; 36(3): 381-397.

Zhang, Y. and W. Zhou. 1999. Deformation and stability of high rock slopes. Beijing, Water Power Press.

Zhao, J., Z. Zhang, et. al.. 1999. A study on drainage system in the high slopes of the Three Gorges Project's permanent lock. Journal of Nanjing Hydraulic Research Institute (Shui Li Shui Yun Ke Xue Yan Jiu); (4): 390-395.